UNIVERSITY OF CALIFORNIA SAN DIEGO

Metal-Organic Framework Polymer Hybrid Materials for Chemical Warfare Agent Degradation

A dissertation submitted in partial satisfaction of the requirements
for the degree Doctor of Philosophy

in

Chemistry

by

Mark Kalaj

Committee in charge:

Professor Seth M. Cohen, Chair
Professor Joshua S. Figueroa
Professor Jeremy K. Klosterman
Professor Jonathan K. Pokorski
Professor Jeffrey D. Rinehart

2021

The Dissertation of Mark Kalaj. is approved, and it is acceptable in quality and form for publication on microfilm and electronically.

University of California San Diego

2021

DEDICATION

To my parents, Leonard and Margerita Kalaj, thank you for all the sacrifices you have made for me, I am forever in your debt. Ju du shumë fort.

TABLE OF CONTENTS

LIST OF FIGURES

LIST OF SCHEMES

LIST OF TABLES

ACKNOWLEDGEMENTS

First, I would like to acknowledge my advisor, Professor Seth M. Cohen, for his guidance and support throughout my graduate studies. His leadership and mentorship were vital for my success in graduate school. Seth is someone who truly leads by example, he is one of the most capable and hardworking people I have ever encountered. His efficiency and leadership (especially during difficult times) have truly inspired me and made be a better scientist and leader. He has built an incredible team of highly motivated and ambitious postdocs and graduate students throughout the years and I look forward to seeing the success of the Cohen Lab in the future. I commend him for always willing to work harder than anyone in his lab despite being one of the most decorated academic professors, it is truly inspiring. Throughout my time at UCSD, Seth has been both a mentor and a friend, and I look forward to a lifelong friendship in the future, thank you Seth!

Thank you to all past and present members of the Cohen lab who have supported me as colleagues and as friends. I want to thank my cohort lab mates Kyle S. Barcus, Ryjul W. Stokes, and Stephanie M. McCabe for their friendship and support throughout graduate school. I would especially like to thank Dr. Kyle C. Bentz for being an awesome mentor and even a better friend in the lab, I will never forget the great times we spend in and out of lab! I would also like to thank all of those who worked on various projects and papers with me your insight was vital to my success.

I would like to acknowledge my outside collaborators, particularly Professor Francesco Paesani and Dr. Mohammed R. Momeni for their theoretical measurements and deeper insight into the catalytic behavior of materials discussed in this thesis. I would especially like to thank Dr. Milan Gembicky for teaching me the nuts and bolts of X-ray Crystallography, you are one

of the most skilled scientists I have ever met, and I am also happy to call you a friend, thank you.

I would especially like to thank Professor Korey P. Carter and Professor Christopher L. Cahill for mentoring me as an undergraduate researcher at The George Washington University. They were instrumental in my decision to pursue a PhD in chemistry, thank you for all your support and friendship throughout the years. I would also like to thank my committee members, especially Professor Joshua S. Figueroa for his guidance, mentorship, and willingness to always push me to the next level, I appreciate it.

I would also like to thank my immediate and extended family for their countless support and unconditional loves throughout the years. In particular, I would like to thank my uncle Fr. Frederik Kalaj for always inspiring me to take a step back and think about my projects more broadly and to think outside the box, our discussions played an important role in my success. I would also like to thank my future in laws, Miguel Sierra and Samantha Sierra for making Bakersfield, CA my home away from home, I always looked forward spending time with you guys and enjoying great company and laughs, thank you. I would especially like to thank my parents Leonard Kalaj and Margerita Kalaj for leading by example and teaching me that anything is possible with hard work and determination. I would also like to thank my siblings, Anita Kalaj, Jozefina Kalaj and Kristian Kalaj for always leading by example and paving the way for me throughout my life, nothing would be possible without your help and support.

Finally, I would like to thank my amazing fiancée Brianna N. Sierra for your unconditional support and love throughout graduate school. Meeting you was the best thing that happened to me in graduate school. Thank you for being my biggest supporter, my everyday lunch date, and always being there to pick me up when things get difficult. I look forward to

spending the rest of my life with you and am very excited to see what the future holds for us! I love you Zemer.

Chapter 1, in part, is a reprint of the following materials: "MOF-Polymer Hybrid Materials: From Simple Composites to Tailored Architectures" *Chem. Rev.* **2020**, *120*, 8267-8302; "Postsynthetic Modification: An Enabling Technology for the Advancement of Metal-Organic Frameworks" *ACS Cent. Sci.* **2020**, *6*, 1046-1057. The dissertation author was the primary author for both of these review articles and gratefully acknowledges the contributions of coauthors Kyle C. Bentz, Sergio Ayala Jr., Joseph M. Palomba, Kyle S. Barcus, Yuji Katayama, and Seth M. Cohen.

Chapter 2, in part, is a reprint of the material, "Nylon-MOF Composites through Postsynthetic Polymerization" *Angew. Chem. Int. Ed.* **2019**, *58*, 2336-2340. The dissertation author was the primary author of this manuscript and gratefully acknowledges the contributions of coauthors Michael S. Denny Jr., Kyle C. Bentz, Joseph M. Palomba, and Seth M. Cohen.

Chapter 3, in part, is a reprint of the following materials: "Multiple Functional Groups in UiO-66 Improve Chemical Warfare Agent Simulant Degradation" *Chem. Commun.* **2019**, *55*; 5367-5370; "Halogen Bonding in UiO-66 Frameworks Promotes Superior Chemical Warfare Agent Simulant Degradation" *Chem. Commun.* **2019**, *55*, 3481-3484. The dissertation author was the primary author for both of these manuscripts and gratefully acknowledges the contributions of coauthors Mohammad R. Momeni, Kyle C. Bentz, Joseph M. Palomba, Kyle S. Barcus, Francesco Paesani, and Seth M. Cohen.

Chapter 4, in part, is a reprint of the material, "Spray Coating of Catalytically Active MOF-Polythiourea through Postsynthetic Polymerization" *Angew. Chem. Int. Ed.* **2020**, *59*,

13984-13989. The dissertation author was the primary author of this manuscript and gratefully acknowledges the contributions of coauthor Seth M. Cohen.

Chapter 5, in part, is a reprint of the material, "Room Temperature Aqueous Synthesis of UiO-66 Derivatives via Postsynthetic Exchange" *Dalton Trans.* **2020**, *49*, 8841-8845. The dissertation author was the primary author of this manuscript and gratefully acknowledges the contributions of coauthors Kathleen E. Prosser and Seth M. Cohen.

VITA

Education

2016	Bachelor of Science, The George Washington University
2019	Master of Science, University of California, San Diego
2021	Doctor of Philosophy, University of California San Diego

Honors and Awards

2021	ACS Division of Inorganic Chemistry Young Investigator Award
2020	ACS Division of Inorganic Chemistry Travel Award – ACS Philadelphia
2019	Teddy G. Traylor Award – UCSD
2019-2021	Achievement Rewards for College Scientists Foundation Fellow – UCSD
2018-2021	National Defense Science and Engineering Graduate Fellow – DoD
2018	NSF Graduate Research Fellowship (Honorable Mention)

Peer-Reviewed Publications (in reverse chronological order):

32. Kelly M. Hunter, Jackson C. Wagner, **Mark Kalaj**, Seth M. Cohen, Wei Xiong, Francesco Paesani. "Simulation Meets Experiment: Unraveling the Properties of Water in Metal-Organic Frameworks Through Vibrational Spectroscopy" *J. Phys. Chem. A* **2021**, **Accepted.**

31. Kathleen E. Prosser, Alysia, J. Kolhbrand, Hyeonglim S. Seo, **Mark Kalaj**, Seth M. Cohen. "^{19}F-Tagged Metal Binding Pharmacophores for NMR Screening of Metalloenzymes" *Chem. Commun.* **2021**, **Accepted.**

30. Joseph M. Palomba, David M. Wirth, Jun Yeong Kim, **Mark Kalaj**, Evan M. Clarke, Gregory W. Peterson, Jonathan K. Pokorski, Seth M. Cohen. "Strong, Ductile MOF-Polyurethane Urea Composites" *Chem. Mater.* **2021**, *33*, 3164-3171.

29. Johannes Karges, **Mark Kalaj**, Milan Gembicky, Seth M. Cohen. "Re(I) Tricarbonyl Complexes as Covalent Inhibitors for the SARS-CoV-2 Main Cysteine Protease" *Angew. Chem. Int. Ed.,* **2021**, *133,* 10811-10818.

28. Korey P. Carter, **Mark Kalaj**, Sapphire McNeil, Andrew Kerridge, Mark H. Schofield, J. August Ridenour, Christopher L. Cahill, "Structural, Spectroscopic, and Computational Evaluations of Cation-Cation and Halogen Bonding Interactions in Heterometallic Uranyl Hybrid Materials" *Inorg. Chem. Front.* **2021**, *8*, 1128-1141.

27. Yijun Xie, Kelsey A. Krug, Kristine Cay, **Mark Kalaj**, Naneki C. McCallum, Zofia E. Siwicka, Zhao Wang, Nathan C. Gianneschi, Michael D. Burkart, Jeffrey D. Rinehart. "Peroxidase-Like Reactivity at Iron-Chelation Sites in a Mesoporous Synthetic Melanin" *CCS Chemistry* **2020**, *2*, 1483-1490.

26. Robert G. Surbella, Korey P. Carter, Trevor D. Lohrey, Dallas Reilly, **Mark Kalaj**, Bruce K. McNamara, Jon Schwantes, Rebecca J. Abergel. "Rational Design of a Uranyl Metal-Organic Framework for the Capture and Colorimetric Detection of Organic Dyes" *Chem. Eur. J.* **2020**, *26*, 13819-13825.

25. **Mark Kalaj**, Kathleen E. Prosser, Seth M. Cohen. "Room Temperature Aqueous Synthesis of UiO-66 Derivatives via Postsynthetic Exchange" *Dalton. Trans.* **2020**, *49*, 8841-8845.

24. **Mark Kalaj**, Seth M. Cohen. "Postsynthetic Modification: An Enabling Technology for the Advancement of Metal-Organic Frameworks" *ACS Cent. Sci.* **2020**, *6*, 1046-1057.

23. **Mark Kalaj**, Seth M. Cohen. "Spray Coating of Catalytically Active MOF-Polythiourea through Postsynthetic Polymerization" *Angew. Chem., Int. Ed.* **2020**, *59,* 13984-13989.

22. Jerika A. Chiong, Jie Zhu, Jake B. Bailey, **Mark Kalaj,** Rohit H. Subramanian, Wenqian Xu, Seth M. Cohen, F. Akif Tezcan. "An Exceptionally Stable Metal-Organic Framework Constructed from Chelate-based Metal-Organic Polyhedra" *J. Am. Chem. Soc.* **2020**, *142,* 6907-6912.

21. Joseph M. Palomba, Steven P. Harvey, **Mark Kalaj**, Brian R. Pimentel, Jared B. Decoste, Gregory W. Peterson, Seth M. Cohen. "High-throughput screening of MOFs for breakdown of V-series nerve agents" *ACS Appl. Mater. Interfaces* **2020**, *12*, 14672-14677.

20. **Mark Kalaj**, Kyle C. Bentz, Sergio Ayala Jr., Joseph M. Palomba, Kyle S. Barcus, Yuji Katayama, Seth M. Cohen. "MOF-Polymer Hybrid Materials: From Simple Composites to Tailored Architectures" *Chem. Rev.* **2020**, *120*, 8267-8302. (*Highlighted Cover Article)*

19. Linfeng Chen, Khin A. San, Michael J. Turo, Milan Gembicky, Shelir Fereidouni, **Mark Kalaj**, Alina M. Schimpf. "Tunable Metal Oxide Frameworks via Coordination Assembly of Preyssler-Type Molecular Clusters" *J. Am. Chem. Soc.* **2019**, *141*, 20261-20268.

18. Yuji Katayama, **Mark Kalaj**, Kyle S. Barcus and Seth M. Cohen. "Self-Assembly of Free-Standing MOF Nanoparticle Monolayers" *J. Am. Chem. Soc.* **2019**, *141*, 20000-20003.

17. Kyle C. Bentz, Sergio Ayala Jr., **Mark Kalaj**, Seth M. Cohen. "Polyacids as Modulators for the Synthesis of UiO-66" *Aust. J. Chem.* **2019**, *72*, 848-851.

16. Korey P. Carter, J. August Ridenour, **Mark Kalaj**, Christopher L. Cahill. "A Thorium Metal-Organic Framework with Outstanding Thermal and Chemical Stability" *Chem. Eur. J.,* **2019**, *25*, 7114-7118.

15. **Mark Kalaj**, Joseph M. Palomba, Kyle C. Bentz, Seth M. Cohen. "Multiple Functional Groups in UiO-66 Improve Chemical Warfare Agent Simulant Degradation" *Chem. Commun.* **2019,** *55*, 5367-5370.

14. **Mark Kalaj**, Mohammad R. Momeni., Kyle C. Bentz, Kyle S. Barcus, Joseph M. Palomba, Francesco Paesani, Seth M. Cohen. "Halogen Bonding in UiO-66 Frameworks Promotes Superior Chemical Warfare Agent Simulant Degradation" *Chem. Commun.* **2019**, *55*, 3481-3484.

13. **Mark Kalaj**, Michael S. Denny Jr., Kyle C. Bentz, Joseph M. Palomba, Seth M. Cohen. "Nylon-MOF Composites through Postsynthetic Polymerization" *Angew. Chem., Int. Ed.* **2019**, *58*, 2336-2340.

12. Michael S. Denny Jr., **Mark Kalaj**, Kyle C. Bentz, Seth M. Cohen. "Multicomponent Metal-organic Framework Membranes for Advanced Functional Composites" *Chem. Sci.* **2018**, *9*, 8842-8849.

11. Joseph M. Palomba, Cy V. Credille, **Mark Kalaj**, Jared B. Decoste, Gregory W. Peterson, Tristan M. Tovar, Seth M. Cohen, "High-Throughput Screening of Solid-State Catalysis for Nerve Agent Degradation" *Chem. Commun.,* **2018**, *54*, 5768-5771.

10. Korey P. Carter, **Mark Kalaj**, Andrew Kerridge, Christopher L. Cahill, "Probing Hydrogen and Halogen-oxo Interactions in Uranyl Coordination Polymers: A Combined Crystallographic and Computational Study" *Cryst. Eng. Comm.* **2018**, *20*, 4916-4925. (*Highlighted Cover Article)*

9. Korey P. Carter, Robert G. Surbella, **Mark Kalaj**, Christopher L. Cahill, "Restricted Speciation and Supramolecular Assembly in the 5f block" *Chem. Eur. J.,* **2018**, *24*, 12747-12756. (*Highlighted "Outstanding Review" by Chem. Eur. J.)*

8. Korey P. Carter, **Mark Kalaj**, Andrew Kerridge, James A. Ridenour, Christopher L. Cahill, "How to Bend the Uranyl Cation via Crystal Engineering" *Inorg. Chem.,* **2018**, *57*, 2714-2723.

7. Korey P. Carter, Simon J. A. Pope, **Mark Kalaj**, R. J. Holmberg, M. Murugesu, Christopher L. Cahill, "Exploring the Promotion of Synthons of Choice: Halogen Bonding in Molecular Lanthanide Complexes Characterized via X-ray Diffraction, Luminescence Spectroscopy, and Magnetic Measurements" *Z. Anorg. Allg. Chem.,* **2017**, *23*, 1948-1955.

6. Korey P. Carter, **Mark Kalaj**, Robert G. Surbella III, Lucas C. Ducati, Jochen Autshbach, Christopher L. Cahill, "Engaging the Terminal: Promoting Halogen Bonding Interactions with Uranyl Oxo Atoms" *Chem. Eur. J.,* **2017**, *61*, 15355-15369. (*Highlighted Cover Article)*

5. **Mark Kalaj**, Korey P. Carter, Christopher L. Cahill, "Isolating Equatorial and Oxo Based Influences on Uranyl Vibrational Spectroscopy in a Family of Hybrid Materials Featuring Halogen Bonding Interactions with the Uranyl Oxo Atoms" *Eur. J. Inorg. Chem.,* **2017**, *40*, 4702-4713. (*Highlighted "Very Important Paper" by EJIC)*

4. **Mark Kalaj**, Korey P. Carter, Anton V. Savchenkov, Mikaela M. Pyrch, Christopher L. Cahill, "Synthesis, Structures, and Comparisons of Heterometallic Uranyl Iodobenzoates with Monovalent Cations" *Inorg. Chem.,* **2017**, *56*, 9156-9168.

3. **Mark Kalaj**, Korey P. Carter, Christopher L. Cahill, "Utilizing Bifurcated Halogen-Bonding Interactions with the Uranyl Oxo Group in the Assembly of a UO2-3-bromo-5-iodobenzoic Acid Coordination Polymer" *Acta. Crystallogr. Sect. B: Struct. Sci. Cryst. Eng. Mater.,* **2017**, *73*, 234-239.

2. Korey P. Carter, **Mark Kalaj**, Christopher L. Cahill, "Harnessing Uranyl Oxo Atoms via Halogen Bonding Interaction in Molecular Uranyl Materials Featuring 2,5-diiodobenzoic acid and N-donor Capping Ligands" *Inorg. Chem. Front.*, **2017**, *4*, 65-78.

1. Korey P. Carter, **Mark Kalaj**, Christopher L. Cahill, "Probing the Influence of N-donor Capping Ligands on Supramolecular Assembly in Molecular Uranyl Materials" *Eur. J. Inorg. Chem.,* **2016**, *2016*, 226-137.

ABSTRACT OF THE DISSERTATION

Metal-Organic Framework Polymer Hybrid Materials for Chemical Warfare Agent Degradation

by

Mark Kalaj

Doctor of Philosophy in Chemistry

University of California San Diego, 2021

Professor Seth M. Cohen, Chair

Since first discovered some two decades ago, metal-organic frameworks (MOFs) have shown interesting properties with regard to storage, separation, and catalysis applications. While MOFs have shown promise in these arenas over the years, a major shortcoming of these materials is their inherently crystalline form factor which hinders their utility in practical applications. To circumvent this issue, we have turned to the hybridization of MOFs with polymers in an effort to form a material that has the desired properties of the MOF and the flexibility of the polymer. In particular, we seek to develop novel textile based (nylon based or

spray coated) MOF-polymer hybrid materials that are catalytically active against harmful organophosphorus chemical warfare agents (CWAs).

Chapter 2 describes the synthesis of a MOF-nylon hybrid material through and interfacial postsynthetic polymerization (PSP) method. The hybrid material contains 29 weight percent MOF and shows catalytic activity against a CWA simulant. Importantly, the covalent MOF-nylon material displays about a seven-fold increase in activity compared to physically mixed controls.

In Chapter 3, we screened a wide range of MOFs with varying organic functional groups to establish structure activity relationships (SAR) between MOF functional groups and CWA simulant degradation. The Zr-based MOF UiO-66 (UiO = University of Oslo) was synthesized with either mixed ligand functional groups or halogenated functional groups. We determined that the mixed ligand approach improves CWA activity by three-fold whereas the UiO-66-Iodine MOF displays a fourfold increase in activity. Through theoretical calculations, the increased activity in UiO-66-I was determined to be a result of halogen bonding with the CWA simulant.

In Chapter 4, we combine the approaches from Chapter 2 and 3, by using the commonly known pseudohalogen isothiocyanate (NCS) functional group in UiO-66 to improve the catalytic activity against CWAs and covalent PSP sites. The UiO-66-NCS MOF was synthesized via postsynthetic modification (PSM) and displayed a ~20 fold increase in activity compared to the presynthetic MOF. More importantly, using amine terminated polypropylene oxides, MOF-polymer materials were formed, and spray coated onto textile fibers. This material showed great durability and catalytic activity compared to physically mixed controls.

Chapter 5 describes the room temperature synthesis of the commonly used UiO-66 MOF as well as a few functional groups derivatives. Starting from a UiO-66-F_4 MOF with relatively labile ligands, postsynthetic exchange (PSE) with four different MOF ligands at room temperature in aqueous conditions was performed with almost complete ligand exchange. These MOFs were thoroughly characterized after PSE and maintained desired properties such as crystallinity and particle size or shape.

ABSTRACT OF THE DISSERTATION

Metal-Organic Framework Polymer Hybrid Materials for Chemical Warfare Agent Degradation

by

Mark Kalaj

Doctor of Philosophy in Chemistry

University of California San Diego, 2021

Professor Seth M. Cohen, Chair

Since first discovered some two decades ago, metal-organic frameworks (MOFs) have shown interesting properties with regard to storage, separation, and catalysis applications. While MOFs have shown promise in these arenas over the years, a major shortcoming of these materials is their inherently crystalline form factor which hinders their utility in practical applications. To circumvent this issue, we have turned to the hybridization of MOFs with polymers in an effort to form a material that has the desired properties of the MOF and the flexibility of the polymer. In particular, we seek to develop novel textile based (nylon based or

spray coated) MOF-polymer hybrid materials that are catalytically active against harmful organophosphorus chemical warfare agents (CWAs).

Chapter 2 describes the synthesis of a MOF-nylon hybrid material through and interfacial postsynthetic polymerization (PSP) method. The hybrid material contains 29 weight percent MOF and shows catalytic activity against a CWA simulant. Importantly, the covalent MOF-nylon material displays about a seven-fold increase in activity compared to physically mixed controls.

In Chapter 3, we screened a wide range of MOFs with varying organic functional groups to establish structure activity relationships (SAR) between MOF functional groups and CWA simulant degradation. The Zr-based MOF UiO-66 (UiO = University of Oslo) was synthesized with either mixed ligand functional groups or halogenated functional groups. We determined that the mixed ligand approach improves CWA activity by three-fold whereas the UiO-66-Iodine MOF displays a fourfold increase in activity. Through theoretical calculations, the increased activity in UiO-66-I was determined to be a result of halogen bonding with the CWA simulant.

In Chapter 4, we combine the approaches from Chapter 2 and 3, by using the commonly known pseudohalogen isothiocyanate (NCS) functional group in UiO-66 to improve the catalytic activity against CWAs and covalent PSP sites. The UiO-66-NCS MOF was synthesized via postsynthetic modification (PSM) and displayed a ~20 fold increase in activity compared to the presynthetic MOF. More importantly, using amine terminated polypropylene oxides, MOF-polymer materials were formed, and spray coated onto textile fibers. This material showed great durability and catalytic activity compared to physically mixed controls.

Chapter 5 describes the room temperature synthesis of the commonly used UiO-66 MOF as well as a few functional groups derivatives. Starting from a UiO-66-F_4 MOF with relatively labile ligands, postsynthetic exchange (PSE) with four different MOF ligands at room temperature in aqueous conditions was performed with almost complete ligand exchange. These MOFs were thoroughly characterized after PSE and maintained desired properties such as crystallinity and particle size or shape.

Chapter 1: Metal-Organic Framework and Polymer Hybrid Materials

1.1 Metal-Organic Frameworks

Since their discovery over two decades ago, metal-organic frameworks (MOFs) have garnered significant interest as solid-state materials due to their inherently uniform structures and high surface areas.[1] MOFs are composed of inorganic metal centers, often referred to as secondary building units (SBUs), linked together by multitopic organic linkers to form uniform two- or three-dimensional frameworks.[1-2] One key distinction between MOFs and other porous inorganic materials that predate them (e.g., zeolites) is that MOFs are comprised of components, both organic and inorganic, that are highly tunable.[1-4] In particular, the organic component of MOFs open an avenue for tailoring these materials with functional groups that can enhance their properties for a wide range applications including gas storage, drug delivery, molecular separations, and catalysis.[3-10]

Judicious selection of metal salts and organic functional linkers has resulted in hundreds of different MOFs with broad structural diversity.[11-12] For example, the Zr(IV)-based MOF, designated as UiO-66 (UiO = University of Oslo) ($Zr_6O_4(OH)_4(bdc)_6$, Figure 1.1), is one of the most commonly used MOFs and is synthesized by combining a Zr(IV) metal source with the ditopic 1,4-benzenedicarboxylic acid (H_2bdc) under solvothermal conditions (80-120° C) in DMF (DMF = N,N-dimethylformamide) or DEF (DEF = N,N-diethylformamide).[13] Sometimes monotopic acid modulators (such as acetic acid and benzoic acid) are also used in the MOF synthesis to slow down the MOF formation to target specific sizes, morphologies, or defect densities in the resulting crystallites.[13-17] UiO-66 is one of the most commonly used MOFs due its high chemical stability, and has been prepared from a wide range of H_2bdc functional group derivatives.[13]

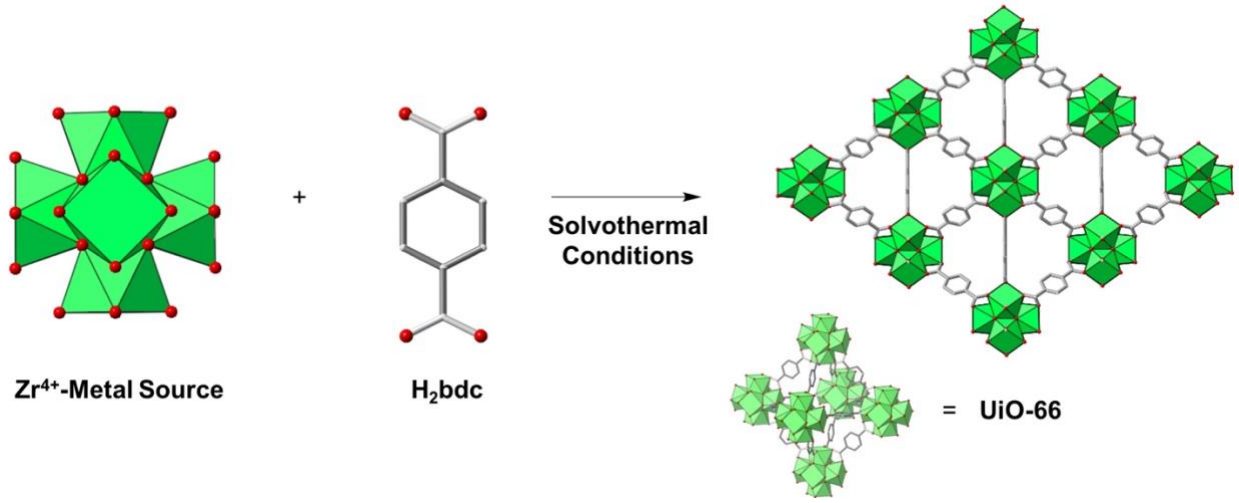

Figure 1.1. Illustrative schematic for the synthesis of UiO-66. A Zr(IV)-metal source is combined with a H_2bdc under solvothermal conditions to form a three-dimensional extended framework (UiO-66). For simplicity, the cartoon of a small subunit (bottom right) of the MOF lattice will be used throughout this chapter to generally depict an entire extended MOF crystallite. Green polyhedra represent Zr(IV) ions, red spheres represent O atoms, and silver sticks represent C bonds.

By tailoring the starting metal salts or organic linkers accordingly under similar conditions, a rich array of MOFs can be achieved. One of the first reported MOFs, IRMOF-1 (IRMOF = isoreticular MOF) is synthesized by simply changing the metal salt from Zr(IV) (UiO-66) to a Zn(II) salt with the same ditopic H_2bdc under similar synthetic conditions (Figure 1.2).[18] However, the connectivity, and in turn, properties of these two MOFs are very different. For example, IRMOF-1 is very unstable to moisture where as UiO-66 is one of the most stable MOFs and this is attributed to its SBUs being connected by 12 organic linkers and the strong coordination between the hard Lewis base carboxylates and hard Lewis acid Zr(IV) metal centers. Using the same metal salt and simply changing the H_2bdc linker to a tritopic 1,3,5-benzenetricarboxylic acid (H_3btc) yields yet another MOF, MOF-808.[19] Finally, by changing the metal salt once again from Zr(IV) to Cu(II) using the H_3btc linker yields yet another MOF known as HKUST-1 that has a Cu(II) paddlewheel SBU (Figure 1.2).[20] As is evident from these examples, with a range of multitopic

organic linkers and varying metal salts, a wide array of different MOFs with unique properties can be prepared.

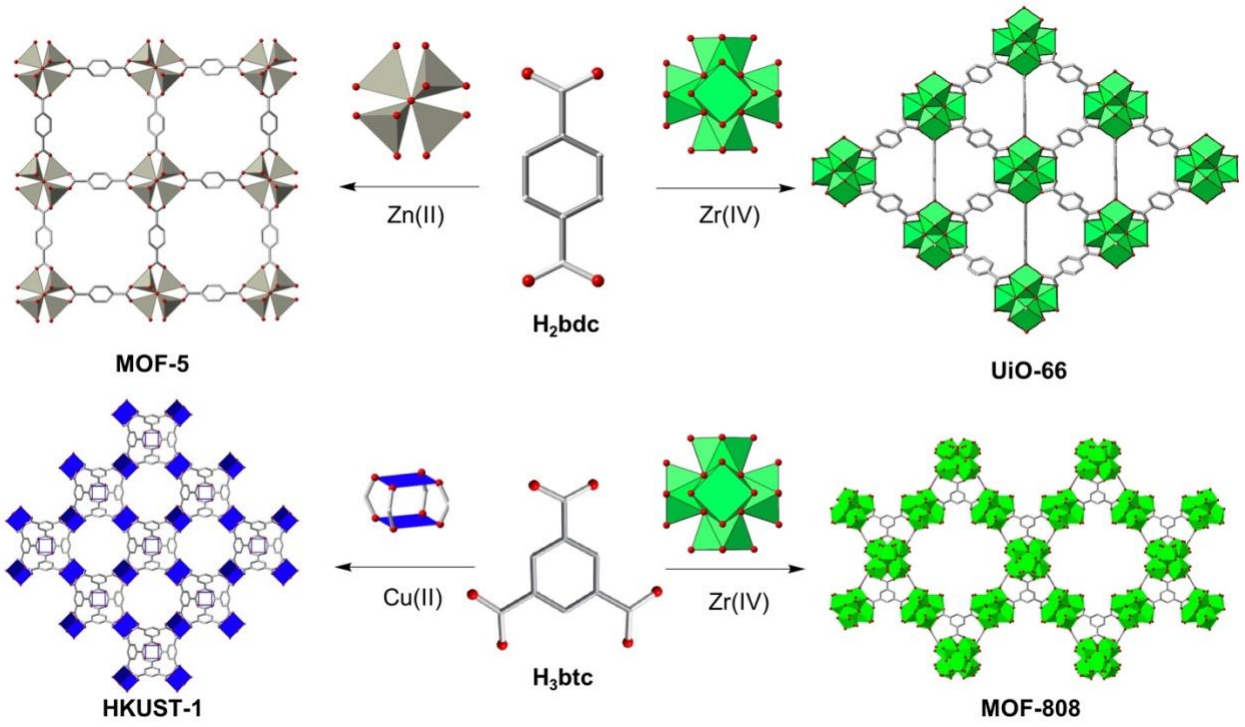

Figure 1.2. A chemical representation of the use of multitopic organic linkers and inorganic metal nodes to form MOFs. *Top:* The synthesis of IRMOF-1 using H_2bdc and Zn(II) SBUs and the synthesis of UiO-66 using the same ligand and Zr(IV) SBUs. *Bottom:* The synthesis of HKUST-1 using H_3btc and Cu(II) SBUs and the synthesis of MOF-808 using the same linker with Zr(IV) SBUs.

Inclusion of functional groups on linkers has the ability to tailor MOF properties; however, the scope of organic molecules that can be included presynthetically (particularly during the time period of these earlier reports) was rather limited.[18, 21] Under these empirically-derived reaction conditions, the diversity of functional groups that could be incorporated into MOFs was small and included only those that were compatible with these somewhat stringent and limited synthetic conditions. Some of the earlier reports on MOFs from Yaghi and coworkers shows that functional

groups were incorporated into the canonical IRMOF-1 (a.k.a., MOF-5) material.[18] IRMOFs were synthesized using a Zn(II) metal source and H_2bdc ligand; these ligands could be derivatized with amino, halide, aromatic, and alkyl groups. As aforementioned, this early report inspired the synthesis of other MOFs with the same H_2bdc linkers, but using different metal sources, such as Zr(IV), Al(III), and Cr(III).[13, 21-23] To expand the scope and versatility of functional groups that can be introduced into MOFs, covalent postsynthetic modification (PSM) was developed and eventually became widely adopted in the field. PSM, is defined as a reaction between a functional group (such as an amine) on the MOF linker and a reagent introduced externally (such as an acyl chloride, Figure 1.3). To successfully achieve PSM, it is essential that the MOF does not degrade during the reaction and maintains its structure, crystallinity, and porosity. This key criterion of PSM has parallels in biorthogonal chemistry that require judicious selection of reagents, reaction conditions, etc. to achieve chemical transformations that do not harm or otherwise damage biomolecules or living cells (with PSM, which do not degrade or damage the framework structure).[24-25]

The earliest examples of covalent PSM were demonstrated by Lee and Kim over two decades ago on MOF-like coordination solids.[26-27] In 2007, nearly a decade after these earliest reports, Cohen and coworkers described the concept of 'postsynthetic modification',[28] and PSM was revived, popularized, and greatly expanded as a synthetic method by many research groups.[28-30] In a rudimentary example of PSM, amine functional groups on IRMOF-3 (IRMOF-3 is an amine functionalized version of IRMOF-1) were combined with acetic anhydride to generate acetamide groups on the MOF linkers. Covalent PSM allowed for MOFs to be functionalized with reagents that could alter the characteristics of the resulting materials, including changes in hydrophobicity, hydrophilicity, catalytic behavior, and others.[31-32] Ultimately, the 2007 report by Cohen and

coworkers ignited several efforts to perform organic chemistry on MOFs through PSM in an effort to produce MOFs with diverse functional groups[28, 33-36] through the use of single or multistep reactions. Importantly, in many cases, these functional groups could not be introduced into the MOF presynthetically.[33-36] Covalent PSM has now become a reliable, and indeed commonplace method for functionalizing MOFs to produce porous materials with a rich array of properties and characteristics. As a result, libraries of MOFs containing an array of functional groups were generated through the use of one, two, or even three step organic reactions.[33-36]

Around the same time, another method for postsynthetically incorporating functional groups, postsynthetic exchange (PSE), was reported.[33-35, 37-38] PSE has been used to exchange metal atoms at the SBU as well as the organic linkers connecting the SBUs together (Figure 1.3). For instance, UiO-66 can be immersed in a solution of NH_2-H_2bdc resulting in a MOF that contains both NH_2-bdc^{2-} and bdc^{2-} linkers. Both PSM and PSE became useful tools for synthesizing mixed ligand or multivariate (MTV) MOFs.[33, 39] Several reports have targeted these functionalized MOFs through presynthetic or postsynthetic routes by synthesizing mixed ligand or multivariate MTV MOFs with varying linker lengths or functionalities.[39-47] This enriched chemical diversity from both PSM and PSE has enabled the advancement of MOFs toward emerging applications.

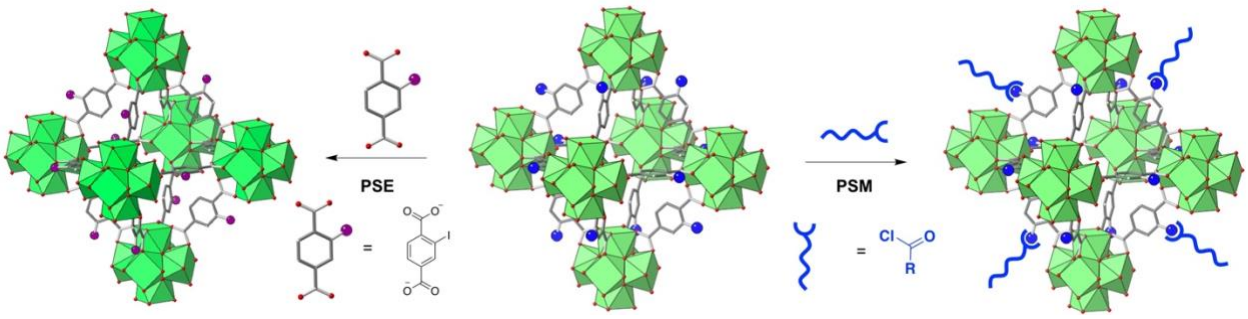

Figure 1.3. Illustrative schematic of PSE and PSM in MOFs. Depiction of PSE is shown through the exchange of amine functionalized (blue spheres) bdc^{2-} linkers with iodine functionalized -bdc^{2-} (purple spheres) linkers. Depiction of covalent PSM using reactive amine groups on the MOF linker for modification by an organic reagent (blue acid chloride reagent).

1.2 MOFs and the Degradation of Chemical Warfare Agents

Since their first use during World War I, chemical warfare agents (CWAs) have periodically been used throughout most of the 20th and 21st century to cause mass destruction on both military personnel and civilians. Despite broad condemnation across the globe and international agreements prohibiting their use, CWAs remain a danger. There remains a pressing need to develop advanced materials to safeguard warfighters and civilians against CWAs.[52-53] While CWAs are broadly generalized as devastating weapons, they have been classified into nuanced categories based on their chemical composition.[54-55] The most acutely toxic and universally known CWAs are organophosphorus nerve agents such as sarin (GB), soman (GD) and VX (Figure 1.4). These have been categorized into two series, the G-series synthesized in Germany during WWII and the V-series synthesized in the United Kingdom after WWII (Figure 1.4). However, other commonly synthesized toxic industrial chemicals (TICs) such as ammonia (NH_3) have also been periodically weaponized as a result of their abundance and availability.[56] As such, the design of materials that can degrade organophosphorus nerve agents and sequester TICs have become increasingly relevant.

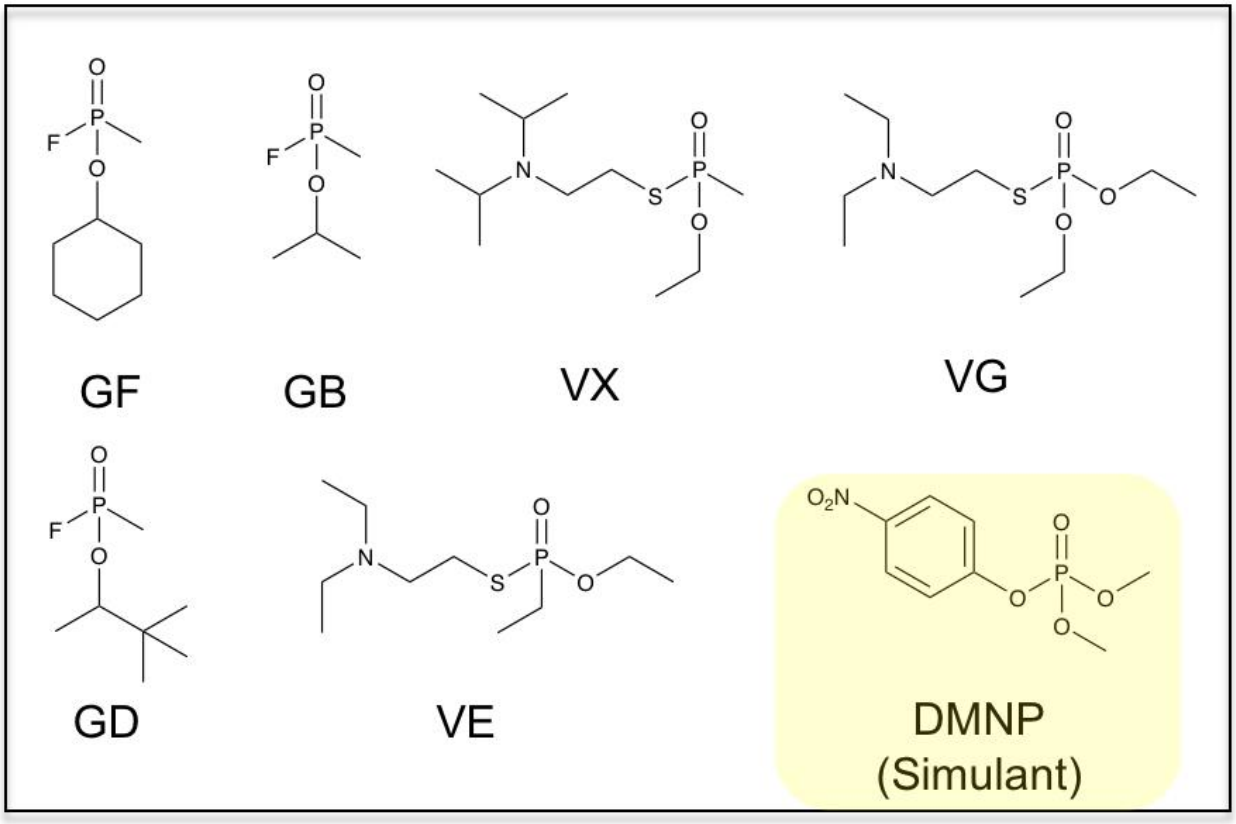

Figure 1.4. Chemical structures of known organophosphorous nerve agents from the G-series and the V-series as well as the chemical structure of the nerve agent simulant DMNP.

MOFs and the Organophosphorus Nerve Agent Degradation. Since 2014, some Zr-based MOFs have demonstrated efficient catalytic degradation of organophosphorus nerve agents.[57-58] Detoxification of organophosphorus nerve agents typically requires breakage of the phosphoester linkage through a hydrolysis step. Due to the high toxicity of nerve agents, nerve agent simulants have been developed as a safer alternative to study the hydrolysis of phosphoester linkages.[54, 58] Since the first report, typical screening methods for monitoring nerve agent degradation with MOFs include the use of a buffered solution (*N*-ethylmorpholine) at highly alkaline pH (10.4).[58] The MOF catalyst is dispersed in this buffered solution and the nerve agent or nerve agent simulant is added. Monitoring of the degradation is conducted by taking aliquots of the solution and measuring the starting material and degradation product using ^{31}P-NMR or

UV-visible spectroscopy.[57, 59] While these screening methods are effective, they are extremely time consuming making it much more difficult to analyze a wide range of materials to find the best catalyst. To circumvent this, Cohen and coworkers developed a high-throughput screening (HTS) method using a nerve agent simulant dimethyl-4-nitrophenyl phosphate (DMNP, Figure 1.4).[60] DMNP has been utilized as a safer alternative to CWAs while most effectively mimicking the phosphoester bond. This method uses a 96-well plate where the MOF catalyst is suspended in a buffered solution and upon addition of DMNP the wells are monitored using UV-Vis at 407 nm wavelength. As the phosphoester linkage in the DMNP molecule breaks apart, the resulting product, *p*-nitrophenoxide absorbs at 407 nm (Figure 1.5). By monitoring the appearance of this product, the rate of catalytic activity from the MOF can be back calculated using pseudo zero order kinetics. Importantly, this HTS method was used to examine the effects of pH on the MOF catalysis rates and found that pH plays a critical role in the activity of these materials. Moreover, this study provided a platform for analyzing a wide range of MOFs with subtle differences to judiciously determine characteristics that are important for increased catalytic activity.

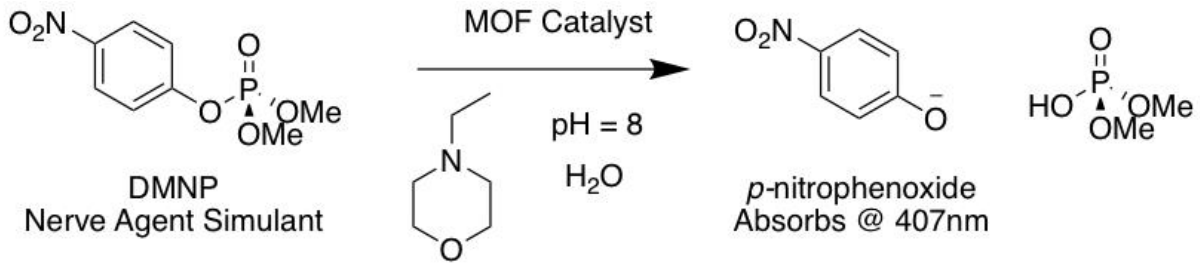

Figure 1.5. Chemical depiction for the monitoring the breakdown of DMNP with a MOF catalyst using UV-Vis absorption spectroscopy.

Whereas Zr-MOFs have been effective for CWA degradation of nerve agents and their simulants, the mechanism of hydrolysis remains relatively unknown. Most experimental work

suggests catalysis is primarily due to the strong Lewis acidity of the metal center, while other studies suggest catalytic activity can been specifically attributed to MOF defect sites.[55, 58, 61] Density functional theory (DFT) calculations indicate the mechanism involves binding of nerve agent to the Zr(IV) metal center followed by hydrolysis of the phosphoester bond resulting in agent degradation (Figure 1.6).[58, 62-64] Two approaches have been used to enhance nerve agent hydrolysis in MOFs: synthesizing MOFs with different ligands or metal centers that improve hydrolysis, or by promoting defective sites at the SBU where catalytic conversion takes place.[61, 65-66] Because DFT calculations have suggested the importance of the SBU, most work in the literature has focused on engineering more catalytic sites into the SBU of the MOF.[62, 66-67] Notably, Farha and coworkers have demonstrated that a reduction in ligand connectivity to the Zr SBU plays a critical role in increasing the catalytic rate as the SBU has more catalytically active sites.[56, 67] However, the only example of ligand derivatization improving CWA simulant degradation has been demonstrated by the addition of amine (-NH_2) functional groups on the MOF linkers.[61, 68] In the case of UiO-66, the amine functionalized derivative, UiO-66-NH_2, displays 20-fold higher activity than the parent MOF at pH = 10.[68] The significance of this amine functionality was also shown in a series of NU-1000 MOFs where *ortho* positioning of the amine groups displays 3-fold greater activity than the unfunctionalized canonical MOF.[61] The increased activity of these MOFs is thought to be a result of the amine working as a Brønsted base to synergistically enhance catalytic activity.[61, 63, 68] As aforementioned, the catalytic activity of these MOFs is pH dependent.[60] Although UiO-66-NH_2 is a faster catalyst than UiO-66 at pH = 10, when examined at pH = 8, UiO-66 actually displays 2-fold faster activity than UiO-66-NH_2.[60] These strides in improving MOFs against CWA degradation are critical in developing better catalysts with the ultimate goal of using

MOFs in membranes, garments or other personal protective equipment form factors for civilian and warfighter protection.

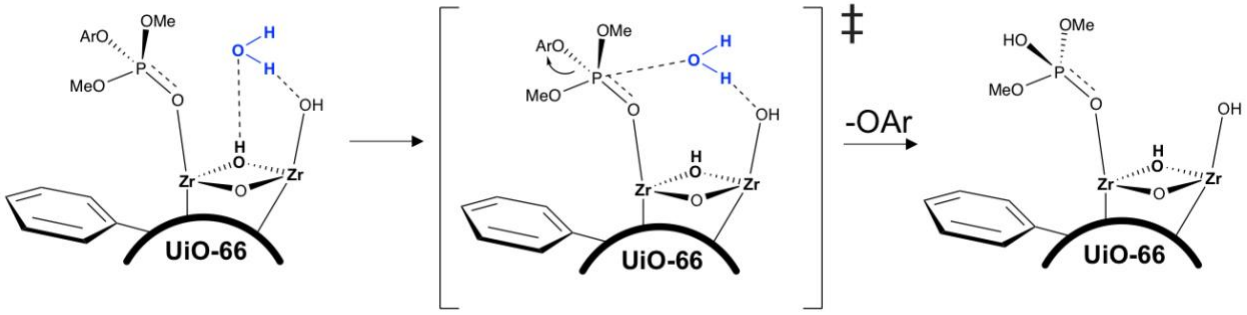

Figure 1.6. a) Chemical depiction of the degradation of DMNP using UiO-66. First, the DMNP molecule binds to an open Zr-metal site through the P=O bond. Subsequently, the transition state where adjacent water molecules bound to the MOF attack the DMNP at the electrophilic P center resulting in elimination of the aryl oxide.

1.3 MOF-Polymer Hybrid Materials

Over the last two decades, research in MOFs has considerably pushed these materials toward a wide range of applications because of their exceptional properties.[69-72] However, the progress of MOFs towards commercialization or implementation has been restricted by their crystalline or microcrystalline (e.g., powder) form factor, which inherently limits their integration into many modern technologies.[73-74] As such, processable form factors containing MOFs and polymers have been sought in an effort to combine the properties of MOFs and polymers to advance the utility of MOFs (Figure 1.7).[75] In one approach, these composites have been targeted through a top down strategy, in which MOFs are initially synthesized and subsequently incorporated into polymeric materials.[73-74, 76-77] Another approach has been used where organic polymer ligands are initially synthesized and then used to form a MOF through solvothermal conditions.[78-80] These distinct approaches have yielded several successful methods to synthesize MOF-polymer hybrid materials.

Beyond integrating MOFs and polymers to enable the utilization of MOFs, many other investigations have focused on other ways in which these two classes of materials can be co-mingled and interact.[73-75] Studies examining the synthesis of polymers in and around MOF crystallites have been reported. Control over the outcome of polymerization reactions within MOF pores has yielded fascinating results, and many methods for decorating the surface of MOFs with polymer chains have been described. Diverse approaches for MOF-polymer hybrid materials have been explored through the synthesis of mixed matrix membranes (MMMs), polymers grafted from MOF particles, polymers grafted through MOFs, polymers templating MOF growth, as well as the synthesis of MOFs using polymer ligands (polyMOFs, Figure 1.7). These approaches have utilized wide range of polymers (Figure 1.8) for the integration of MOF-polymer hybrid materials to achieve form factors of distinct polymer characteristics for several desired applications such as, separations, sensing, catalysis, and storage.[73, 76-77] Realization of MOF-polymer hybrid materials that maintains the properties of MOFs in a flexible form factor would provide a platform for these materials to be incorporated into the real world.

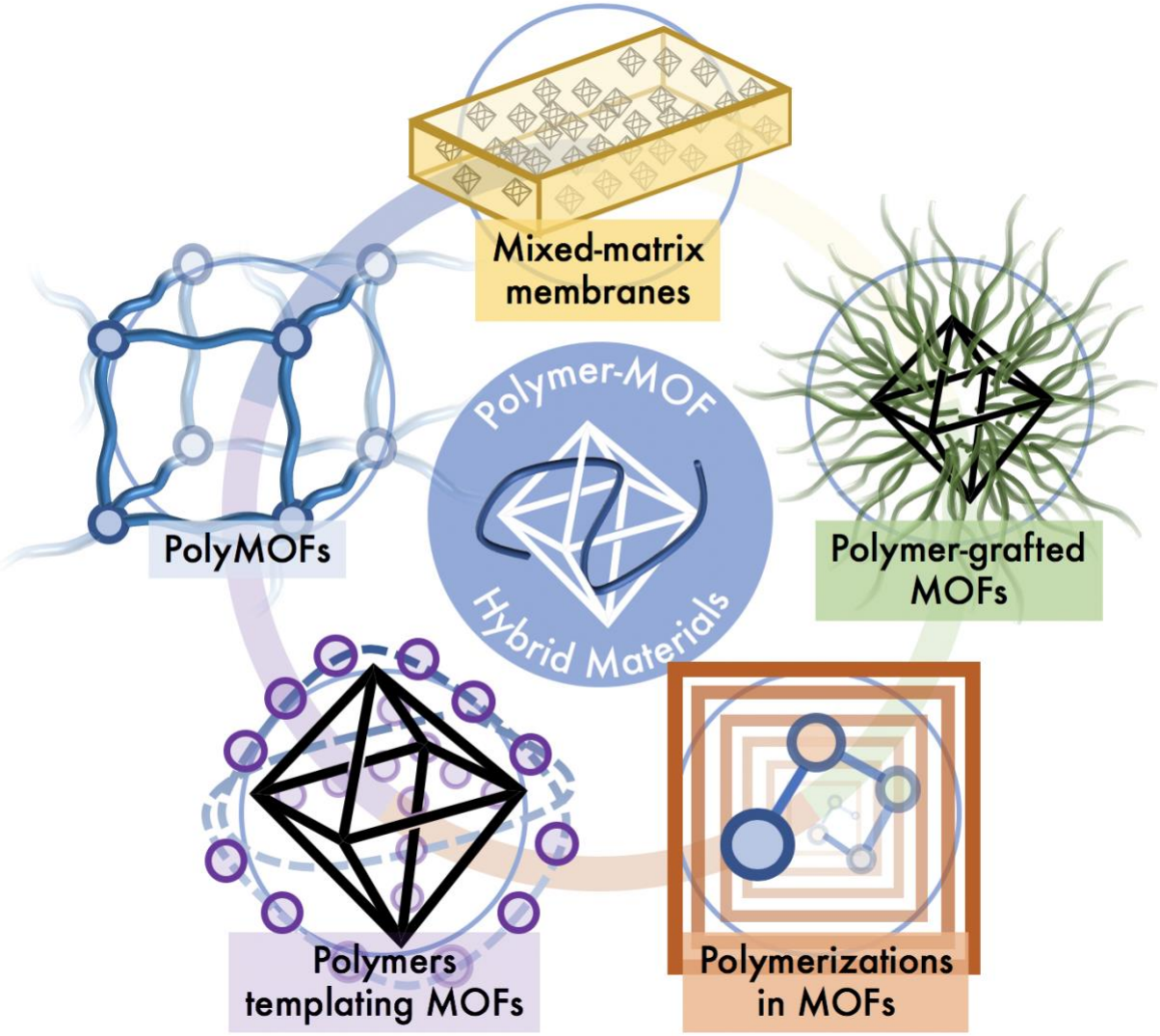

Figure 1.7. An illustrative overview of various MOF-polymer hybrid materials.

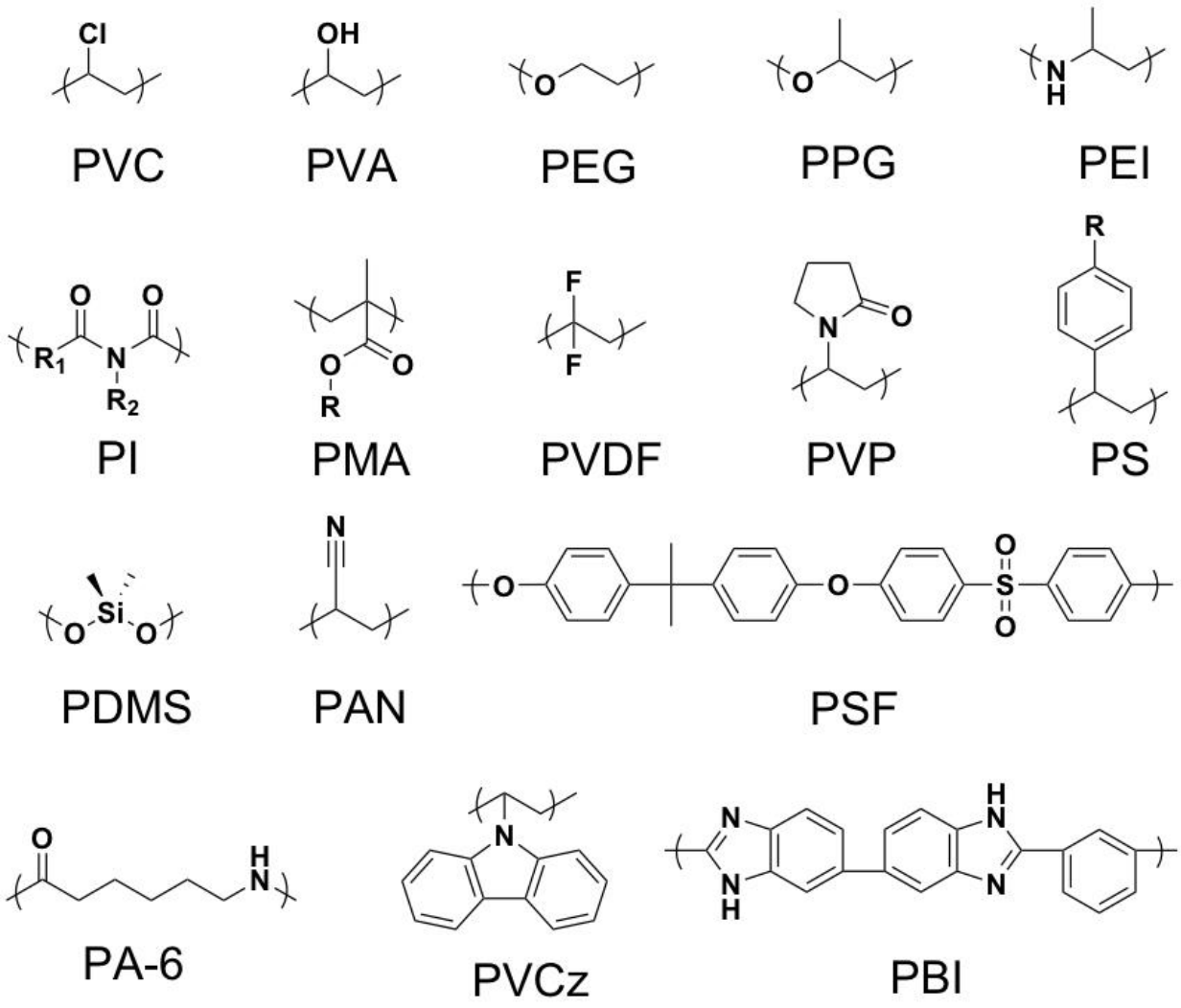

Figure 1.8. Common polymers used in the synthesis of MOF-polymer hybrid materials.

MOF-based Mixed-Matrix Membranes. One strategy to hybridize MOFs, is via the synthesis of MMMs. MMMs serve as a means to incorporating rigid materials into flexible, polymeric form factors.[81-82] MMMs consist of a polymer combined with a solid filler to make a hybrid material that contains the flexibility of the polymer while retaining the desired properties of the porous filler.[81, 83] The application of these materials has centered around gas separations, liquid separations and water purification. Issues with these materials have risen at the MOF polymer interface as the MOF and polymer are incompatible and often macrovoids, or gaps at the

interface, are created rendering these materials somewhat useless for the desired applications. To circumvent this issue, synthesizing materials with covalent linkages between the MOF and polymer component was utilized to 'bridge the gap'. One of the earliest, clever approaches to covalently combining MOFs and polymers was reported by Wang and coworkers, who developed a covalent MOF-polymer linkage through postsynthetic polymerization (PSP) (Figure 1.8).[84] This approach used reactive amine handles in a UiO-66-NH_2 MOF as a site for PSM converting these amines to methacrylamides (UiO-66-NH-Met). This modified UiO-66-NH-Met was mixed with butyl methacrylate (BMA) and phenylbis(2,4,6-trimethylbenzoyl)phosphine oxide and subsequently cast out into a Teflon mold. This mixture was then cured with UV light, thereby polymerizing the MOF through the methacrylamide handles to give a stand-alone membrane. CO_2 isotherms of the membrane showed retained porosity in the MOF particles, suggesting that the MOF pores are not infiltrated by the polymer, but rather decorated around the outside of the particles. The PSP membranes were characterized compared to physical mixtures of MOF and BMA which showed better adhesion of the MOF and polymer components in the covalently linked material (Figure 1.9). Using PSP, MMMs were obtained where the MOFs are directly, covalently integrated into the surrounding polymer matrix. The general concept of PSP includes a MOF that is modified with functional groups that can react with polymer monomers in a step growth fashion or directly react with a polymer matrix (Figure 1.9). This seminal work by Wang et al. inspired several other researchers to utilize PSP in the synthesis of covalently grafted polymer MOF MMMs[85] as well as other hybrid materials.[86-88] PSP has played a key role in facilitating the development of novel MOF materials for a myriad of applications not simply limited to gas adsorption and separations.

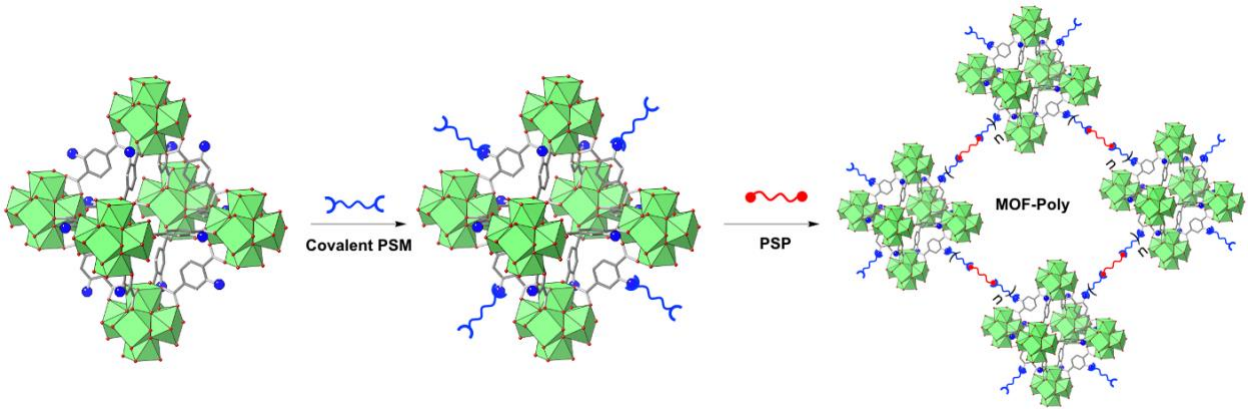

Figure 1.9. An illustrative schematic depicting PSP in MOFs. First, a PSM step in which the organic linkers in the MOF are covalently attached to a polymeric molecule. Subsequently, through the introduction of a crosslinking agent, a monolithic MOF-polymer hybrid is formed through PSP.

MOF-Polymer Hybrid Materials for CWA Degradation. As outlined above, one of the emerging applications for the use of MOFs is the catalytic degradation of CWAs and the adsorption of TICs. The goal of this work focuses on developing a MOF material that can protect soldiers with potential exposure to these harmful chemicals. As such, the use of MOF-polymer hybrid materials has gained attention in this realm. Combining MOFs with polymers to form textile like fibers is heavily sought after.[54-56] A number of different methods have been reported for synthesizing textile like MOF based composite materials.[62, 89-99] The most well developed work in this realm is by Parsons and coworkers through the use of Atomic Layer Deposition (ALD).[100-101] In this top down approach, polymeric fibers are coated with metal oxides and subsequently subjected to solvothermal conditions using MOF ligands and metal salts. The metal oxide coating provides nucleation sites for MOF growth and the final product is a textile fiber densely coated with MOF particles. A strength of the ALD MOF fibers is that they perform very well when screened against nerve agents.[100, 102-103] While these results are promising, the ALD method has limitations as it is laborious, time consuming, and expensive. Farha and coworkers have also

developed a method for coating textile fibers with MOFs for the catalytic degradation of nerve agents.[104] Similar to the previous method, in this approach textile fibers are treated under solvothermal conditions with metal salt and ligand precursors for MOF-808. First, an amorphous coordination polymer forms on the surface of the fibers, then MOF nucleation sites begin to appear, and finally exponential MOF growth is observed on the fiber surface. In both of these top-down approaches, the final product is a physical mixture of MOF and polymer materials. Thus, an inherent drawback is the cohesiveness between the MOF and polymer component and its limitations if exposed to strain. As such, there remains a pressing need to develop highly functional and cohesive MOF textile fibers for the degradation of nerve agents.

1.4 Scope of this Dissertation

This dissertation will discuss novel approaches for developing MOFs and MOF-polymer hybrid materials for the degradation of chemical warfare agents. Chapter 2 describes the synthesis of a Nylon-MOF hybrid material using UiO-66-NH_2 and polyamide 6,6 (PA-66) through PSP. The hybrid material was thoroughly characterized and screened for the degradation of DMNP. The report shows that the Nylon-MOF material remains catalytically active against DMNP and that having a covalent linkage between MOF and polymer components is significant in achieving a highly functional material.

Chapter 3 describes the effects that various functional groups on the MOF organic linkers have in the degradation of the nerve agent simulant DMNP. A library of 29 UiO-66 derivatives that include MTV UiO-66 with up to five ligand combinations have been screened for DMNP degradation using HTS. The MTV MOFs display up to three-fold increased catalytic activity compared to physical mixtures of MOFs using the same ligand components. Furthermore, the halogenated UiO-66 series was also screened, and the UiO-66-I displays over four times the

activity of the unfunctionalized MOF. Through theoretical calculations, this activity was found to be an artifact of halogen bonding occurring between the MOF linker and the DMNP molecule.

Chapter 4 describes the preparation of UiO-66-NCS (NCS = isothiocyanate) through PSM. This chapter combines efforts from chapter 2 and 3 as the -NCS functional groups are pseudohalogenated moieties that contain reactive handles available for PSP. The UiO-66-NCS MOF displays significantly increased activity against DMNP and has been shown to be a strong adsorbent for NH_3 through chemisorption. Further, the MOF was subjected to PSP resulting in the formation of a MOF-polymer composite. The MOF-polymer material was also spray coated onto textile fibers and displayed good adhesion to the fibers and maintained catalytic activity.

Chapter 5 describes the preparation of UiO-66 using green synthetic conditions. A series of UiO-66 derivatized MOFs were synthesized at aqueous and room temperature conditions using PSE. UiO-66-F_4 was used as a precursor MOF as the electron withdrawing effects of the -F atoms make the ligands labile allowing for a rapid PSE. Materials were synthesized and characterized displaying different properties derived from varying incorporated functional groups.

1.5 Acknowledgements

Chapter 1, in part, is a reprint of the following materials: "MOF-Polymer Hybrid Materials: From Simple Composites to Tailored Architectures" *Chem. Rev.* **2020**, *120*, 8267-8302; "Postsynthetic Modification: An Enabling Technology for the Advancement of Metal-Organic Frameworks" *ACS Cent. Sci.* **2020**, *6*, 1046-1057. The dissertation author was the primary author for both of these review articles and gratefully acknowledges the contributions of coauthors Kyle C. Bentz, Sergio Ayala Jr., Joseph M. Palomba, Kyle S. Barcus, Yuji Katayama, and Seth M. Cohen.

1.6 References

1. Furukawa, H.; Cordova, K. E.; O'Keeffe, M.; Yaghi, O. M., The Chemistry and Applications of Metal-Organic Frameworks. *Science* **2013,** *341*, 1230444.

2. Eddaoudi, M.; Kim, J.; Rosi, N.; Vodak, D.; Wachter, J.; O'Keeffe, M.; Yaghi, O. M., Systematic Design of Pore Size and Functionality in Isoreticular MOFs and Their Application in Methane Storage. *Science* **2002,** *295*, 469-472.

3. Zhou, H.-C.; Long, J. R.; Yaghi, O. M., Introduction to Metal–Organic Frameworks. *Chem. Rev.* **2012,** *112*, 673-674.

4. Long, J. R.; Yaghi, O. M., The Pervasive Chemistry of Metal–Organic Frameworks. *Chem. Soc. Rev.* **2009,** *38*, 1213-1214.

5. Teplensky, M. H.; Fantham, M.; Li, P.; Wang, T. C.; Mehta, J. P.; Young, L. J.; Moghadam, P. Z.; Hupp, J. T.; Farha, O. K.; Kaminski, C. F., et al., Temperature Treatment of Highly Porous Zirconium-Containing Metal–Organic Frameworks Extends Drug Delivery Release. *J. Am. Chem. Soc.* **2017,** *139*, 7522-7532.

6. Wu, M.-X.; Yang, Y.-W., Metal–Organic Framework (MOF)-Based Drug/Cargo Delivery and Cancer Therapy. *Adv. Mater.* **2017,** *29*, 1606134.

7. Murray, L. J.; Dincă, M.; Long, J. R., Hydrogen Storage in Metal–Organic Frameworks. *Chem. Soc. Rev.* **2009,** *38*, 1294-1314.

8. Diercks, C. S.; Liu, Y.; Cordova, K. E.; Yaghi, O. M., The Role of Reticular Chemistry in the Design of CO2 Reduction Catalysts. *Nat. Mater.* **2018,** *17*, 301-307.

9. Zhu, J.; Usov, P. M.; Xu, W.; Celis-Salazar, P. J.; Lin, S.; Kessinger, M. C.; Landaverde-Alvarado, C.; Cai, M.; May, A. M.; Slebodnick, C., et al., A New Class of Metal-Cyclam-Based Zirconium Metal–Organic Frameworks for CO2 Adsorption and Chemical Fixation. *J. Am. Chem. Soc.* **2018,** *140*, 993-1003.

10. Liu, J.; Chen, L.; Cui, H.; Zhang, J.; Zhang, L.; Su, C.-Y., Applications of Metal–Organic Frameworks in Heterogeneous Supramolecular Catalysis. *Chem. Soc. Rev.* **2014,** *43*, 6011-6061.

11. Moghadam, P. Z.; Li, A.; Wiggin, S. B.; Tao, A.; Maloney, A. G. P.; Wood, P. A.; Ward, S. C.; Fairen-Jimenez, D., Development of a Cambridge Structural Database Subset: A Collection of Metal–Organic Frameworks for Past, Present, and Future. *Chem. Mater.* **2017,** *29*, 2618-2625.

12. Altintas, C.; Avci, G.; Daglar, H.; Nemati Vesali Azar, A.; Erucar, I.; Velioglu, S.; Keskin, S., An Extensive Comparative Analysis of Two MOF Databases: High-Throughput Screening of Computation-Ready MOFs for CH4 and H2 Adsorption. *J. Mater. Chem. A* **2019,** *7*, 9593-9608.

13. Cavka, J. H.; Jakobsen, S.; Olsbye, U.; Guillou, N.; Lamberti, C.; Bordiga, S.; Lillerud, K. P., A New Zirconium Inorganic Building Brick Forming Metal Organic Frameworks with Exceptional Stability. *J. Am. Chem. Soc.* **2008,** *130*, 13850-13851.

14. Yaghi, O. M.; O'Keeffe, M.; Ockwig, N. W.; Chae, H. K.; Eddaoudi, M.; Kim, J., Reticular Synthesis and the Design of New Materials. *Nature* **2003,** *423*, 705-714.

15. Férey, G., Hybrid Porous Solids: Past, Present, Future. *Chem. Soc. Rev.* **2008,** *37*, 191-214.

16. Shearer, G. C.; Chavan, S.; Bordiga, S.; Svelle, S.; Olsbye, U.; Lillerud, K. P., Defect Engineering: Tuning the Porosity and Composition of the Metal–Organic Framework UiO-66 via Modulated Synthesis. *Chem. Mater.* **2016,** *28*, 3749-3761.

17. Shearer, G. C.; Chavan, S.; Ethiraj, J.; Vitillo, J. G.; Svelle, S.; Olsbye, U.; Lamberti, C.; Bordiga, S.; Lillerud, K. P., Tuned to Perfection: Ironing Out the Defects in Metal–Organic Framework UiO-66. *Chem. Mater.* **2014,** *26*, 4068-4071.

18. Li, H.; Eddaoudi, M.; O'Keeffe, M.; Yaghi, O. M., Design and Synthesis of an Exceptionally Stable and Highly Porous Metal-Organic Framework. *Nature* **1999,** *402*, 276-279.

19. Furukawa, H.; Gándara, F.; Zhang, Y.-B.; Jiang, J.; Queen, W. L.; Hudson, M. R.; Yaghi, O. M., Water Adsorption in Porous Metal–Organic Frameworks and Related Materials. *J. Am. Chem. Soc.* **2014,** *136*, 4369-4381.

20. Chui, S. S. Y.; Lo, S. M. F.; Charmant, J. P. H.; Orpen, A. G.; Williams, I. D., A Chemically Functionalizable Nanoporous Material [Cu3(TMA)2(H2O)3]n. *Science* **1999,** *283*, 1148.

21. Kandiah, M.; Nilsen, M. H.; Usseglio, S.; Jakobsen, S.; Olsbye, U.; Tilset, M.; Larabi, C.; Quadrelli, E. A.; Bonino, F.; Lillerud, K. P., Synthesis and Stability of Tagged UiO-66 Zr-MOFs. *Chem. Mater.* **2010,** *22*, 6632-6640.

22. Férey, G.; Latroche, M.; Serre, C.; Millange, F.; Loiseau, T.; Percheron-Guégan, A., Hydrogen Adsorption in the Nanoporous Metal-Benzenedicarboxylate M(OH)(O2C–C6H4–CO2) (M = Al3+, Cr3+), MIL-53. *Chem. Commun.* **2003**, 2976-2977.

23. Horcajada, P.; Serre, C.; Vallet-Regí, M.; Sebban, M.; Taulelle, F.; Férey, G., Metal–Organic Frameworks as Efficient Materials for Drug Delivery. *Angew. Chem., Int. Ed.* **2006,** *45*, 5974-5978.

24. Sletten, E. M.; Bertozzi, C. R., Bioorthogonal Chemistry: Fishing for Selectivity in a Sea of Functionality. *Angew. Chem., Int. Ed.* **2009,** *48*, 6974-6998.

25. Sletten, E. M.; Bertozzi, C. R., From Mechanism to Mouse: A Tale of Two Bioorthogonal Reactions. *Acc. Chem. Res.* **2011,** *44*, 666-676.

26. Kiang, Y. H.; Gardner, G. B.; Lee, S.; Xu, Z.; Lobkovsky, E. B., Variable Pore Size, Variable Chemical Functionality, and an Example of Reactivity within Porous Phenylacetylene Silver Salts. *J. Am. Chem. Soc.* **1999,** *121*, 8204-8215.

27. Seo, J. S.; Whang, D.; Lee, H.; Jun, S. I.; Oh, J.; Jeon, Y. J.; Kim, K., A Homochiral Metal–Organic Porous Material for Enantioselective Separation and Catalysis. *Nature* **2000,** *404*, 982-986.

28. Wang, Z.; Cohen, S. M., Postsynthetic Covalent Modification of a Neutral Metal−Organic Framework. *J. Am. Chem. Soc.* **2007,** *129*, 12368-12369.

29. Taylor-Pashow, K. M. L.; Della Rocca, J.; Xie, Z.; Tran, S.; Lin, W., Postsynthetic Modifications of Iron-Carboxylate Nanoscale Metal−Organic Frameworks for Imaging and Drug Delivery. *J. Am. Chem. Soc.* **2009,** *131*, 14261-14263.

30. Haneda, T.; Kawano, M.; Kawamichi, T.; Fujita, M., Direct Observation of the Labile Imine Formation through Single-Crystal-to-Single-Crystal Reactions in the Pores of a Porous Coordination Network. *J. Am. Chem. Soc.* **2008,** *130*, 1578-1579.

31. Nguyen, J. G.; Cohen, S. M., Moisture-Resistant and Superhydrophobic Metal−Organic Frameworks Obtained via Postsynthetic Modification. *J. Am. Chem. Soc.* **2010,** *132*, 4560-4561.

32. Aguado, S.; Canivet, J.; Farrusseng, D., Facile Shaping of an Imidazolate-Based MOF on Ceramic Beads for Adsorption and Catalytic Applications. *Chem. Commun.* **2010,** *46*, 7999-8001.

33. Cohen, S. M., Postsynthetic Methods for the Functionalization of Metal–Organic Frameworks. *Chem. Rev.* **2012,** *112*, 970-1000.

34. Cohen, S. M., The Postsynthetic Renaissance in Porous Solids. *J. Am. Chem. Soc.* **2017,** *139*, 2855-2863.

35. Wang, Z.; Cohen, S. M., Postsynthetic Modification of Metal-Organic Frameworks. *Chem. Soc. Rev.* **2009,** *38*, 1315-1329.

36. Tanabe, K. K.; Cohen, S. M., Postsynthetic Modification of Metal–Organic Frameworks—a Progress Report. *Chem. Soc. Rev.* **2011,** *40*, 498-519.

37. Kim, M.; Cahill, J. F.; Fei, H.; Prather, K. A.; Cohen, S. M., Postsynthetic Ligand and Cation Exchange in Robust Metal–Organic Frameworks. *J. Am. Chem. Soc.* **2012,** *134*, 18082-18088.

38. Kim, M.; Cahill, J. F.; Su, Y.; Prather, K. A.; Cohen, S. M., Postsynthetic Ligand Exchange as a route to Functionalization of 'inert' Metal–Organic Frameworks. *Chem. Sci.* **2012,** *3*, 126-130.

39. Boissonnault, J. A.; Wong-Foy, A. G.; Matzger, A. J., Core–Shell Structures Arise Naturally During Ligand Exchange in Metal–Organic Frameworks. *J. Am. Chem. Soc.* **2017,** *139*, 14841-14844.

40. Kalaj, M.; Palomba, J. M.; Bentz, K. C.; Cohen, S. M., Multiple Functional Groups in UiO-66 Improve Chemical Warfare Agent Simulant Degradation. *Chem. Commun.* **2019,** *55*, 5367-5370.

41. Deng, H.; Doonan, C. J.; Furukawa, H.; Ferreira, R. B.; Towne, J.; Knobler, C. B.; Wang, B.; Yaghi, O. M., Multiple Functional Groups of Varying Ratios in Metal-Organic Frameworks. *Science* **2010,** *327*, 846-850.

42. Yuan, S.; Huang, L.; Huang, Z.; Sun, D.; Qin, J.-S.; Feng, L.; Li, J.; Zou, X.; Cagin, T.; Zhou, H.-C., Continuous Variation of Lattice Dimensions and Pore Sizes in Metal–Organic Frameworks. *J. Am. Chem. Soc.* **2020,** *142*, 4732-4738.

43. Cheetham, A. K.; Kieslich, G.; Yeung, H. H. M., Thermodynamic and Kinetic Effects in the Crystallization of Metal–Organic Frameworks. *Acc. Chem. Res.* **2018,** *51*, 659-667.

44. Feng, L.; Wang, K.-Y.; Willman, J.; Zhou, H.-C., Hierarchy in Metal–Organic Frameworks. *ACS Cent. Sci.* **2020,** *6*, 359-367.

45. Yuan, S.; Qin, J.-S.; Li, J.; Huang, L.; Feng, L.; Fang, Y.; Lollar, C.; Pang, J.; Zhang, L.; Sun, D., et al., Retrosynthesis of Multi-Component Metal−Organic Frameworks. *Nat. Commun.* **2018,** *9*, 808.

46. Feng, L.; Wang, K.-Y.; Lv, X.-L.; Powell, J. A.; Yan, T.-H.; Willman, J.; Zhou, H.-C., Imprinted Apportionment of Functional Groups in Multivariate Metal–Organic Frameworks. *J. Am. Chem. Soc.* **2019,** *141*, 14524-14529.

47. Kirchon, A.; Feng, L.; Drake, H. F.; Joseph, E. A.; Zhou, H.-C., From Fundamentals to Applications: A Toolbox for Robust and Multifunctional MOF Materials. *Chem. Soc. Rev.* **2018,** *47*, 8611-8638.

48. Katayama, Y.; Kalaj, M.; Barcus, K. S.; Cohen, S. M., Self-Assembly of Metal–Organic Framework (MOF) Nanoparticle Monolayers and Free-Standing Multilayers. *J. Am. Chem. Soc.* **2019,** *141*, 20000-20003.

49. Yu, X.; Cohen, S. M., Photocatalytic Metal–Organic Frameworks for Selective 2,2,2-Trifluoroethylation of Styrenes. *J. Am. Chem. Soc.* **2016,** *138*, 12320-12323.

50. Feng, L.; Yuan, S.; Qin, J.-S.; Wang, Y.; Kirchon, A.; Qiu, D.; Cheng, L.; Madrahimov, S. T.; Zhou, H.-C., Lattice Expansion and Contraction in Metal-Organic Frameworks by Sequential Linker Reinstallation. *Matter* **2019,** *1*, 156-167.

51. Fan, W.; Yuan, S.; Wang, W.; Feng, L.; Liu, X.; Zhang, X.; Wang, X.; Kang, Z.; Dai, F.; Yuan, D., et al., Optimizing Multivariate Metal–Organic Frameworks for Efficient C2H2/CO2 Separation. *J. Am. Chem. Soc.* **2020**.

52. Hakonen, A.; Andersson, P. O.; Stenbæk Schmidt, M.; Rindzevicius, T.; Käll, M., Explosive and Chemical Threat Detection by Surface-Enhanced Raman Scattering: A Review. *Anal. Chim. Acta.* **2015,** *893*, 1-13.

53. Hakonen, A.; Rindzevicius, T.; Schmidt, M. S.; Andersson, P. O.; Juhlin, L.; Svedendahl, M.; Boisen, A.; Käll, M., Detection of Nerve Gases Using Surface-Enhanced Raman Scattering Substrates with High Droplet Adhesion. *Nanoscale* **2016,** *8*, 1305-1308.

54. DeCoste, J. B.; Peterson, G. W., Metal–Organic Frameworks for Air Purification of Toxic Chemicals. *Chem. Rev.* **2014,** *114*, 5695-5727.

55. Bobbitt, N. S.; Mendonca, M. L.; Howarth, A. J.; Islamoglu, T.; Hupp, J. T.; Farha, O. K.; Snurr, R. Q., Metal–Organic Frameworks for the Removal of Toxic Industrial Chemicals and Chemical Warfare Agents. *Chem. Soc. Rev.* **2017,** *46*, 3357-3385.

56. Islamoglu, T.; Chen, Z.; Wasson, M. C.; Buru, C. T.; Kirlikovali, K. O.; Afrin, U.; Mian, M. R.; Farha, O. K., Metal–Organic Frameworks against Toxic Chemicals. *Chem. Rev.* **2020**.

57. Katz, M. J.; Mondloch, J. E.; Totten, R. K.; Park, J. K.; Nguyen, S. T.; Farha, O. K.; Hupp, J. T., Simple and Compelling Biomimetic Metal–Organic Framework Catalyst for the Degradation of Nerve Agent Simulants. *Angew. Chem., Int. Ed.* **2014,** *53*, 497-501.

58. Mondloch, J. E.; Katz, M. J.; Isley Iii, W. C.; Ghosh, P.; Liao, P.; Bury, W.; Wagner, G. W.; Hall, M. G.; DeCoste, J. B.; Peterson, G. W., et al., Destruction of Chemical Warfare Agents using Metal–Organic Frameworks. *Nat. Mater.* **2015,** *14*, 512-516.

59. Peterson, G. W.; Moon, S.-Y.; Wagner, G. W.; Hall, M. G.; DeCoste, J. B.; Hupp, J. T.; Farha, O. K., Tailoring the Pore Size and Functionality of UiO-Type Metal–Organic Frameworks for Optimal Nerve Agent Destruction. *Inorg. Chem.* **2015,** *54*, 9684-9686.

60. Palomba, J. M.; Credille, C. V.; Kalaj, M.; DeCoste, J. B.; Peterson, G. W.; Tovar, T. M.; Cohen, S. M., High-Throughput Screening of Solid-State Catalysts for Nerve Agent Degradation. *Chem. Commun.* **2018,** *54*, 5768-5771.

61. Islamoglu, T.; Ortuño, M. A.; Proussaloglou, E.; Howarth, A. J.; Vermeulen, N. A.; Atilgan, A.; Asiri, A. M.; Cramer, C. J.; Farha, O. K., Presence versus Proximity: The Role of Pendant Amines in the Catalytic Hydrolysis of a Nerve Agent Simulant. *Angew. Chem., Int. Ed.* **2018,** *57*, 1949-1953.

62. López-Maya, E.; Montoro, C.; Rodríguez-Albelo, L. M.; Aznar Cervantes, S. D.; Lozano-Pérez, A. A.; Cenís, J. L.; Barea, E.; Navarro, J. A. R., Textile/Metal–Organic-Framework Composites as Self-Detoxifying Filters for Chemical-Warfare Agents. *Angew. Chem., Int. Ed.* **2015,** *54*, 6790-6794.

63. Momeni, M. R.; Cramer, C. J., Dual Role of Water in Heterogeneous Catalytic Hydrolysis of Sarin by Zirconium-Based Metal–Organic Frameworks. *ACS Appl. Mater. Interfaces* **2018,** *10*, 18435-18439.

64. Momeni, M. R.; Cramer, C. J., Structural Characterization of Pristine and Defective [Zr12(μ3-O)8(μ3-OH)8(μ2-OH)6]18+ Double-Node Metal–Organic Framework and Predicted Applications for Single-Site Catalytic Hydrolysis of Sarin. *Chem. Mater.* **2018,** *30*, 4432-4439.

65. Islamoglu, T.; Atilgan, A.; Moon, S.-Y.; Peterson, G. W.; DeCoste, J. B.; Hall, M.; Hupp, J. T.; Farha, O. K., Cerium(IV) vs Zirconium(IV) Based Metal–Organic Frameworks for Detoxification of a Nerve Agent. *Chem. Mater.* **2017,** *29*, 2672-2675.

66. Peterson, G. W.; Destefano, M. R.; Garibay, S. J.; Ploskonka, A.; McEntee, M.; Hall, M.; Karwacki, C. J.; Hupp, J. T.; Farha, O. K., Optimizing Toxic Chemical Removal through Defect-Induced UiO-66-NH2 Metal–Organic Framework. *Chem. Eur. J.* **2017,** *23*, 15913-15916.

67. Kirlikovali, K. O.; Chen, Z.; Islamoglu, T.; Hupp, J. T.; Farha, O. K., Zirconium-Based Metal–Organic Frameworks for the Catalytic Hydrolysis of Organophosphorus Nerve Agents. *ACS Appl. Mater. Interfaces* **2020,** *12*, 14702-14720.

68. Katz, M. J.; Moon, S.-Y.; Mondloch, J. E.; Beyzavi, M. H.; Stephenson, C. J.; Hupp, J. T.; Farha, O. K., Exploiting Parameter Space in MOFs: A 20-fold Enhancement of Phosphate-Ester Hydrolysis with UiO-66-NH2. *Chem. Sci.* **2015,** *6*, 2286-2291.

69. Li, J.-R.; Sculley, J.; Zhou, H.-C., Metal–Organic Frameworks for Separations. *Chem. Rev.* **2012,** *112*, 869-932.

70. Suh, M. P.; Park, H. J.; Prasad, T. K.; Lim, D.-W., Hydrogen Storage in Metal–Organic Frameworks. *Chem. Rev.* **2012,** *112*, 782-835.

71. Khan, N. A.; Hasan, Z.; Jhung, S. H., Adsorptive Removal of Hazardous Materials Using Metal-Organic Frameworks (MOFs): A Review. *J. Hazard. Mater.* **2013,** *244-245*, 444-456.

72. Yuan, S.; Feng, L.; Wang, K.; Pang, J.; Bosch, M.; Lollar, C.; Sun, Y.; Qin, J.; Yang, X.; Zhang, P., et al., Stable Metal–Organic Frameworks: Design, Synthesis, and Applications. *Adv. Mater.* **2018,** *30*, 1704303.

73. Denny, M. S., Jr.; Moreton, J. C.; Benz, L.; Cohen, S. M., Metal-Organic Frameworks for Membrane-Based Separations. *Nat. Rev. Mater.* **2016,** *1*, 16078.

74. Kitao, T.; Zhang, Y.; Kitagawa, S.; Wang, B.; Uemura, T., Hybridization of MOFs and polymers. *Chem. Soc. Rev.* **2017,** *46*, 3108-3133.

75. Kalaj, M.; Bentz, K. C.; Ayala, S.; Palomba, J. M.; Barcus, K. S.; Katayama, Y.; Cohen, S. M., MOF-Polymer Hybrid Materials: From Simple Composites to Tailored Architectures. *Chem. Rev.* **2020,** *120*, 8267-8302.

76. Gascon, J.; Kapteijn, F., Metal-Organic Framework Membranes—High Potential, Bright Future? *Angew. Chem., Int. Ed.* **2010,** *49*, 1530-1532.

77. Seoane, B.; Coronas, J.; Gascon, I.; Benavides, M. E.; Karvan, O.; Caro, J.; Kapteijn, F.; Gascon, J., Metal–Organic Framework Based Mixed Matrix Membranes: A Solution for Highly Efficient CO2 Capture? *Chem. Soc. Rev.* **2015,** *44*, 2421-2454.

78. Ayala, S.; Bentz, K. C.; Cohen, S. M., Block co-polyMOFs: Morphology Control of Polymer–MOF Hybrid Materials. *Chem. Sci.* **2019,** *10*, 1746-1753.

79. Zhang, Z.; Nguyen, H. T. H.; Miller, S. A.; Cohen, S. M., polyMOFs: A Class of Interconvertible Polymer-Metal-Organic-Framework Hybrid Materials. *Angew. Chem., Int. Ed.* **2015,** *54*, 6152-6157.

80. Zhang, Z.; Nguyen, H. T. H.; Miller, S. A.; Ploskonka, A. M.; DeCoste, J. B.; Cohen, S. M., Polymer–Metal–Organic Frameworks (polyMOFs) as Water Tolerant Materials for Selective Carbon Dioxide Separations. *J. Am. Chem. Soc.* **2016,** *138*, 920-925.

81. Chung, T.-S.; Jiang, L. Y.; Li, Y.; Kulprathipanja, S., Mixed Matrix Membranes (MMMs) Comprising Organic Polymers with Dispersed Inorganic Fillers for Gas Separation. *Prog. Polym. Sci.* **2007,** *32*, 483-507.

82. Bastani, D.; Esmaeili, N.; Asadollahi, M., Polymeric Mixed Matrix Membranes Containing Zeolites as a Filler for Gas Separation Applications: A review. *J. Ind. Eng. Chem.* **2013,** *19*, 375-393.

83. Zimmerman, C. M.; Singh, A.; Koros, W. J., Tailoring Mixed Matrix Composite Membranes for Gas Separations. *J. Membr. Sci.* **1997,** *137*, 145-154.

84. Zhang, Y.; Feng, X.; Li, H.; Chen, Y.; Zhao, J.; Wang, S.; Wang, L.; Wang, B., Photoinduced Postsynthetic Polymerization of a Metal-Organic Framework toward a Flexible Stand-Alone Membrane. *Angew. Chem., Int. Ed.* **2015,** *54*, 4259-4263.

85. Anjum, M. W.; Vermoortele, F.; Khan, A. L.; Bueken, B.; De Vos, D. E.; Vankelecom, I. F. J., Modulated UiO-66-Based Mixed-Matrix Membranes for CO2 Separation. *ACS Appl. Mater. Interfaces* **2015,** *7*, 25193-25201.

86. Kalaj, M.; Denny Jr, M. S.; Bentz, K. C.; Palomba, J. M.; Cohen, S. M., Nylon–MOF Composites through Postsynthetic Polymerization. *Angew. Chem., Int. Ed.* **2019,** *58*, 2336-2340.

87. Nam, D.; Huh, J.; Lee, J.; Kwak, J. H.; Jeong, H. Y.; Choi, K.; Choe, W., Cross-Linking Zr-Based Metal–Organic Polyhedra via Postsynthetic Polymerization. *Chem. Sci.* **2017,** *8*, 7765-7771.

88. Chin, J. M.; Reithofer, M. R.; Tan, T. T. Y.; Menon, A. G.; Chen, E. Y.; Chow, C. A.; Hor, A. T. S.; Xu, J., Supergluing MOF Liquid Marbles. *Chem. Commun.* **2013,** *49*, 493-495.

89. Bunge, M. A.; Davis, A. B.; West, K. N.; West, C. W.; Glover, T. G., Synthesis and Characterization of UiO-66-NH2 Metal–Organic Framework Cotton Composite Textiles. *Ind. Eng. Chem. Res.* **2018,** *57*, 9151-9161.

90. Chen, Z.; Islamoglu, T.; Farha, O. K., Toward Base Heterogenization: A Zirconium Metal–Organic Framework/Dendrimer or Polymer Mixture for Rapid Hydrolysis of a Nerve-Agent Simulant. *ACS Appl. Nano Mater.* **2019,** *2*, 1005-1008.

91. Dwyer, D. B.; Dugan, N.; Hoffman, N.; Cooke, D. J.; Hall, M. G.; Tovar, T. M.; Bernier, W. E.; DeCoste, J.; Pomerantz, N. L.; Jones, W. E., Chemical Protective Textiles of UiO-66-Integrated PVDF Composite Fibers with Rapid Heterogeneous Decontamination of Toxic Organophosphates. *ACS Appl. Mater. Interfaces* **2018,** *10*, 34585-34591.

92. Kim, M.-K.; Kim, S. H.; Park, M.; Ryu, S. G.; Jung, H., Degradation of Chemical Warfare Agents Over Cotton Fabric Functionalized with UiO-66-NH2. *RSC Adv.* **2018,** *8*, 41633-41638.

93. Liang, H.; Yao, A.; Jiao, X.; Li, C.; Chen, D., Fast and Sustained Degradation of Chemical Warfare Agent Simulants Using Flexible Self-Supported Metal–Organic Framework Filters. *ACS Appl. Mater. Interfaces* **2018,** *10*, 20396-20403.

94. McCarthy, D. L.; Liu, J.; Dwyer, D. B.; Troiano, J. L.; Boyer, S. M.; DeCoste, J. B.; Bernier, W. E.; Jones, J. W. E., Electrospun Metal–Organic Framework Polymer Composites for the Catalytic Degradation of Methyl Paraoxon. *New J. Chem.* **2017,** *41*, 8748-8753.

95. Moon, S.-Y.; Proussaloglou, E.; Peterson, G. W.; DeCoste, J. B.; Hall, M. G.; Howarth, A. J.; Hupp, J. T.; Farha, O. K., Detoxification of Chemical Warfare Agents Using a Zr6-Based Metal–Organic Framework/Polymer Mixture. *Chem. Eur. J.* **2016,** *22*, 14864-14868.

96. Peterson, G. W.; Browe, M. A.; Durke, E. M.; Epps, T. H., Flexible SIS/HKUST-1 Mixed Matrix Composites as Protective Barriers against Chemical Warfare Agent Simulants. *ACS Appl. Mater. Interfaces* **2018,** *10*, 43080-43087.

97. Peterson, G. W.; Lu, A. X.; Epps, T. H., Tuning the Morphology and Activity of Electrospun Polystyrene/UiO-66-NH2 Metal–Organic Framework Composites to Enhance Chemical Warfare Agent Removal. *ACS Appl. Mater. Interfaces* **2017,** *9*, 32248-32254.

98. Peterson, G. W.; Lu, A. X.; Hall, M. G.; Browe, M. A.; Tovar, T.; Epps, T. H., MOFwich: Sandwiched Metal–Organic Framework-Containing Mixed Matrix Composites for Chemical Warfare Agent Removal. *ACS Appl. Mater. Interfaces* **2018,** *10*, 6820-6824.

99. Yao, A.; Jiao, X.; Chen, D.; Li, C., Photothermally Enhanced Detoxification of Chemical Warfare Agent Simulants Using Bioinspired Core–Shell Dopamine–Melanin@Metal–Organic Frameworks and Their Fabrics. *ACS Appl. Mater. Interfaces* **2019,** *11*, 7927-7935.

100. Zhao, J.; Lee, D. T.; Yaga, R. W.; Hall, M. G.; Barton, H. F.; Woodward, I. R.; Oldham, C. J.; Walls, H. J.; Peterson, G. W.; Parsons, G. N., Ultra-Fast Degradation of Chemical Warfare Agents Using MOF–Nanofiber Kebabs. *Angew. Chem., Int. Ed.* **2016,** *55*, 13224-13228.

101. Zhao, J.; Losego, M. D.; Lemaire, P. C.; Williams, P. S.; Gong, B.; Atanasov, S. E.; Blevins, T. M.; Oldham, C. J.; Walls, H. J.; Shepherd, S. D., et al., Metal–Organic Frameworks: Highly Adsorptive, MOF-Functionalized Nonwoven Fiber Mats for Hazardous Gas Capture Enabled by Atomic Layer Deposition (Adv. Mater. Interfaces 4/2014). *Adv. Mater. Interfaces* **2014,** *1*.

102. Lee, D. T.; Zhao, J.; Oldham, C. J.; Peterson, G. W.; Parsons, G. N., UiO-66-NH2 Metal–Organic Framework (MOF) Nucleation on TiO2, ZnO, and Al2O3 Atomic Layer Deposition-Treated Polymer Fibers: Role of Metal Oxide on MOF Growth and Catalytic Hydrolysis of Chemical Warfare Agent Simulants. *ACS Appl. Mater. Interfaces* **2017,** *9*, 44847-44855.

103. Lee, D. T.; Zhao, J.; Peterson, G. W.; Parsons, G. N., Catalytic "MOF-Cloth" Formed via Directed Supramolecular Assembly of UiO-66-NH2 Crystals on Atomic Layer Deposition-Coated Textiles for Rapid Degradation of Chemical Warfare Agent Simulants. *Chem. Mater.* **2017,** *29*, 4894-4903.

104. Ma, K.; Islamoglu, T.; Chen, Z.; Li, P.; Wasson, M. C.; Chen, Y.; Wang, Y.; Peterson, G. W.; Xin, J. H.; Farha, O. K., Scalable and Template-Free Aqueous Synthesis of Zirconium-Based Metal–Organic Framework Coating on Textile Fiber. *J. Am. Chem. Soc.* **2019,** *141*, 15626-15633.

Chapter 2: Nylon-MOF Composites through Postsynthetic Polymerization

2.1 Introduction

As discussed in Chapter 1, assembly of composite materials with MOFs has proven to be an effective way to exploit the desired properties of MOFs, such as porosity and catalytic activity, in a form factor that makes their handling and implementation considerably easier than in the native, powder form.[7-11] Nylon 6,6 (PA-66), is a simple linear polyamide (PA) prepared from hexamethylenediamine (HMDA) and adipic acid. PA-66 remains one of the most widely used polymers today, especially in high-durability textiles. Given their utility, ubiquity, and facile preparation, polyamides are a natural choice for preparation of covalent composites with MOFs via PSP. However, no methods, to our knowledge, have been reported to create covalently linked nylon-MOF hybrid materials. Formation of amide bonds on ligands has been well established by PSM studies with MOFs.[12-14] Indeed, many common MOFs can be prepared with amine functionalized ligands where the amine is amenable to chemical modification to amide groups.[15-17] In related work by Choe et al., acyl chloride ligands were utilized to crosslink amine functionalized metal-organic polyhedral (MOPs).[18]

In Chapter 2, the preparation of PA-66-MOF composites is described using an interfacial polymerization technique. The synthesis described here covalently attaches UiO-66-NH_2 to a growing PA-66 fiber (designated as PA-66-UiO-66-NH_2) via PSP (Scheme 2.1). The Zr(IV)-based UiO-series was selected due to its chemical stability and previously reported catalytic activity toward CWAs.[1-3] The activity of this polymer-MOF hybrid toward CWA simulant degradation is also evaluated, which has not been widely reported for polymer-MOF hybrids, with the majority of reports on CWA simulant degradation by MOFs being described for powdered or microcrystalline samples.[3] The PSP materials prepared here show good activity compared to non-covalent, nylon-entrapped MOF particles.[2]

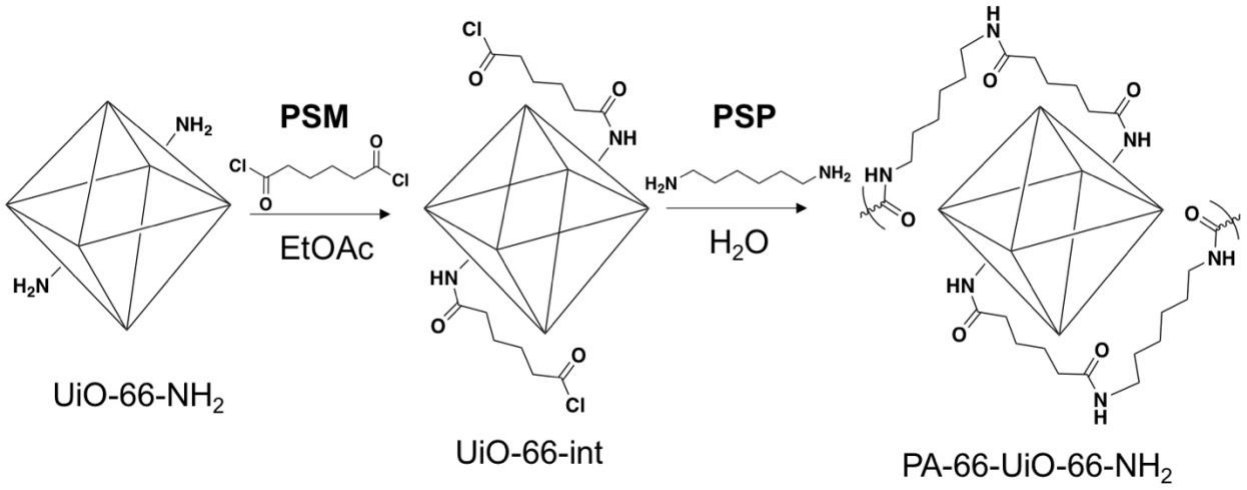

Scheme 2.1. PSM and PSP scheme used to prepare PA-66-UiO-66-NH_2.

2.2 Synthesis and Characterization of MOFs.

To synthesize the nylon composite, UiO-66-NH_2 was dispersed in ethyl acetate and PSM was performed with ten equivalents of adipoyl chloride. This forms the acid chloride UiO-66-int (int = intermediate, Scheme 1). Samples of UiO-66-int were isolated and analyzed by ^{1}H NMR to determine the extent of amine functionality. Exposure of UiO-66-NH_2 to adipoyl chloride for 10 min resulted in ~25% functionalization (Table S2.1). The ^{1}H NMR spectra suggested the formation of two different amide linked products, as well as free adipic acid (from hydrolyzed adipoyl chloride, a byproduct of the workup, Figure 2S.4). One amide product is the desired condensation of amino-benzene dicarboxylic acid (NH_2-H_2bdc) with adipoyl chloride, while the second product is a bis(amide) wherein the adipoyl chloride has linked two NH_2-bdc ligands (Figure 2S.5). The ^{1}H NMR data revealed that after 10 min of PSM, 25% of the ligands in the MOF were functionalized with a ~1:1 ratio of the two amide products (Table 2S.2). To interrogate the possibility of inter- (vs. intra-) particle cross-linking, dynamic light scattering (DLS)

experiments were performed. DLS shows essentially identical particle hydrodynamic radii for UiO-66-NH_2 and UiO-66-int during the PSM reaction, indicating that intraparticle crosslinking is the predominant source of the aforementioned bis(amide) product (Figure 2S.9).

After PSM with adipoyl chloride, a suspension of UiO-66-int in EtOAc (containing ten equivalents of adipoyl chloride) was carefully layered on top of an aqueous solution of HMDA. Polymerization occurs at the interface of the two layers, during which UiO-66-int is covalently incorporated into the forming polyamide, resulting in the desired PA-66-UiO-66-NH_2 hybrid material (Figure 2S.1). The resulting PSP product retains the flexibility of the PA-66 fiber after incorporation of MOF. Presence of MOF throughout the entire fiber was determined via powder X-ray Diffraction (PXRD) and Scanning Electron Microscopy (SEM). Pieces of the composite material were cut every 12 inches and analyzed by PXRD and SEM, which both indicated that the MOF was present throughout the length of the fiber (Figure 2S.10 and 2S.16). Sections of fibers were cut and analyzed via thermogravimetric analysis (TGA) to determine the loading of MOF throughout the fiber and the results showed minor differences(Figure 2S.19).

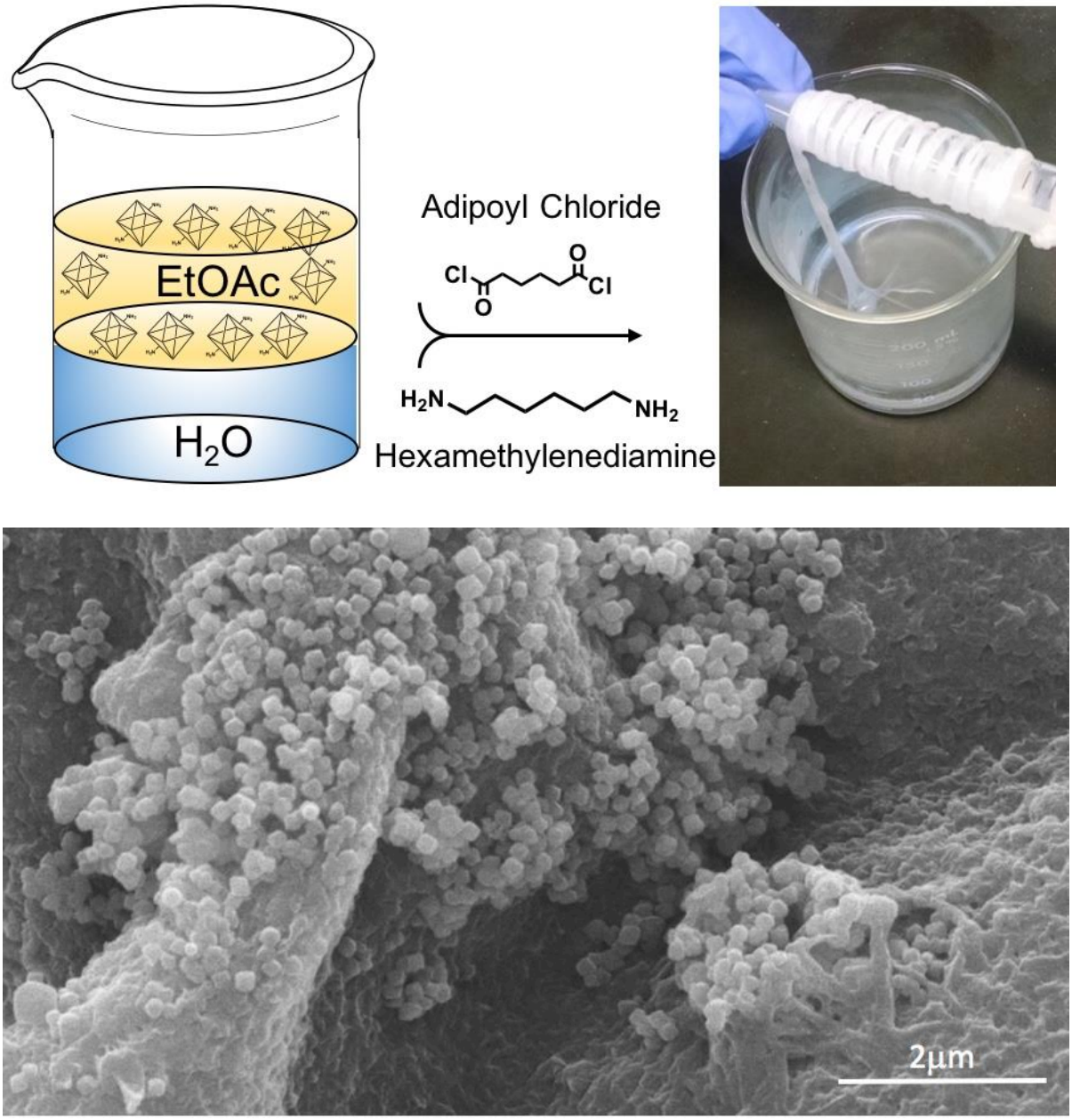

Figure 2.1. *Top*: Interfacial fabrication of PA-66-MOF composites through PSP. *Bottom*: SEM image of PA-66-UiO-66-NH_2.

2.3 Synthesis and Characterization of PA-66-MOF Composites.

Control studies were performed with three different MOFs to confirm that covalent linkages between UiO-66-NH_2 and PA-66 was achieved, as opposed to physical entrapment of the MOF particles within or onto the polymer. The parent UiO-66 material and two UiO-66

derivatives (UiO-66-AM6, UiO-66-AM6COOH) were investigated to compare with UiO-66-NH_2 (Figure 2.2). MOFs without chemical reactive handles (e.g. UiO-66, UiO-66-AM6 and UiO-66-AM6COOH) for covalent integration failed to produce long drawn out fibers from the interfacial polymerization reaction. For example, with UiO-66 only a ~30 cm continuous fiber could be pulled from the interface under identical conditions as used with UiO-66-int (which gave >100 cm fibers as described above). This is likely due to the UiO-66 interfering with the polymerization at the interface (detailed synthesis and characterization of these control materials can be found in section 2.5). Distinct differences can be seen between the PSP product and noncovalent hybrids, for example, the noncovalent PA-66@UiO-66 material is extremely thin and brittle compared to the PA-66-UiO-66-NH_2 PSP product (Figure 2S.17).

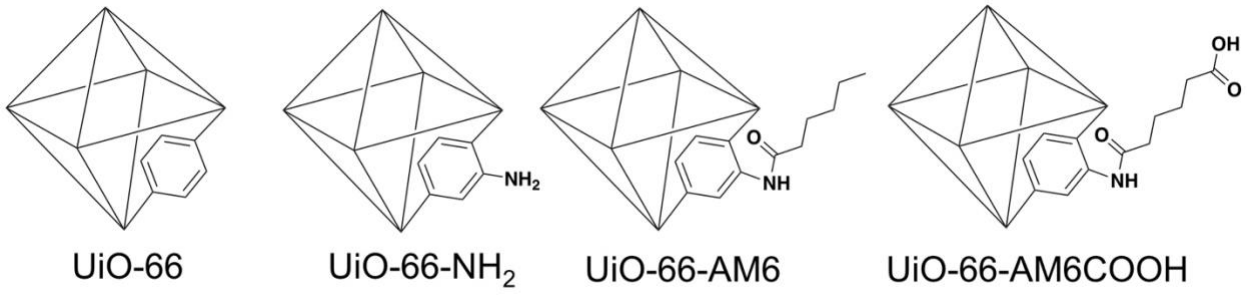

Figure 2.2. Four different MOFs used for PSP in PA-66 composites.

TGA and differential scanning calorimetry (DSC) analysis of the PSP product (PA-66-UiO-66-NH_2), as well as all three control materials (PA-66@UiO-66, PA-66@UiO-66-AM6COOH, and PA-66@UiO-66-AM6), were conducted in an effort to determine the extent of MOF incorporation into the polymer as well as the melting point of the materials. TGA indicates 29±6% by weight of MOF incorporation for the PSP product (PA-66-UiO-66-NH_2) compared to

20±3% incorporation for PA-66@UiO-66, 27±5% incorporation for PA-66@UiO-66-AM6COOH, and 23±6% incorporation for PA-66@UiO-66-AM6 (Table 2S.3).

Covalent crosslinking of the polyamides in PA-66-UiO-66-NH_2 is supported by DSC melting point data (Table 2.1). Specifically, samples were heated to 280 °C at 10 °C/min, then cooled to 100 °C at 10 °C/min, and finally heated to 600 °C at 10 °C/min to determine the thermal characteristics of the composite materials. The initial heating step is performed to clear the thermal history of the material whereas the second heating step is used to determine the accurate melting point of the material. Melt curves were integrated and assessed by the onset and peak of the curve. Pure PA-66 has an experimental second melt point onset of 237 °C and melt peak of 252 °C. The PA-66@UiO-66 material shows a very similar second melt suggesting that the PA-66 and UiO-66 are phase segregated after the first melt leading to a nearly pure nylon-like second melt (Table 2.1). PA-66@UiO-66-AM6COOH shows a second melting point depression of ~5 °C at the onset and ~5 °C at the peak, relative to PA-66. PA-66@UiO-66-AM6 has a second melting point depression of ~5 °C at the onset and ~4 °C at the peak. In contrast, the same melt with PA-66-UiO-66-NH_2 results in a depression of the melting point by ~20 °C at the onset and ~12 °C at the peak, when compared to pure PA-66. This large melting point depression suggests the covalent attachment of MOF as part of the nylon fibers, which significantly disrupts polymer crystallization. These results are consistent with other findings where covalent attachment of large inorganic particles disrupt polymer crystallinity and results in reduced melt temperature.[19-20]

Table 2.1. Second melting point of PA-66 and PA-66-MOF hybrid materials highlighting the melting point depression of PA-66-UiO-66-NH_2.

Material	2nd MP Onset (°C)	2nd MP peak (°C)
PA-66	236 ± 2	252 ± 1
PA-66@UiO-66	238 ± 3	252 ± 2
PA-66@UiO-66-AM6	231 ± 1	248 ± 1
PA-66@UiO-66-AM6COOH	232 ± 1	247 ± 1
PA-66-UiO-66-NH_2	216 ± 5	240 ± 2

Pore accessibility of the hybrid materials was determined by measuring the BET surface area of both MOFs and composite materials. Surface area analysis by N_2 gas sorption measurements show that the porosity of the MOFs is better retained in the covalent hybrid materials relative to the non-covalent materials. BET surface area measurements were done on all MOF powders (Figure 2S.31). Based on the percent MOF in the composite materials, the expected BET surface area of the composites was calculated. For example, if the MOF component were fully accessible in the BET experiment the surface areas are estimated to be 293 m^2/g and 223 m^2/g, for PA-66-UiO-66-NH_2 (29 wt%) and PA-66@UiO-66 (20 wt%), respectively. The measured quantities were found to be 107±2 m^2/g and 35±1 m^2/g for the PA-66-UiO-66-NH_2 and PA-66@UiO-66, respectively (Figure 2S.32). Whereas pore accessibility is decreased for both samples compared to the free MOF, this result indicates that pore accessibility is significantly better in the PSP product (37% of estimated) compared to the non-covalent product (16% of estimated, Table 2S.3).

Covalent attachment of MOFs into processable polymer materials is critical for the utilization of MOFs in real-world applications. To assess the applicability of the materials as functional textiles, the PA-66-MOF hybrid materials were screened for catalytic activity against the nerve agent simulant, DMNP (Figure 2.3). An HTS approach using UV-visible spectroscopy

was used to detect degradation of the DMNP simulant,[2, 21] at pH = 8 using UiO-66, UiO-66-NH_2, UiO-66-AM6, and UiO-66-AM6COOH, as both nylon composites and powders. As shown in Figure 2.3, UiO-66 and UiO-66-AM6 free powders are approximately three times more active than the UiO-66-NH_2 and UiO-66-AM6COOH MOFs, which is consistent with prior reports.[21] Incorporation of the various functionalized MOFs into PA-66 composites had a dramatic effect on the catalytic degradation of DMNP. The covalently attached hybrid material, PA-66-UiO-66-NH_2, was nearly an order of magnitude more active than any of the non-covalent incorporated PA-66 composites. Further, composite materials were recycled and displayed no loss in catalytic activity toward DMNP degradation through four cycles (Figure 2S.30). These results, along with the gas sorption analysis, demonstrate that more MOF particles in the PA-66-UiO-66-NH_2 composite are accessible and active than in the nylon-entrapped materials (i.e., PA-66@UiO-66, PA-66@UiO-66-AM6COOH, and PA-66@UiO-66-AM6).

Several MOF materials in powder form have been screened for CWA catalysis, there are only a few examples in the literature of CWA screening using polymer-MOF hybrid materials.[5-6] Recent studies by Parsons et al. have utilized atomic layer deposition (ALD) by coating polymer fibers with an intermediate metal oxide layer that provides a nucleation site for MOF synthesis.[5-6] DMNP hydrolysis (pH = 10) using the ALD generated materials indicated decreased performance compared to the free MOF powders.[5] When comparing fibers with different ALD coatings, increased activity was observed when using ALD films that promoted a higher quality of MOF crystal growth.[5] Expectedly, their studies showed the MOF was required for catalytic activity when compared to the polymer alone.[6] Moreover, the ALD composite materials display loss of activity after the materials were recycled two times whereas our materials showed retention of

activity through four cycles (Figure 2S.30).[6] Our materials provide a straightforward, covalent alternative to catalytically active, MOF-containing polymer fibers.

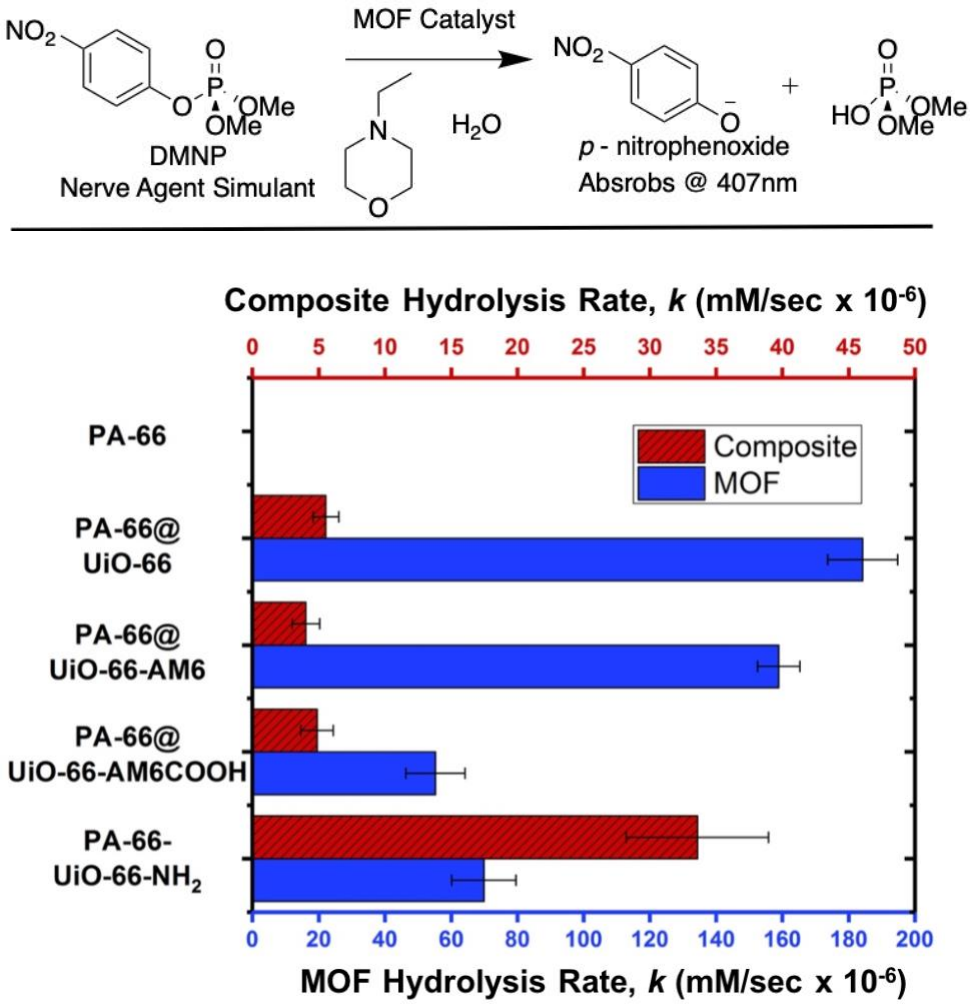

Figure 2.3. *Top:* DMNP degradation reaction. *Bottom:* Rate of catalytic degradation of DMNP by MOF powders and PA-66-MOF composites measured by UV-visible adsorption at 407nm.

2.4 Conclusions

In conclusion, PSP is shown to be an efficient method to incorporate UiO-66-NH_2 into nylon (PA-66) polymer fibers. MOF materials were subjected to PSM to modify the ligand components, after which PSP was used to generate PA-66-MOF hybrid materials. ^{1}H NMR studies

on small molecule models, melting point measurements through DSC, and surface area determination, were all indicative of a covalent link between the MOF particles and the nylon fibers. The covalently linked hybrid material showed significantly higher activity against CWA simulant degradation compared to MOF particles that were simply physically entrapped in the polymer. This result underscores the benefits of PSP over physical adhesion or entrapment of MOFs to polymer materials. This is a rare example of examining CWA degradation in a polymer-MOF hybrid material that is closer to a usable form factor. Current experiments are focusing on engineering of this material for potential textile incorporation.

2.5 Appendix: Supporting Information

Materials

All solvents and starting materials were purchased from chemical suppliers and used without further purification (Sigma Aldrich, Alfa Aesar, EMD, and TCI).

MOF Synthesis

UiO-66. Zirconium(IV) chloride (61 mg, 0.26 mmol) and terephthalic acid (43 mg, 0.26 mmol) were dissolved in 15 mL DMF with 0.45 mL glacial acetic acid in a 20 mL vial with Teflon-lined cap. The vial was then placed in a 120 °C oven for 24 h. After cooling to ambient temperature, the particles were collected by centrifugation (fixed-angle rotor, 6000 rpm, 5 min), followed by washing with 3×10 mL DMF and 3×10 mL MeOH. The particles were then soaked in MeOH for 3 d with solvent changed daily, before being dried under vacuum at room temperature. The procedure was repeated in parallel 40 times and all products were combined (2.73 g, 86%).

UiO-66-NH_2. Zirconium(IV) chloride (61 mg, 0.26 mmol) and 2-aminoterephthalic acid (43 mg, 0.26 mmol) were dissolved in 15 mL DMF with 0.45 mL glacial acetic acid in a 20mL vial with Teflon-lined cap. The vial was then placed in a 120 °C oven for 24 h. After cooling to ambient temperature, the particles were collected by centrifugation (fixed-angle rotor, 6000 rpm, 5 min), followed by washing with 3×10 mL DMF and 3×10 mL MeOH. Using a modified procedure, the formyl groups were restored to free amine. 2 g of UiO-66-NH_2 was added to 100 mL MeOH:H_2O 1:1 mixture with 5 mL of conc. HCl and refluxed overnight. Solid was collected by filtration and washed with MeOH. The procedure was repeated in parallel 40 times and all products were combined (2.92 g, 88%).

UiO-66-AM6. UiO-66-NH_2 (0.27 mmol, 80 mg) was dispersed in ethyl acetate (20 mL) with ultrasonication for 10 min. Hexanoyl chloride (3.45 mmol, 0.48 mL) was then added to this dispersion and allowed to sit for 24 h. The particles were then soaked in MeOH for 3 days with solvent changed daily and H_2O for 3 d with solvent changed daily, before being dried under vacuum at room temperature (80 mg, 96%). ^{1}H NMR digestion data confirmed 11% ligand functionalization.

UiO-66-AM6COOH. UiO-66-NH_2 (0.27 mmol, 80 mg) was dispersed in ethyl acetate (20 mL) with ultrasonication for 10 min. Adipoyl chloride (3.45 mmol, 0.50 mL) was then added to this dispersion and allowed to sit for 24 h. The particles were then soaked in MeOH for 3 d with solvent changed daily and H_2O for 3 d with solvent changed daily, before being dried under vacuum at room temperature (80 mg, 96%,). ^{1}H NMR digestion data confirmed 33% ligand functionalization.

PA-66-MOF Fabrication

A series of MOF-PA composites were prepared by this method and the materials were characterized to assess the integrity of the MOF component after fabrication. In a typical preparation, a quantity of UiO-66-NH_2 (0.27 mmol, 80 mg) was dispersed in 20mL ethyl acetate with ultrasonication for 20 min. Adipoyl chloride (3.4 mmol, 0.63 g, 0.50 mL) was then added to this dispersion and further sonicated for 10 min (time was varied for specific studies). Upon addition of the adipoyl chloride, a reaction is evident by a color change of the MOF particles to a paler shade of yellow. A series of samples were prepared containing UiO-66 and UiO-66-NH_2 quantities ranging from 5 mg to 100 mg of MOF.

Separately, a solution of HMDA (3.45 mmol, 0.400 g, 0.45 mL) in 20 mL H_2O was prepared and layered into a 100-mL beaker as the bottom layer. The ethyl acetate dispersion was then carefully layered on top of the aqueous layer. Polymerization occurred at the interface of the two layers and the PA-MOF product was slowly pulled from the interface, forming a continuous fiber. The product was removed until fiber formation became discontinuous, indicated a depletion of the monomer feedstocks. The product was washed with water and dried at 70 °C overnight, then dried under vacuum at room temperature for 24 h.

Materials Characterization

Powder X-ray Diffraction (PXRD). PXRD data was collected at room temperature on a Bruker D8 Advance diffractometer running at 40 kV, 40 mA for Cu Kα (λ = 1.5418 Å), with a scan speed of 0.5 sec/step, a step size of 0.01° in 2θ, and a 2θ range of 3-50° at room temperature.

Scanning Electron Microscopy (SEM). MOFs were placed on conductive carbon tape on a sample holder and coated using an Ir-sputter coating for 7 sec. A Zeiss Sigma 500 ESEM microscope was used for acquiring images using a 2-3 kV energy source under vacuum at a working distance of 5 mm.

Thermogravimetric analysis and differential scanning calorimetry (TGA/DSC). ~10 mg of sample were placed in a 100 μL aluminum crucible. Samples were analyzed on a Mettler Toledo Star TGA/DSC using a temperature range of 30-600 °C scanning at 5 °C/min under an N_2 atmosphere (75 cm^3/min N_2 flow rate) for sample degradation measurements and a heat-cool-heat procedure at 10 °C/min for melting point determination.

Nuclear Magnetic Resonance. Proton nuclear magnetic resonance spectra (^{1}H NMR) were recorded on a Varian FT-NMR spectrometer (400 MHz). Chemical shifts are quoted in parts per million (ppm) referenced to the appropriate solvent peak or 0 ppm for TMS. MOFs were digested for NMR analysis by immersion of ~8-10 mg MOF in 580 μL DMSO-d_6 with 20 μL HF (48% in water). Samples were kept in this acidic solution at room temperature until the MOF was fully dissolved.

Dynamic Light Scattering (DLS). 2 mg of MOF sample was dispersed in 3 mL of water, the solution was transferred into a quartz cuvette and inserted in a Malvern Instruments Zetasizer Nano ZS90.

Catalysis Experiments. All catalytic monitoring was carried out using a BioTek Synergy H4 plate reader using single wavelength absorbance mode. 20 and 40 mM of *N*-ethylmorpholine buffer was prepared from deionized water adjusted to pH = 8.0 and pH = 10 for specific tests. First a plot of absorbance of *p*-nitrophenol at varying concentrations was measured yielding a conversion factor of 3.48 Abs/mM.[21] MOF powder samples were prepared by weighing 6 mg of MOF and diluting with 10 mL of deionized water. These solutions were rigorously sonicated and vortexed (>3× of each) and diluted ½ with 40 mM buffer solution yielding 300 μg/mL MOF in 20 mM buffer solution. Dimethyl *p*-nitrophenylphosphate (DMNP) hydrolysis assays with MOF powders were carried out in Olympus Plastics clear, flat-bottom 96-well plates. Each well was prepared with 100 μL total volume containing: 95 μL MOF suspension in buffer and 5 μL substrate (25 mM DMNP in methanol; 1.25 mM total concentration; 0.125 μmol). Upon the addition of substrate with multi-channel pipette hydrolysis was monitored by change in absorbance (λ_{max} = 407 nm) at over 60 min at 24 °C with 5 sec shaking of plate every 40 sec. Activity was measured as initial linear rate, measured from 10 to 50 min using Excel software. Reported activities for MOF-only samples are an average slope of seven replicates.[21] MOF-polymer composite testing was carried out with minor modifications to MOF powder screen due physical parameters of fibers. Fibers of each composite were cut to 3±0.2 mg segments and placed into well of a Grenier Bio-one Cellstar 24-well plate. Each well was prepared with 1.02 mL total volume containing: a single 3 mg fiber, 1 mL 20 mM buffer, and 20 μL substrate (25 mM DMNP in methanol; 0.39 mM total

concentration; 0.5 μmol). DMNP hydrolysis was monitored in the same way as above for MOF powders. Reported activities for MOF-polymer composites are an average slope of six replicates.

Supporting Tables and Figures

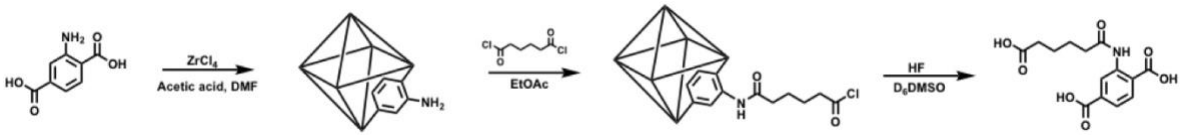

Scheme 2S.1. Synthetic route towards adipoyl chloride functional UiO-66-NH_2 and subsequent digestion.

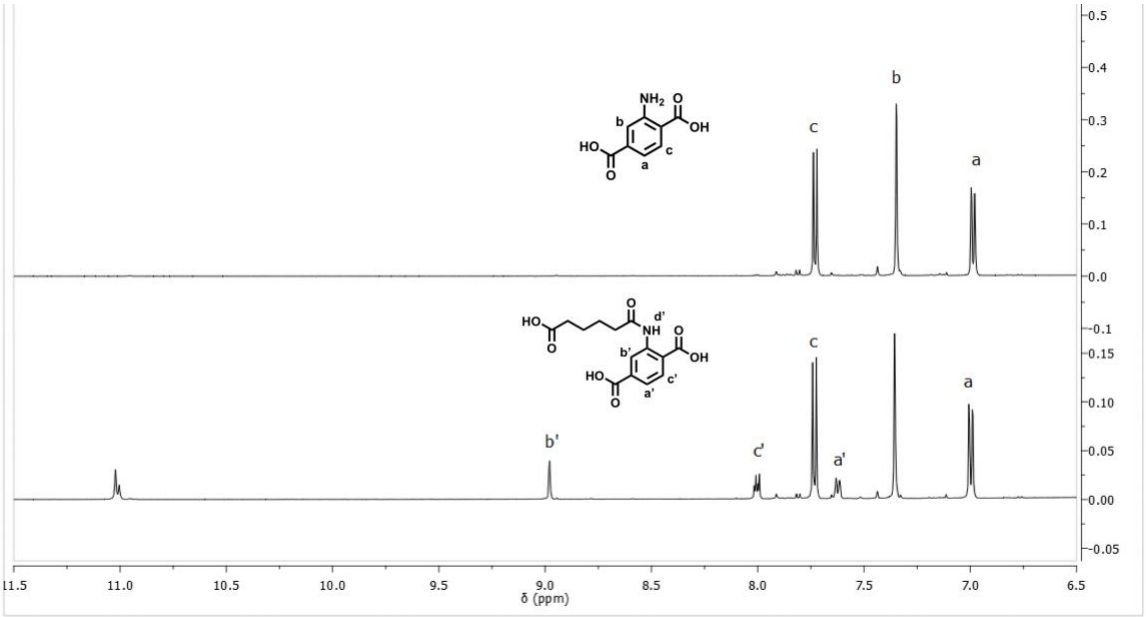

Figure 2S.1. *Top:* ^{1}H NMR spectrum of amino-BDC. *Bottom:* ^{1}H NMR spectrum of adipoyl chloride functionalized NH_2-bdc. As shown in Error! Reference source not found., there are distinct downfield peak shifts upon functionalization of amino-BDC with adipoyl chloride. The percent functionalization can be quantified by the ratio:

$$\frac{\int c'}{\int c' + \int c}$$

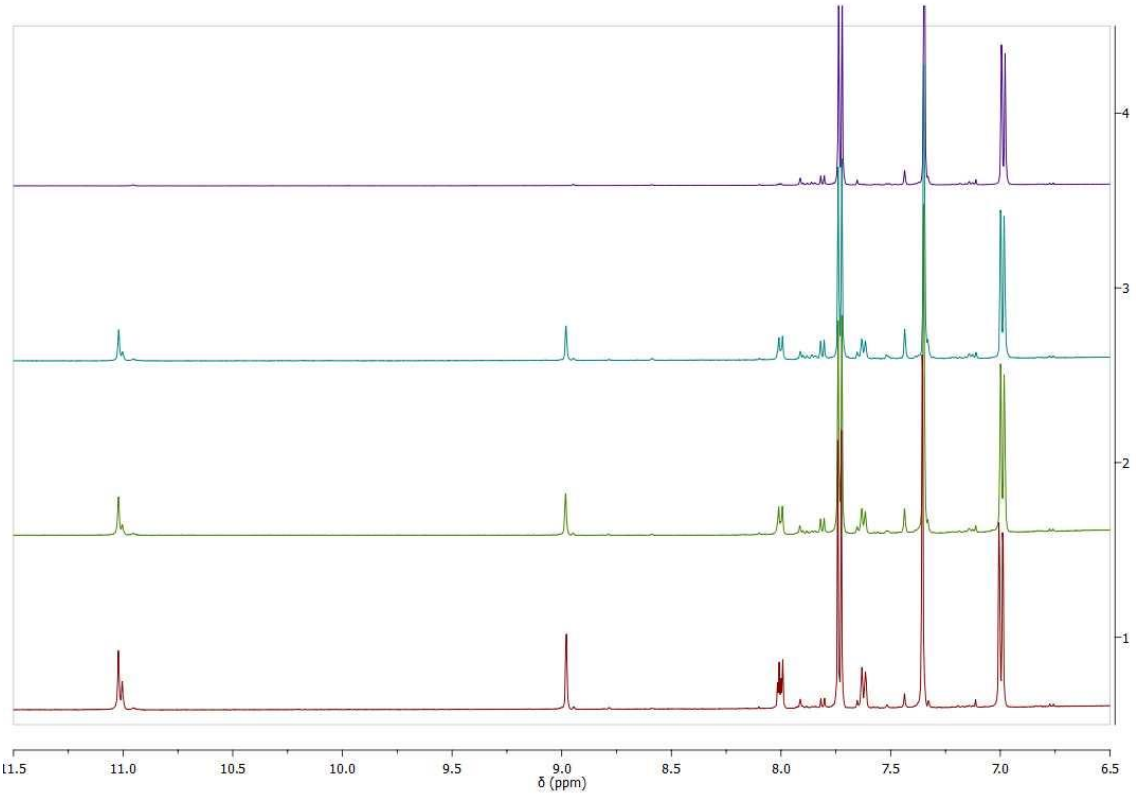

Figure 2S.2. From top to bottom, ^{1}H NMR spectra of 0 min, 1 min, 5 min, and 10 min, reaction time of UiO-66-NH_2 with adipoyl chloride following digestion.

Table 2S.1. Percent functionalization of UiO-66-NH_2 amino-BDC with adipoyl chloride at different reaction times.

Reaction time (min)	Percent functionalization
1	16 %
5	19 %
10	25 %

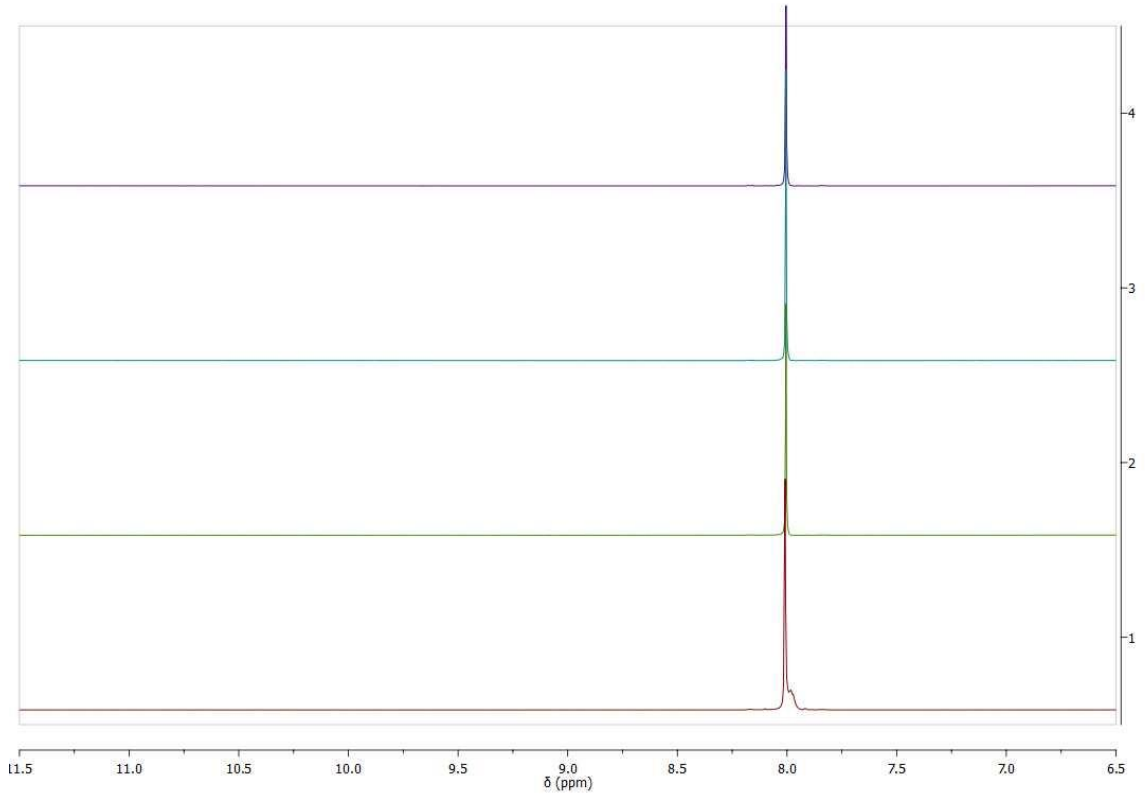

Figure 2S.3. ^{1}H NMR spectra reaction of 1 min, 5 min, 10 min, and 0 min reaction times of UiO-66 with adipoyl chloride following digestion.

Determination of Percent Crosslinking. In a similar fashion as discussed above to quantify the percent of functionalized NH_2-bdc, the percent of "crosslinked" bdc, that is the percentage of adipoyl chloride that has reacted with NH_2-bdc on both sides can be quantified by the ratio of doubly reacted adipoyl chloride to single addition. Due to the symmetry of the doubly reacted adipoyl chloride only two peaks are observed, and they are shifted slightly downfield of adipic acid, as shown below in Figure .

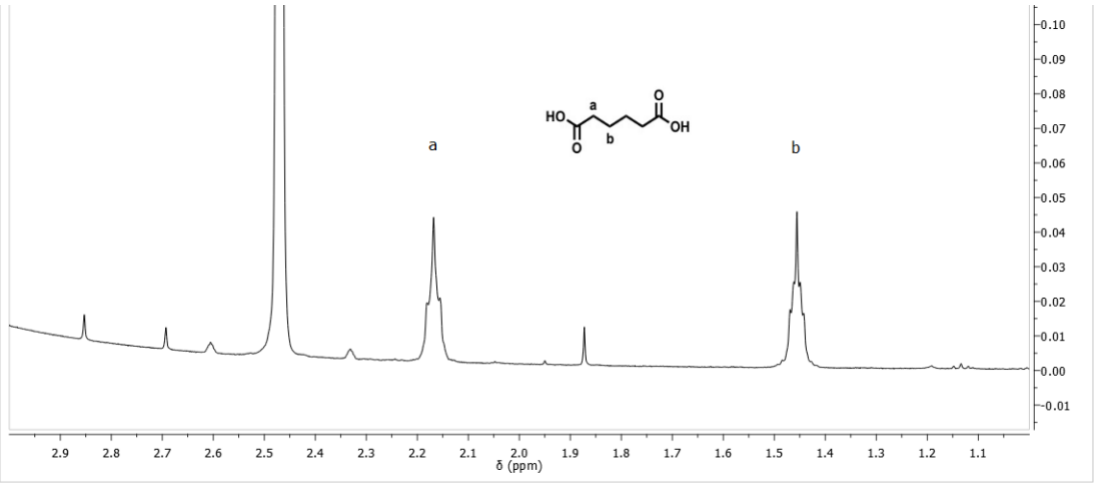

Figure 2S.4. ^{1}H NMR spectrum of UiO-66 (unfunctionalized) after treatment with adipoyl chloride and subsequent digestion. Due to hydrolysis during digestion adipoyl chloride is converted to adipic acid.

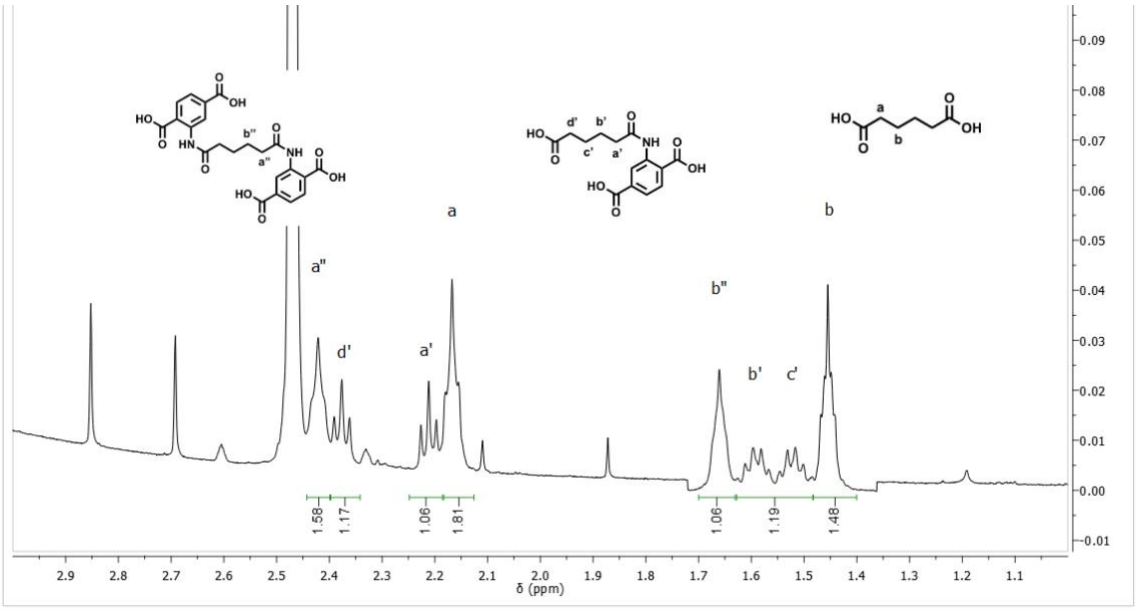

Figure 2S.5. Peak assignments for possible products of UiO-66-NH_2 and adipoyl chloride following digestion.

$$percent\ single\ addition\ adipoyl\ chloride = \frac{\int b' + c'}{\int a'' + \int b' + c'}$$

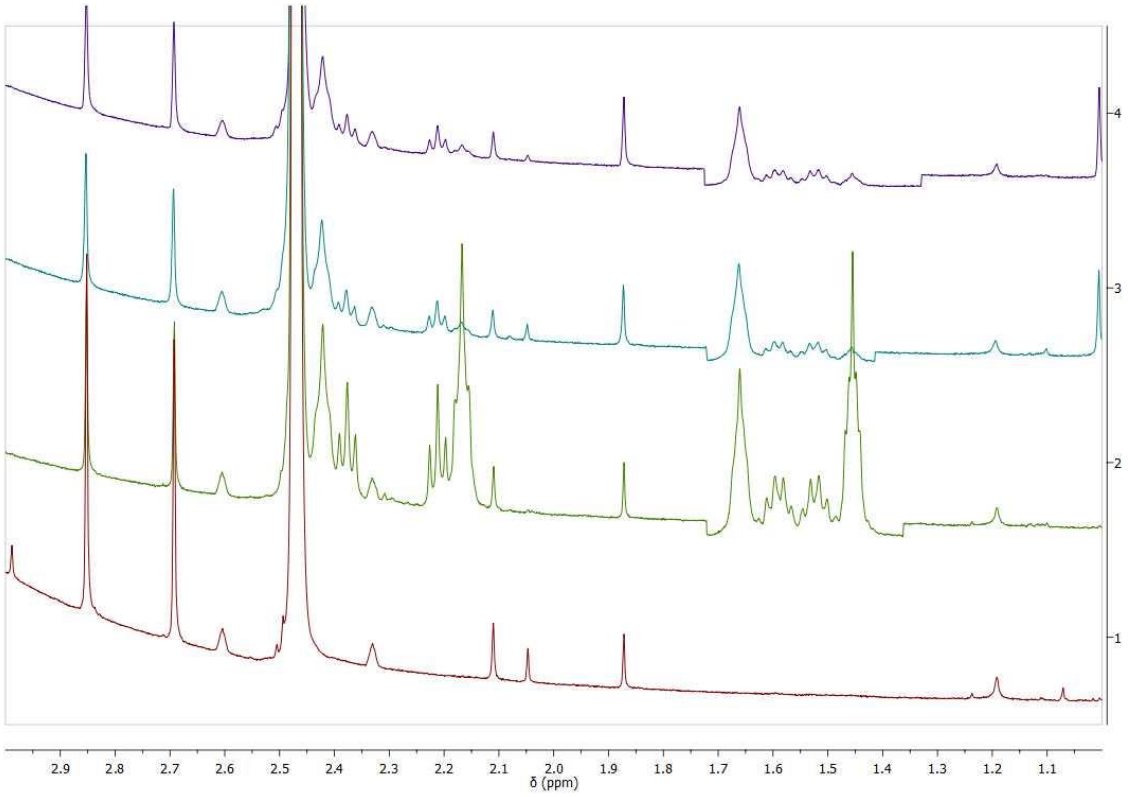

Figure 2S.6. From top to bottom, ^{1}H NMR spectra of 1 min, 5 min, 10 min, and 0 min reaction time of UiO-66-NH_2 with adipoyl chloride following digestion, showing adipoyl chloride region of spectra.

Table 2S.2. Percent single addition of adipoyl chloride on UiO-66-NH_2 at different reaction times.

Reaction time (min)	Percent single addition
1	39 %
5	37 %
10	53 %

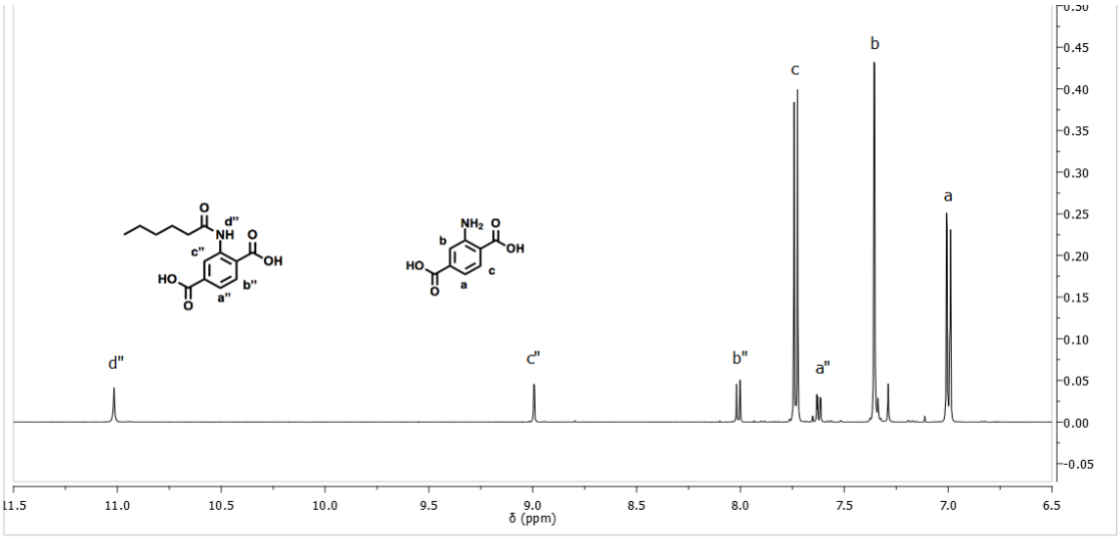

Figure 2S.7. ^{1}H NMR spectra of digested UiO-66-AM6.

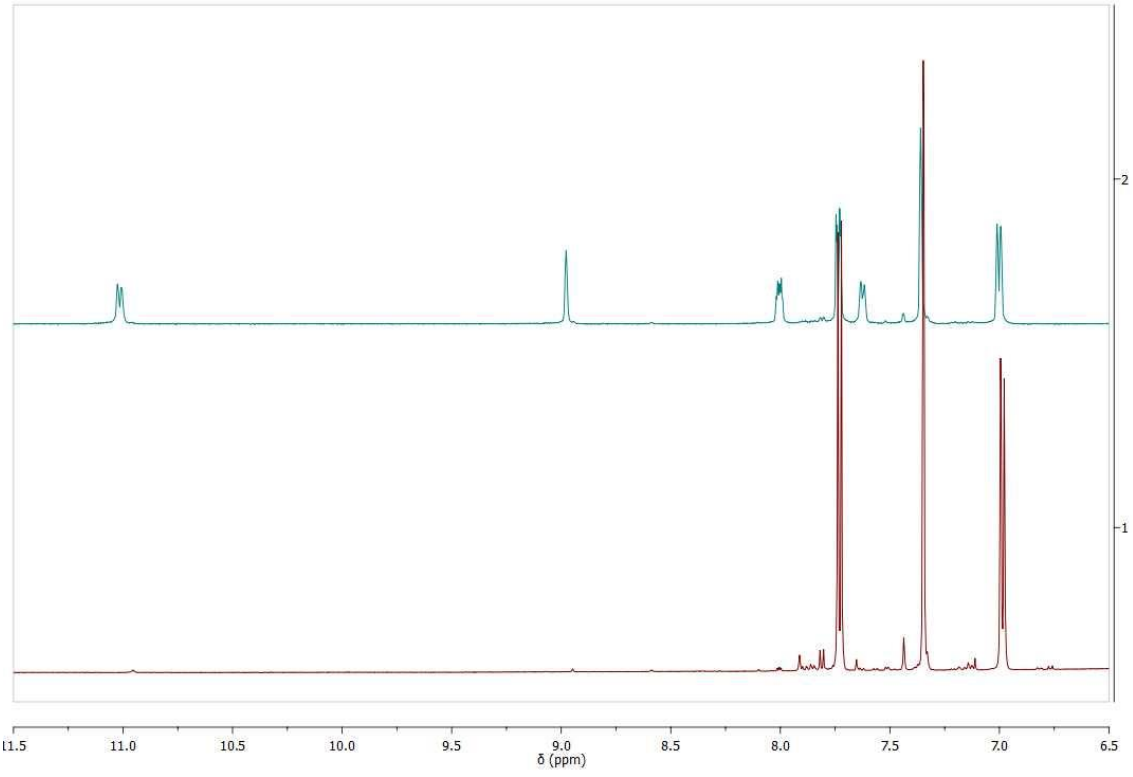

Figure 2S.8. ^{1}H NMR spectra of digested UiO-66-AM6COOH.

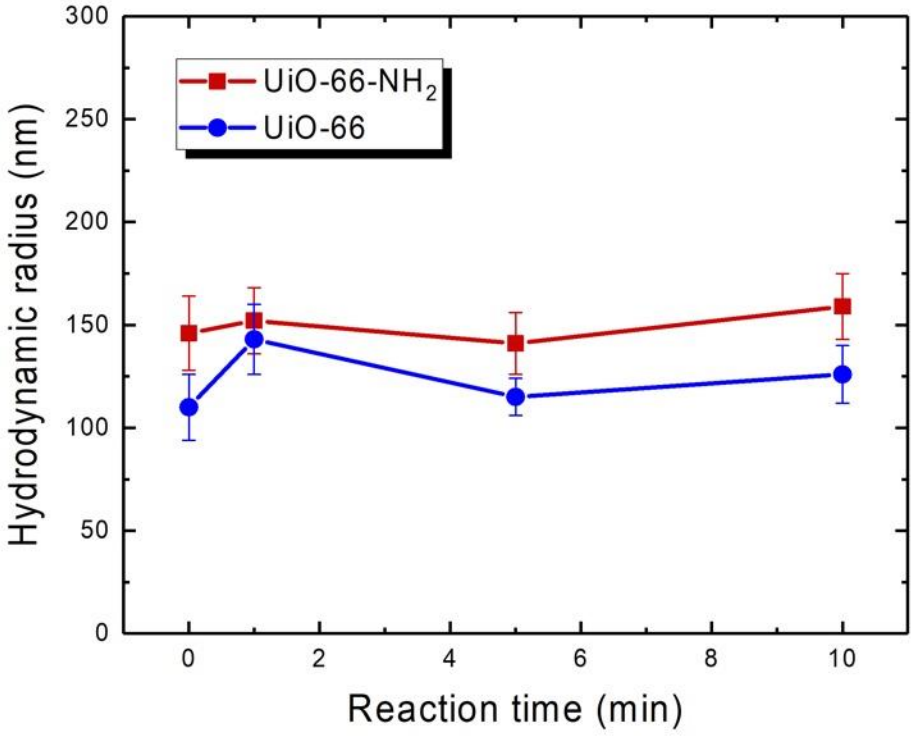

Figure 2S.9. Hydrodynamic radius indicating no change through 10 min of PSM as determined by DLS.

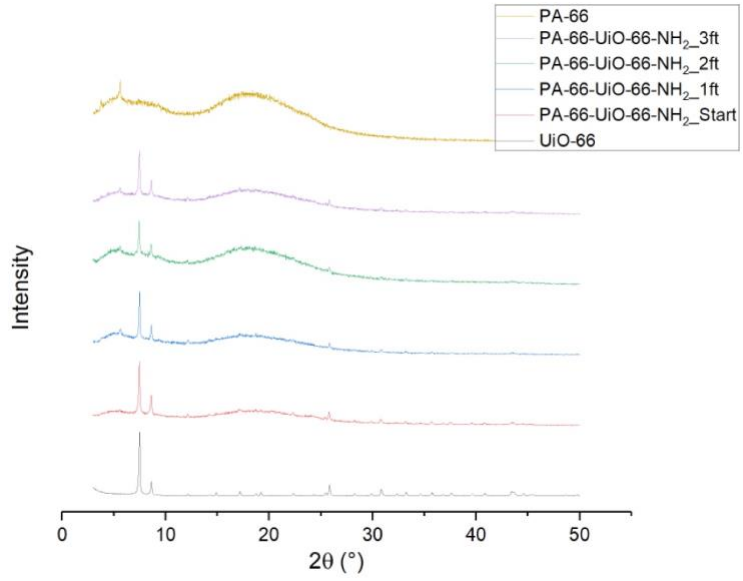

Figure 2S.10. PXRD of PA-66-UiO-66-NH_2 through 3 ft of material with 80 mg total loading of UiO-66-NH_2.

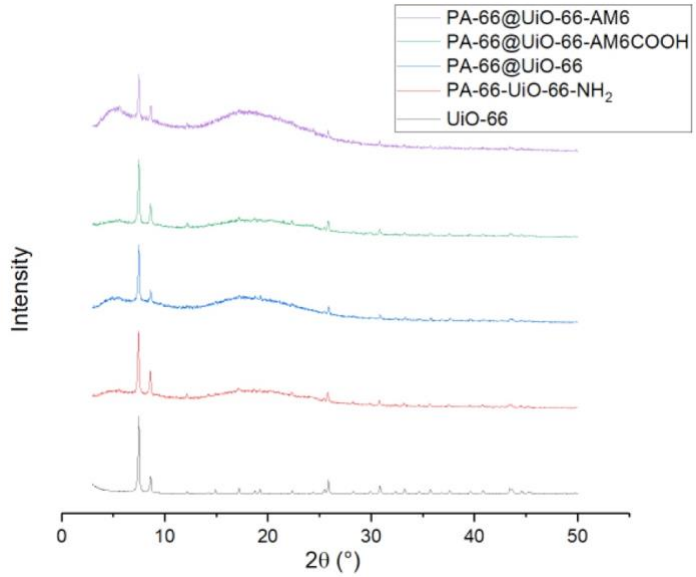

Figure 2S.11. PXRD of PA-66-UiO-66-NH_2, PA-66@UiO-66, PA-66@UiO-66-AM6COOH, and PA-66@UiO-66-AM6 through 3 feet of material with 80 mg loading.

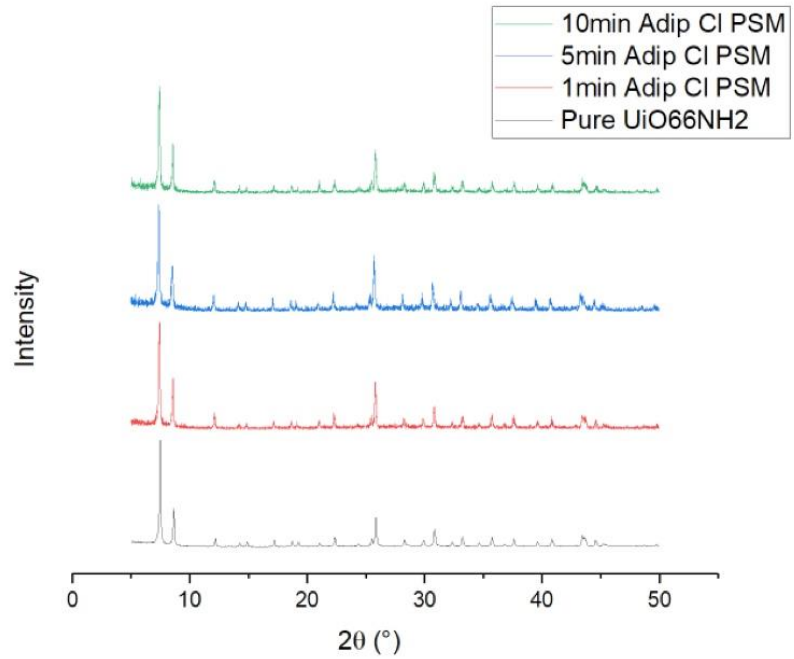

Figure 2S.12. PXRD of UiO-66-NH_2 at 1, 5, and 10 min PSM with adipoyl chloride.

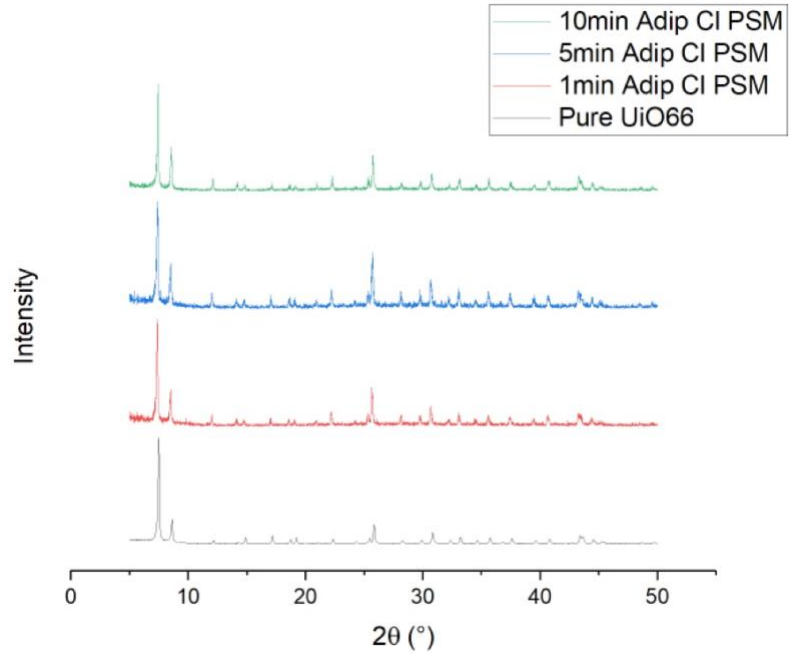

Figure 2S.13. PXRD of UiO-66 at 1, 5, and 10 min PSM with adipoyl chloride.

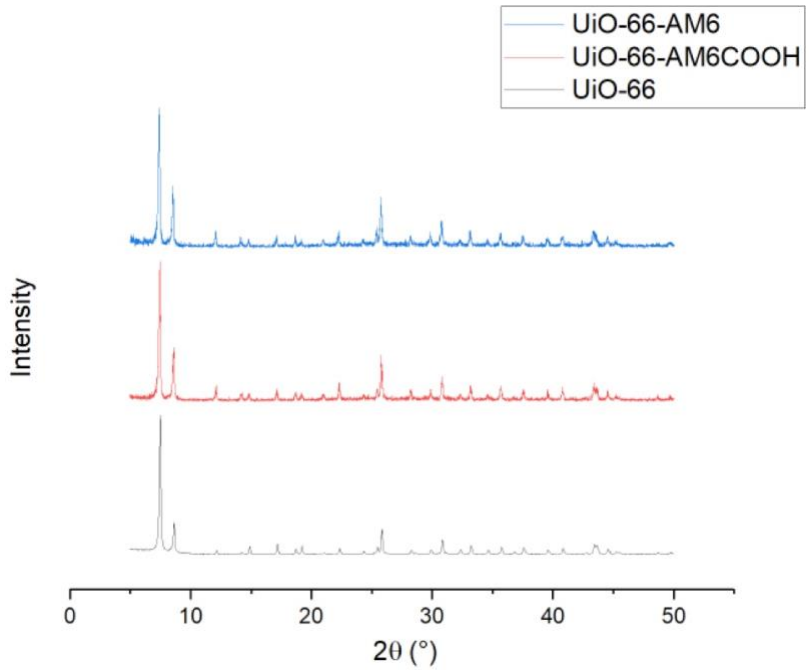

Figure 2S.14. PXRD of UiO-66-AM6 and UiO-66-AM6COOH.

Figure 2S.15. *Left:* Image of PA-66. Middle: Image of PA-66@UiO-66 fiber. *Right:* Image of PA-66-UiO-66-NH_2 fiber.

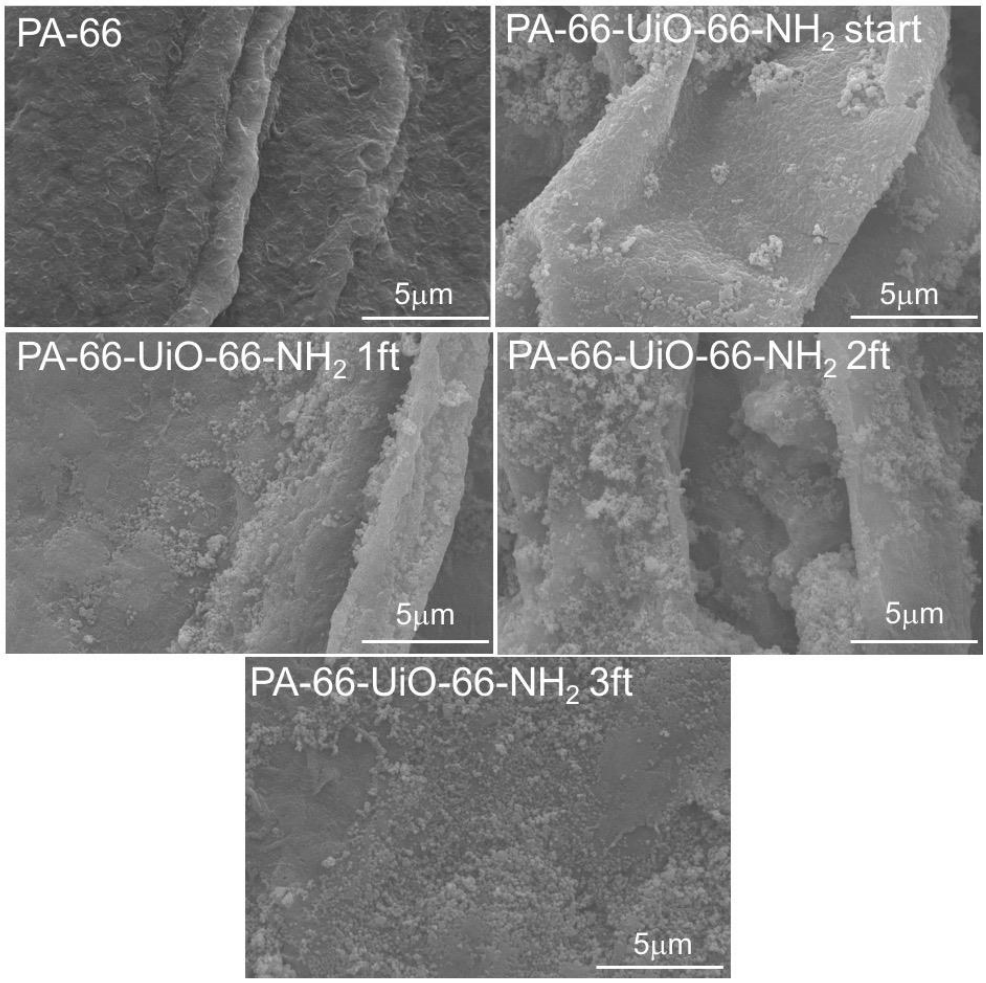

Figure 2S.4. SEM images of PA-66 and PA-66-UiO-66-NH_2 (5 μm scale bar).

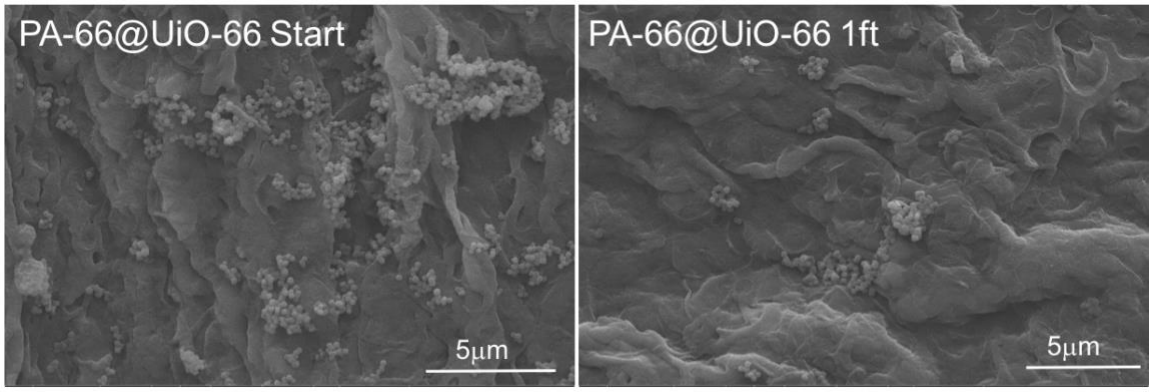

Figure 2S.17. SEM images of PA-66@UiO-66.

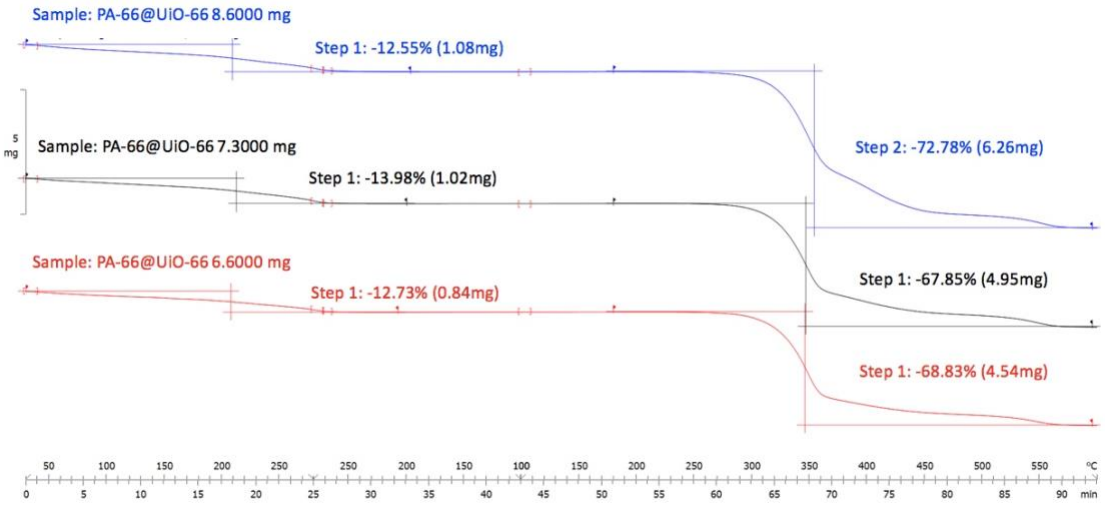

Figure 2S.18. TGA data of PA-66@UiO-66.

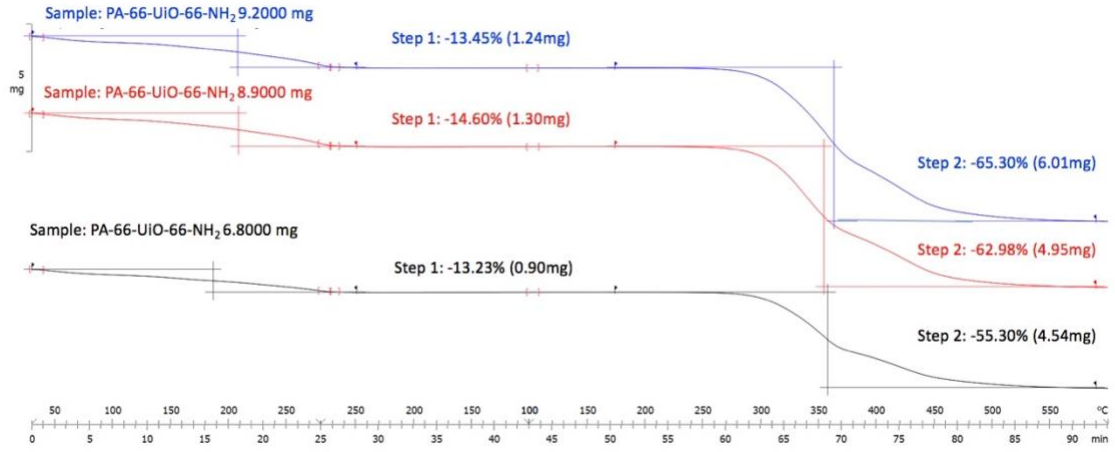

Figure 2S.19. TGA data of PA-66-UiO-NH_2.

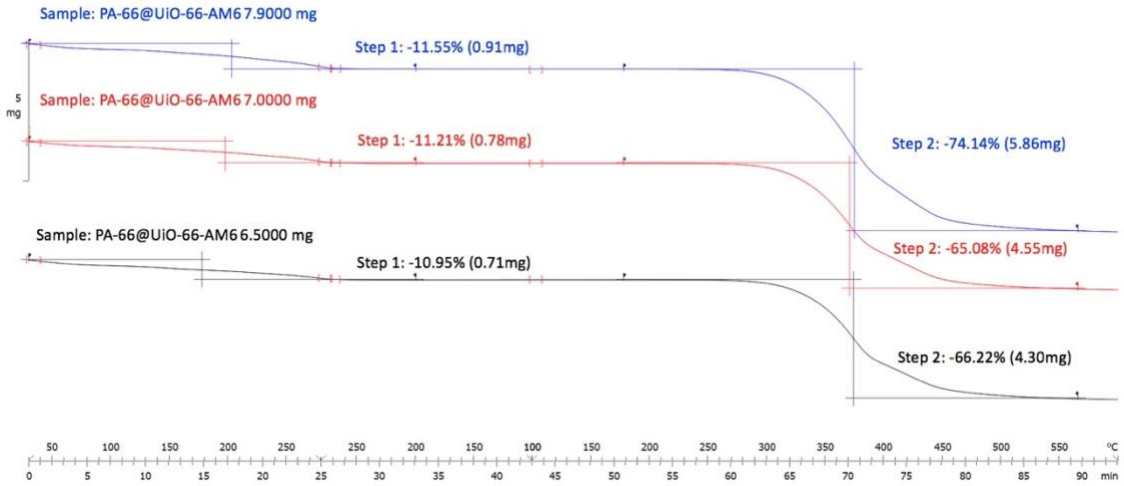

Figure 2S.20. TGA data of PA-66@UiO-AM6.

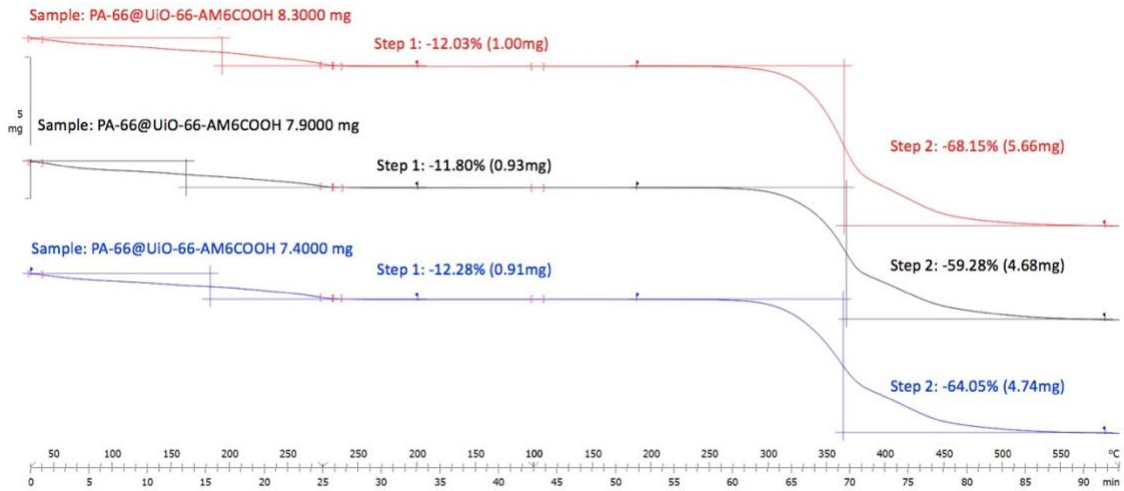

Figure 2S.5. TGA data of PA-66@UiO-66-AM6COOH.

Table 2S.3. MOF percent in PA-66-MOF hybrid materials as determined by TGA.

MOF Material	Percent MOF loaded
PA-66@UiO-66	19.67 ± 2.51%
PA-66-UiO-66-NH_2	29.42 ± 6.11%
PA-66@UiO-66-AM6COOH	27.44 ± 5.14%
PA-66@UiO-66-AM6	22.84 ± 5.80%

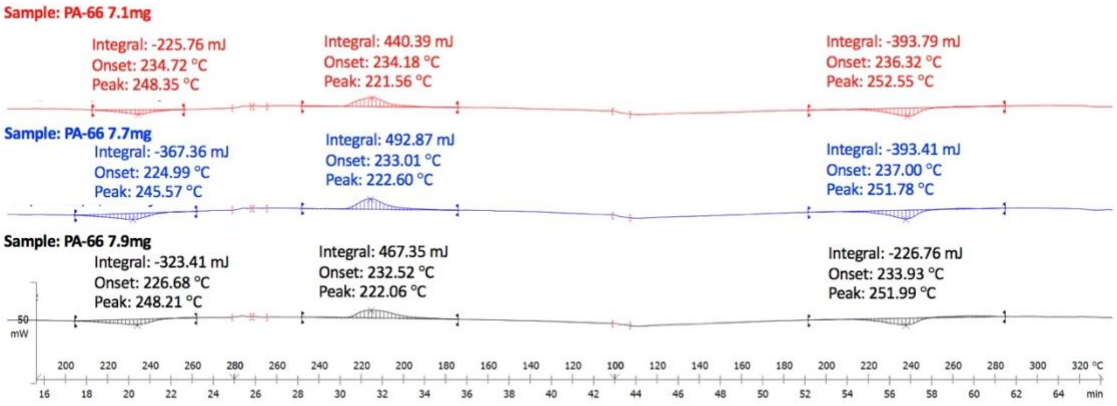

Figure 2S.22. DSC data of as synthesized PA-66 material.

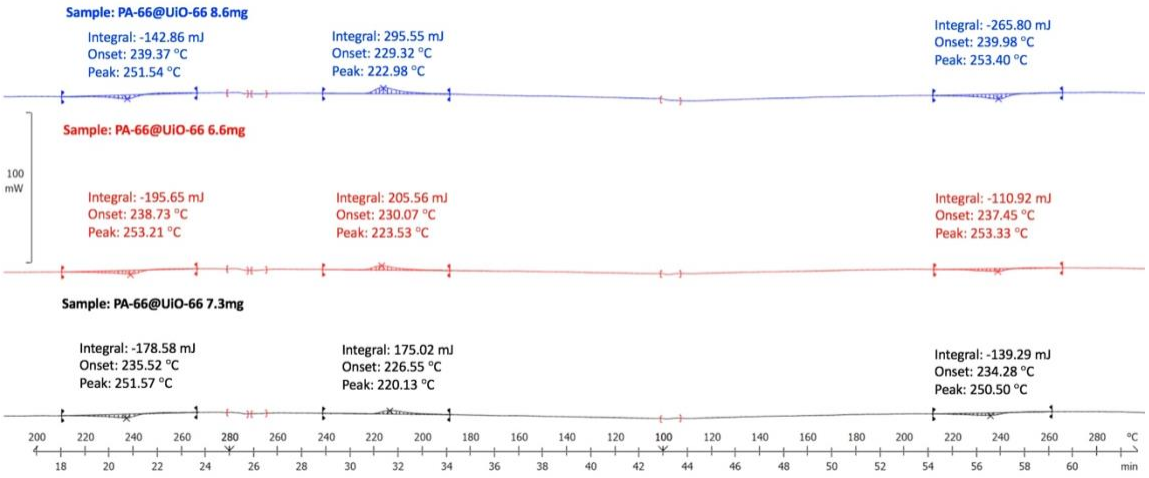

Figure 2S.23. DSC data of synthesized PA-66@UiO-66.

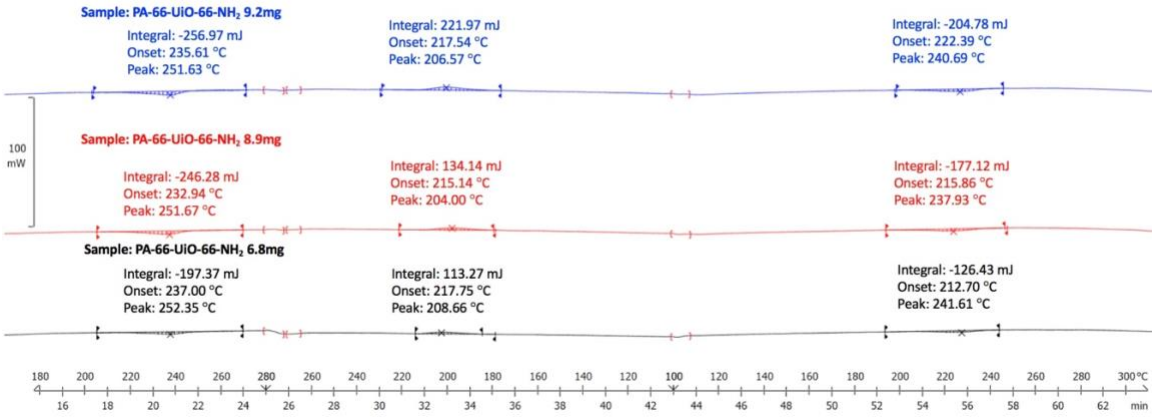

Figure S2.24. DSC data of synthesized PA-66-UiO-66-NH_2.

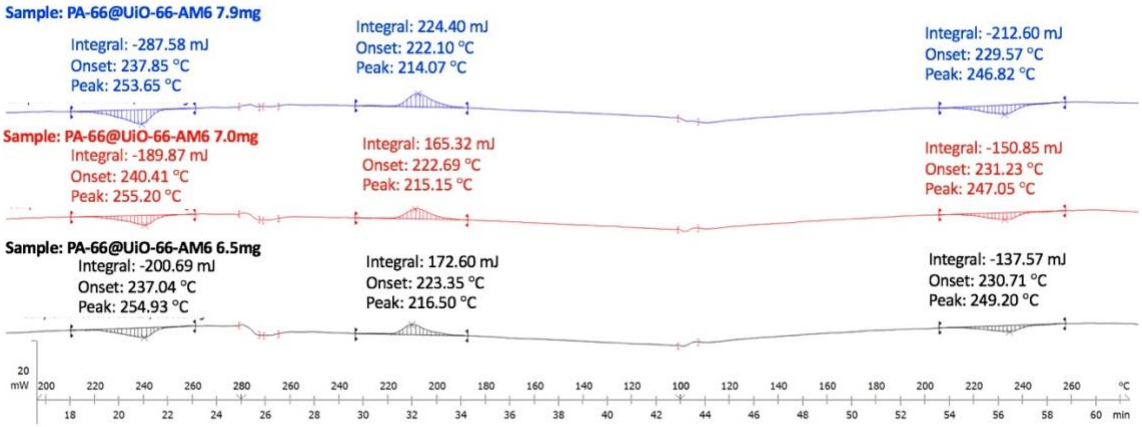

Figure 2S.25. DSC data of synthesized PA-66@UiO-66-AM6.

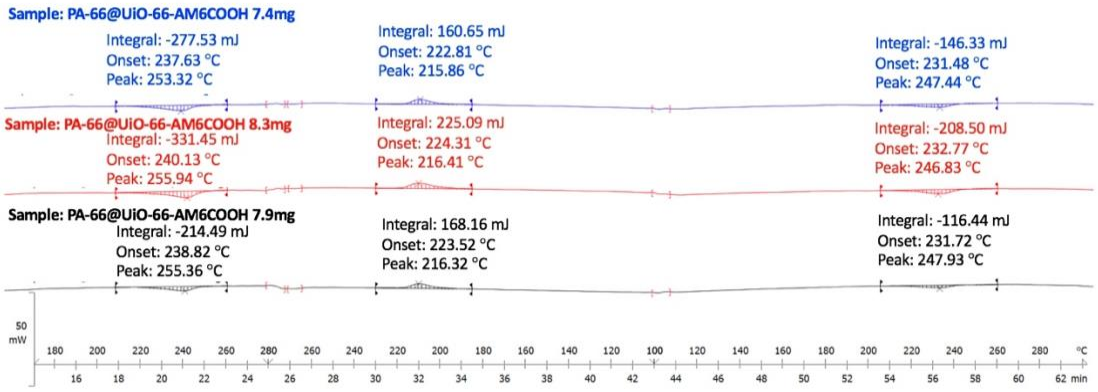

Figure 2S.6. DSC data of synthesized PA-66@UiO-66-AM6COOH.

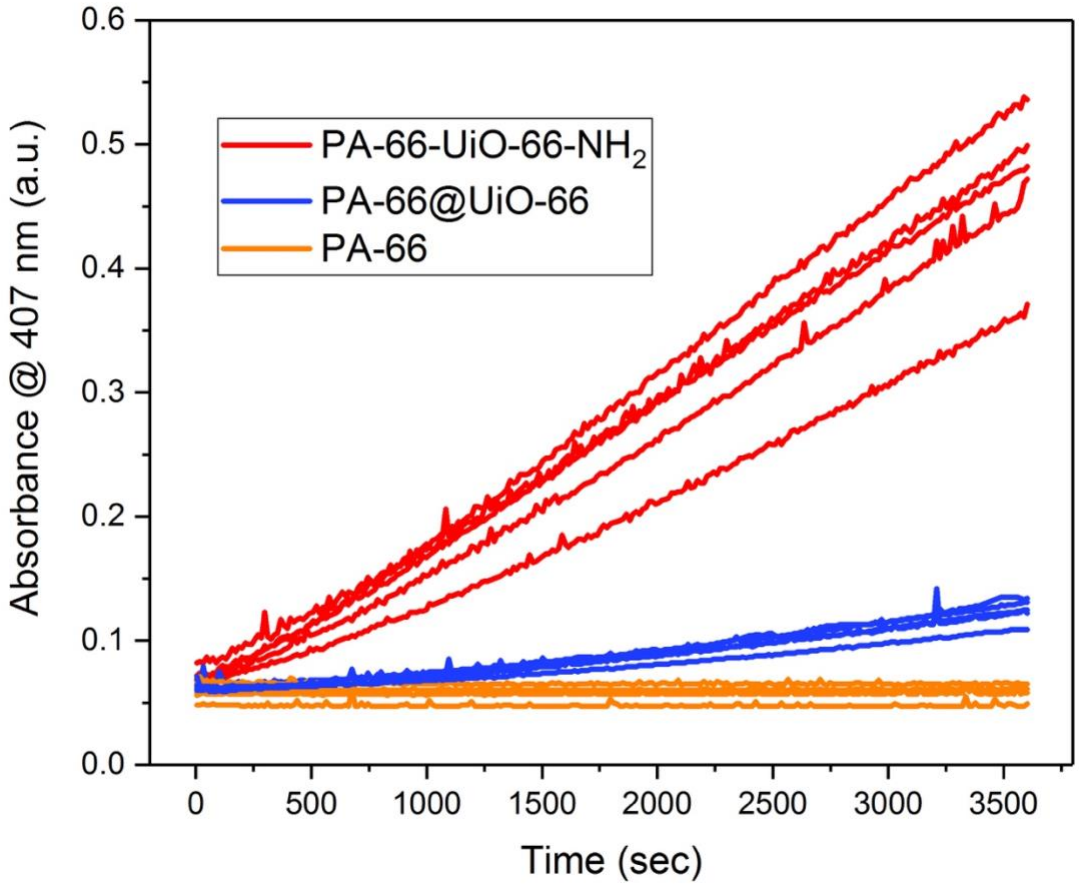

Figure 2S.7. Absorbance (407nm) vs time (sec) monitoring the conversion of DMNP to p-nitrophenol for PA-66, PA-66@UiO66, and PA-66-UiO-66-NH_2. All slopes are calculated from 10 min to 50 min and averaged per the procedure above. Representative individual tiles for PA-66, PA-66@UiO-66, and PA-66-UiO-66NH_2 are shown for comparison.

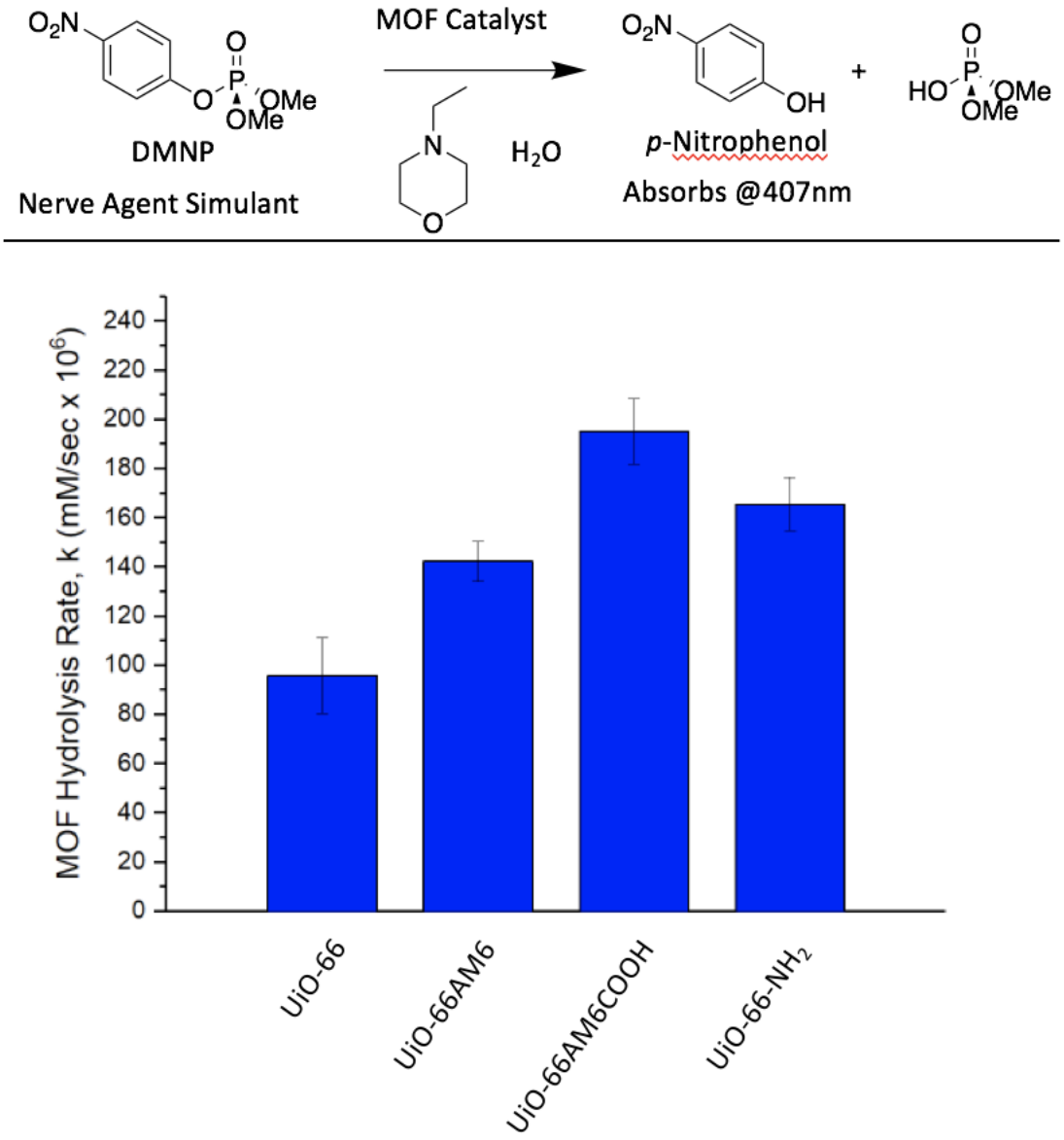

Figure 2S.28. *Top:* DMNP degradation reaction. *Bottom:* rate of catalytic degradation of MOF powders at pH = 10 measured by UV-visible adsorption at 407nm.

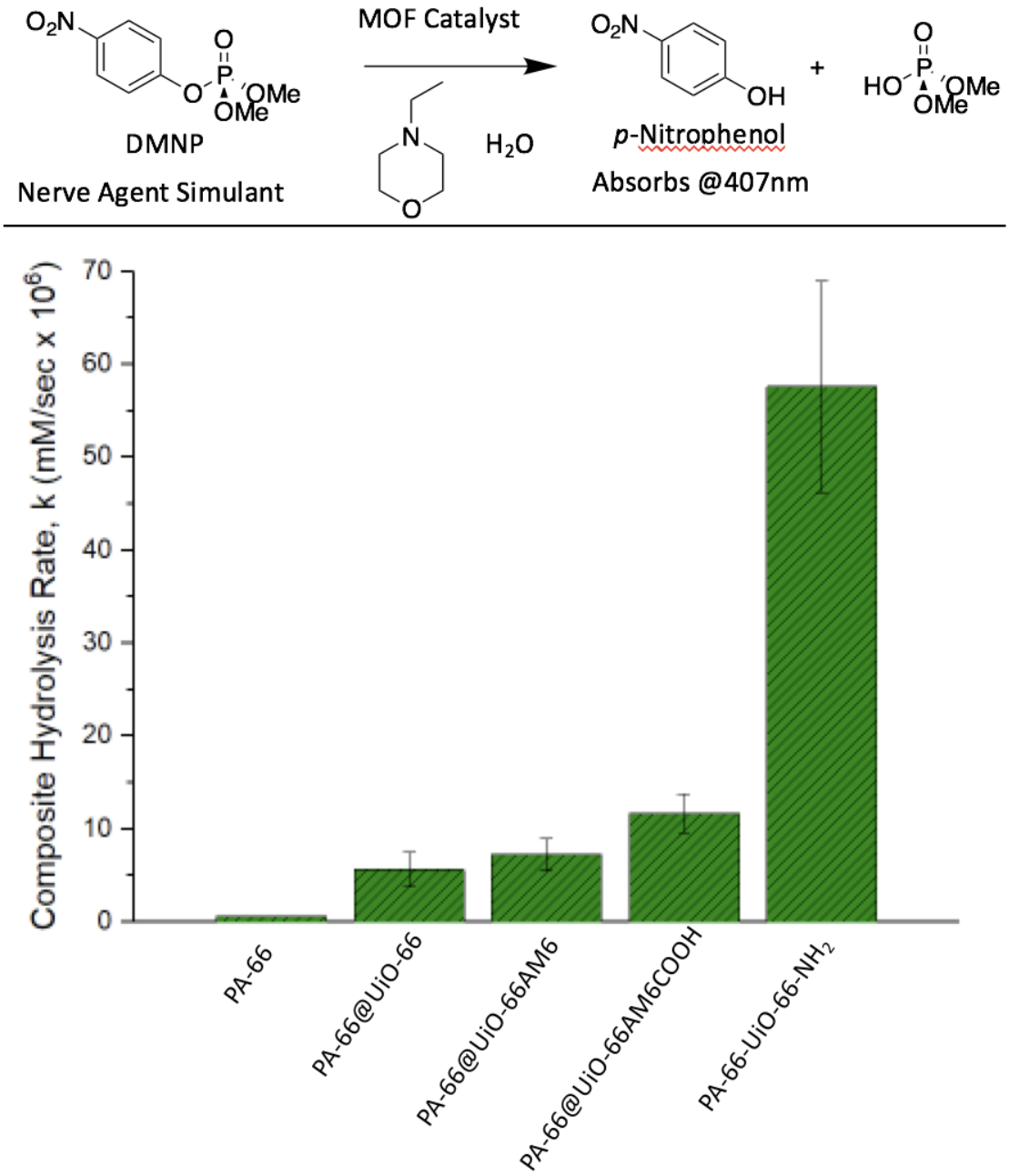

Figure 2S.29. *Top*: DMNP degradation reaction. *Bottom*: rate of catalytic degradation of PA-66-MOF composites at pH = 10 measured by UV-visible adsorption at 407nm.

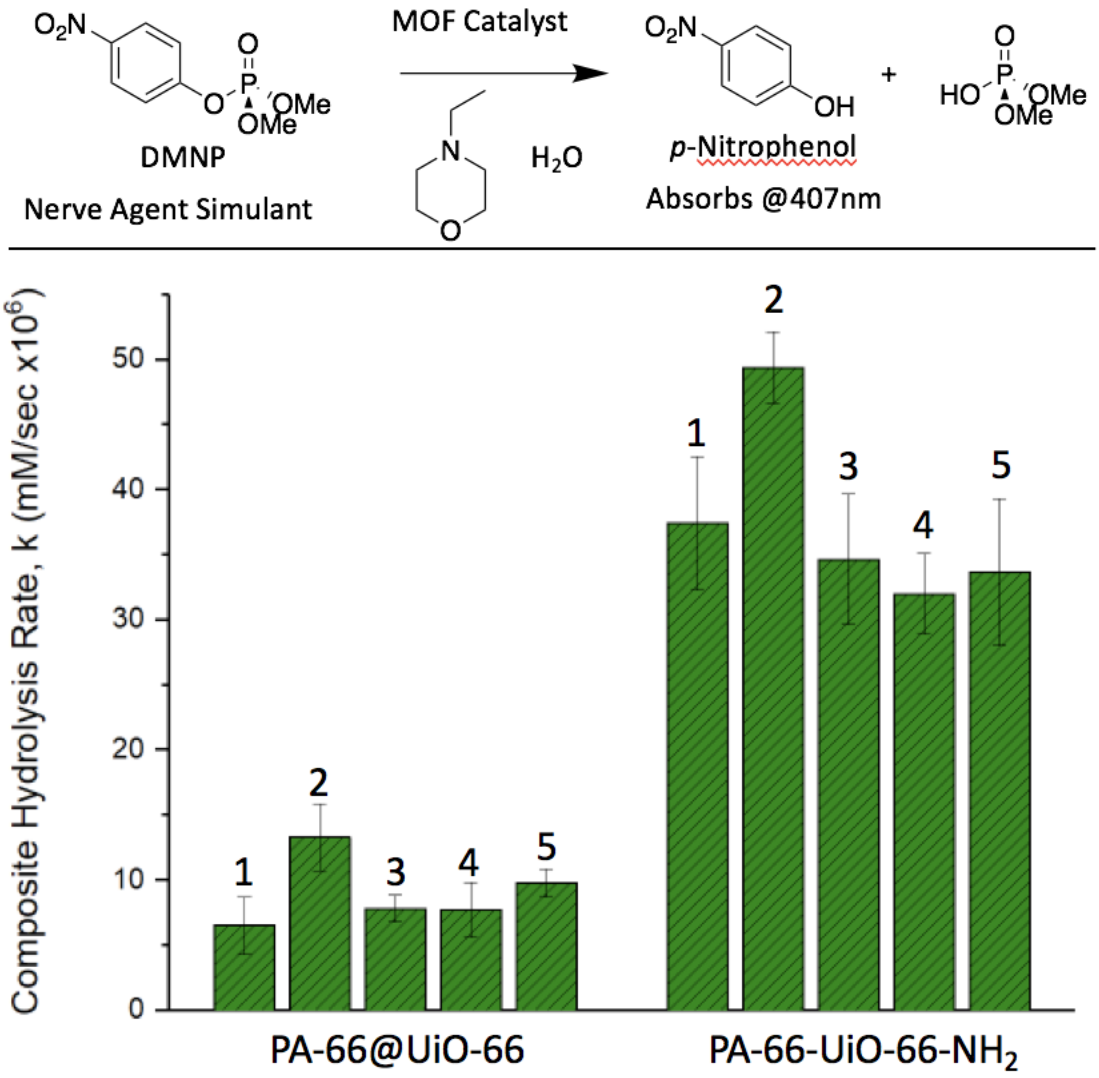

Figure 2S.30. *Top*: DMNP degradation reaction. *Bottom*: rate of catalytic degradation of recycled PA-66-MOF composites at pH = 8 measured by UV-visible adsorption at 407nm. Composite materials were washed thoroughly in water and methanol (3 times each) with sonication and then dried under vacuum at room temperature overnight between each DMNP hydrolysis experiment.

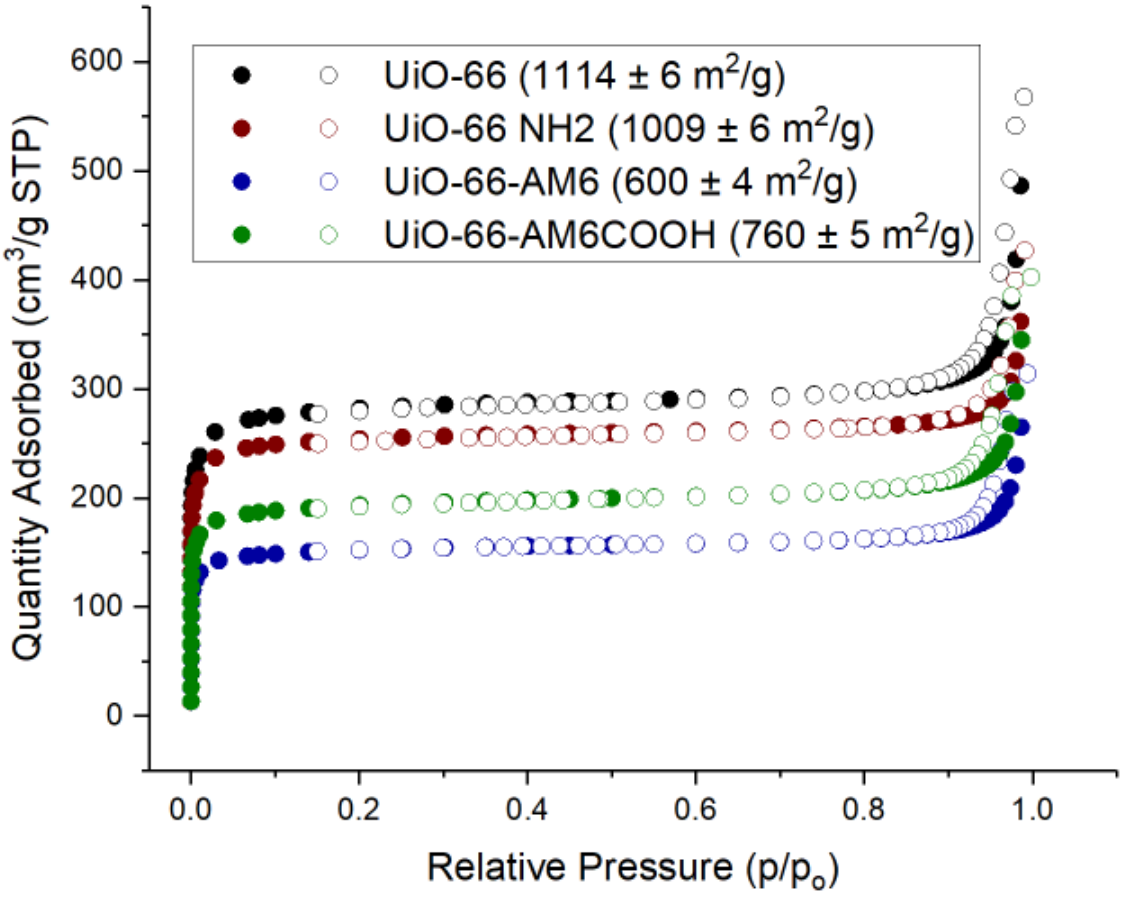

Figure 2S.31. N2 Sorption isotherm of UiO-66, UiO-66-NH_2, UiO-66AM6, and UiO-66AM6COOH with respective BET surface areas.

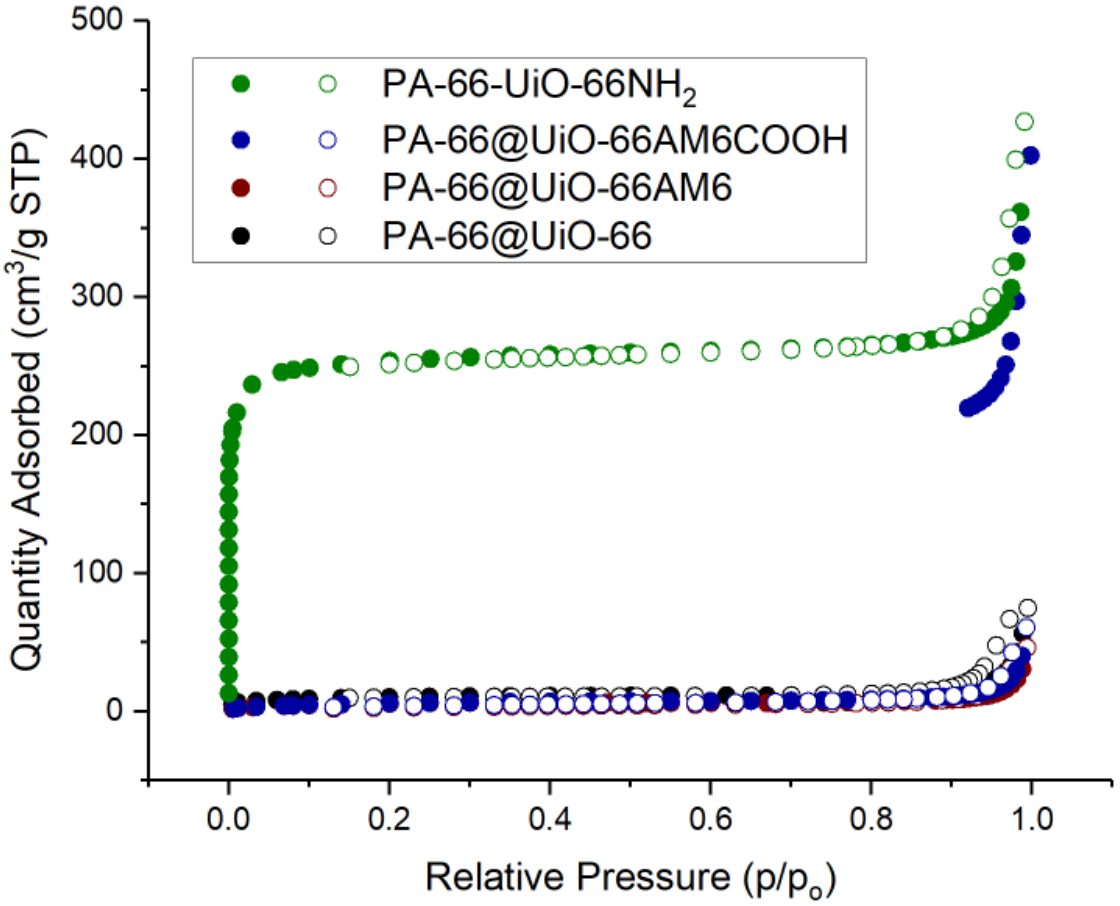

Figure 2S.32. N2 Sorption isotherm of PA-66@UiO-66, PA-66@UiO-66AM6, PA-66@UiO-66AM6COOH and PA-66-UiO-66NH$_2$. BET surface area: 35 ± 3 m^2/g, 20 ± 3 m^2/g, 19 ± 2 m^2/g, and 109 ± 2 m^2/g, respectively. BET calculation based on only MOF content (~20 wt% for PA-66@UiO-66, ~23 wt% for PA-66@UiO-66AM6, ~27 wt% for PA-66@UiO-66AM6COOH and ~29 wt% for PA-66-UiO-66-NH$_2$): 223 ± 6 m^2/g, 138 ± 4 m^2/g, 205 ± 5 m^2/g and 293±6 m^2/g, respectively. Gas sorption measurements were also performed on the PA-66 fiber resulting in a negligible BET surface area, as expected.

2.6 Acknowledgements

Chapter 2, in part, is a reprint of the material, "Nylon-MOF Composites through Postsynthetic Polymerization" *Angew. Chem. Int. Ed.* **2019**, *58*, 2336-2340. The dissertation author was the primary author of this manuscript and gratefully acknowledges the contributions of coauthors Michael S. Denny Jr., Kyle C. Bentz, Joseph M. Palomba, and Seth M. Cohen.

2.7 References

1. Islamoglu, T.; Ortuno, M. A.; Proussaloglou, E.; Howarth, A. J.; Vermeulen, N. A.; Atilgan, A.; Asiri, A. M.; Cramer, C. J.; Farha, O. K., Presence Versus Proximity: Role of Pendant Amines in Catalytic Hydrolysis of Nerve Agent Simulant. *Angew. Chem., Int. Ed.* **2018,** *57*, 1949-1953.

2. Bobbitt, N. S.; Mendonca, M. L.; Howarth, A. J.; Islamoglu, T.; Hupp, J. T.; Farha, O. K.; Snurr, R. Q., Metal-Organic Frameworks for the Removal of Toxic Industrial Chemicals and Chemical Warfare Agents. *Chem. Soc. Rev.* **2017,** *46*, 3357-3385.

3. Liu, Y.; Howarth, A. J.; Vermeulen, N. A.; Moon, S.-Y.; Hupp, J. T.; Farha, O. K., Catalytic degradation of chemical warfare agents and their simulants by metal-organic frameworks. *Coord. Chem. Rev.* **2017,** *346*, 101-111.

4. Moon, S.-Y.; Wagner, G. W.; Mondloch, J. E.; Peterson, G. W.; DeCoste, J. B.; Hupp, J. T.; Farha, O. K., Effective, Facile, and Selective Hydrolysis of the Chemical Warfare Agent VX Using Zr6-Based Metal-Organic Frameworks. *Inorg. Chem.* **2015,** *54* (22), 10829-10833.

5. Lee, D. T.; Zhao, J.; Oldham, C. J.; Peterson, G. W.; Parsons, G. N., UiO-66-NH2 Metal-Organic Framework (MOF) Nucleation on TiO2, ZnO, and Al2O3 Atomic Layer Deposition-Treated Polymer Fibers: Role of Metal Oxide on MOF Growth and Catalytic Hydrolysis of Chemical Warfare Agent Simulants. *ACS Appl. Mater. Interfaces* **2017,** *9* (51), 44847-44855.

6. Zhao, J.; Lee, D. T.; Yaga, R. W.; Hall, M. G.; Barton, H. F.; Woodward, I. R.; Oldham, C. J.; Walls, H. J.; Peterson, G. W.; Parsons, G. N., Ultra-Fast Degradation of Chemical Warfare Agents Using MOF-Nanofiber Kebabs. *Angew. Chem., Int. Ed.* **2016,** *55* (42), 13224-13228.

7. Li, X.; Liu, Y.; Wang, J.; Gascon, J.; Li, J.; Van der Bruggen, B., Metal-Organic Frameworks Based Membranes for Liquid Separation. *Chem. Soc. Rev.* **2017,** *46*, 7124-7144.

8. Gascon, J.; Kapteijn, F., Metal-Organic Framework Membranes-High Potential, Bright Future? *Angew. Chem., Int. Ed.* **2010,** *49*, 1530-1532.

9. Denny, M. S., Jr.; Cohen, S. M., In Situ Modification of Metal-Organic Frameworks in Mixed-Matrix Membranes. *Angew. Chem., Int. Ed.* **2015,** *54*, 9029-9032.

10. Denny, M. S., Jr.; Moreton, J. C.; Benz, L.; Cohen, S. M., Metal-Organic Frameworks for Membrane-Based Separations. *Nat. Rev. Mater.* **2016,** *1*, 16078.

11. Chung, T.-S.; Jiang, L. Y.; Li, Y.; Kulprathipanja, S., Mixed Matrix Membranes (MMMs) Comprising Organic Polymers with Dispersed Inorganic Fillers for Gas Separation. *Prog. Polym. Sci.* **2007,** *32*, 483-507.

12. Cohen, S. M., The Postsynthetic Renaissance in Porous Solids. *J. Am. Chem. Soc.* **2017,** *139*, 2855-2863.

13. Zhang, Y.; Feng, X.; Li, H.; Chen, Y.; Zhao, J.; Wang, S.; Wang, L.; Wang, B., Photoinduced Postsynthetic Polymerization of a Metal-Organic Framework toward a Flexible Stand-Alone Membrane. *Angew. Chem., Int. Ed.* **2015,** *54*, 4259-4263.

14. Wang, Z.; Cohen, S. M., Postsynthetic Modification of Metal-Organic Frameworks. *Chem. Soc. Rev.* **2009,** *38*, 1315-1329.

15. Furukawa, H.; Cordova, K. E.; O'Keeffe, M.; Yaghi, O. M., The Chemistry and Applications of Metal-Organic Frameworks. *Science* **2013,** *341*, 1230444.

16. Eddaoudi, M.; Kim, J.; Rosi, N.; Vodak, D.; Wachter, J.; O'Keeffe, M.; Yaghi, O. M., Systematic Design of Pore Size and Functionality in Isoreticular MOFs and their Application in Methane Storage. *Science* **2002,** *295*, 469-72.

17. Garibay, S. J.; Cohen, S. M., Isoreticular Synthesis and Modification of Frameworks with the UiO-66 Topology. *Chem. Commun.* **2010,** *46*, 7700-2.

18. Nam, D.; Huh, J.; Lee, J.; Kwak, J. H.; Jeong, H. Y.; Choi, K.; Choe, W., Cross-Linking Zr-based Metal-Organic Polyhedra via Postsynthetic Polymerization. *Chem. Sci.* **2017,** *8*, 7765-7771.

19. Kumar, S. K.; Jouault, N.; Benicewicz, B.; Neely, T., Nanocomposites with Polymer Grafted Nanoparticles. *Macromolecules* **2013,** *46*, 3199-3214.

20. Li, L.; Li, C. Y.; Ni, C.; Rong, L.; Hsiao, B., Structure and Crystallization Behavior of Nylon 66/Multi-Walled Carbon Nanotube Nanocomposites at Low Carbon Nanotube Contents. *Polym.* **2007,** *48*, 3452-3460.

21. Palomba, J. M.; Credille, C. V.; Kalaj, M.; DeCoste, J. B.; Peterson, G. W.; Tovar, T. M.; Cohen, S. M., High-Throughput Screening of Solid-State Catalysts for Nerve Agent Degradation. *Chem. Commun.* **2018,** *54*, 5768-5771.

Chapter 3: Improving MOF Catalysts for the Degradation of Chemical Warfare Agents through a Ligand Based Approach

3.1 Introduction

As described in Chapter 1, different approaches have been taken for improving MOFs for the catalytic degradation of the organophosphorous class of CWAs.[1] Because the catalytically active site for these reactions is at the MOF SBU, a majority of approaches in the literature have focused on either reducing the connectivity at the SBU or synthesizing MOFs with experimentally induced defect sites.[2-3] The idea behind this approach is rather simple, by engineering more defects into the MOF a greated number of open metal sites is generated, which act as the catalytically active sites, thereby promoting more rapid CWA degradation. Conversely, only a handful of approaches have focused on derivatizing the MOF ligand with functional groups.[4-5] As outlined in Chapter 1, these approaches focus on attaching functional groups to the MOF and during the catalytic step, these groups facilitate the rapid degradation of CWAs by either acting as a general acid/base or through noncovalent interactions such as hydrogen or halogen bonding. It was hypothesized that functional groups on the organic linkers might play a larger role in the degradation of CWAs. As such, with a previously validated HTS method for evaluating these materials, this screening system was used to rapidly screening materials with a wide range of varied ligand substituents.[6]

3.2 Multiple Functional Groups in UiO-66 Improve CWA Simulant Degradation

A library of 26 mixed ligand UiO-66 derivatives, using various combinations of five different ligands (Figure 3.1), were synthesized and screened for catalytic degradation of DMNP using HTS. Some of the mixed ligand derivatives display superior ability for DMNP degradation (at pH = 8) than physical mixtures of MOFs containing the functionalized linkers. This result underscores the significance of the HTS methodology to rapidly assess catalytic activity of

materials, reducing a major barrier to evaluating catalytic mixed ligand or multivariate (MTV) MOFs. To accurately determine the cause of this increased activity the defect sites in several MOFs in our study (high/medium/low activity) were quantified. MOF defect sites were quantified via TGA and the results show no correlation with catalytic activity, suggesting the differences in activity between materials was a ligand-based effect. These findings suggest that multiple ligand functional groups in a MOF can play a synergistic role to increase the catalytic activity against DMNP.

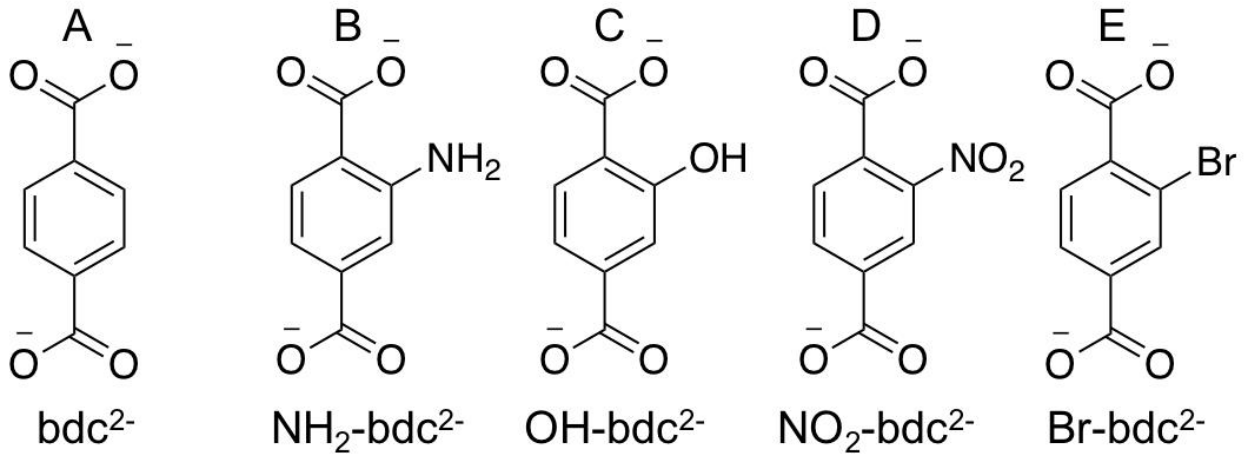

Figure 3.1. Ligands used for MTV-UiO-66 mixed ligand synthesis.

All MOFs in this study were synthesized using an acetic acid modulated synthesis procedure (see appendix).[7] For mixed ligand synthesis of UiO-66, five ligands were selected, including bdc^{2-} and four derivatives (Figure 3.1): two with electron donating functional groups (NH_2-bdc^{2-}, OH-bdc^{2-}) and two with electron withdrawing groups (NO_2-bdc^{2-} and Br-bdc^{2-}). Using these ligands, all possible ligand combinations (e.g., one, two, three, four and five ligands in a single MOF) were synthesized leading to a library of 26 different mixed ligand UiO-66 derivatives termed multivariate UiO-66 (MTV-UiO-66). MOFs were named according to which ligands they

are composed of; for example, MTV-UiO-66-AB contains a 1:1 mixture of bdc^{2-} and NH_2-bdc^{2-} ligands whereas MTV-UiO-66-BCE contains a 1:1:1 mixture of NH_2-bdc^{2-}, OH-bdc^{2-}, and Br-bdc^{2-}.

MTV-UiO-66 MOFs were characterized via PXRD to confirm MOF formation and crystallinity. MOF samples were also digested in dilute acid and characterized via ^{1}H NMR to determine the percent incorporation of each ligand (Figure 3.2, Figures 3S.1-3S.31, Table 3S.1). To quantify the ligand incorporation in each MOF, characteristic peaks of each ligands ^{1}H NMR spectra were identified and used to quantify the components in the MTV-UiO-66 MOFs (Figure 3.2). Once synthesized and characterized, the library of MOFs was screened for their ability to degrade the CWA simulant DMNP using a the aforementioned HTS method (Figure 3.3).[6]

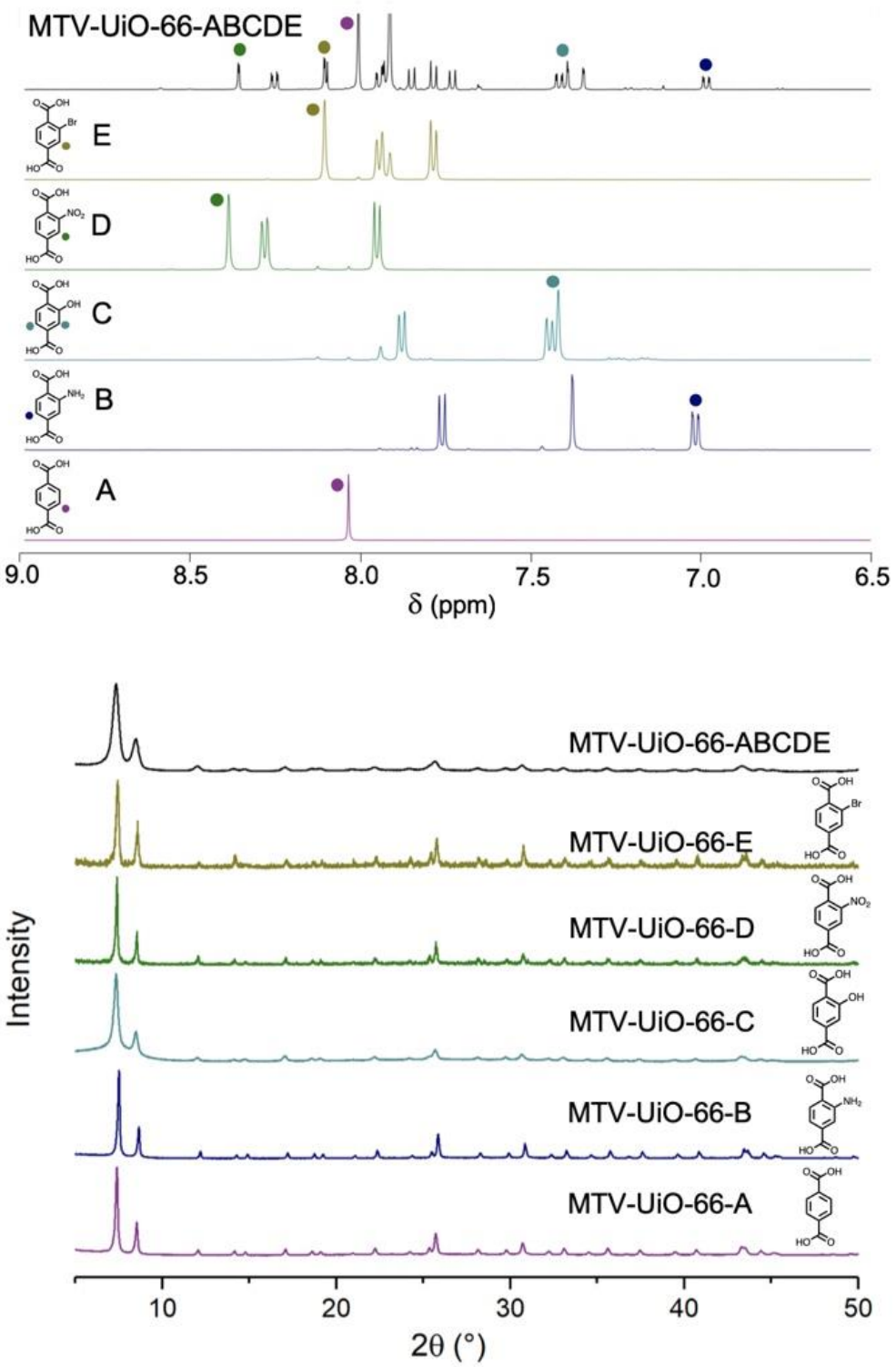

Figure 3.2. *Top*: ^{1}H NMR of digested single ligand MOFs and MTV-UiO-66-ABCDE highlighting peak labels used to quantify ligand incorporation. *Bottom*: PXRD of single ligand MOFs and MTV-UiO-66-ABCDE.

As outlined in Chapters 1 and 2, this highly reproducible HTS method requires dispensing a specific amount of each MOF (~6 mg), suspending the MOF powder in a buffered aqueous solution, and analyzing the reaction with DMNP using UV-Vis spectroscopy in a plate reader format.[6] Rates were calculated to account for the substantial difference in moles of MOF catalyst between samples (due to the increased mass of the functionalized MOFs, see appendix) so that a direct comparison could be made across all materials. Reported rates are averages of seven replicates per sample across three independently prepared materials for each MOF.

The HTS data indicates that most of the MTV-UiO-66 MOFs display significantly higher activity than MOFs with single ligands. For example, MTV-UiO-66-B MOF and the MTV-UiO-66-E MOF display about 3-fold slower activity than when these ligands are both incorporated together into the MTV-UiO-66-BE. However, this was not the case for all MTV-MOFs, as in the case of MTV-UiO-66-ACDE, which is a slower catalyst than MTV-UiO-66-A, MTV-UiO-66-C, and MTV-UiO-66-E. To gain further insight into the origins of this increased activity in some MTV-MOFs, the CWA degradation data was analyzed for potential trends. In particular, the data was analyzed to determine if there was a trend in activity based on the electron withdrawing or donating nature of the functional groups on the MOF linkers. The electron withdrawing or donating functional groups could potentially affect the metal to ligand bond at the SBU resulting in altered catalytic activity for the MOF. However, after analyzing the data there was no trend found as a function of electron withdrawing or donating nature of the functional groups. The data was also analyzed to see if one particular ligand promotes an increase in catalytic activity in the mixed ligand systems. Interestingly, seven of the top eight MTV-UiO-66 MOFs contain the B linker (NH_2-bdc^{2-}) linker while the single ligand MTV-UiO-66-B is one of the poorest performing

MOFs. This result suggests there is a possible synergistic ligand effect occurring when multiple functional groups are incorporated into a single MOF.

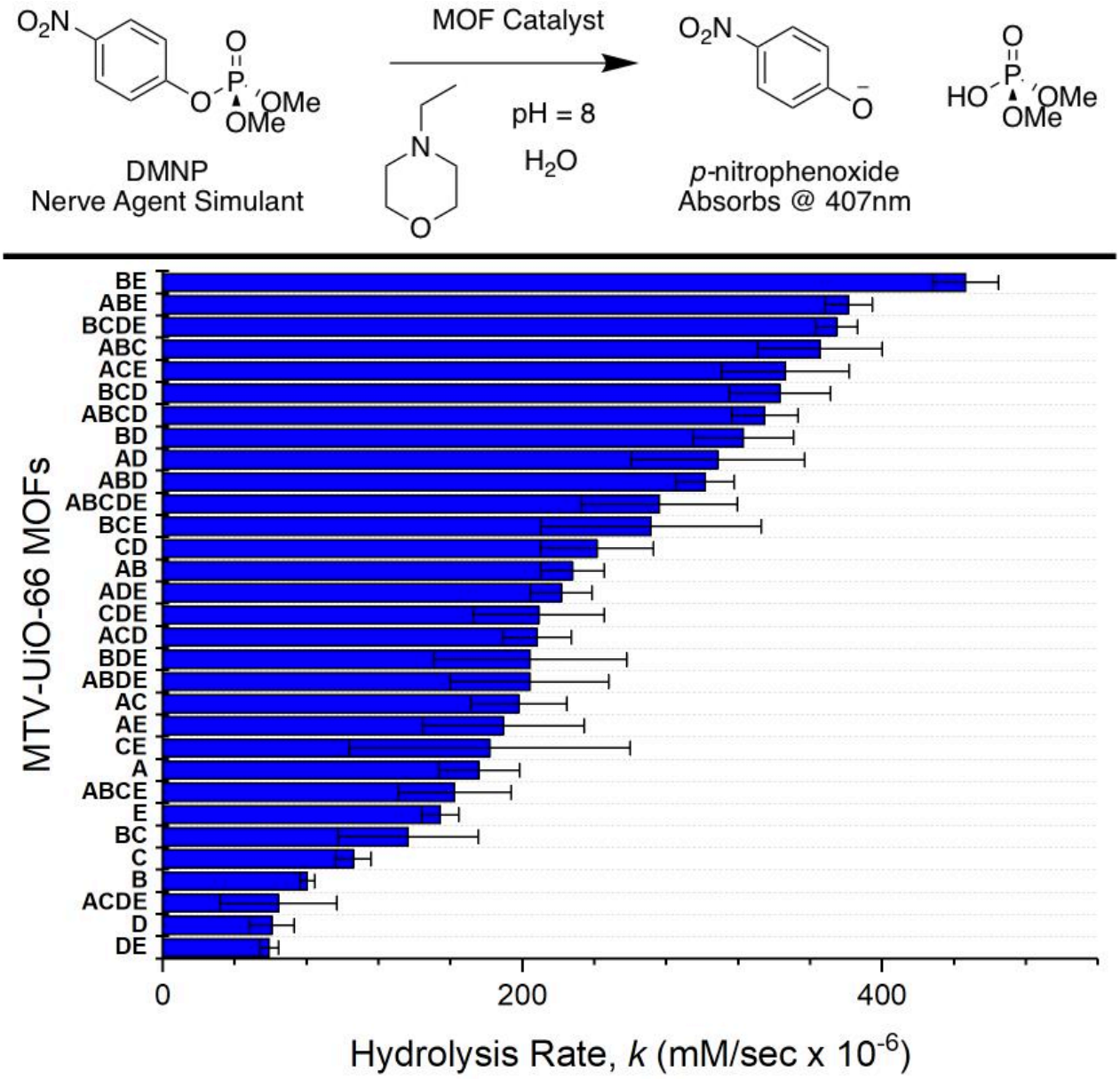

Figure 3.3. *Top:* Scheme of DMNP assay conditions. *Bottom:* Rate of catalytic degradation of DMNP by all MTV-UiO-66 MOFs.

Other features of these MOFs were examined to rule out characteristics that might affect catalytic activity unrelated to ligand composition. Previous reports have suggested that smaller

MOF particle size could play a role in increasing the catalytic activity of MOFs against CWAs.[3, 8] As such, the MOF particle sizes were analyzed by SEM (Figure 3.4); however, the results showed no correlation between particle size and DMNP degradation across ten of the MOFs investigated in this chapter. Moreover, reports have also suggested that increased MOF surface area can potentially result in increased catalytic activity due to more rapid mass transport of the simulant to MOF active sites.[3, 8] Thus, the surface area of eleven representative MOFs from this study was measured via N_2 gas sorption (Figure 3S.32-3S.42). Again, no trend in DMNP degradation ability of the MOFs based on surface area was observed. Finally, as outlined in Chapter 1 and in the introduction of this chapter, some studies have shown that an increased number of defect sites in MOFs can result promote faster CWA degradation.[9] TGA was performed to quantify the number of ligand defect sites in the MOFs using a procedure previously published by Lillerud et al.[10] The defects of six MOFs (high, medium, and low catalytic activity) were quantified and found that all of the MOFs have a nearly identical amounts of defect sites per SBU and hence found no meaningful correlation between activity and ligand defect sites (Figure 3S.43-3S.49, Table 3.1).

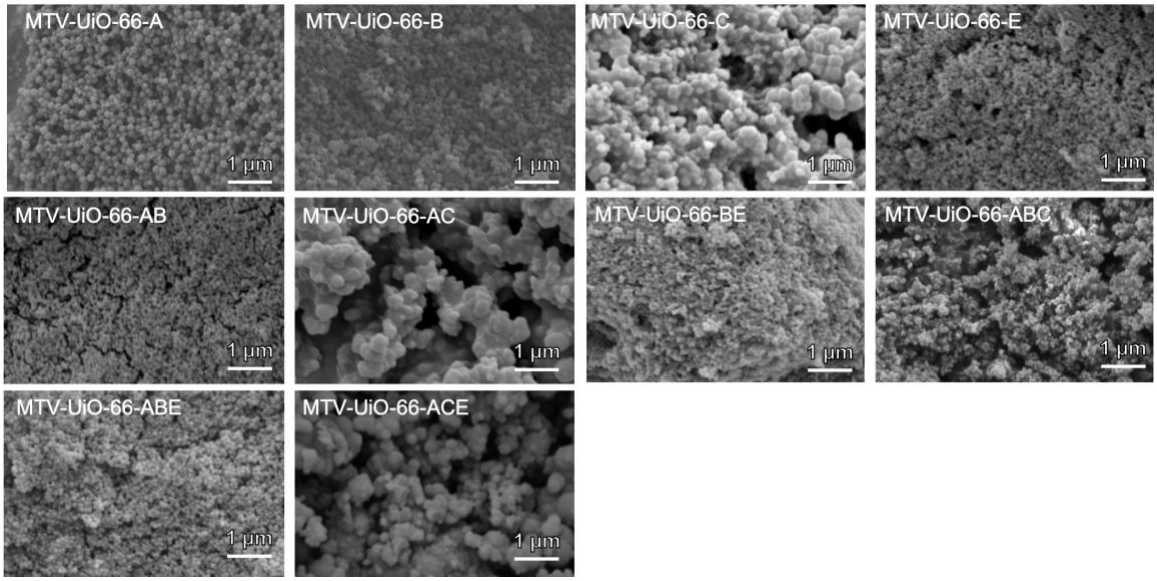

Figure 3.4. Representative SEM images of MTV-UiO-66 MOFs prepared in this study.

Table 3.1. MTV-UiO-66 MOF defects quantified as carboxylates per SBU via TGA analysis.

MTV-UiO-66 MOF	**Carboxylates/SBU (12 = pristine)**
MTV-UiO-66-DE	9.4 ± 1.1
MTV-UiO-66-B	10.2 ± 0.8
MTV-UiO-66-BDE	9.2 ± 1.4
MTV-UiO-66-ABC	8.4 ± 1.0
MTV-UiO-66-BCDE	9.8 ± 1.1
MTV-UiO-66-BE	10.4 ± 0.9

To further verify the aforementioned synergistic effects of multiple ligand functional groups, single ligand MOFs were physically mixed using recreate the same ratios as those present in the MTV-UiO-66. These physical mixtures of MOFs were then screened for DMNP degradation (Figure 3.5). For example, a 1:1 mixture of MTV-UiO-66-B and MTV-UiO-66-E

were compared for catalytic activity against MTV-UiO-66-BE (Figure 3.5). The mixed ligand MTV-UiO-66-BE displayed 3-fold increased activity when compared to the physical mixture indicating ligand incorporation within the MTV-UiO-66 significantly increases the catalytic degradation of DMNP. In a second example, the MTV-UiO-66-ABE derivative displays over 3-fold better activity than a physical mixture combining equal molar amounts of MTV-UiO-66-A, MTV-UiO-66-B, and MTV-UiO-66-E. In total, four MTV and physical mixture MOFs were screened and compared and in all cases the MTV MOFs outperform their physical mixture counterparts by about two-fold. Mixtures of single component MOFs with differing functional groups perform essentially the same as the individual MOF materials. These results further denote a synergistic ligand effect contributing to the degradation of DMNP in the mixed ligand systems.

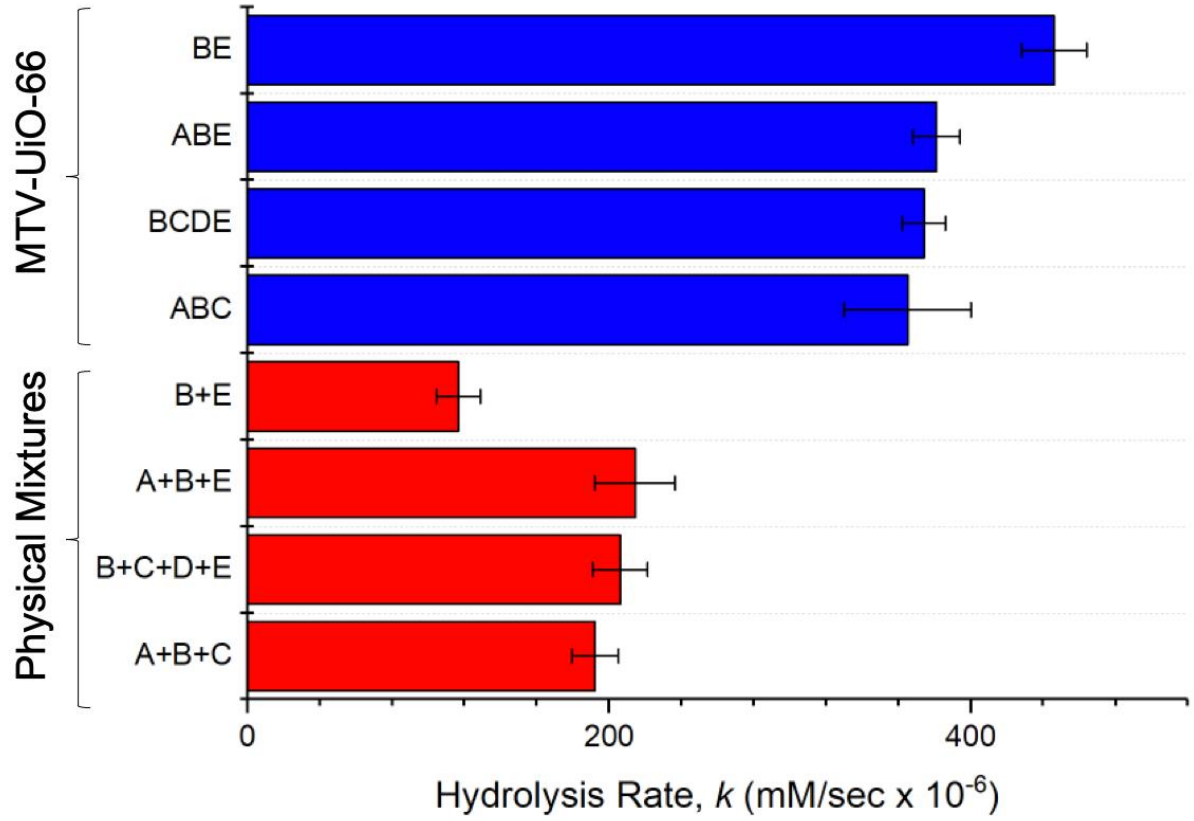

Figure 3.5. Rate of catalytic degradation of DMNP by top MTV-UiO-66 MOFs (blue) compared to their physical MOF mixtures (red).

As previously mentioned in Chapter 1, Yaghi et al., utilized multiple functional groups to enhance the gas sorption properties of MOF-5. These studies showed that through incorporation of multiple ligands in MTV-MOF-5, the H_2 gas sorption capacity more than doubled. Furthermore, using other combinations of ligands in MTV-MOF-5, specific combinations gave a four-fold increase in selectivity for CO_2 over CO. These enhancements in the gas sorption properties of MTV-MOF-5 were significant, but the origin of these effects remains unknown. Similarly, in this report a 3-fold increase in the catalytic degradation of DMNP by MTV-UiO-66-BE has been shown, and this is attributed to a synergistic ligand effect; however, the precise origin of this effect is unclear at this time. Nevertheless, this study shows that numerous derivatives of MOFs can be screened, and trends rapidly established across many materials using our HTS methodology.

3.3 Halogen Bonding in UiO-66 Frameworks Display Superior Ability for CWA Simulant Degradation.

In this section of Chapter 3, a more targeted library of MOFs with varying functional groups was analyzed in an effort to specifically determine the effects of functional groups on MOF CWA degradation. While screening a larger library of functionalized MOFs (as highlighted in section 3.2) one MOF in particular displayed exceptional CWA degradation ability (UiO-66-I). To probe the potential origins and trends behind this activity the entire halogenated UiO-66 series UiO-66-F, UiO-66-Cl, UiO-66-Br, and UiO-66-I were synthesized and screened for the catalytic degradation of DMNP using the same HTS method (Figure 3.6).[6] The UiO-66-I derivative displays ~4-fold greater catalytic activity than the parent UiO-66, while the other halogenated derivatives show no enhancement over unfunctionalized UiO-66. Similar to the prior section of this chapter, MOF defect sites were quantified via TGA, which showed nearly identical defect site

abundance across the series of MOFs. Computational analysis indicates that the more polarizable iodine moiety enables a halogen bonding effect that enhances the catalytic degradation of DMNP hydrolysis at the phosphoester linkage. Few other reports in the literature demonstrate that heterogenous catalysts have faster rates as a function of halogen bonding.[11-12] More specifically, in MOFs, previous reports of halogen bonding have been demonstrated as a means of crystal engineering,[13] but this is the first-time halogen bonding as a means of enhancing catalysis has been demonstrated in a MOF.

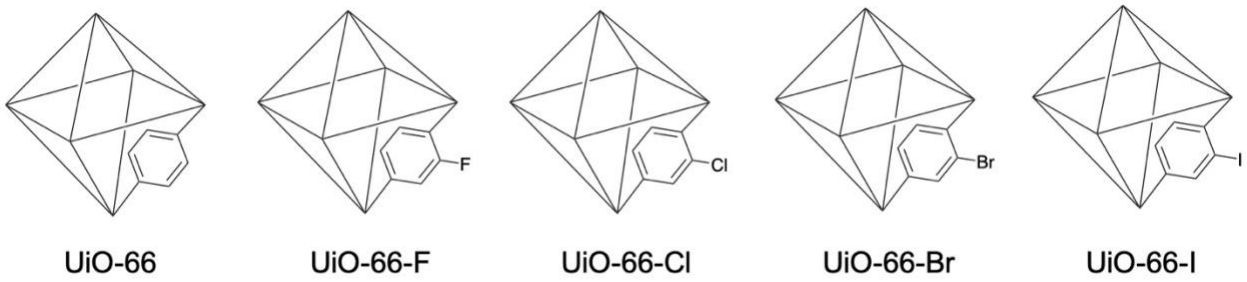

Figure 3.6. Chemical schematic of UiO-66 and four halogenated UiO-66 MOFs.

The parent UiO-66 and all of its halogenated derivatives were synthesized using an acetic acid modulated synthesis.[7] All MOF samples were digested in dilute acid and analyzed via ^{1}H NMR, confirming the ligands were intact after MOF synthesis (Figures 3S.50-3S.58). PXRD results confirm the formation of the MOF (Figure 3.7) and SEM images show similar particle sizes (~200 nm) for all the samples (Figure 3S.59-3S.64). All MOFs were also analyzed via N_2 gas sorption measurements to determine the surface area of the materials. The surface area of the MOFs decreased as the halogen size increases (F < Cl < Br < I) indicating the expected pore occupancy by the halogen (Figure 3.7).

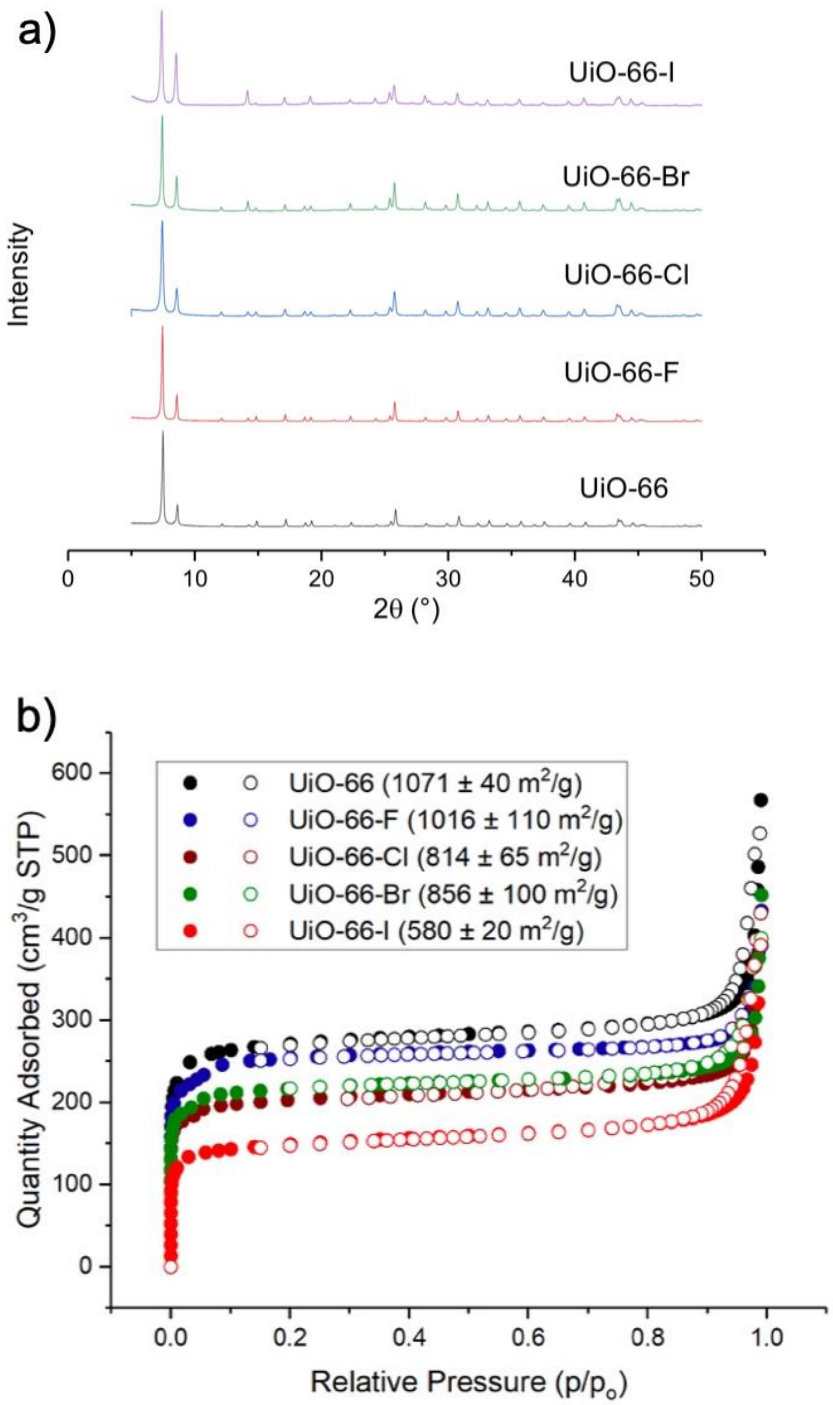

Figure 3.7. a) PXRD pattern of UiO-66 MOFs used in this study. b) N_2 sorption isotherms of UiO-66 MOFs, black traces represent UiO-66, blue traces represent UiO-66-F, brown traces represent UiO-66-Cl, green traces represent UiO-66-Br, and red traces represent UiO-66-I.

The catalytic activity of these materials with the CWA simulant DMNP was evaluated using the aforementioned HTS method.[6] An equal mass (~6 mg) of MOF was utilized in each well for monitoring catalytic reactions. As outlined in the previous section, rates were measured to account for varying molar mass of MOFs due to the additional mass of the functional groups (Table 3S.2). HTS evaluation of the five materials in Figure 3.6 at pH = 8 show that UiO-66-I is four times more active than the parent UiO-66 MOF and another very catalytically active MOF NU-1000 (vide infra). The UiO-66-I MOF displays the highest activity of any MOF previously reported in the literature under these HTS assay conditions (96 total MOFs previously screened, at this point in time).

To further probe the ligand effect, we synthesized a mixed linker MOF (termed UiO-66-$I_{50\%}$) containing ~50% bdc^{2-} linkers and ~50% I-bdc^{2-} that was characterized by PXRD and gas sorption measurements (Figure 3S.65-3S.66). When screened for catalytic activity against DMNP, the mixed ligand UiO-66-$I_{50\%}$ performs better than UiO-66, but poorer than UiO-66-I indicating that increased iodine content in the MOF correlates with improved catalytic activity (Figure 3.8).

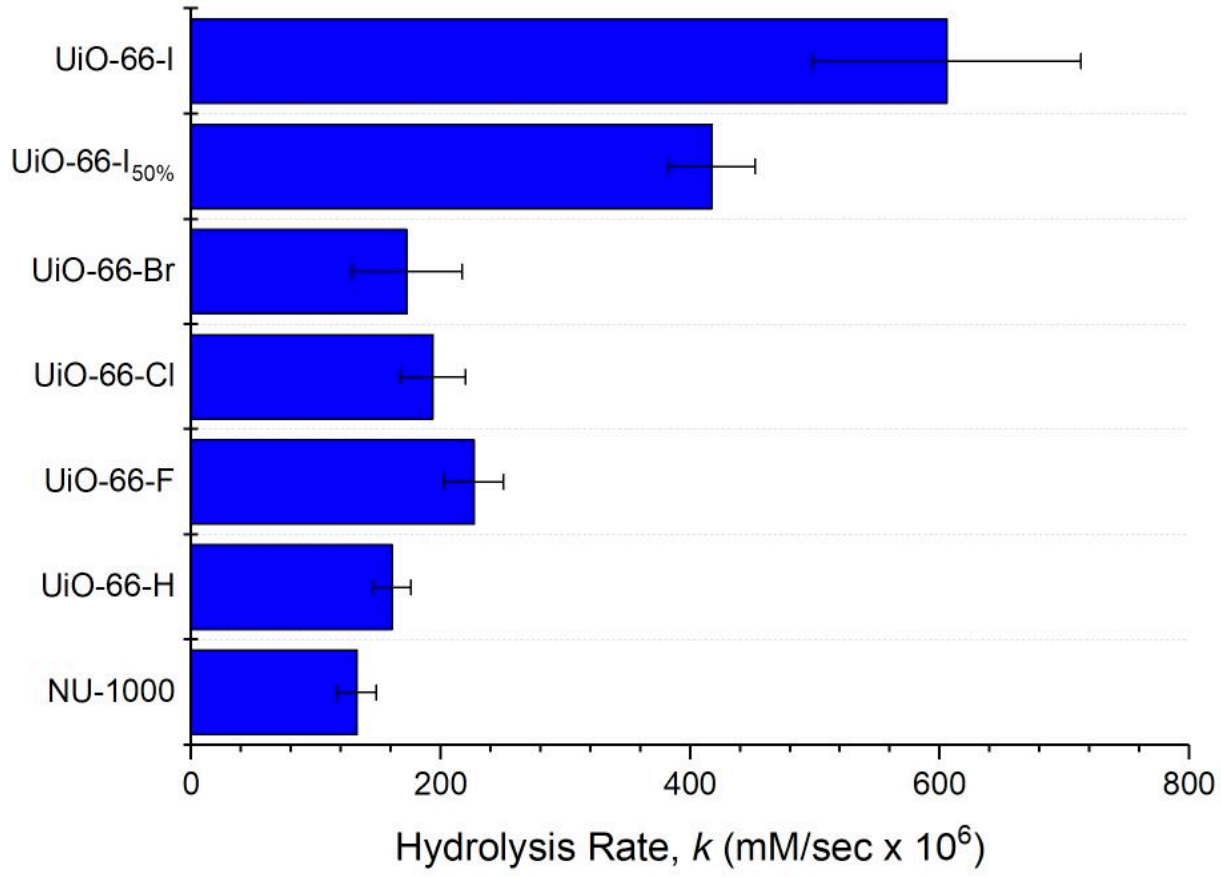

Figure 3.8. Molar mass corrected rate of catalytic degradation of DMNP by MOFs measured by UV-visible absorption (407 nm) at pH = 8.

As detailed in section 3.2, TGA of the MOFs was conducted to quantify the missing ligand defect sites in the materials.[10] The results show similar levels of defects across all five of the MOFs used in this study (Figure 3.8). Specifically, TGA data (Figure 3S.67-3S.72) shows that each MOF contains about ten carboxylates per cluster, indicating ~2 missing carboxylate linkers per SBU (~17% ligand defect abundance, Figure 3.9). Therefore, the increased activity of UiO-66-I is not correlated with a difference in defects created during MOF synthesis using the iodine functionalized linker. Furthermore, as expected, the BET surface area of the MOFs decreases with increasing size of the halogen indicating similar defect sites abundance across all of the MOF materials. Finally, the rate of DMNP degradation is not correlated with increasing halogen

electronegativity (F > I) ruling out the possibility of the enhanced activity being due to an inductive electron withdrawing effect. Because these MOFs had similar particle sizes, surface areas, and number of defect sites, other potential explanations for the observed differences in catalytic activity were explored. This increased activity was only observed in the presence of iodine functional groups which suggests that the iodine atom activates an electronic or steric effect at the catalytically active site resulting in increased activity.

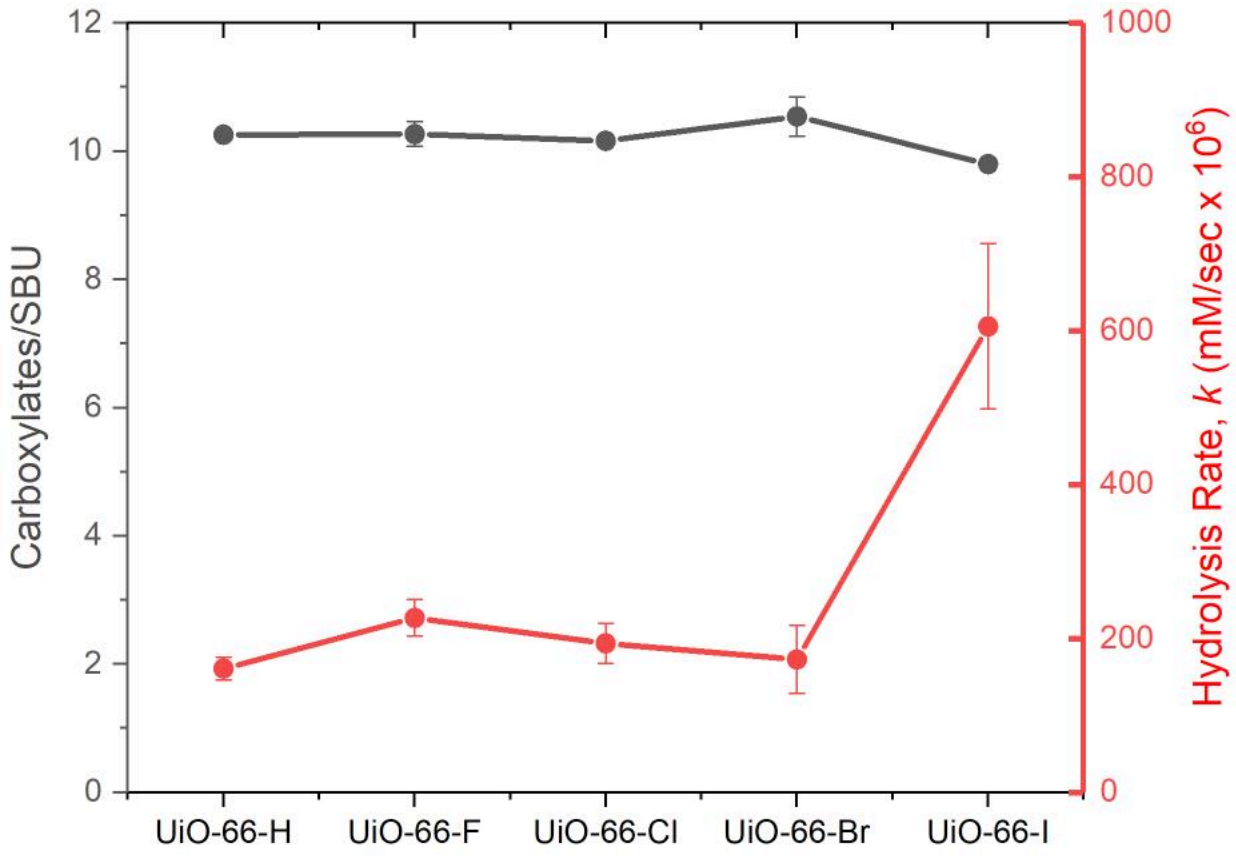

Figure 3.9. Ratio of organic linkers per SBU of UiO-66 MOFs (black) vs. rate of DMNP degradation by MOFs (red).

As mentioned in the introduction of this chapter, another possible source of increase activity could be noncovalent (e.g., hydrogen or halogen bonding) interactions between the ligand

functional groups and the catalytically active site. Due to the nature of the ligands in this study, a potential halogen bonding effect between the MOF ligands and the DMNP simulant to increase simulant hydrolysis was explored. Halogen bonding is described as an interaction between an electrophilic region associated with a halogen atom and a nucleophilic region of another molecule.[14-15] The electrophilic region in the halogen atom is referred to as the sigma hole and this area increases as a function of halogen polarizability (e.g., I > Br > Cl > F).[14-15] Across the series of halogens, halogen bonding is rarely observed in the case of fluorine and chlorine, but more often with bromine and iodine.[14-15] Several examples in the halogen bonding literature dictate instances where, across a family of analogous materials, the halogen bond is only observed with the most polarizable iodine atom.[16-19]

To model the effect of halogen bonding on catalytic hydrolysis of DMNP, DFT M06-L[20] calculations were performed on different isolated SBU cluster models of UiO-66 and UiO-66-I. The models were built from the optimized periodic crystal structure of mono-defective UiO-66 (i.e., UiO-66 with ten carboxylates linkers) consistent with the defect population determined by TGA (see appendix for details of the periodic and cluster calculations, Figure 3S.75-3S.76). In the as-synthesized UiO-66-I, the relative position of the halogens on the bdc^{2-} linkers with respect to the zirconium SBU is random. Therefore, when examining an isolated cluster there arise three possible arrangements of the iodine atoms around the SBU. UiO-66-I cluster models were designed to model these three possible conformations: one with iodine groups in all *ortho (ortho*-UiO-66-I*)*, a second with all *meta* (*meta*-UiO-66-I), and a third, alternating *ortho*/*meta* substitution pattern (*alter*-UiO-66-I, Figure 3S.76) with respect to the SBU. The aim of these calculations is not to quantitatively reproduce the experimental data, but rather to qualitatively describe the observed trends in catalytic activity and provide mechanistic insights. Recent mechanistic studies

on DMNP hydrolysis on different MOFs have shown the nucleophilic attack by water on the phosphorous center to be the rate-limiting step and hence this was the focus of the calculations performed here on UiO-66 and UiO-66-I.[4, 21]

Theory shows that in both the *ortho*- and *alter*-UiO-66-I MOFs, the iodine atoms of the MOF and the methoxy groups of DMNP are involved in a strong halogen bond. The M06-L computed I–OMe bond distances in DMNP bonded and transition state structures of the *ortho*-UiO-66-I are 0.095 Å and 0.233 Å shorter than the sum of the van der Waals radii of the iodine and the oxygen atoms, respectively (Figure 3.10). The computed activation free energies ($\Delta G^{\ddagger}$) for UiO-66, *ortho*-UiO-66-I, *meta*-UiO-66-I, and *alter*-UiO-66-I are 19.9, 11.0, 19.5, and 12.2 kcal/mol, respectively. Computed CM5 charges further confirm formation of the halogen bonding between iodine and -OMe group of the DMNP in both *ortho*- and *alter*-UiO-66-I systems. This is in stark contrast to the *meta*-UiO-66-I MOF where the iodine atoms are positioned far away from the oxygen atoms of the DMNP bonded UiO-66 (>5.7 Å) resulting in similar $\Delta G^{\ddagger}$ values for water addition in *meta*-UiO-66-I and the parent UiO-66 (19.5 kcal/mol and 19.9 kcal/mol, respectively. Overall, these calculations show that the sigma hole of the iodine atom forms a rather strong halogen bond with the nucleophilic methoxy group of DMNP which in turn results in a more electrophilic oxygen atom on the DMNP molecule accelerating the hydrolysis reaction.

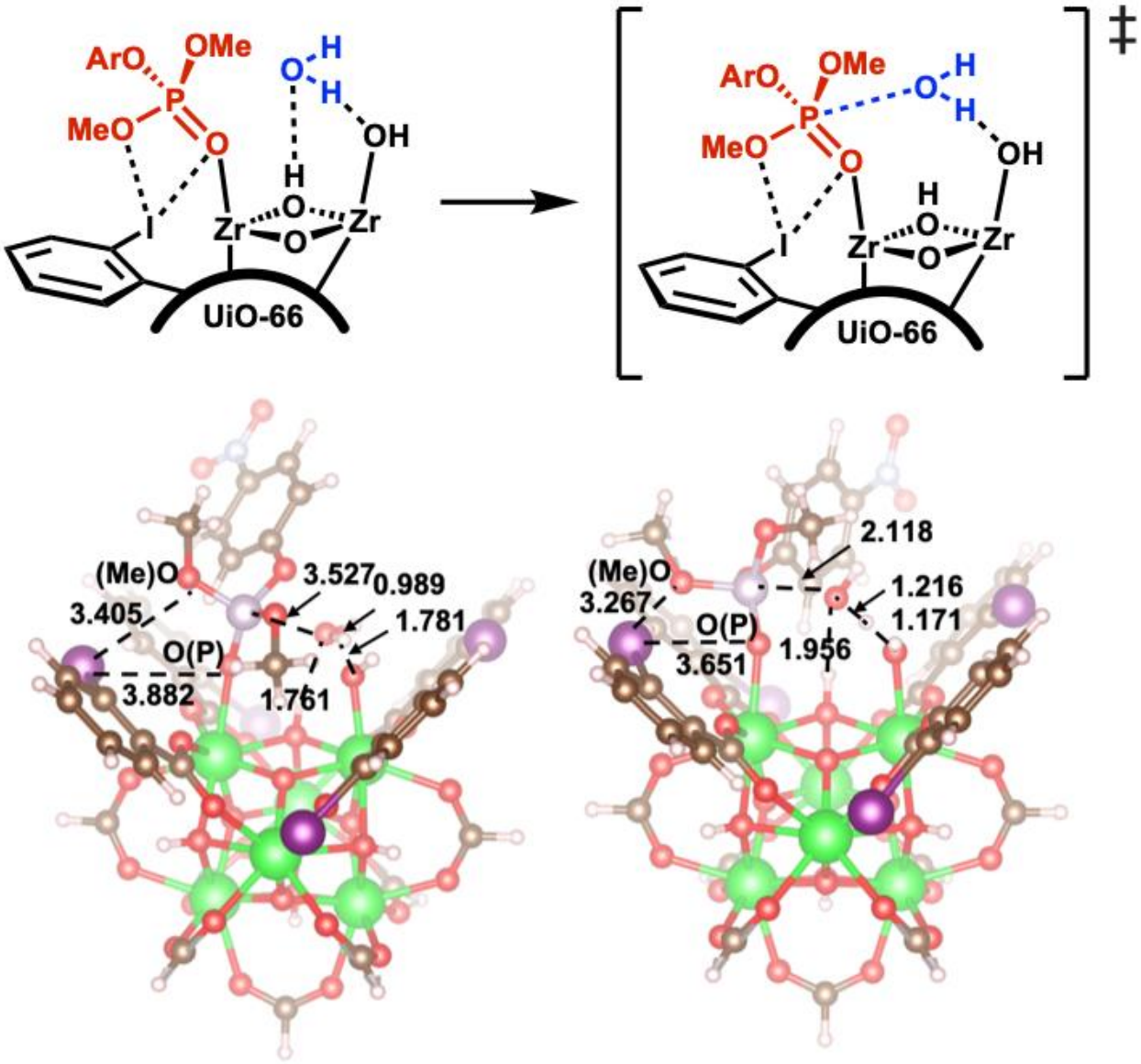

Figure 3.10. M06-L computed bond lengths (Å) in *ortho*-UiO-66-I cluster models of DMNP bonded (*left*) and transition state for nucleophilic attack of water to the P center (*right*) (ArO = 4-nitrophenoxide). Gray, white, red, blue, light purple, dark purple and green represent C, H, O, N, P, I, and Zr atoms, respectively.

3.4 Conclusion

In conclusion, a ligand-based strategy has been shown to be effective at improving UiO-66 for the degradation of the CWA simulant DMNP. A library of 26 mixed ligand UiO-66 MOFs was synthesized and screened for the catalytic degradation of the CWA simulant DMNP. The top performer in our library is MTV-UiO-66-BE which consists of NH_2-bdc and Br-bdc linkers. This MOF is over three times more active than either the single ligand MTV-UiO-66-B (UiO-66-NH_2) and MTV-UiO-66-E (UiO-66-Br) or a physical mixture of these two MOFs. Full characterization and defect quantification were conducted that indicate no correlation or increased activity as a result of defects. As such, this increased activity in the MTV-UiO-66 series originates from a synergistic ligand effect enabling more rapid degradation of DMNP. These results further underscore the significance of functional groups on MOF ligands in the degradation of CWAs and their simulants and the nature of the synergy observed in mixed ligand MOFs is currently the subject of ongoing studies. In addition, a halogenated UiO-66 series was screened to analyze the effects of these functional groups. The halogenated UiO-66-I shows a substantially enhanced degradation of the CWA simulant DMNP. Theoretical calculations suggest that halogen bonding is the origin of this increased activity and facilitates the catalytic hydrolysis of the phosphoester linkage. These findings offer new avenues for designing MOFs to more rapidly degrade CWAs.

3.5 Appendix: Supporting Information

General Materials and Methods. All solvents and starting materials were purchased from chemical suppliers and used without further purification (Sigma Aldrich, Alfa Aesar, EMD, and TCI).

Ligand Syntheses

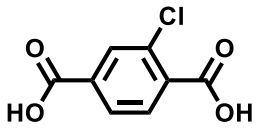

2-Chloroterephthalic acid. 2-Chloro-1,4-dimethylbenzene (6 mL, 43 mmol), 60 mL of deionized water and 16 ml of nitric acid (70%) were poured into a 100 ml Teflon-lined steel autoclave. The autoclave was sealed and placed into a 170 °C oven for 16 h. After cooling to room temperature, the solution was vacuum filtered and 2-chloroterephthalic acid was recovered as a white crystalline powder which was washed with water and dried in a vacuum oven at 70 °C overnight. Yield: 5.4 g (63%). ^{1}H NMR (400 MHz, d_6-DMSO): δ 13.65 (s, 2H), 7.98 (d, J = 1.2 Hz, 1H), 7.95 (dd, J = 8.0, 1.5 Hz, 1H), 7.87 (d, J = 8.0 Hz, 1H). MS (m/z) calcd. for $C_8H_5ClO_4$ $[M-H]^-$: 198.99; Found: 199.07.

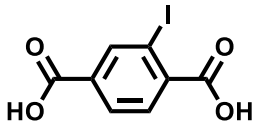

2-Iodoterephthalic acid. To a suspension of 2-aminoterephthalic acid (3.0 g, 16.6 mmol) in 100 mL of H_2O/ conc. HCl (1:1, v/v) at 0 °C, an aqueous solution of $NaNO_2$ (2.85 g, 41.3 mmol) was added dropwise over a period of 45 min. After being stirred for an additional 30 min at 0 °C, the diazonium salt was poured into a solution of KI (16.5 g, 99.4 mmol) in 150 mL of water and the resulting dark solution was left stirring at room temperature for 18 h. Solid $NaHSO_3$ was added in portions until the dark color of the solution faded, leaving a behind a suspension of tan colored solid in the solvent mixture. The solid was filtered and triturated with 150 mL of CH_2Cl_2:H_2O (1:1, v/v) and dried overnight in a vacuum oven. Yield: 4.03 g (83%). ^{1}H NMR (400 MHz d_6-DMSO): δ 13.57 (s, 2H), 8.42 (d, J = 1.4 Hz, 1H), 7.99 (dd, J = 8.0, 1.6 Hz, 1H), 7.77 (d, J = 8.0 Hz, 1H). MS (m/z) calcd. for $C_8H_5IO_4$ $[M-H]^-$: 290.92; Found: 290.97.

MOF Syntheses

One Ligand Synthesis:

Zirconium(IV) chloride (0.26 mmol) and one of the following: terephthalic acid (0.26 mmol, 43 mg), 2-aminoterephthalic acid (0.26 mmol, 47 mg) , 2-hydroxyterephthalic acid (0.26 mmol, 47 mg), 2-nitroterephthalic acid (0.26 mmol, 55 mg), or 2-bromoterephthalic acid (0.26 mmol, 64 mg) were dissolved in 15 mL DMF with 0.447 mL glacial acetic acid in a 20-mL vial. The capped vial was placed in an oven and heated to 120 °C for 24 h. After cooling to room temperature, the particles were collected by centrifugation (fixed-angle rotor, 6500 rpm, 15 min), washed with 3×10 mL portions of MeOH, and 1×10 mL hexanes and dried under vacuum at room temperature.

Two Ligand Synthesis:

Zirconium(IV) chloride (0.26 mmol) and a combination of two of the following: terephthalic acid (0.13 mmol, 22 mg), 2-aminoterephthalic acid (0.13 mmol, 24 mg), 2-hydroxyterephthalic acid (0.13 mmol, 24 mg), 2-nitroterephthalic acid (0.13 mmol, 28 mg), or 2-bromoterephthalic acid (0.13 mmol, 32 mg) were dissolved in 15 mL DMF with 0.447 mL glacial acetic acid in a 20 mL vial. The capped vial was placed in an oven and heated to 120 °C for 24 h. After cooling to room temperature, the particles were collected by centrifugation (fixed-angle rotor, 6500 rpm, 15 min), washed with 3×10 mL portions of MeOH, and 1×10 mL hexanes and dried under vacuum at room temperature.

Three Ligand Synthesis:

Zirconium(IV) chloride (0.26 mmol) and a combination of three of the following: terephthalic acid (0.087 mmol, 14 mg), 2-aminoterephthalic acid (0.087 mmol, 16 mg), 2-hydroxyterephthalic acid

(0.087 mmol, 16 mg), 2-nitroterephthalic acid (0.087 mmol, 18 mg) ,or 2-bromoterephthalic acid (0.087 mmol, 21 mg) were dissolved in 15 mL DMF with 0.447 mL glacial acetic acid in a 20 mL vial. The capped vial was placed in an oven and heated to 120 °C for 24 h. After cooling to room temperature, the particles were collected by centrifugation (fixed-angle rotor, 6500 rpm, 15 min), washed with 3×10 mL portions of MeOH, and 1×10 mL hexanes and dried under vacuum at room temperature.

Four Ligand Synthesis:

Zirconium(IV) chloride (0.26 mmol) and a combination of four of the following: terephthalic acid (0.065 mmol, 11 mg), 2-aminoterephthalic acid (0.065 mmol, 12 mg), 2-hydroxyterephthalic acid (0.065 mmol, 12 mg), 2-nitroterephthalic acid (0.065 mmol, 14 mg), or 2-bromoterephthalic acid (0.065 mmol, 16 mg) were dissolved in 15 mL DMF with 0.447 mL glacial acetic acid in a 20 mL vial. The capped vial was placed in an oven and heated to 120 °C for 24 h. After cooling to room temperature, the particles were collected by centrifugation (fixed-angle rotor, 6500 rpm, 15 min), washed with 3×10 mL portions of MeOH, and 1×10 mL hexanes and dried under vacuum at room temperature.

Five Ligand Synthesis:

Zirconium(IV) chloride (0.26 mmol) and terephthalic acid (0.052 mmol, 9 mg), 2-aminoterephthalic acid (0.052 mmol, 9 mg), 2-hydroxyterephthalic acid (0.052 mmol, 9 mg), 2-nitroterephthalic acid (0.052 mmol, 11 mg), or 2-bromoterephthalic acid (0.052 mmol, 13 mg) were dissolved in 15 mL DMF with 0.447 mL glacial acetic acid in a 20 mL vial. The capped vial was placed in an oven and heated to 120 °C for 24 h. After cooling to room temperature, the

particles were collected by centrifugation (fixed-angle rotor, 6500 rpm, 15 min), washed with 3×10 mL portions of MeOH, and 1×10 mL hexanes and dried under vacuum at room temperature.

UiO-66-F. Zirconium(IV) chloride (61 mg, 0.26 mmol) and 2-fluoroterephthalic acid (48 mg, 0.26 mmol) were dissolved in 15 mL DMF with 0.45 mL glacial acetic acid in a 20mL vial with Teflon-lined cap. The vial was then placed in a 120 °C oven for 24 h. After cooling to ambient temperature, the particles were collected by centrifugation (fixed-angle rotor, 6000 rpm, 5 min), followed by washing with 3×10 mL DMF and 3×10 mL MeOH. The particles were then soaked in MeOH for 3 d with solvent changed daily, before being dried under vacuum at room temperature.

UiO-66-Cl. Zirconium(IV) chloride (61 mg, 0.26 mmol) and 2-chloroterephthalic acid (52 mg, 0.26 mmol) were dissolved in 15 mL DMF with 0.45 mL glacial acetic acid in a 20 mL vial with Teflon-lined cap. The vial was then placed in a 120 °C oven for 24 h. After cooling to ambient temperature, the particles were collected by centrifugation (fixed-angle rotor, 6000 rpm, 5 min), followed by washing with 3×10 mL DMF and 3×10 mL MeOH. The particles were then soaked in MeOH for 3 d with solvent changed daily, before being dried under vacuum at room temperature.

UiO-66-Br. Zirconium(IV) chloride (61 mg, 0.26 mmol) and 2-bromoterephthalic acid (64 mg, 0.26 mmol) were dissolved in 15 mL DMF with 0.45 mL glacial acetic acid in a 20mL vial with Teflon-lined cap. The vial was then placed in a 120 °C oven for 24 h. After cooling to ambient temperature, the particles were collected by centrifugation (fixed-angle rotor, 6000 rpm, 5 min), followed by washing with 3×10 mL DMF and 3×10 mL MeOH. The particles were then soaked

in MeOH for 3 d with solvent changed daily, before being dried under vacuum at room temperature.

UiO-66-I. Zirconium(IV) chloride (61 mg, 0.26 mmol) and 2-iodoterephthalic acid (76 mg, 0.26 mmol) were dissolved in 15 mL DMF with 0.45 mL glacial acetic acid in a 20 mL vial with Teflon-lined cap. The vial was then placed in a 120 °C oven for 24 h. After cooling to ambient temperature, the particles were collected by centrifugation (fixed-angle rotor, 6000 rpm, 5 min), followed by washing with 3×10 mL DMF and 3×10 mL MeOH. The particles were then soaked in MeOH for 3 d with solvent changed daily, before being dried under vacuum at room temperature.

UiO-66-I$_{50\%}$. Zirconium (IV) chloride (61 mg, 0.26 mmol), 2-iodoterephthalic acid (38 mg, 0.13 mmol) and terephthalic acid (22 mg, 0.13 mmol) were dissolved in 15 mL DMF with 0.45 mL glacial acetic acid in a 20 mL vial with Teflon-lined cap. The vial was then placed in a 120 °C oven for 24 h. After cooling to ambient temperature, the particles were collected by centrifugation (fixed-angle rotor, 6000 rpm, 5 min), followed by washing with 3×10 mL DMF and 3×10 mL MeOH. The particles were then soaked in MeOH for 3 d with solvent changed daily, before being dried under vacuum at room temperature.

Characterization Methods

Nuclear Magnetic Resonance (NMR). NMR experiments were carried out on a JOEL ECA 500 MHz spectrometer equipped with a Jeol 2 ^{1}H probe. Chemical shifts are quoted in parts per million (ppm) referenced to the appropriate solvent peak or 0 ppm for TMS. MOFs were digested for NMR analysis by immersion of ~8-10 mg MOF in 580 μL DMSO-d_6 with 20 μL HF (48% in

water). Samples were kept in this acidic solution at room temperature until the MOF was fully dissolved.

Powder X-ray Diffraction (PXRD). PXRD data was collected at room temperature on a Bruker D8 Advance diffractometer running at 40 kV, 40 mA for Cu Kα ($\lambda = 1.5418$ Å), with a scan speed of 0.5 sec/step, a step size of 0.01° in 2θ, and a 2θ range of 3-50° at room temperature.

Scanning Electron Microscopy (SEM). MOFs were placed on conductive carbon tape on a sample holder and coated using an Ir-sputter coating for 7 sec. A Zeiss Sigma 500 ESEM microscope was used for acquiring images using a 2-3 kV energy source under vacuum at a working distance of 5 mm.

Thermogravimetric analysis (TGA). ~10 mg of sample were placed in a 100 μL aluminum crucible. Samples were analyzed on a Mettler Toledo Star TGA/DSC using a temperature range of 30-600 °C scanning at 5 °C/min synthetic air (75 cm^3/min air flow rate) for sample degradation measurements and a heat-cool-heat procedure at 10 °C/min for melting point determination.

N_2 Gas Sorption Analysis: Samples for analysis were evacuated in a vacuum oven overnight at room temperature prior to analysis. ~50 mg of sample were then transferred to pre-weighed sample tubes and degassed at 105° C on a Micromeritics ASAP 2020 Adsorption Analyzer for a minimum of 12 h or until the outgas rate was <5 mmHG. After degassing, the sample tubes were re-weighed to obtain a consistent mass for the samples. Sorption data and BET surface area (m^2/g)

measurements were collected at 77 K with N_2 on a Micromeritics ASAP 2020 Adsorption Analyzer using volumetric technique.

Catalysis Experiments. DMNP hydrolysis was measured using a modified version of a previously reported procedure.[6] All catalytic monitoring was carried out using a BioTek Synergy H4 plate reader using single wavelength absorbance mode. 20 and 40 mM of *N*-ethylmorpholine buffer was prepared from deionized water adjusted to pH = 8.0. A plot of absorbance of *p*-nitrophenol at varying concentrations was measured yielding a calibration curve with a slope of 3.48 Abs/mM.[6] MOF samples were prepared by weighing 6 mg of MOF powder and diluting this powder in 10 mL of deionized water. These solutions were rigorously sonicated and vortexed (>3× of each) and diluted in half with 40 mM buffer solution yielding 300 μg/mL MOF in 20 mM buffer solution. DMNP hydrolysis assays with MOF powders were carried out in Olympus Plastics clear, flat-bottom 96-well plates. Each well was prepared with 100 μL total volume containing: 95 μL MOF suspension in buffer and 5 μL substrate (25 mM DMNP in MeOH; 1.25 mM total concentration; 0.125 μmol). Upon the addition of substrate using a multi-channel pipette, hydrolysis was monitored by the change in absorbance (λ_{max} = 407 nm) over 15 min at 24 °C with 3 sec shaking of the plate every 10 sec. The absorbance was monitored from the 30 to 360 sec time period, instead of the previously reported 600 to 3000 sec time period.[6] This adjustment was made because raw data of our most active sample, UiO-66-I, displays a drastic difference in slope after ~500 sec in the absorbance vs. time curve (Figure 3S.73). When the data is analyzed in the 30 to 360 sec regions, the slope of the line is consistent throughout. As such, in an attempt to obtain a more accurate value of the rate of catalysis, data from 30 sec to 360 sec was used to calculate the hydrolysis of DMNP (Figure 3S.73) for all samples. Activity was measured as initial

linear rate, measured from 30 to 360 sec using Excel software. Reported activities for MOF samples are an average of seven replicates. Hydrolysis rates were adjusted to account for the increased mass of the halogenated species such that a direct comparison could be made across all materials in this study (Figure 3S.74). Rates were calculated to account for the substantial difference in moles of MOF catalyst between samples (due to the increased mass of the halogenated MOFs) such that a direct comparison could be made across all materials in this study. For example, a single SBU of UiO-66 has a molecular mass of 1628 g/mol, whereas a single SBU of UiO-66-I has a molecular mass of 2383 g/mol. The difference in number of moles per sample well was account for as shown in Table 3S.2.

Computational Details

Periodic Calculations. PBE[22] density functional calculations with damped D3 dispersion correction[23] as implemented in CP2K version 5.1[24] were performed to fully relax both atomic positions and cell parameters of the pristine (6 bdc^{2-}, 12 carboxylates, 456 atoms) and mono-defective (5 bdc^{2-}, 10 carboxylates, 450 atoms) UiO-66 MOFs (Figure 3S.75). For the latter, the two open Zr^{IV} metal-sites resulted after one bdc^{2-} removal were saturated and charge balanced by adding one water and one hydroxyl group.[25]

The double-zeta valence with polarization DZVP-MOLOPT basis sets and core electron pseudopotentials according to the Geodecker−Teter−Hutter formulation[26] were used. The plane-wave cutoff of the finest grid and REL_CUTOFF were set to 360 RY and 60 RY. MAX_FORCE (hartree/bohr), RMS_FORCE, MAX_DR (bohr), and RMS_DR were set to 0.0030, 0.0050, 0.0020, and 0.0050, respectively. Vibrational frequency calculations were performed numerically at the Γ point on a fragment comprised of the metal−oxide node (without the linkers) to assure

presence of a local minimum on the potential energy surface.

Cluster Calculations. Cluster models were cut from the optimized periodic conventional unit cell of the mono-defective UiO-66. To obtain these cluster models, the organic linkers around the metal−oxide node were truncated to four benzoate linkers on top face, which are toward DMNP, with the 8 remaining linkers truncated to formate (Figure 3S.76, Cartesian coordinates of all optimized structures are included as part of the appendix).

The carbon atoms of all the carboxylate linkers were fixed to keep the rigidity of the MOF. The meta-GGA local M06-L[20] density functional was used for all geometry optimizations in gas phase using the Def2-SVP[27] basis set and the ECP28MDF effective core potential[28] for I and Zr^{IV}. All basis sets were obtained from the basis set exchange database (https://bse.pnl.gov/bse/portal). The grid used for numerical integration in DFT was set to "ultrafine," i.e., a pruned grid of 99 radial shells and 590 angular points per shell. The natures of all stationary points were determined by calculation of analytic vibrational frequencies, which were also used to compute molecular partition functions (298 K, 1 atm) using the conventional particle-in-a-box, rigid-rotator, quantum mechanical harmonic oscillator approximation,[29] except that all vibrational frequencies below 50 cm^{-1} were replaced with values of 50 cm^{-1} (the quasi-harmonic-oscillator approximation.[29] Zero-point vibrational energies and thermal contributions to enthalpy were determined from these partition functions. For transition-state structures, the presence of a single imaginary frequency corresponding to the reaction path of interest was confirmed.

Electronic energies were further refined by performing single point calculations with the M06-2X[30] meta-GGA hybrid density functional on gas phase optimized geometries with the larger Def2-TZVP[27] basis set on all elements and ECP28MDF on I and Zr^{IV} atoms using the SMD

continuum solvation model[31] with parameters for water (ε = 78.355). CM5 charges were also computed for all systems considered in this study at the M06-2X(SMD, water)/def2-TZVP|ECP28MDF//M06-L(gas)/Def2-SVP|ECP28MDF.[32] Default convergence criteria for geometry optimizations and single point energy calculations were used. All reported extended and truncated cluster free energies and enthalpies are computed by combining M06-2X(SMD, water) single point energies with thermochemical contributions obtained at the M06-L (gas phase) level. All cluster computations for mechanistic studies were carried out with Gaussian 16.[33]

Figures and Tables

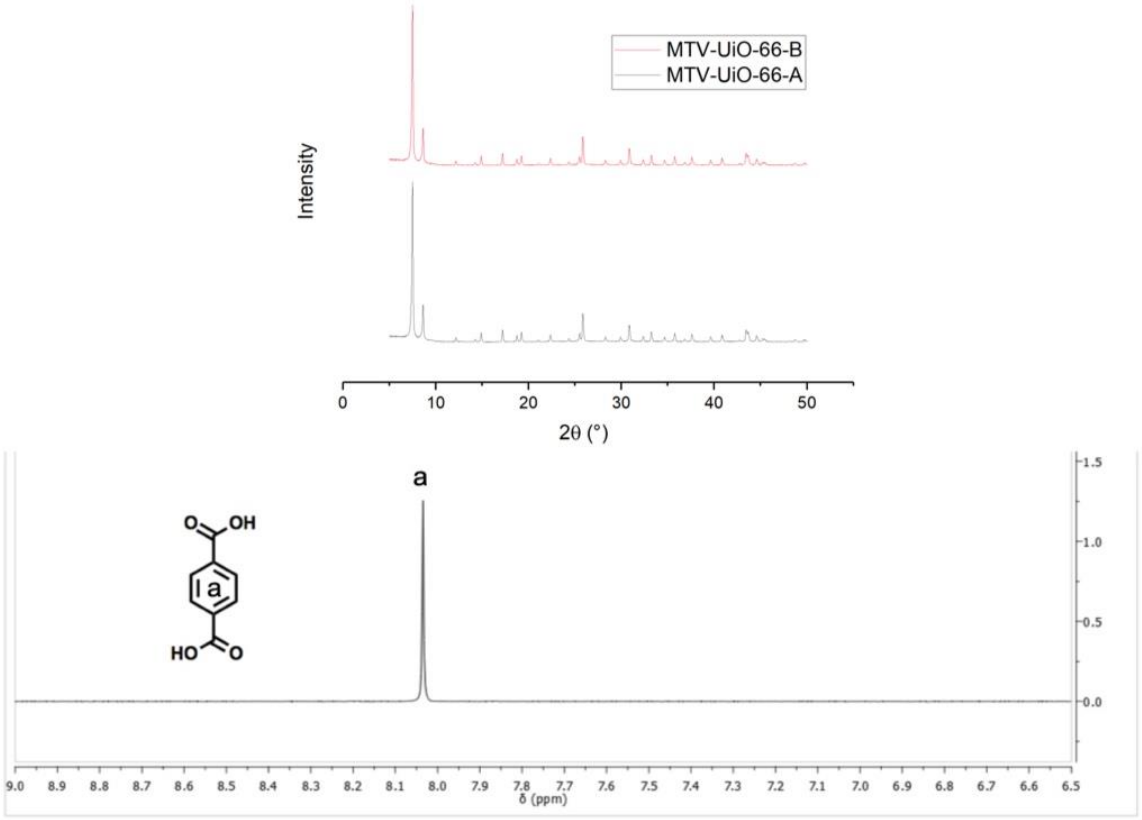

Figure 3S.1. *Top*: PXRD of MTV-UiO-66-A. *Bottom*: ^{1}H NMR digestion of MTV-UiO-66-A.

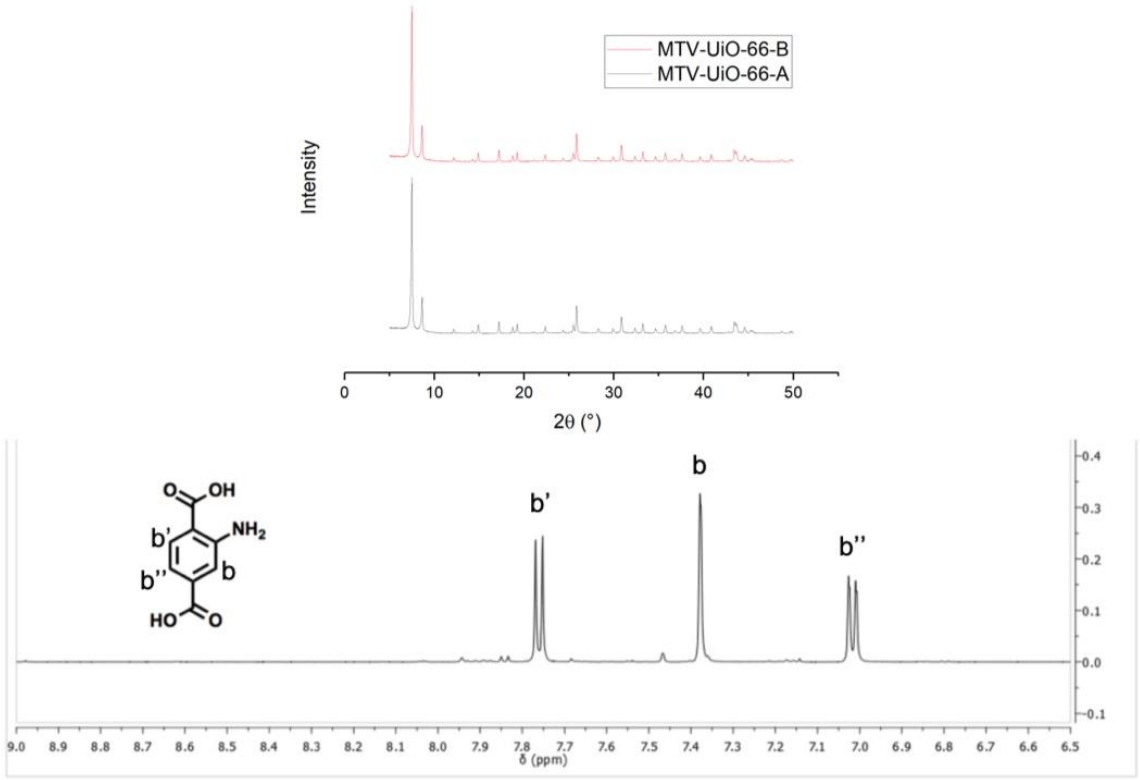

Figure 3S.2. *Top*: PXRD of MTV-UiO-66-B. *Bottom*: ^{1}H NMR digestion of MTV-UiO-66-B.

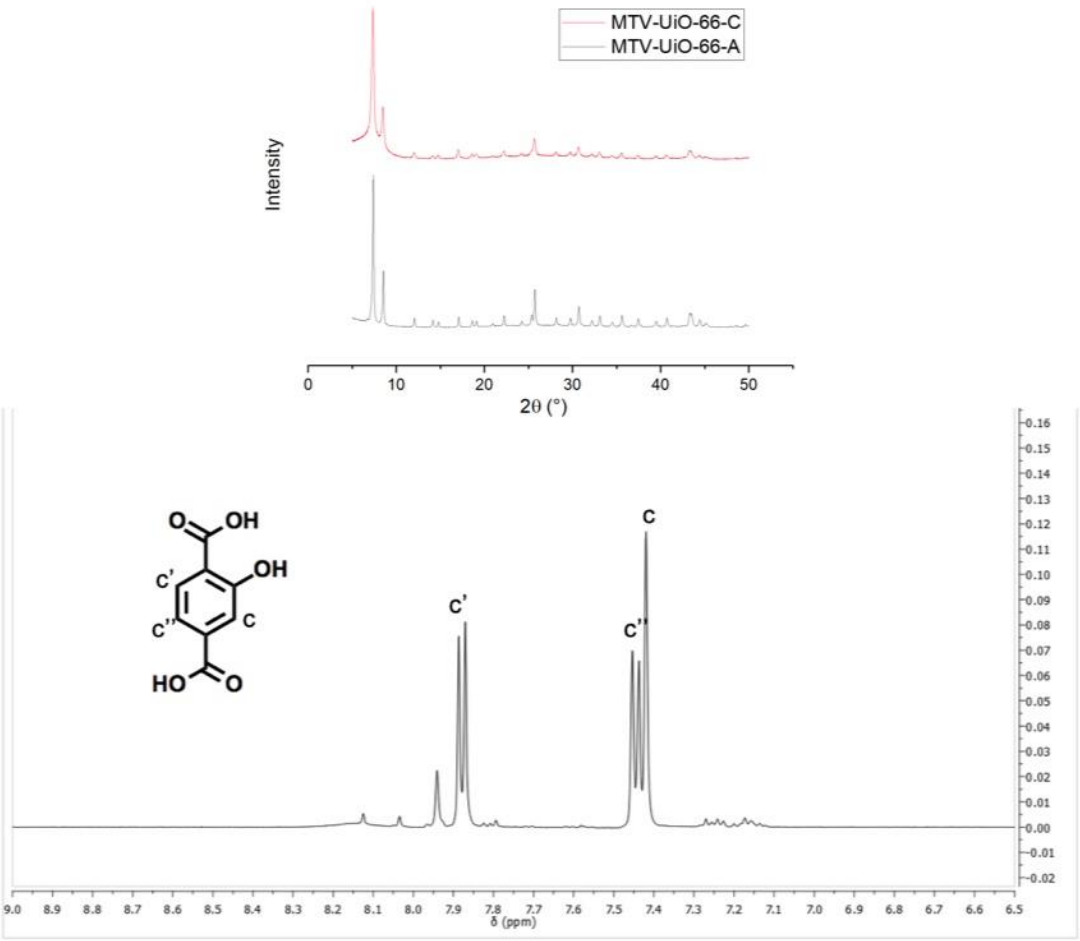

Figure 3S.3. *Top*: PXRD of MTV-UiO-66-C. *Bottom*: ^{1}H NMR digestion of MTV-UiO-66-C.

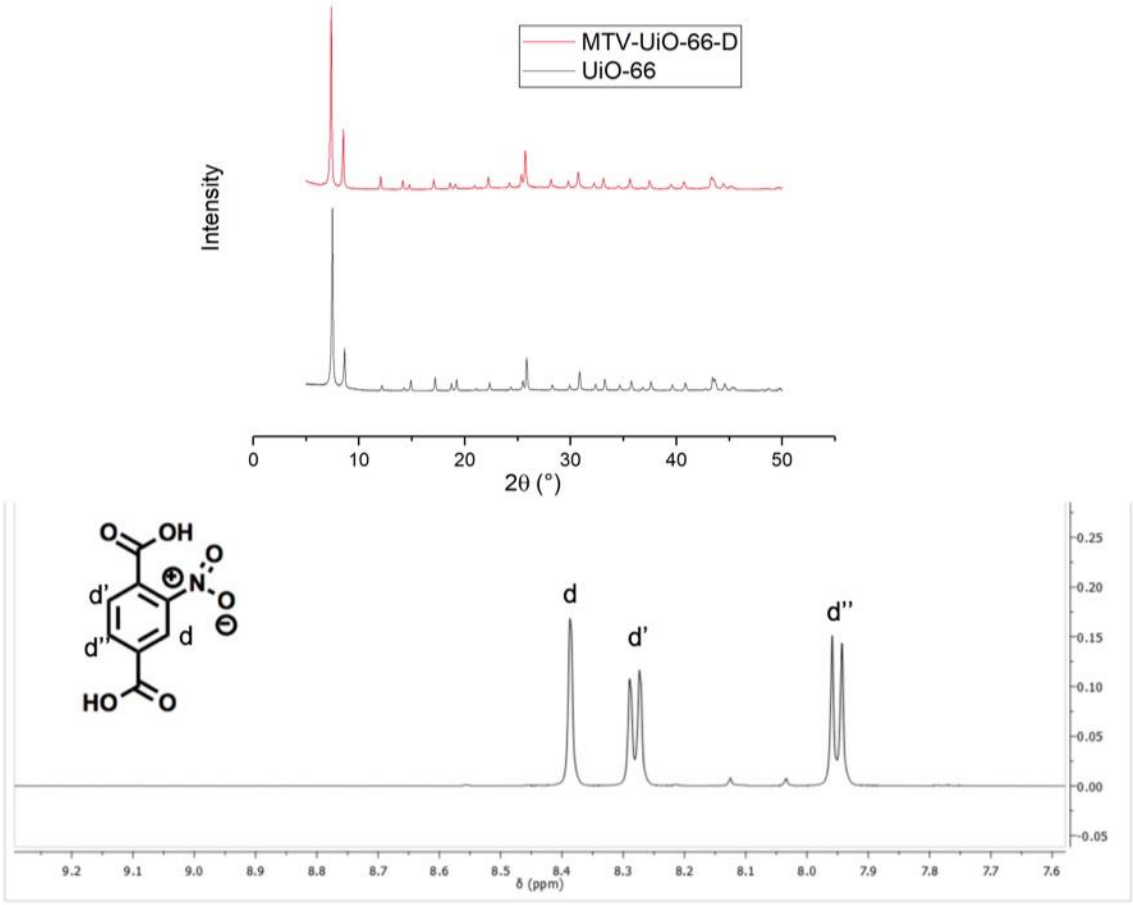

Figure 3S.4. *Top*: PXRD of MTV-UiO-66-D. *Bottom*: ^{1}H NMR digestion of MTV-UiO-66-D.

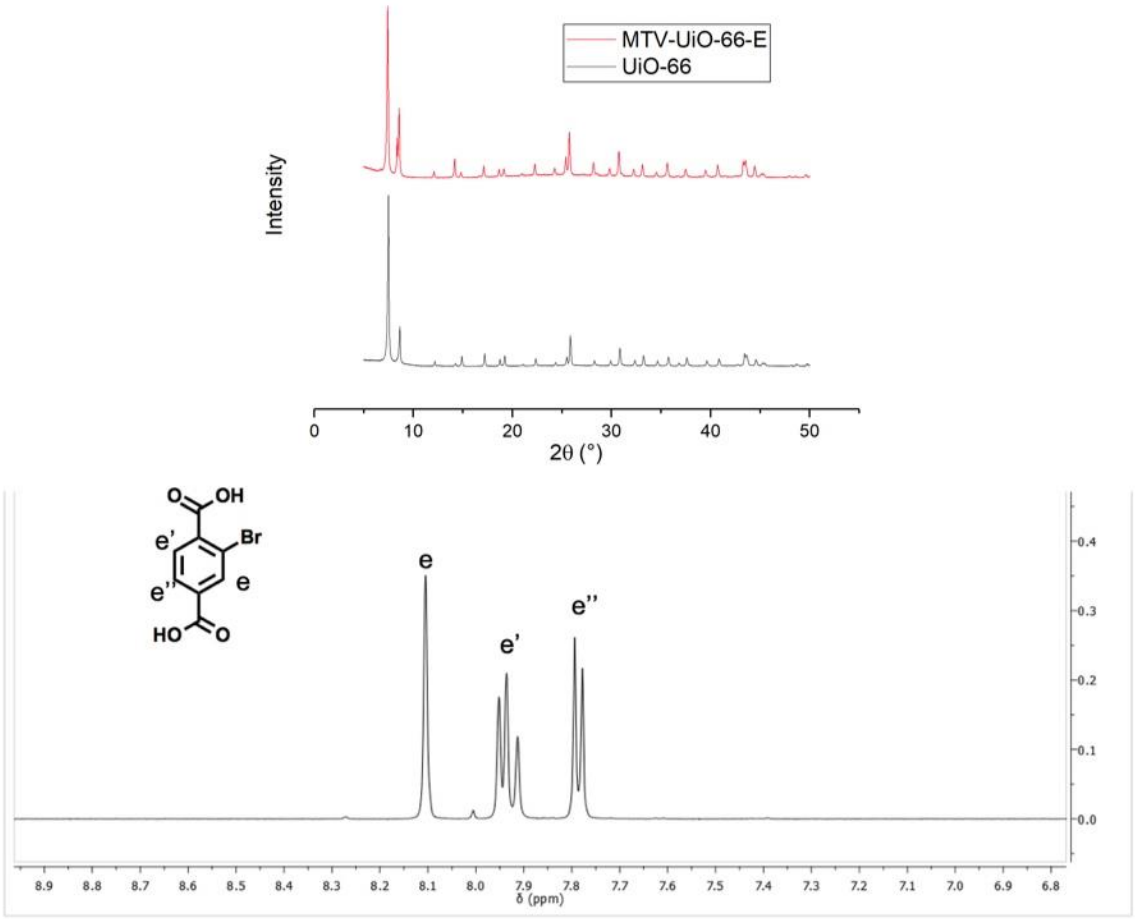

Figure 3S.5. *Top*: PXRD of MTV-UiO-66-E. *Bottom*: ^{1}H NMR digestion of MTV-UiO-66-E.

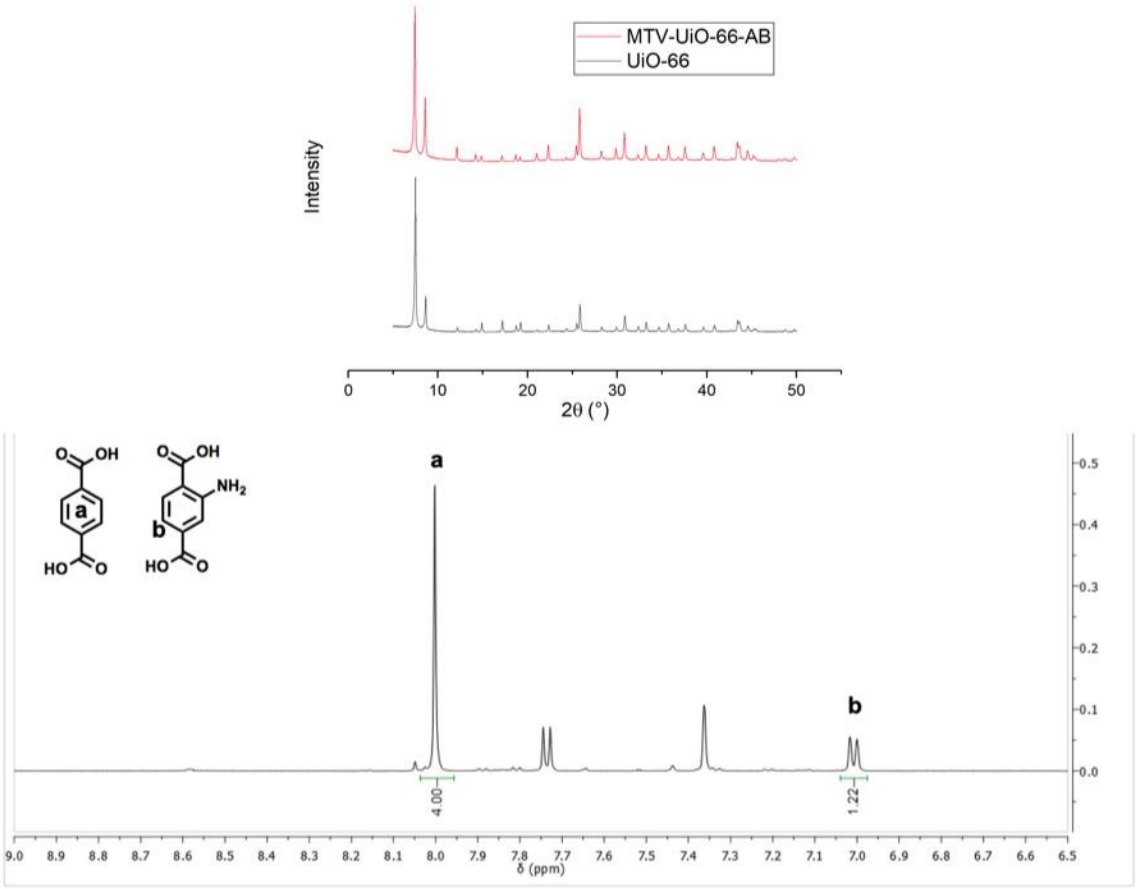

Figure 3S.6. *Top*: PXRD of MTV-UiO-66-AB. *Bottom*: ^{1}H NMR digestion of MTV-UiO-66-AB.

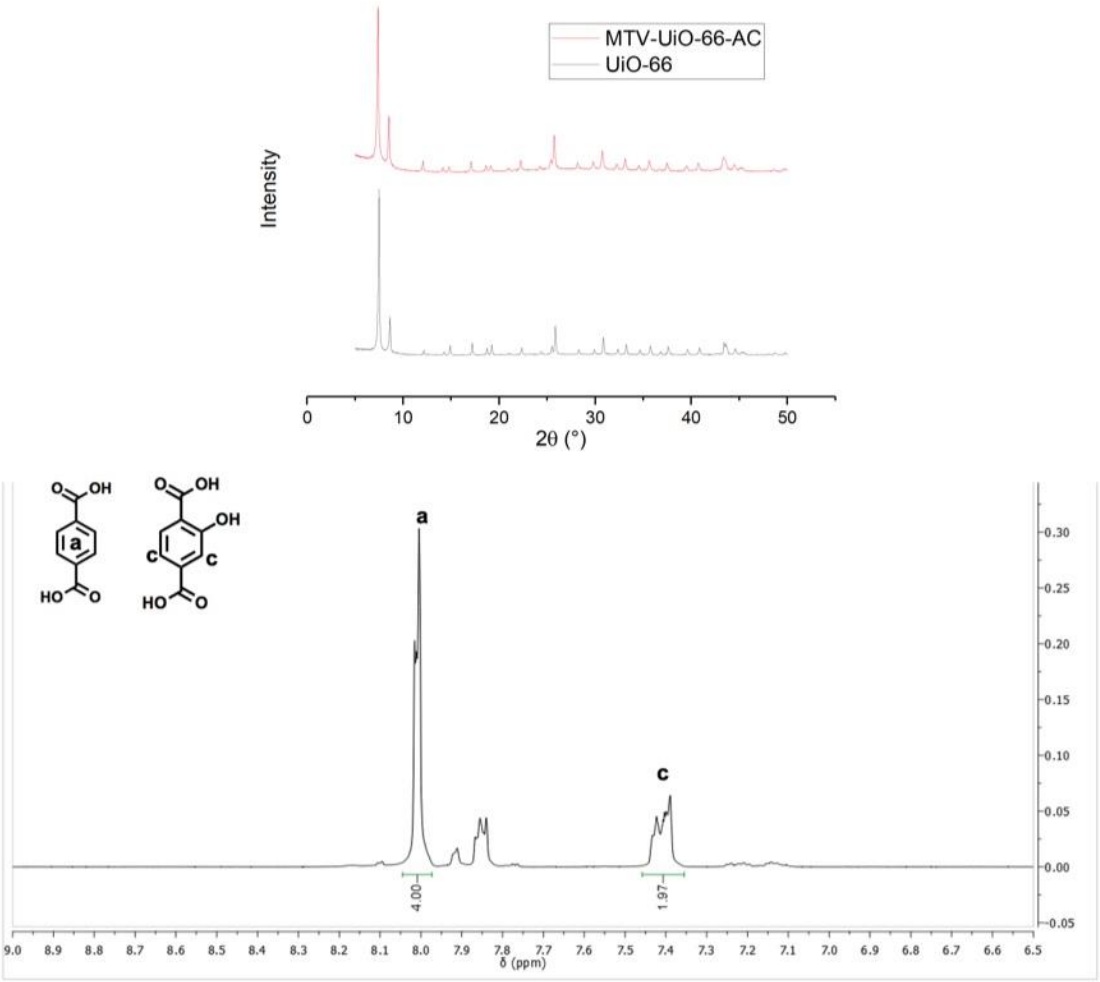

Figure 3S.7. *Top*: PXRD and SEM of MTV-UiO-66-AC. *Bottom*: ^{1}H NMR digestion of MTV-UiO-66-AC.

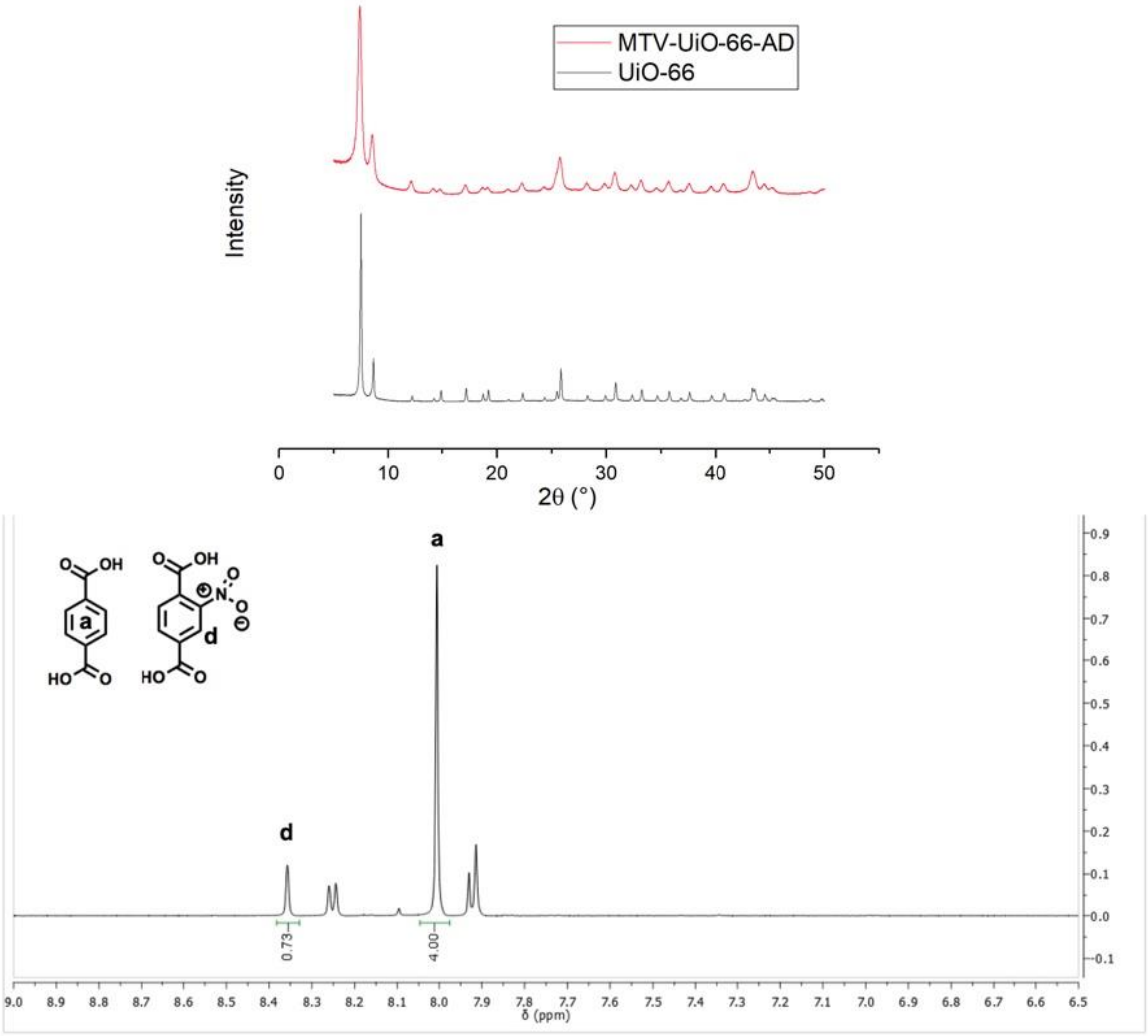

Figure 3S.8. *Top*: PXRD of MTV-UiO-66-AD. *Bottom*: ^{1}H NMR digestion of MTV-UiO-66-AD.

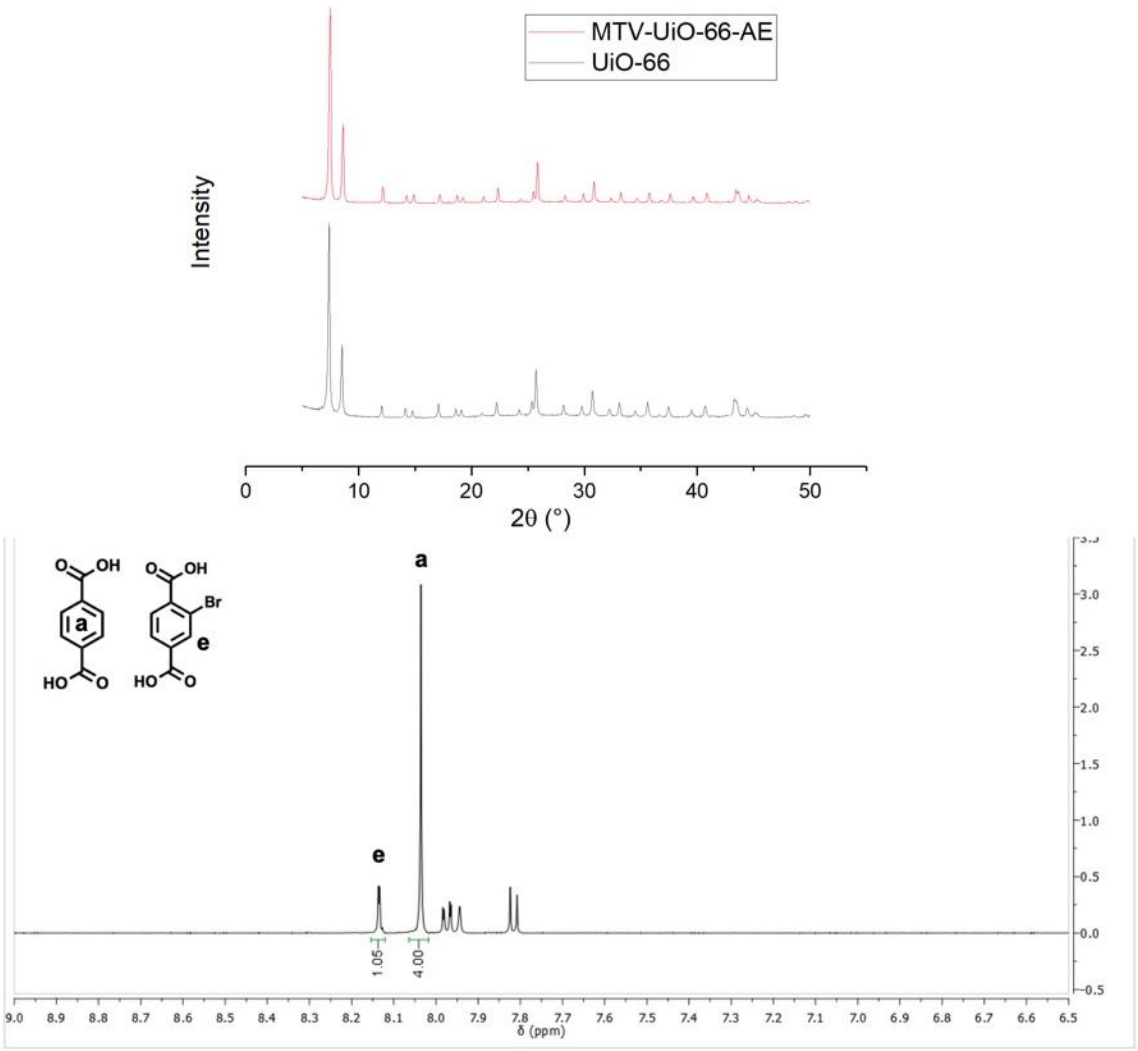

Figure 3S.9. *Top*: PXRD of MTV-UiO-66-AE. *Bottom*: ^{1}H NMR digestion of MTV-UiO-66-AE.

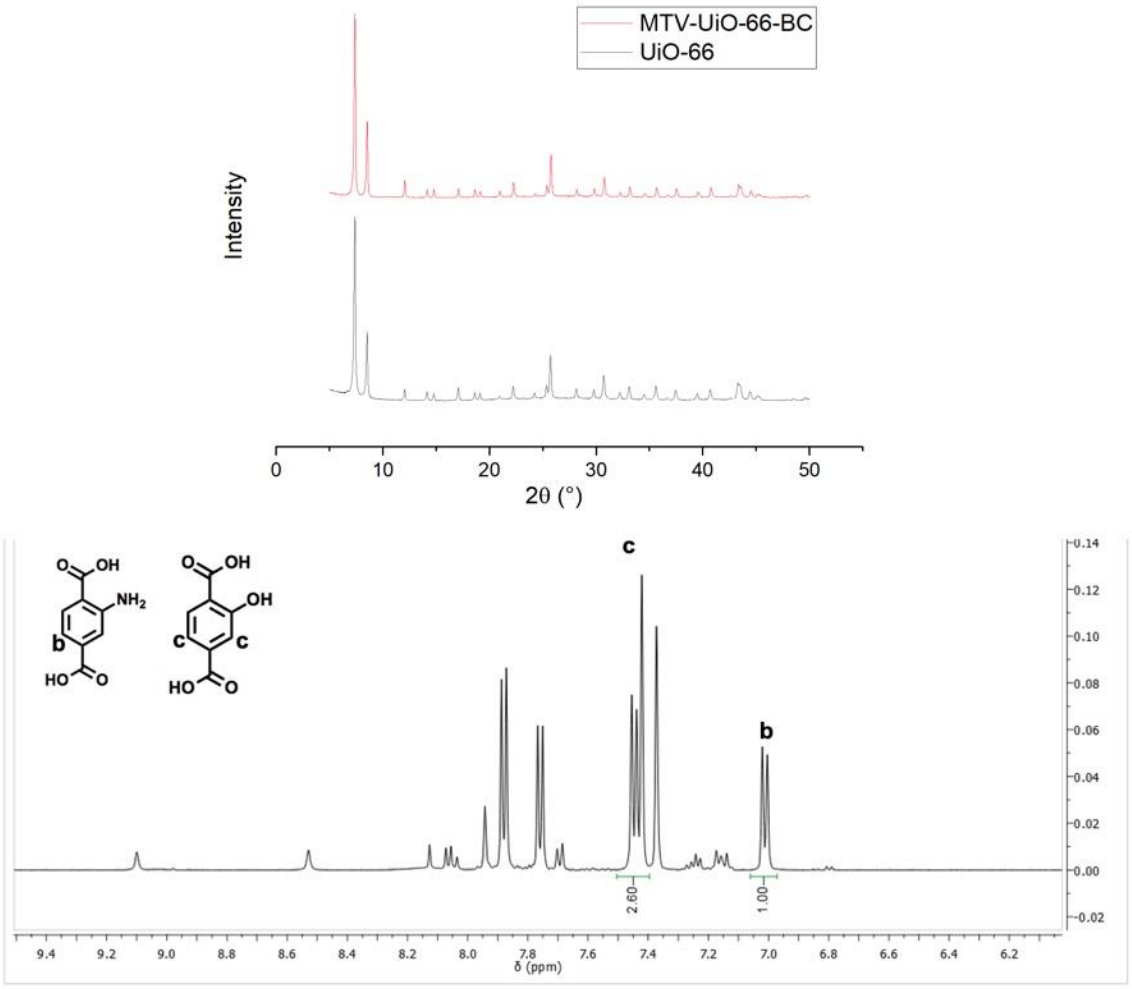

Figure 3S.10. *Top*: PXRD of MTV-UiO-66-BC. *Bottom*: ^{1}H NMR digestion of MTV-UiO-66-BC.

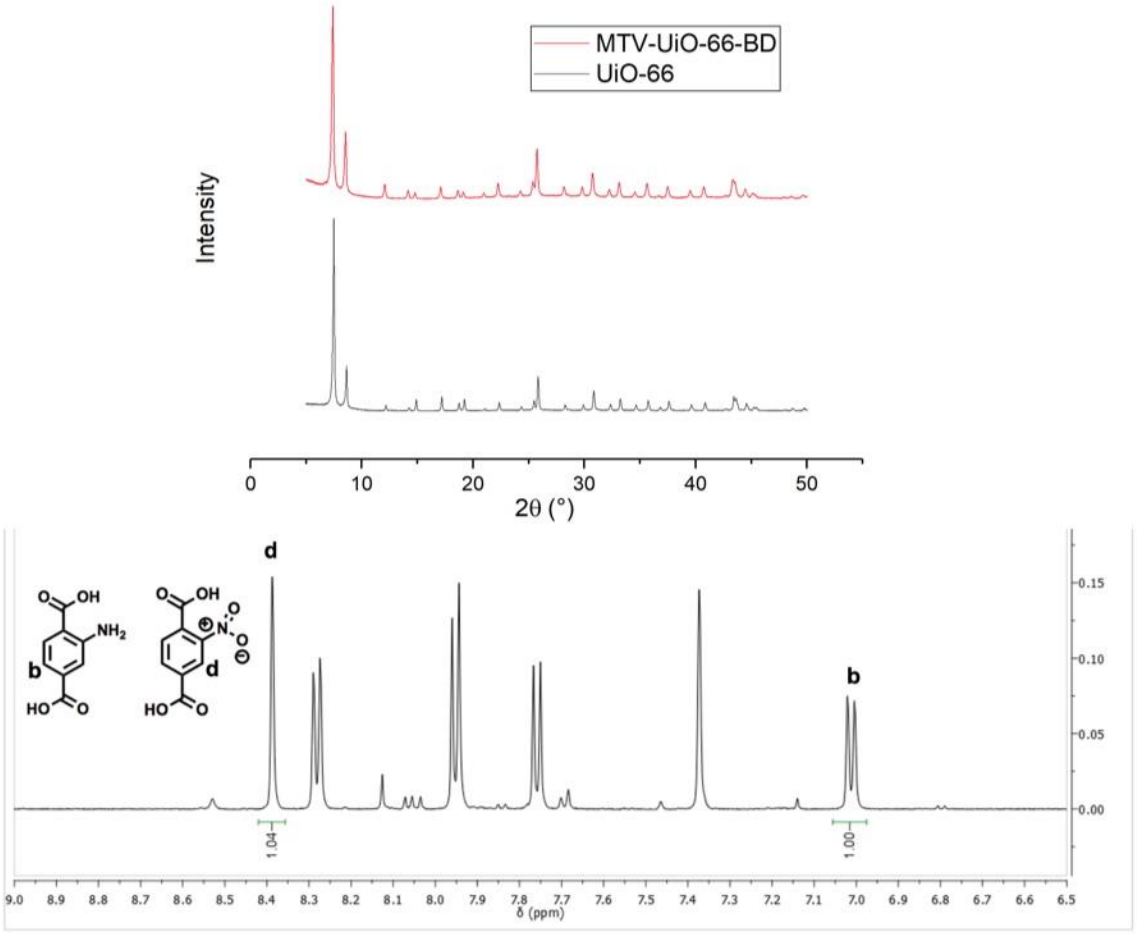

Figure 3S.11. *Top*: PXRD of MTV-UiO-66-BD. *Bottom*: ^{1}H NMR digestion of MTV-UiO-66-BD.

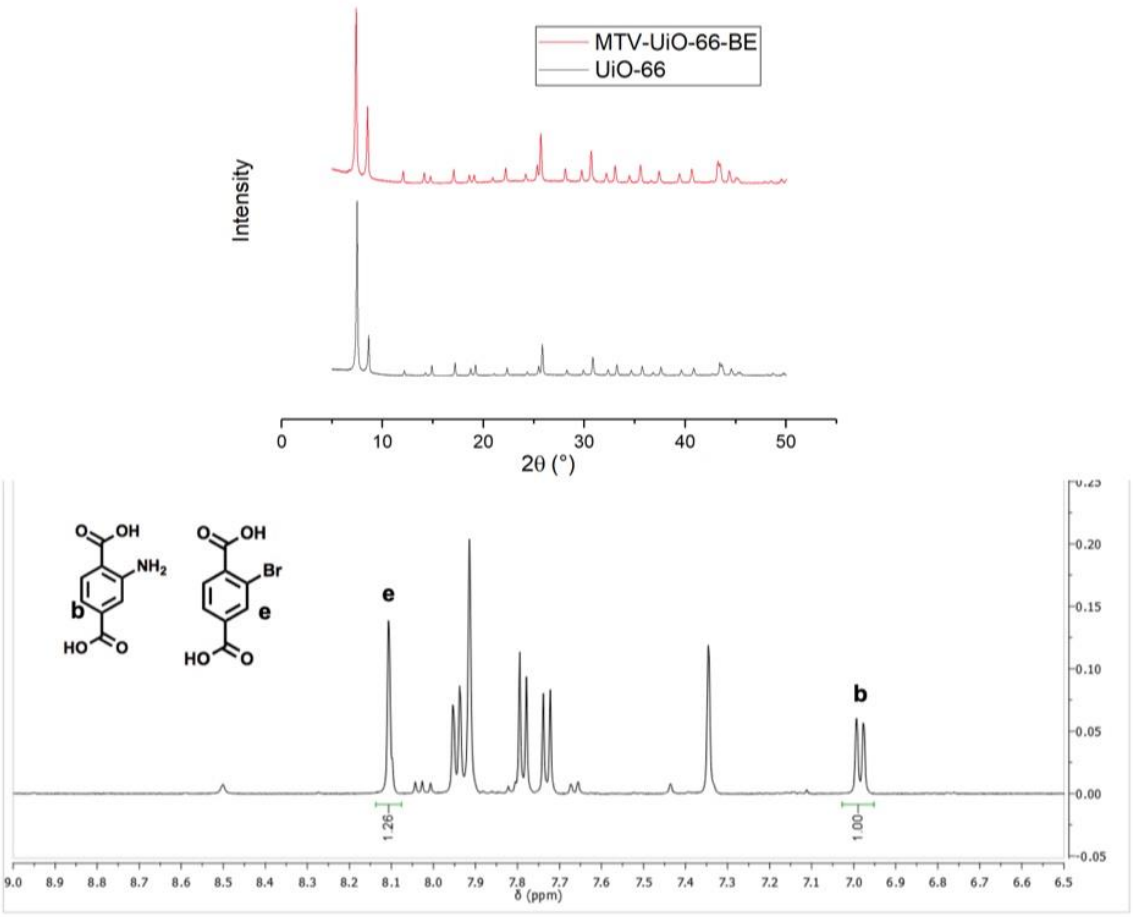

Figure 3S.12. *Top*: PXRD of MTV-UiO-66-BE. *Bottom*: ^{1}H NMR digestion of MTV-UiO-66-BE.

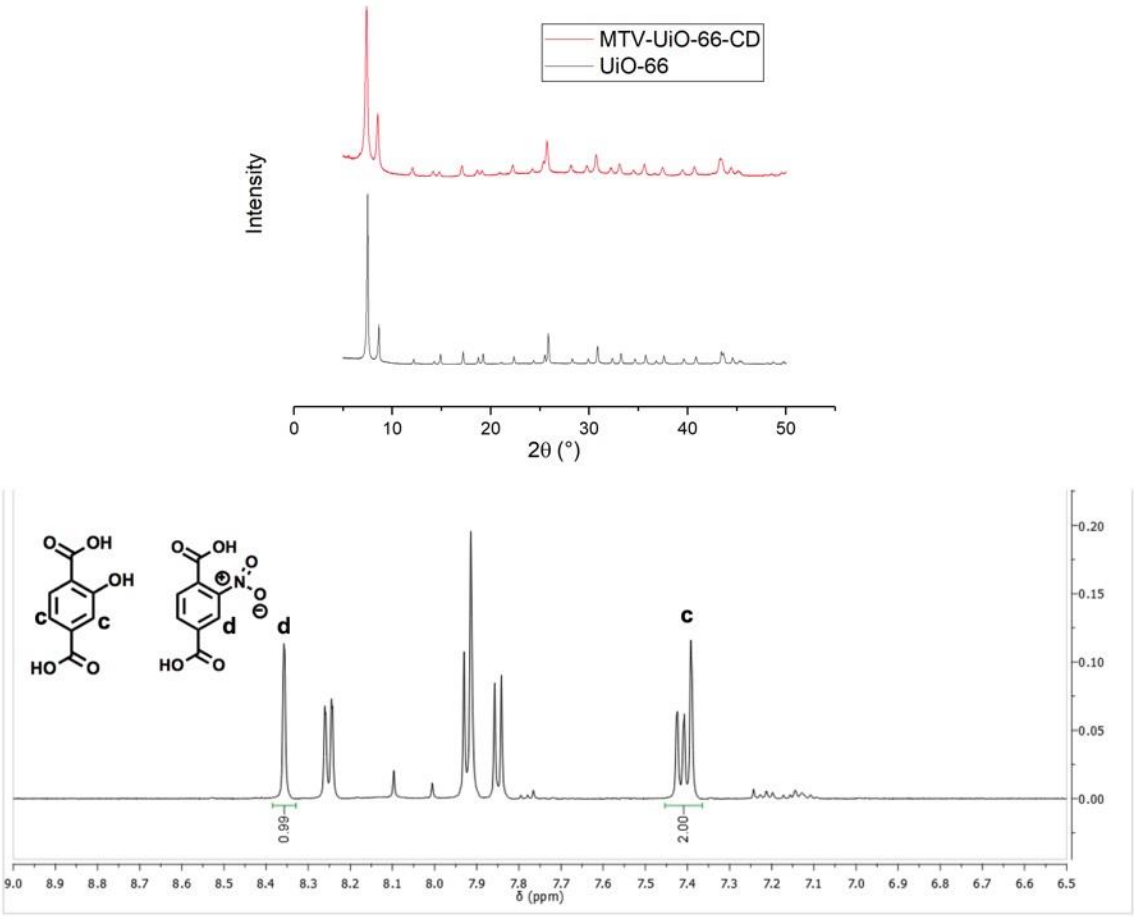

Figure 3S.13. *Top*: PXRD of MTV-UiO-66-CD. *Bottom*: ^{1}H NMR digestion of MTV-UiO-66-CD.

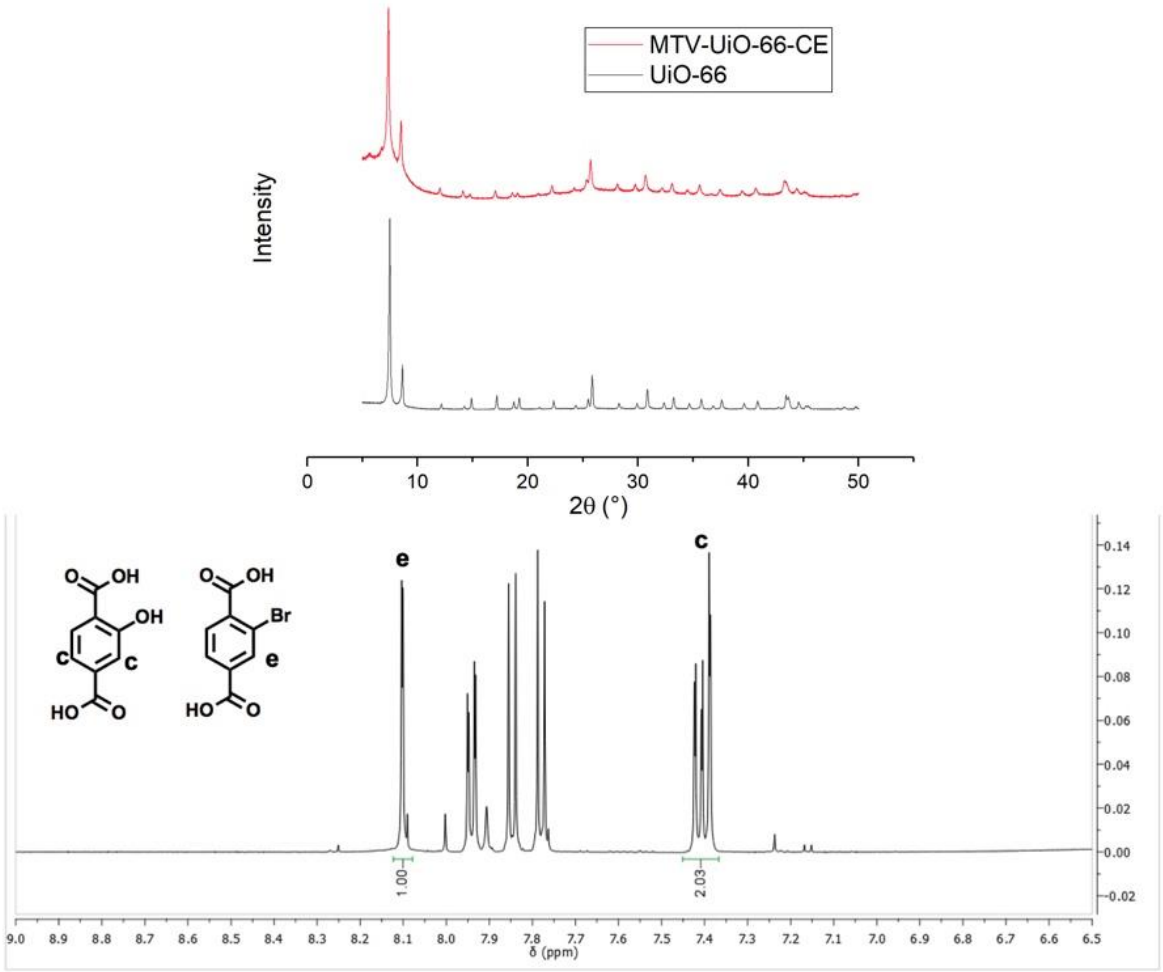

Figure 3S.14. *Top*: PXRD of MTV-UiO-66-CE. *Bottom*: ^{1}H NMR digestion of MTV-UiO-66-CE.

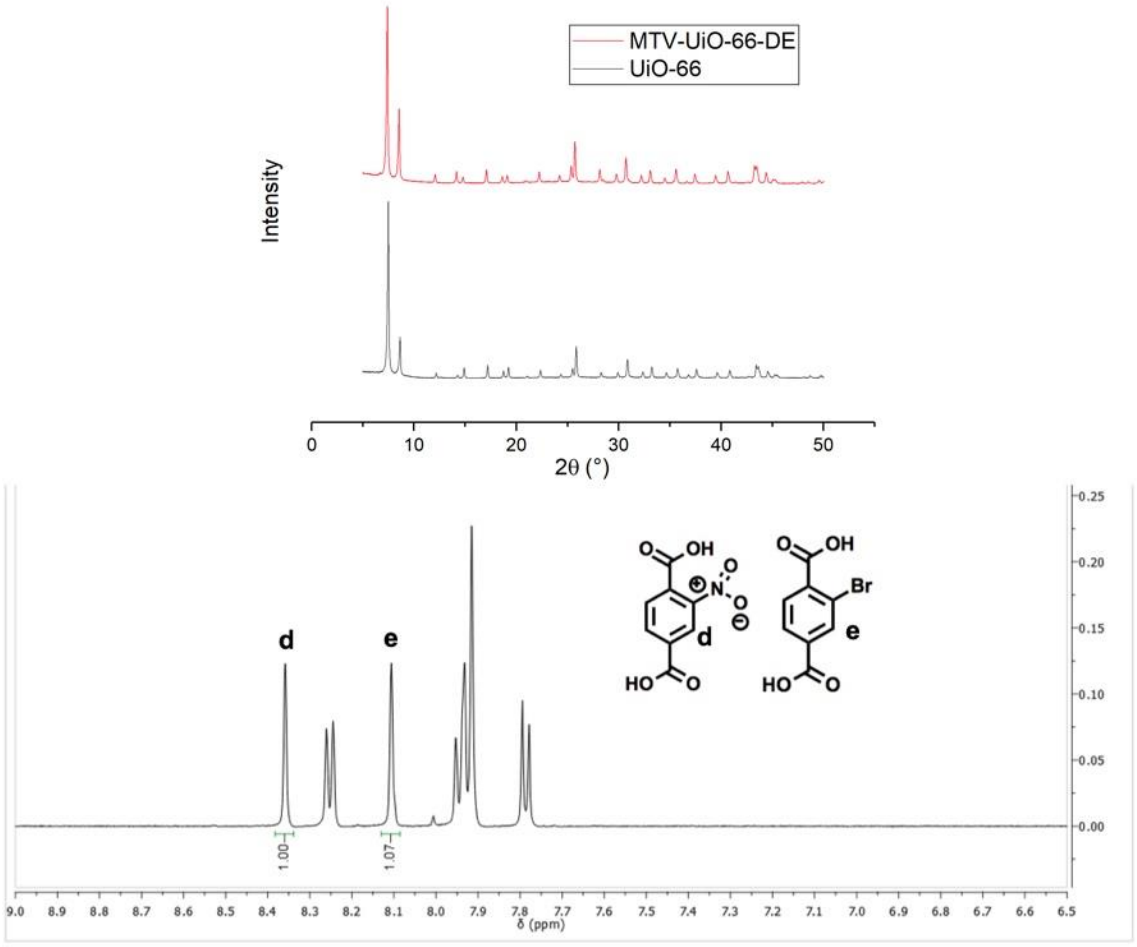

Figure 3S.15. *Top*: PXRD of MTV-UiO-66-DE. *Bottom*: ^{1}H NMR digestion of MTV-UiO-66-DE.

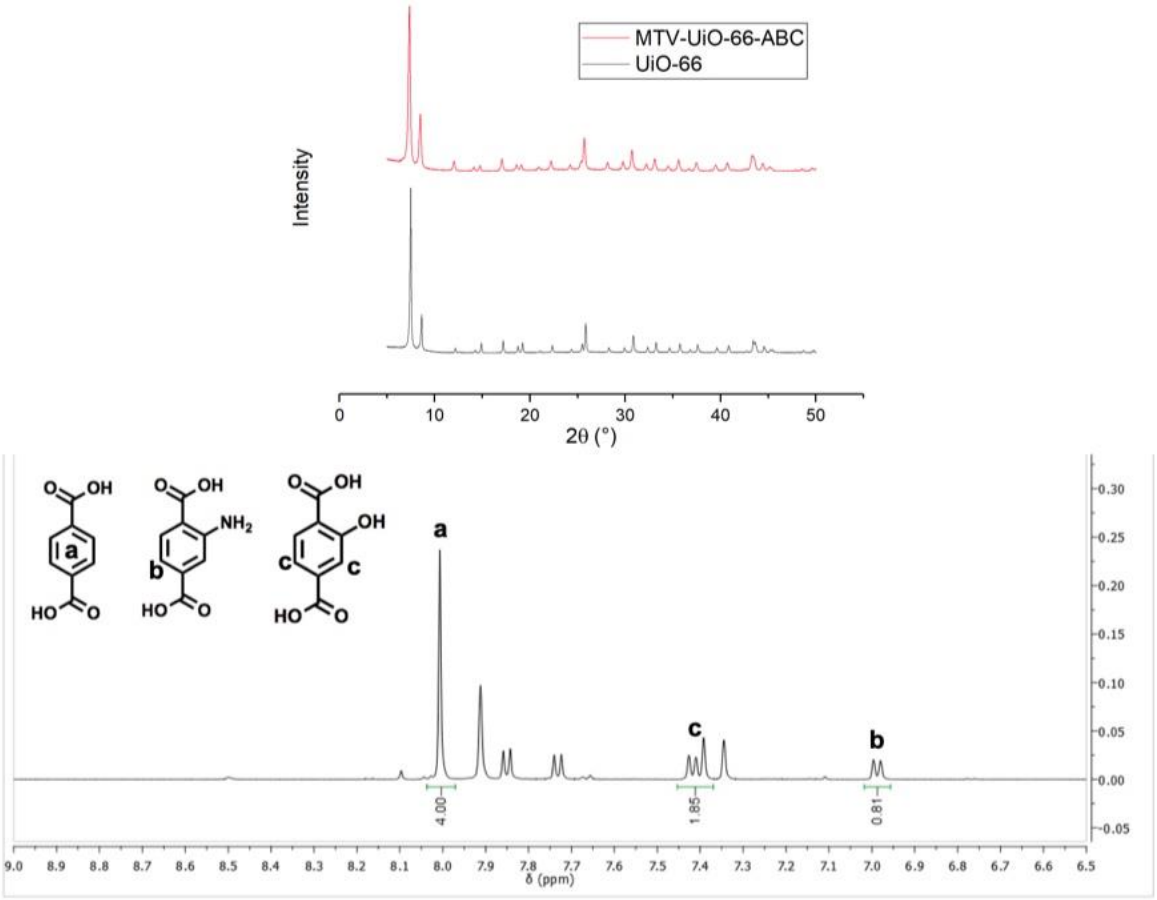

Figure 3S.16. *Top*: PXRD of MTV-UiO-66-ABC. *Bottom*: ^{1}H NMR digestion of MTV-UiO-66-ABC.

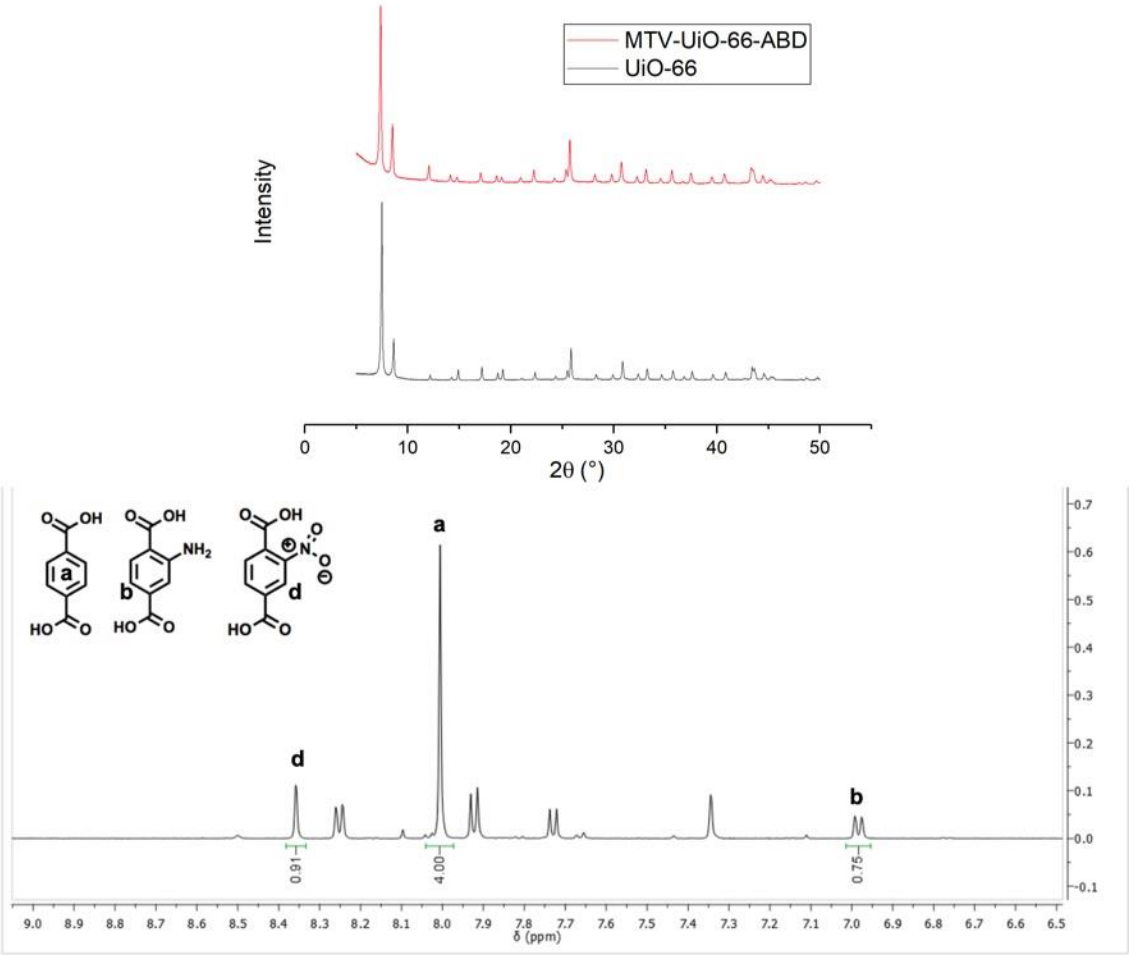

Figure 3S.17. *Top*: PXRD of MTV-UiO-66-ABD. *Bottom*: ^{1}H NMR digestion of MTV-UiO-66-ABD.

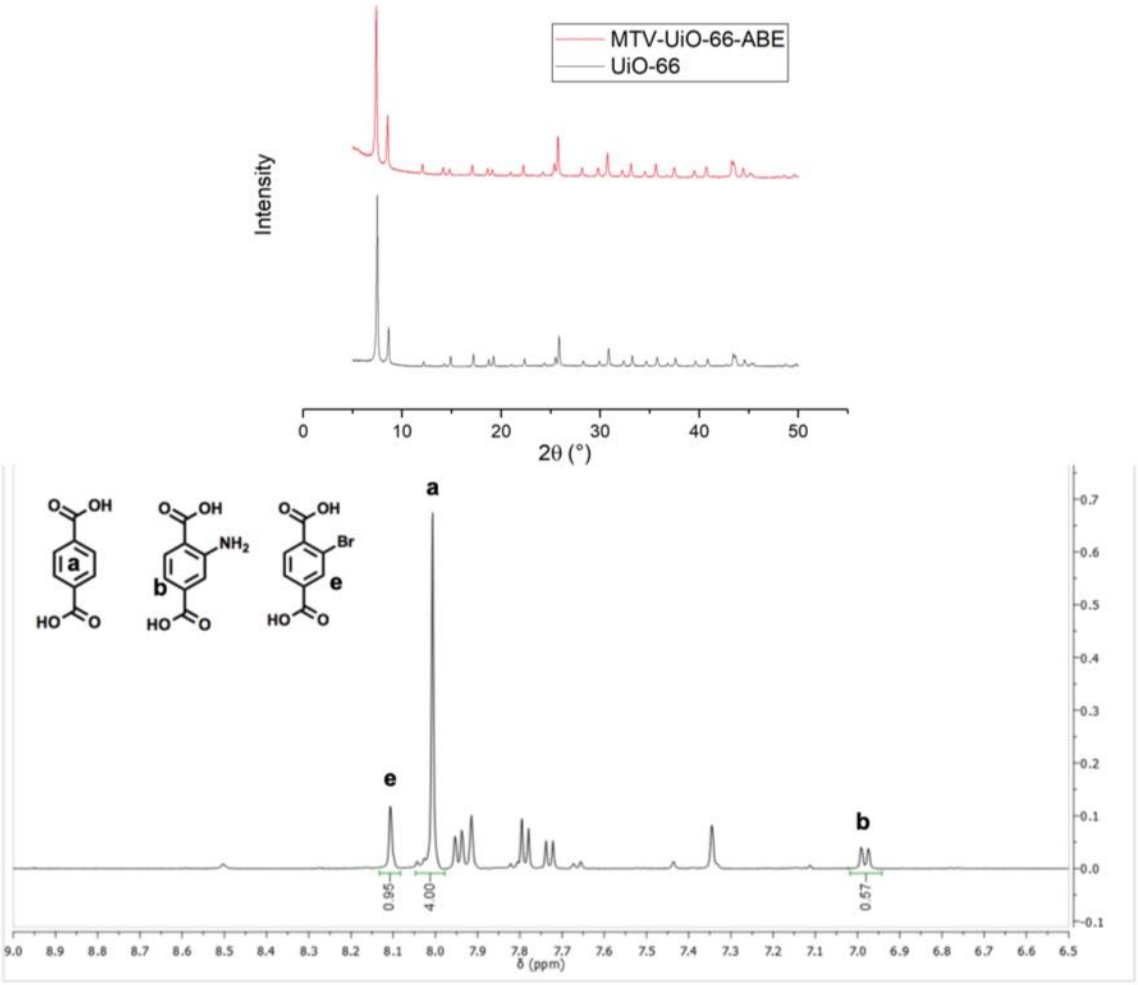

Figure 3S.18. *Top*: PXRD of MTV-UiO-66-ABE. *Bottom*: ^{1}H NMR digestion of MTV-UiO-66-ABE.

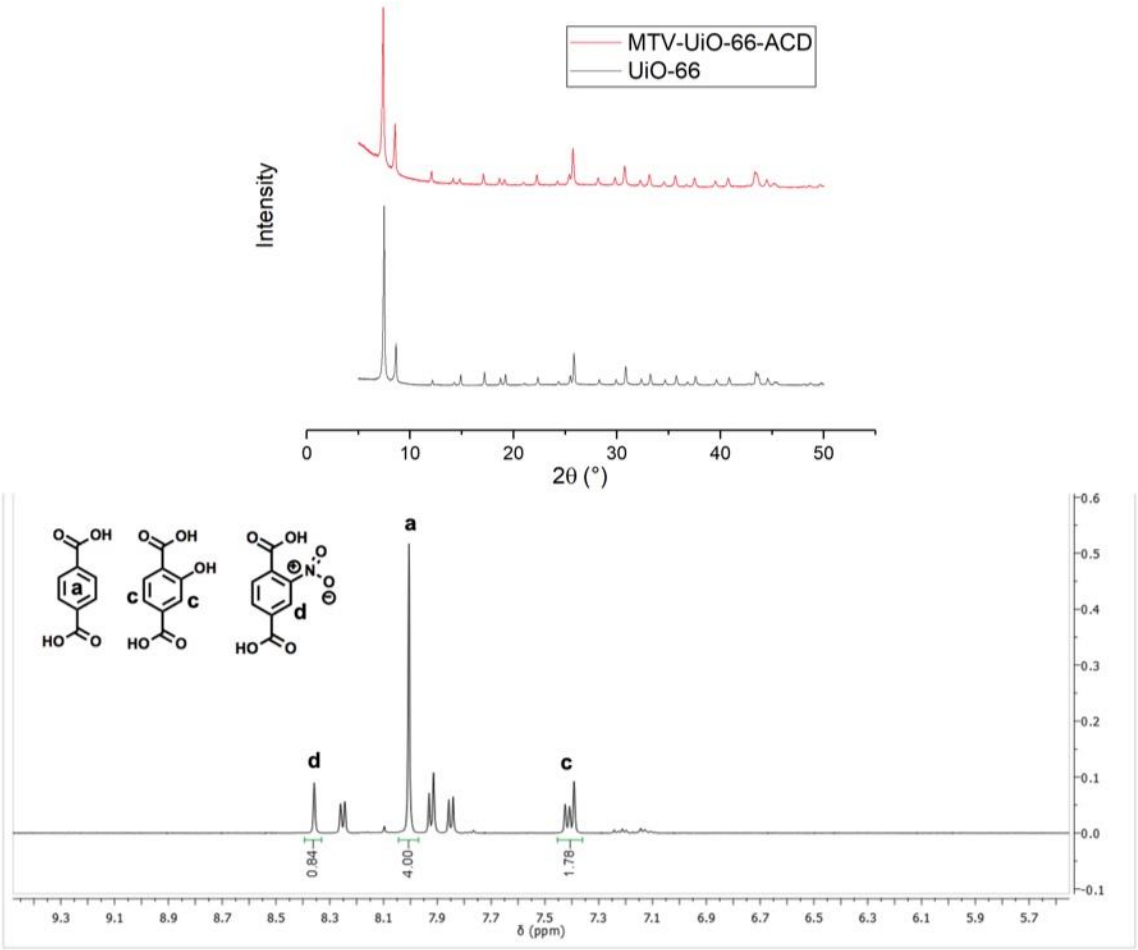

Figure 3S.19. *Top*: PXRD of MTV-UiO-66-ACD. *Bottom*: ^{1}H NMR digestion of MTV-UiO-66-ACD.

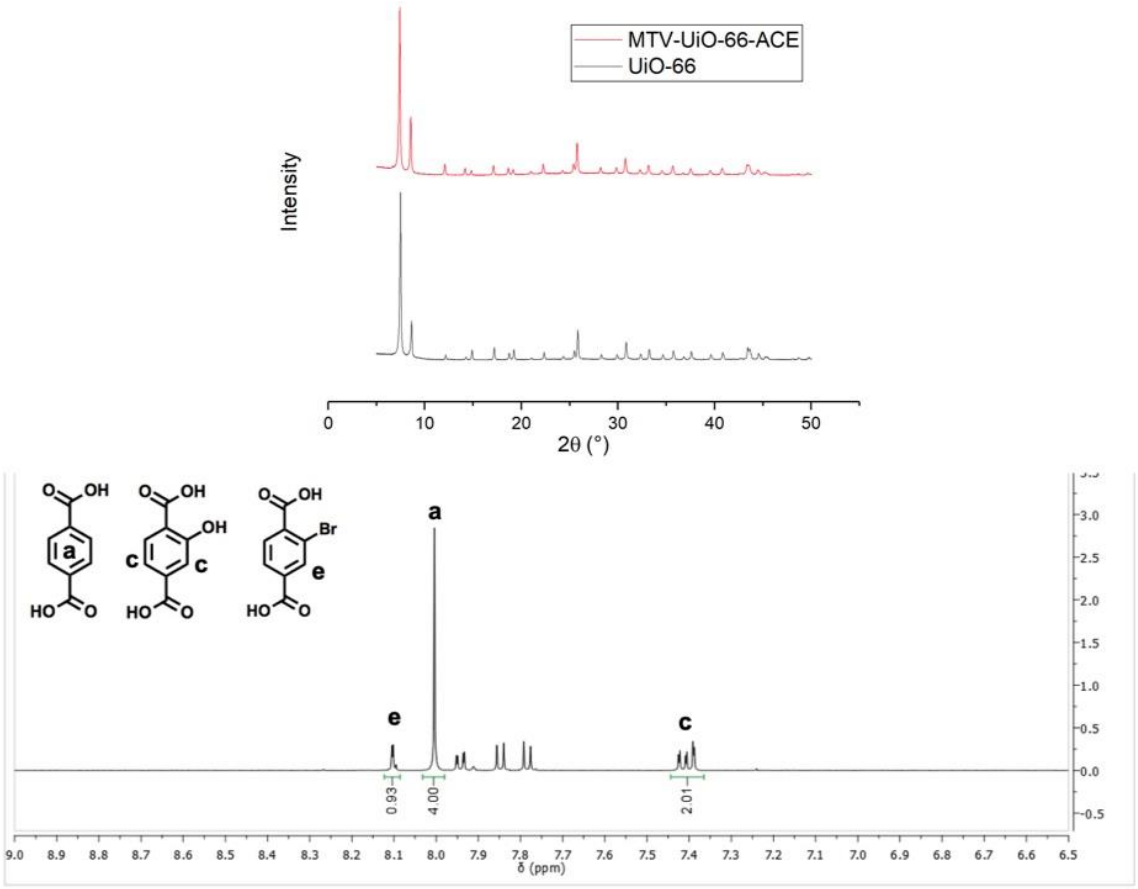

Figure 3S.20. *Top*: PXRD of MTV-UiO-66-ACE. *Bottom*: ^{1}H NMR digestion of MTV-UiO-66-ACE.

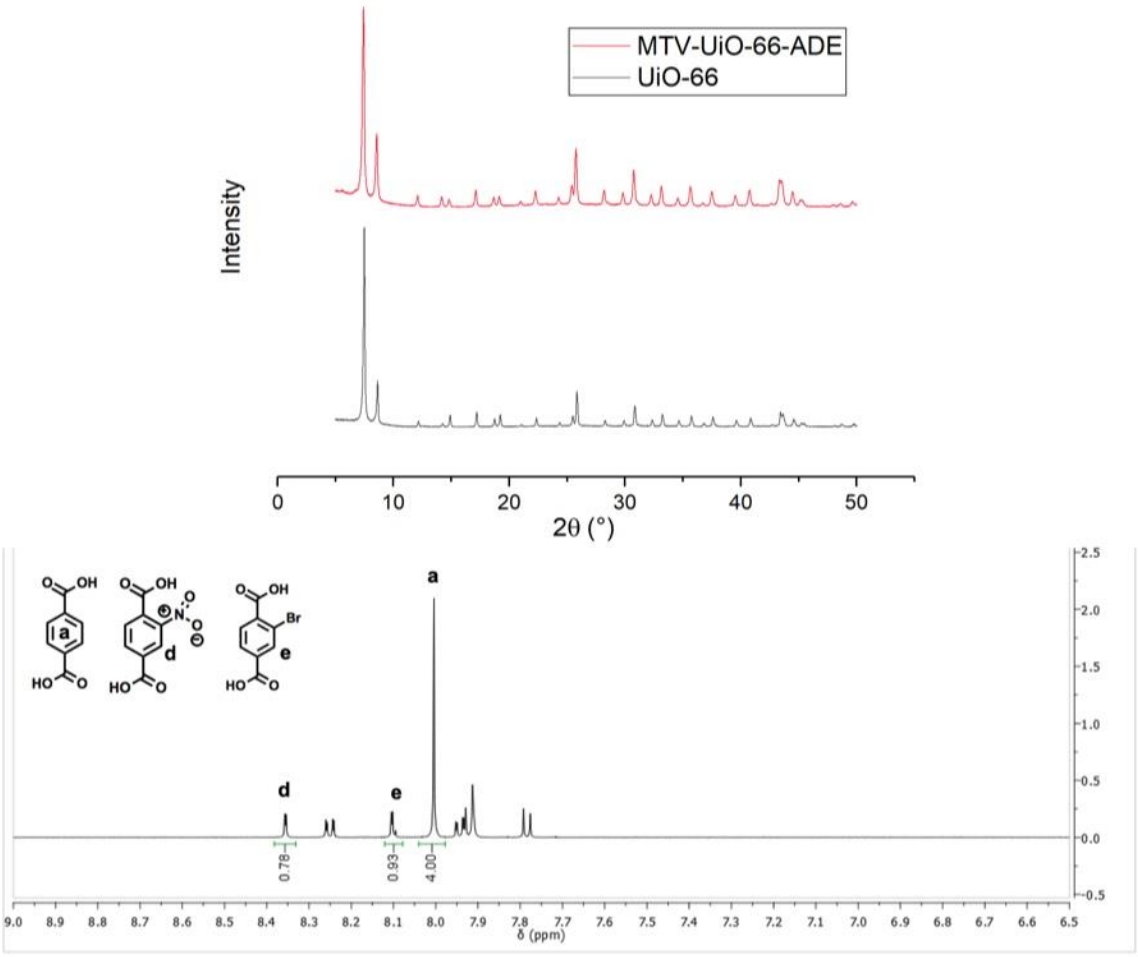

Figure 3S.21. *Top*: PXRD of MTV-UiO-66-ADE. *Bottom*: ^{1}H NMR digestion of MTV-UiO-66-ADE.

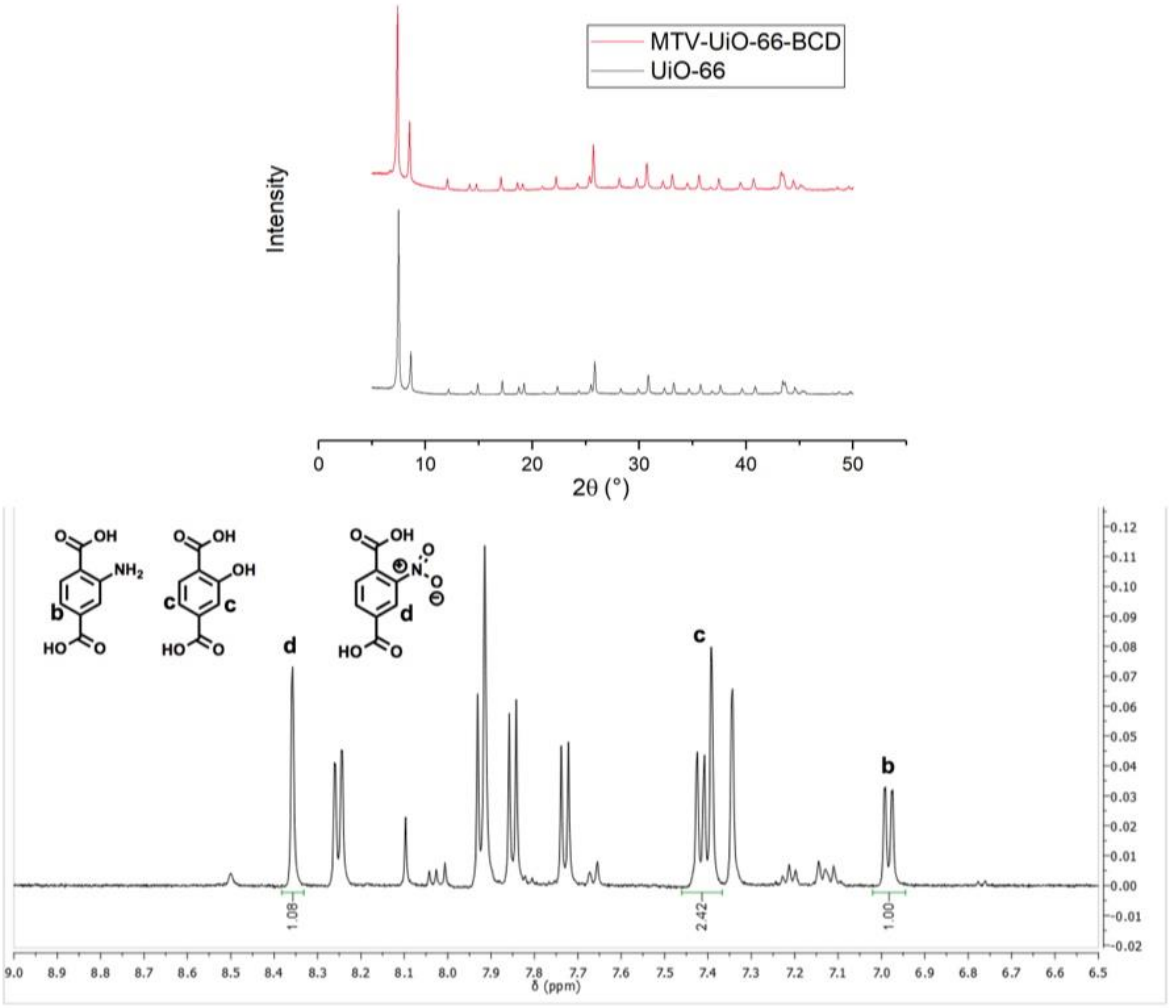

Figure 3S.22. *Top*: PXRD of MTV-UiO-66-BCD. *Bottom*: ^{1}H NMR digestion of MTV-UiO-66-BCD.

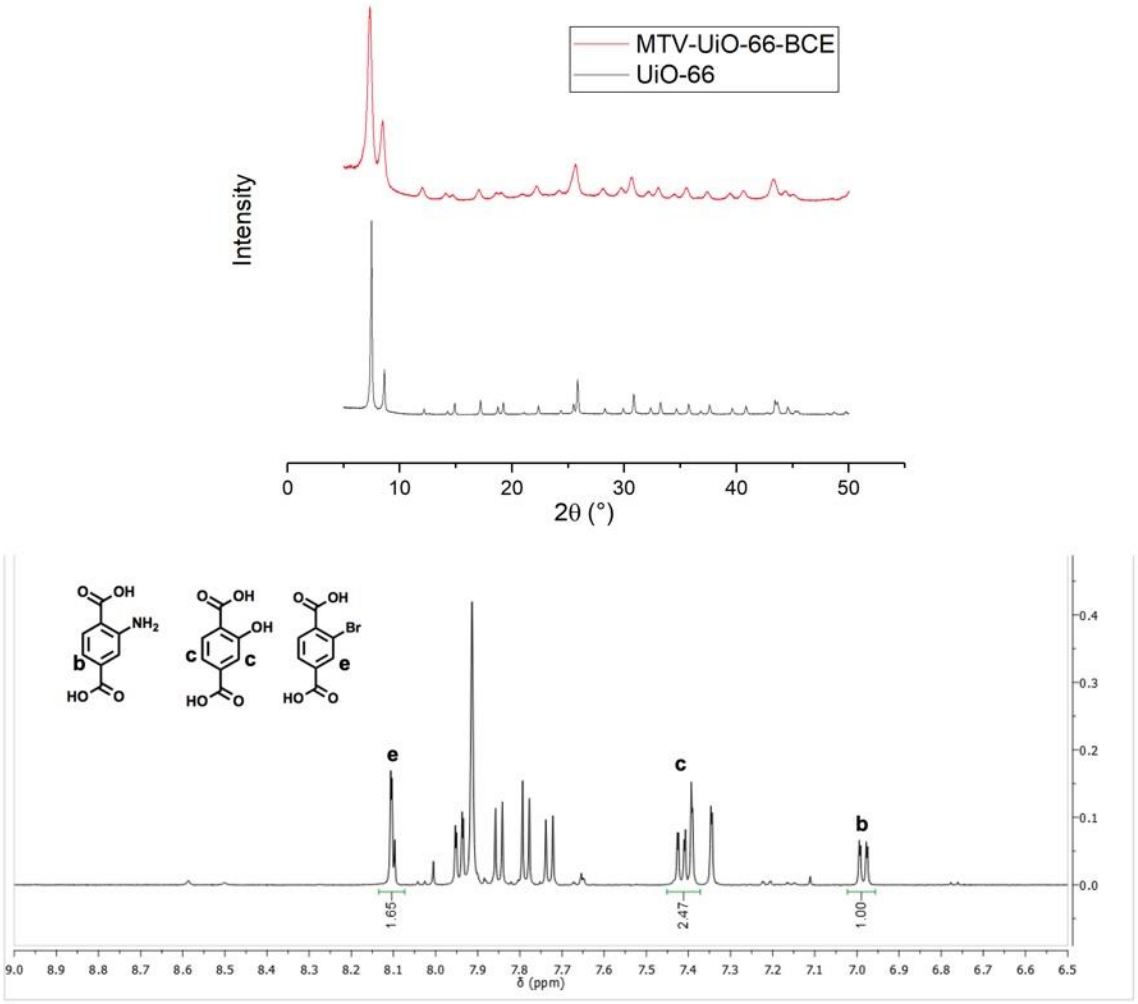

Figure 3S.23. *Top*: PXRD of MTV-UiO-66-BCE. *Bottom*: ^{1}H NMR digestion of MTV-UiO-66-BCE.

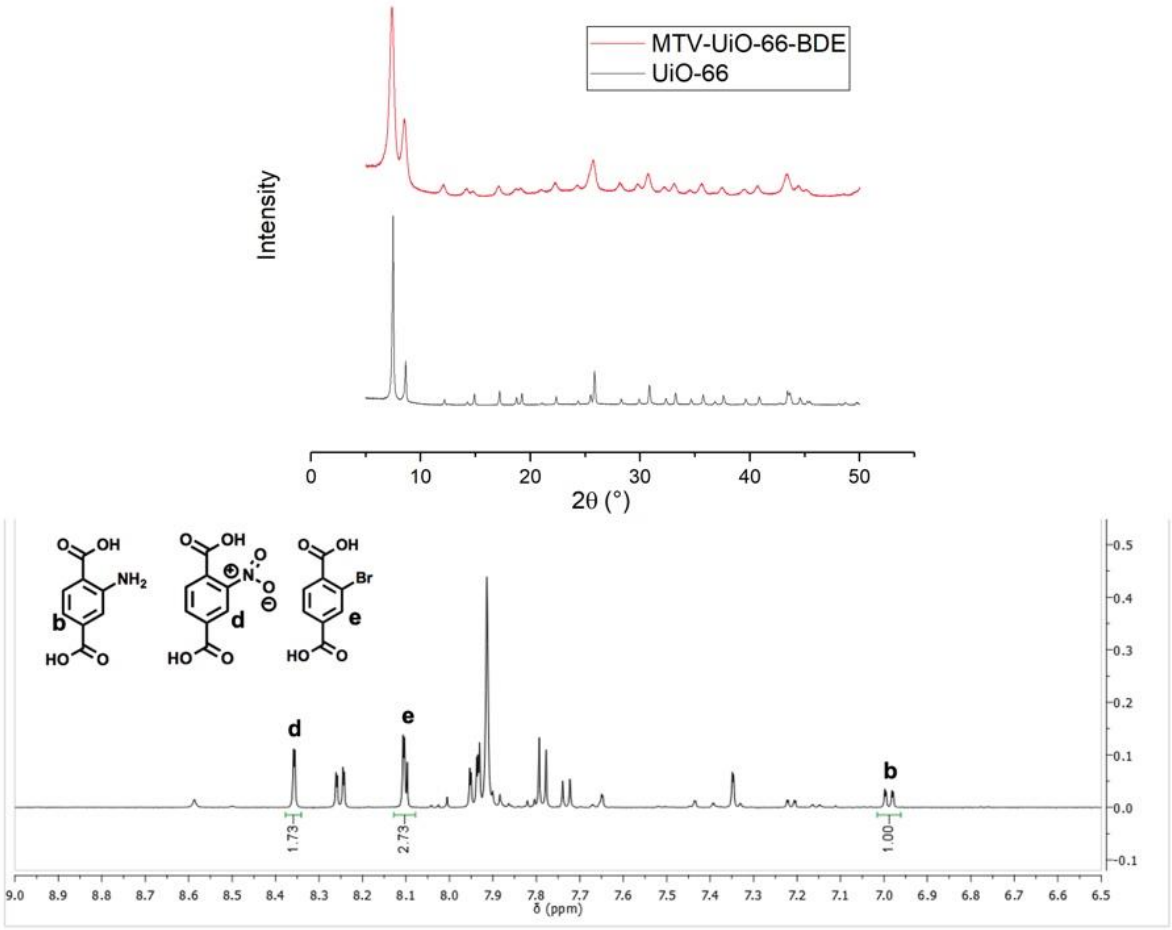

Figure 3S.24. *Top*: PXRD of MTV-UiO-66-BDE. *Bottom*: ^{1}H NMR digestion of MTV-UiO-66-BDE.

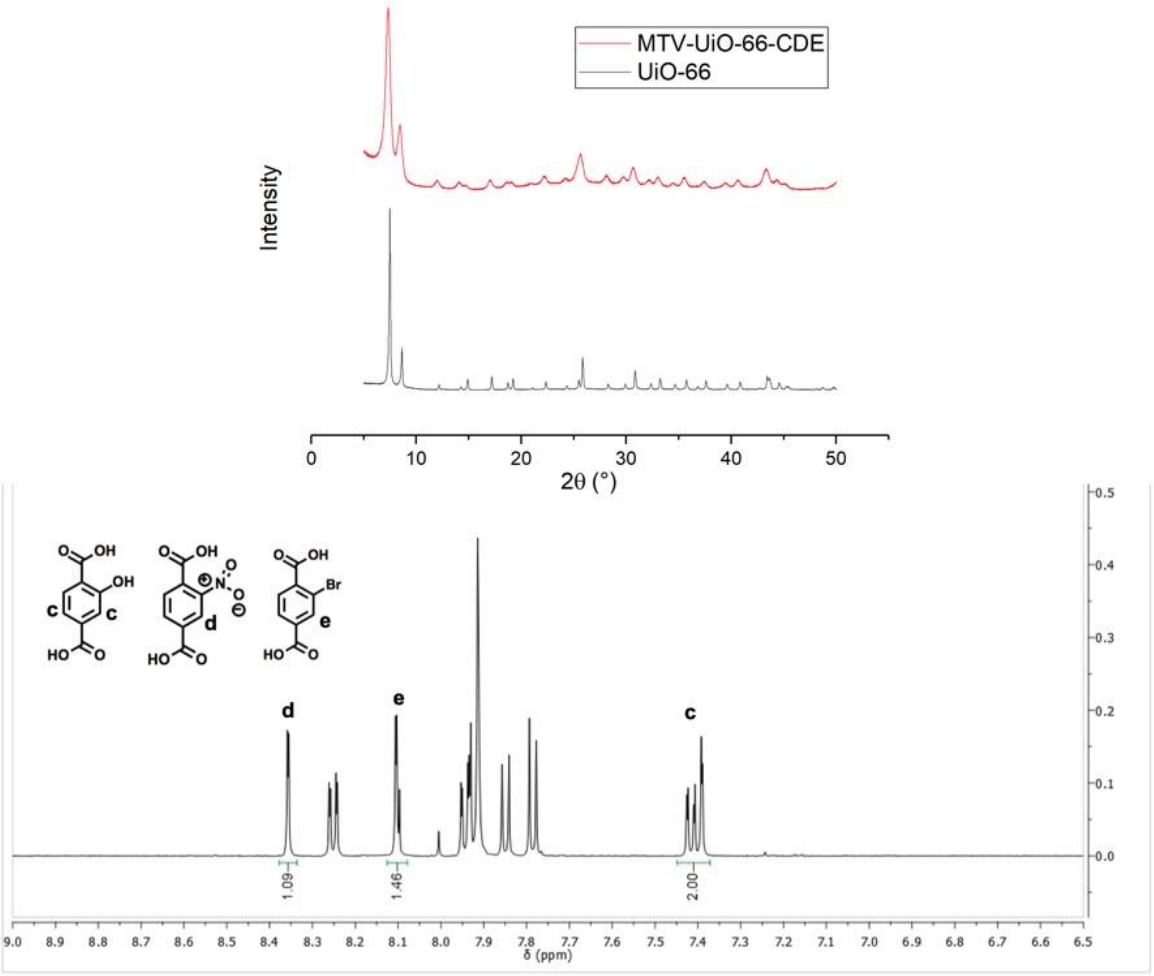

Figure 3S.25. *Top*: PXRD of MTV-UiO-66-CDE. *Bottom*: ^{1}H NMR digestion of MTV-UiO-66-CDE.

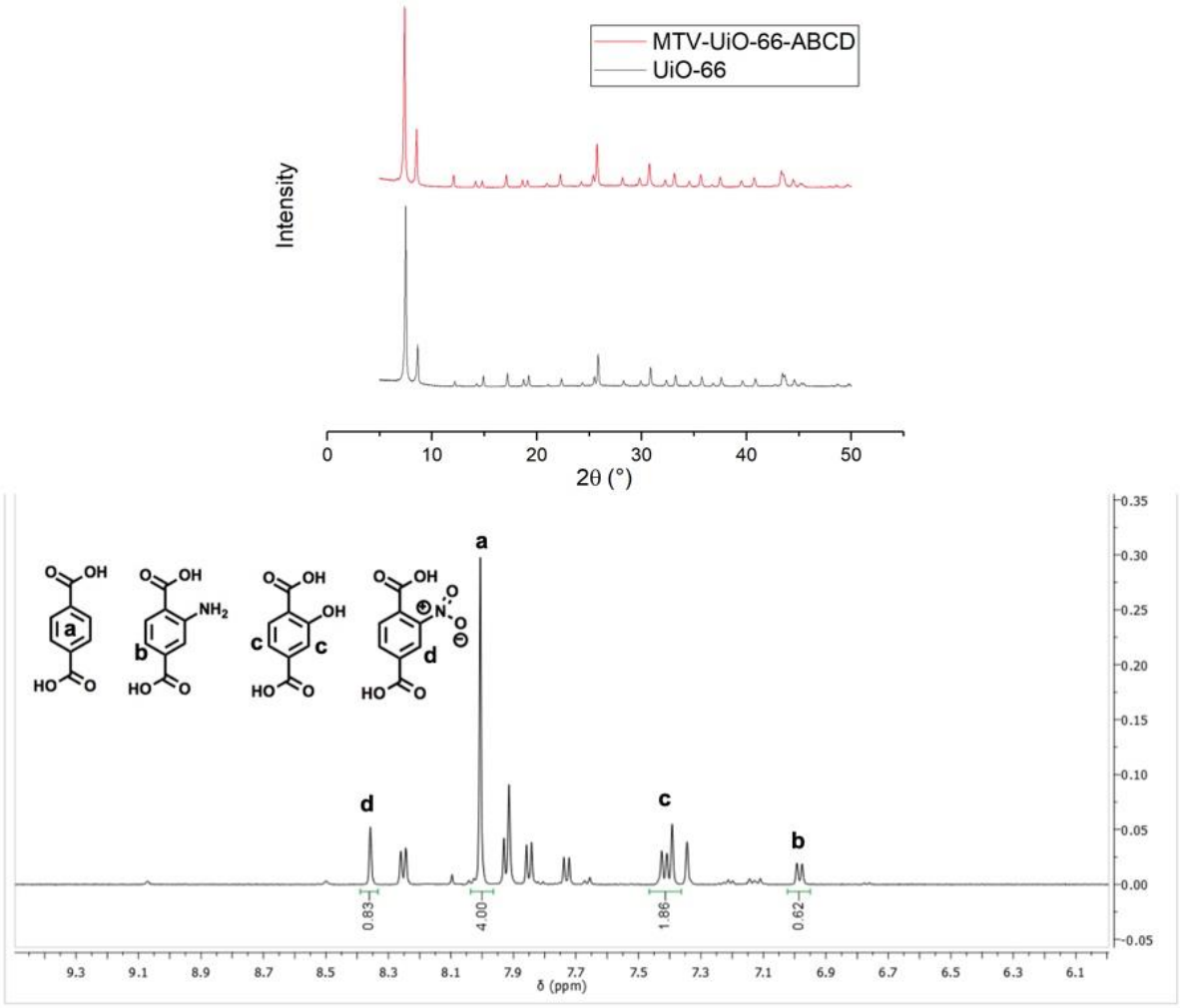

Figure 3S.26. *Top*: PXRD of MTV-UiO-66-ABCD. *Bottom*: ^{1}H NMR digestion of MTV-UiO-66-ABCD.

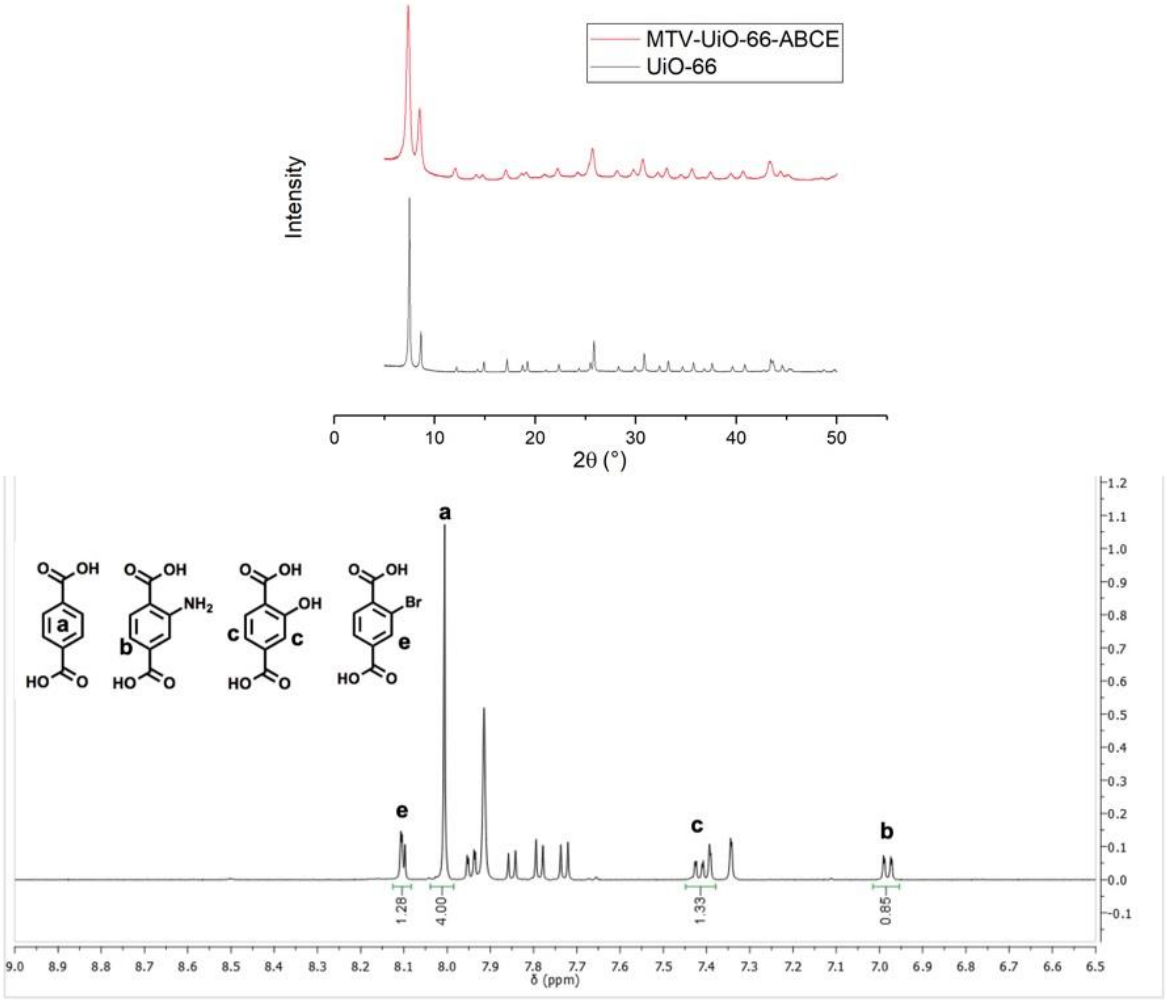

Figure 3S.27. *Top*: PXRD of MTV-UiO-66-ABCE. *Bottom*: ^{1}H NMR digestion of MTV-UiO-66-ABCE.

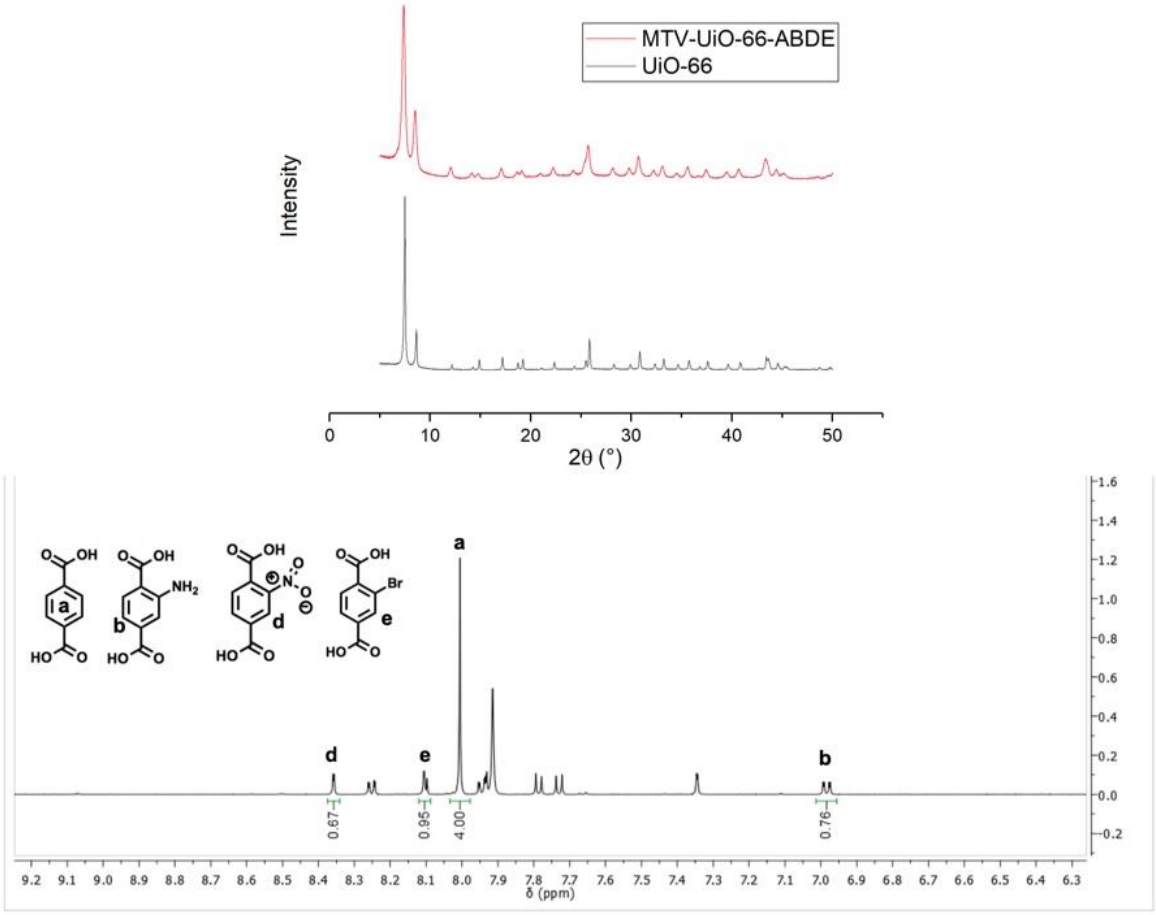

Figure 3S.28. *Top*: PXRD of MTV-UiO-66-ABDE. *Bottom*: ^{1}H NMR digestion of MTV-UiO-66-ABDE.

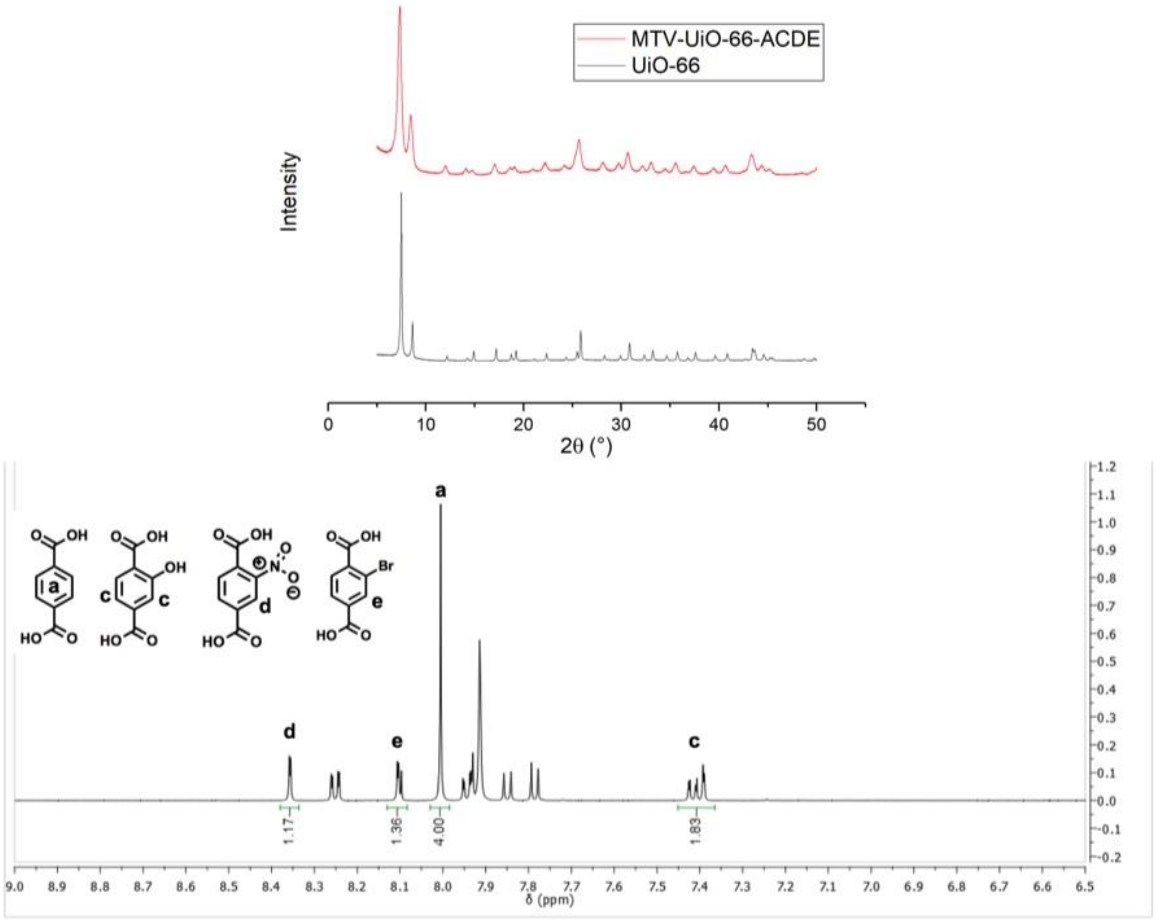

Figure 3S.29. *Top*: PXRD of MTV-UiO-66-ACDE. *Bottom*: ^{1}H NMR digestion of MTV-UiO-66-ACDE.

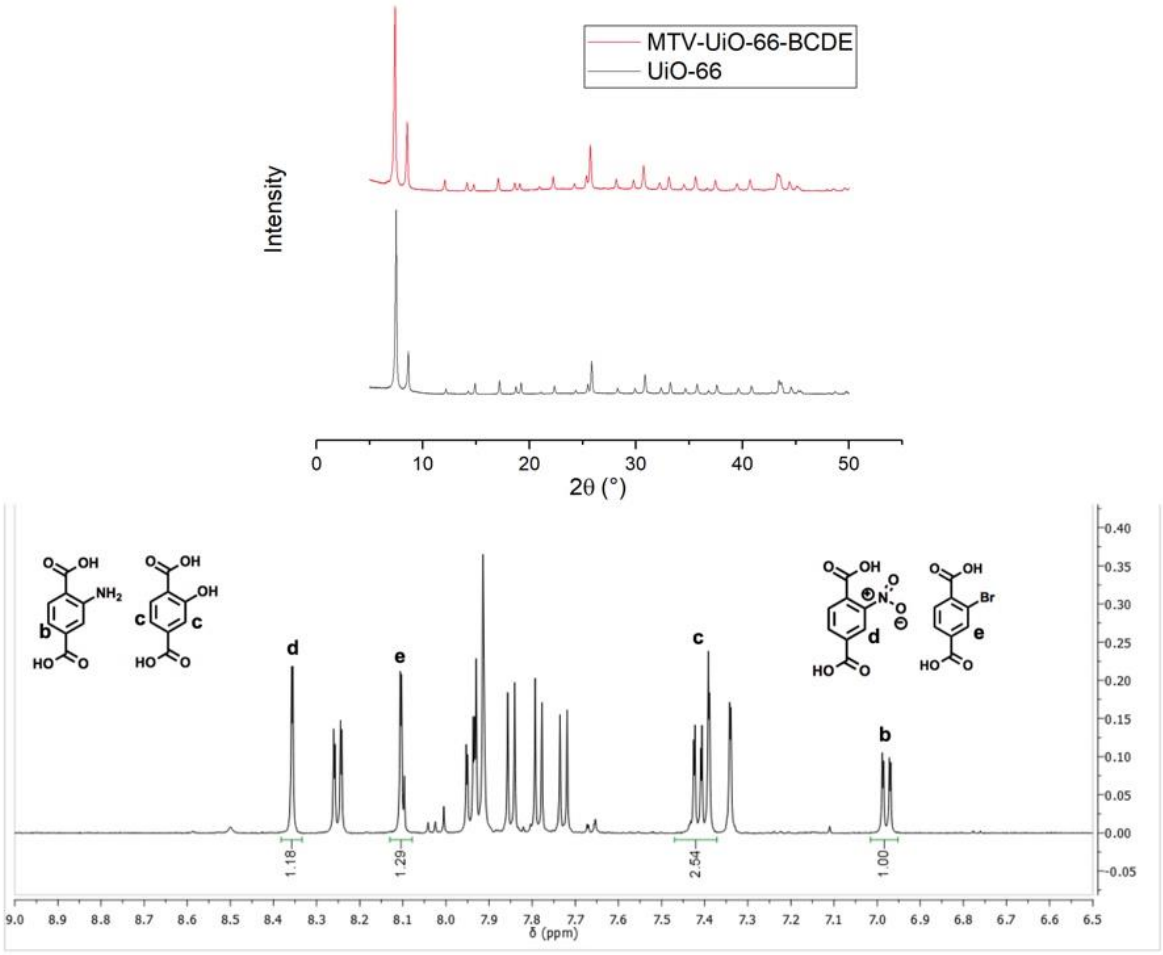

Figure 3S.30. *Top*: PXRD of MTV-UiO-66-BCDE. *Bottom*: ^{1}H NMR digestion of MTV-UiO-66-BCDE.

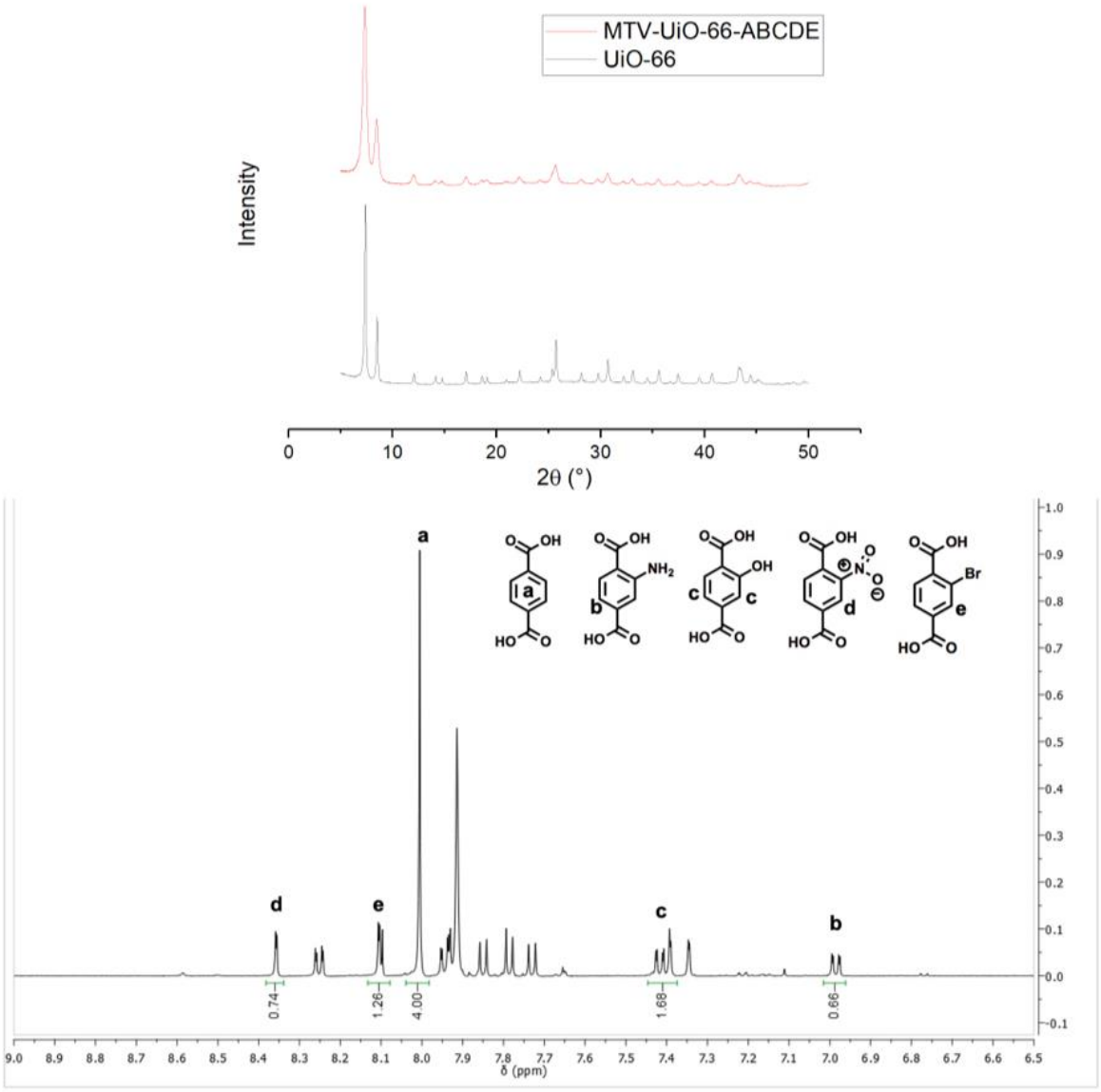

Figure 3S.31. *Top*: PXRD of MTV-UiO-66-ABCDE. *Bottom*: ^{1}H NMR digestion of MTV-UiO-66-ABCDE.

Table 3S.1. Ratio of MOF ligands determined by ^{1}H NMR and their respective stoichiometry in parentheses. The ratios are normalized to a value of one.

MTV-UiO-66 MOF	(A) BDC	(B) NH_2-BDC	(C) OH-BDC	(D) NO_2-BDC	(E) Br-BDC
A	1.00 (1)	N/A	N/A	N/A	N/A
B	N/A	1.00 (1)	N/A	N/A	N/A
C	N/A	N/A	1.00 (1)	N/A	N/A
D	N/A	N/A	N/A	1.00 (1)	N/A
E	N/A	N/A	N/A	N/A	1.00 (1)
AB	0.45 (1)	0.55 (1)	N/A	N/A	N/A
AC	0.50 (1)	N/A	0.50 (1)	N/A	N/A
AD	0.58 (1)	N/A	N/A	0.42 (1)	N/A
AE	0.49 (1)	N/A	N/A	N/A	0.51 (1)
BC	N/A	0.44 (1)	0.56 (1)	N/A	N/A
BD	N/A	0.49 (1)	N/A	0.51 (1)	N/A
BE	N/A	0.44 (1)	N/A	N/A	0.56 (1)
CD	N/A	N/A	0.50 (1)	0.50 (1)	N/A
CE	N/A	N/A	0.51 (1)	N/A	0.49 (1)
DE	N/A	N/A	N/A	0.48 (1)	0.52 (1)
ABC	0.36 (1)	0.30 (1)	0.34 (1)	N/A	N/A
ABD	0.38 (1)	0.28 (1)	N/A	0.34 (1)	N/A
ABE	0.40 (1)	0.23 (1)	N/A	N/A	0.37 (1)
ACD	0.36 (1)	N/A	0.33 (1)	0.31 (1)	N/A

ACE	0.34 (1)	N/A	0.34 (1)	N/A	0.32 (1)
ADE	0.37 (1)	N/A	N/A	0.29 (1)	0.34 (1)
BCD	N/A	0.30 (1)	0.37 (1)	0.33 (1)	N/A
BCE	N/A	0.26 (1)	0.32 (1)	N/A	0.42 (1)
BDE	N/A	0.18 (1)	N/A	0.32 (1)	0.50 (1)
CDE	N/A	N/A	0.28 (1)	0.31 (1)	0.41 (1)
ABCD	0.30 (1)	0.18 (1)	0.27 (1)	0.25 (1)	N/A
ABCE	0.26 (1)	0.22 (1)	0.18 (1)	N/A	0.34 (1)
ABDE	0.30 (1)	0.22 (1)	N/A	0.20 (1)	0.28 (1)
ACDE	0.23 (1)	N/A	0.21 (1)	0.26 (1)	0.30 (1)
BCDE	N/A	0.21 (1)	0.27 (1)	0.25 (1)	0.27 (1)
ABCDE	0.22 (1)	0.15 (1)	0.19 (1)	0.16 (1)	0.28 (1)

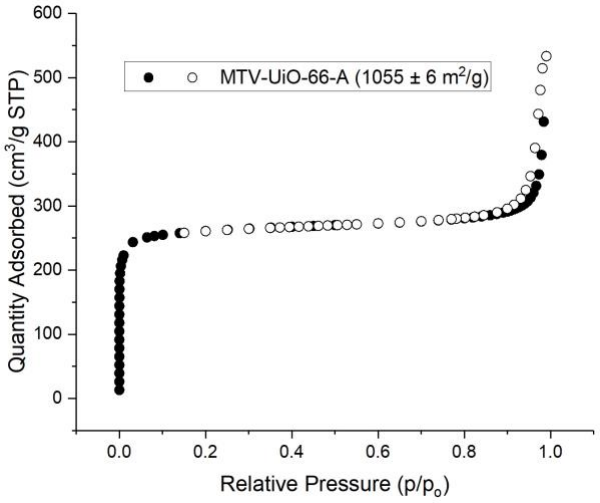

Figure 3S.32. N_2 sorption isotherm for MTV-UiO-66-A.

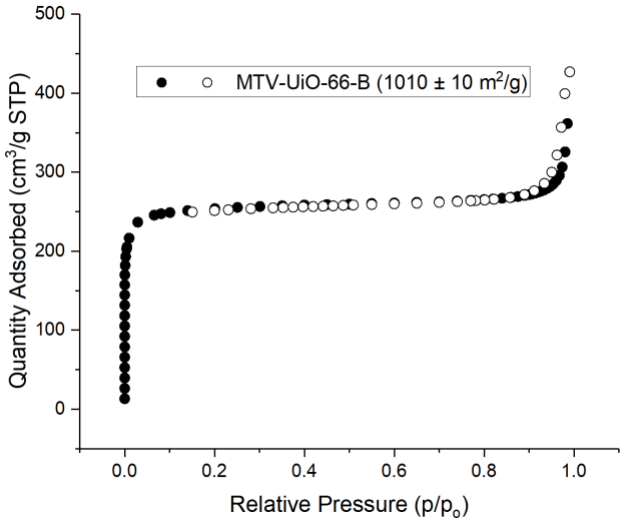

Figure 3S.33. N_2 sorption isotherm for MTV-UiO-66-B.

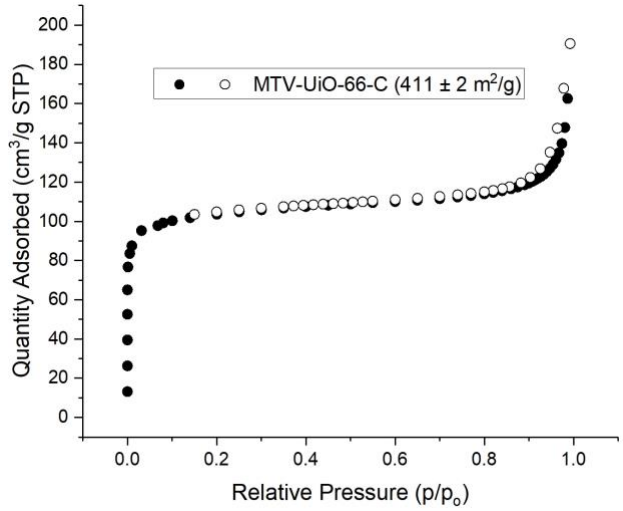

Figure 3S.34. N_2 sorption isotherm for MTV-UiO-66-C.

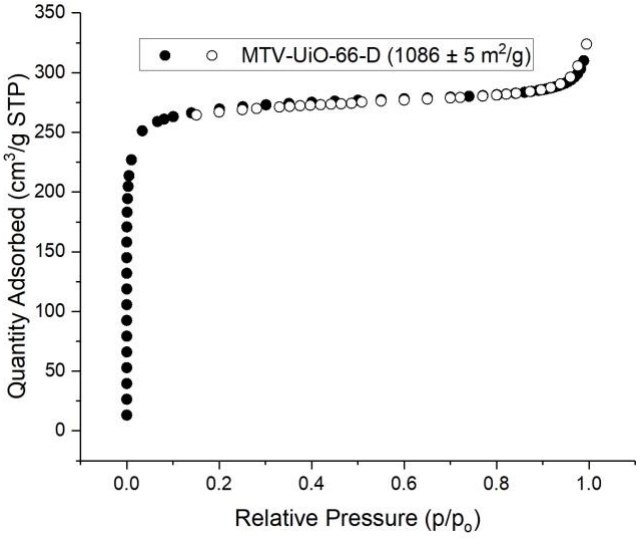

Figure 3S.35. N_2 sorption isotherm for MTV-UiO-66-D.

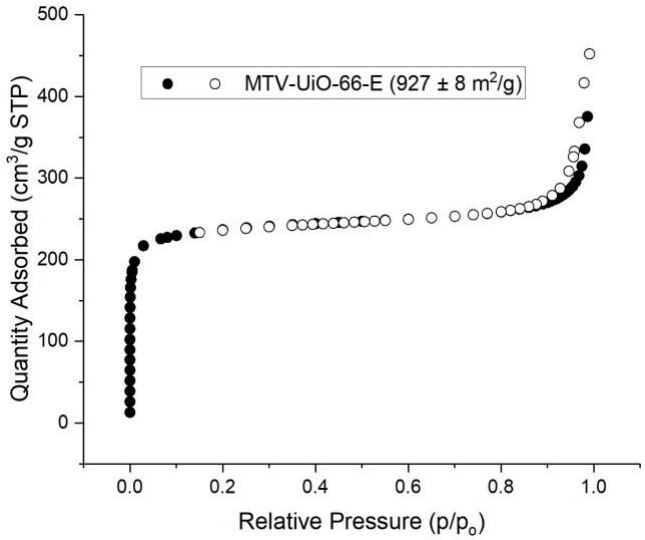

Figure 3S.36. N_2 sorption isotherm for MTV-UiO-66-E.

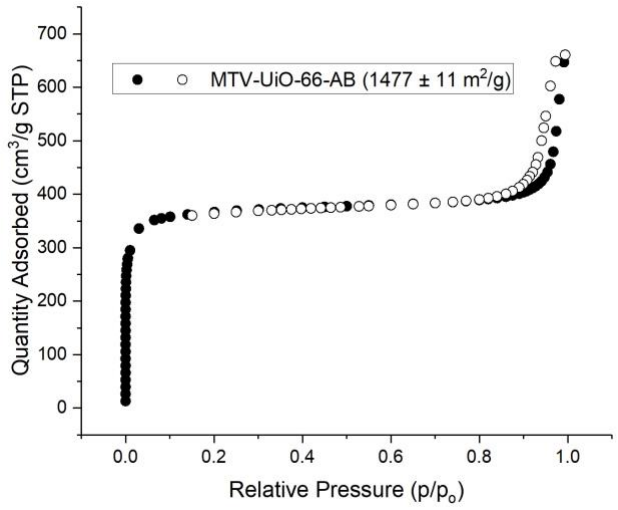

Figure 3S.37. N_2 sorption isotherm for MTV-UiO-66-AB.

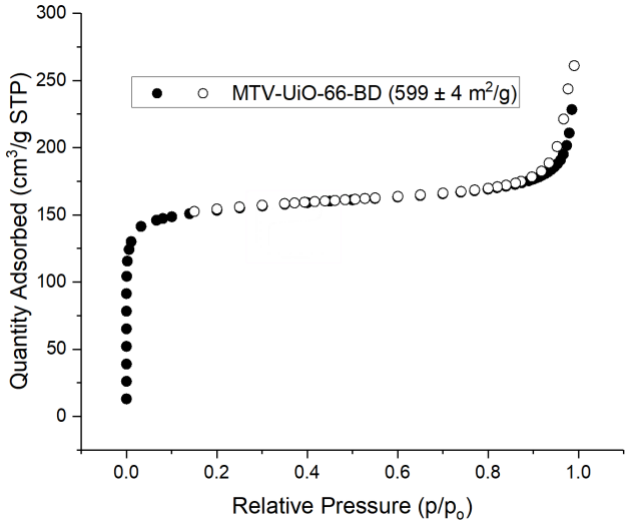

Figure 3S.38. N_2 sorption isotherm for MTV-UiO-66-BD.

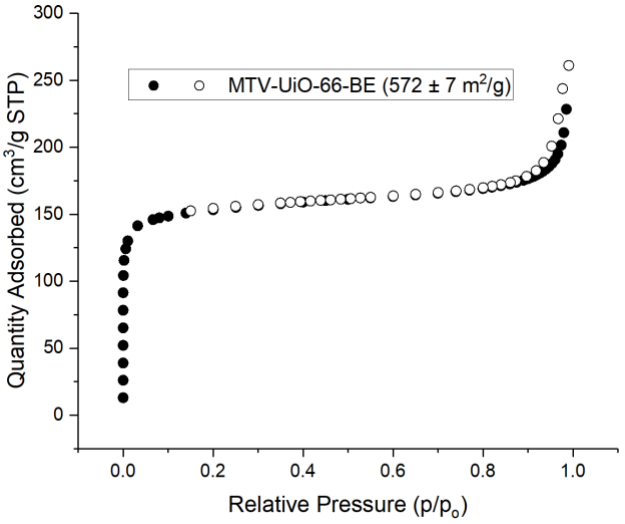

Figure 3S.39. N_2 sorption isotherm for MTV-UiO-66-BE.

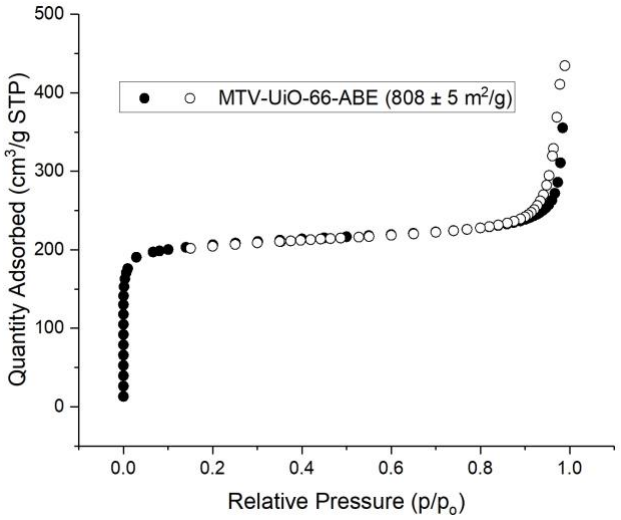

Figure 3S.40. N_2 sorption isotherm for MTV-UiO-66-ABE.

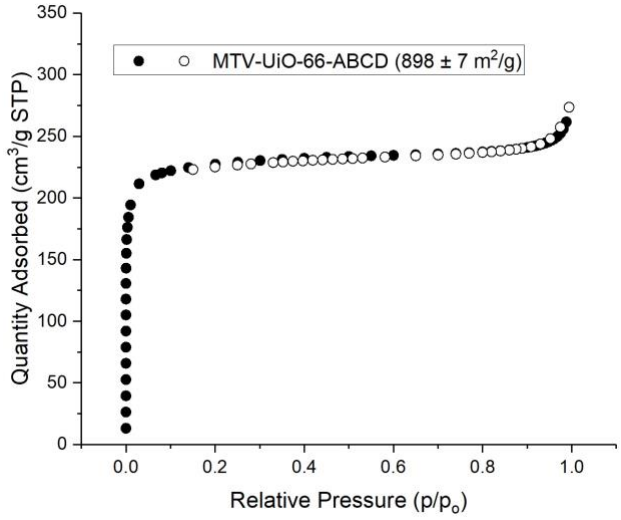

Figure 3S.41. N_2 sorption isotherm for MTV-UiO-66-ABCD.

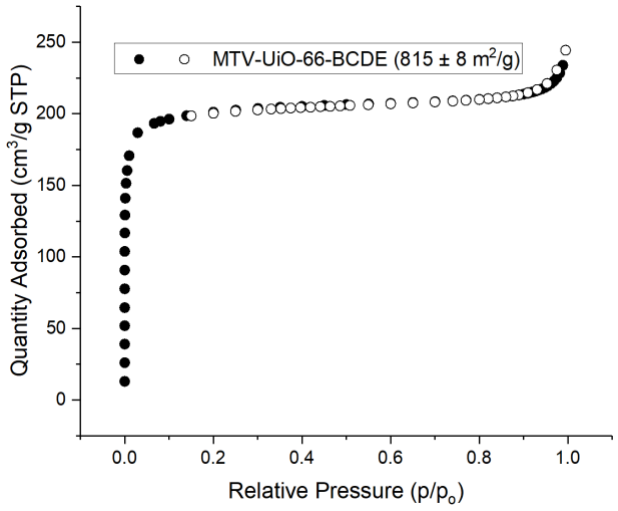

Figure 3S.42. N_2 sorption isotherm for MTV-UiO-66-BCDE.

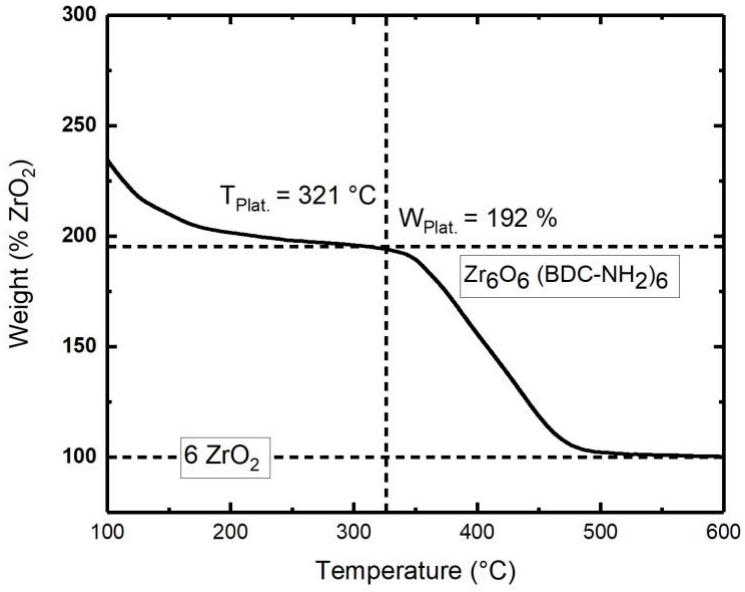

Figure 3S.43. TGA trace for MTV-UiO-66-B.

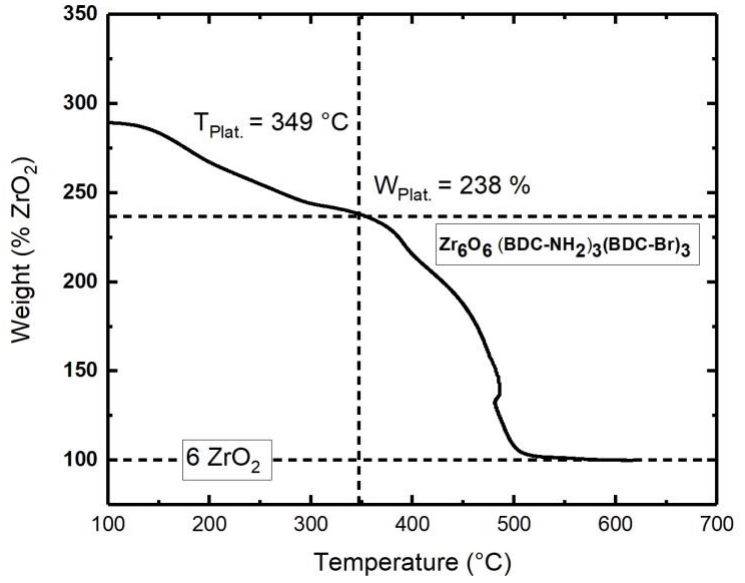

Figure 3S.44. TGA trace for MTV-UiO-66-BE.

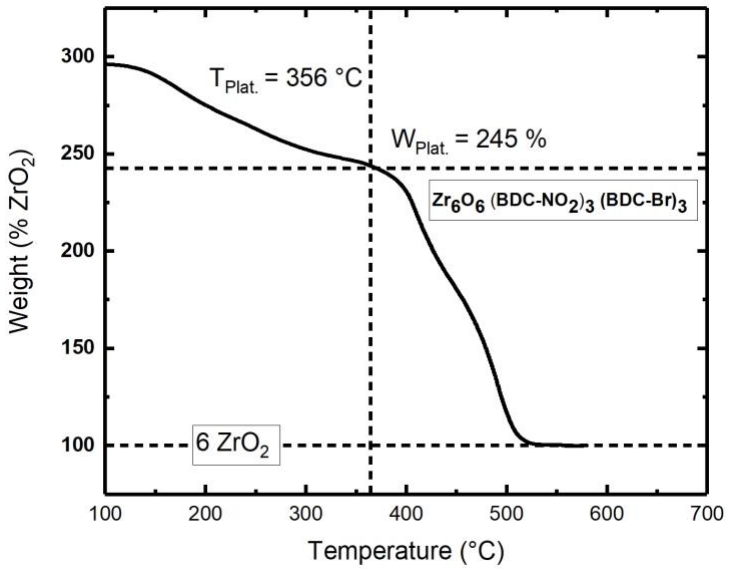

Figure 3S.45. TGA trace for MTV-UiO-66-DE.

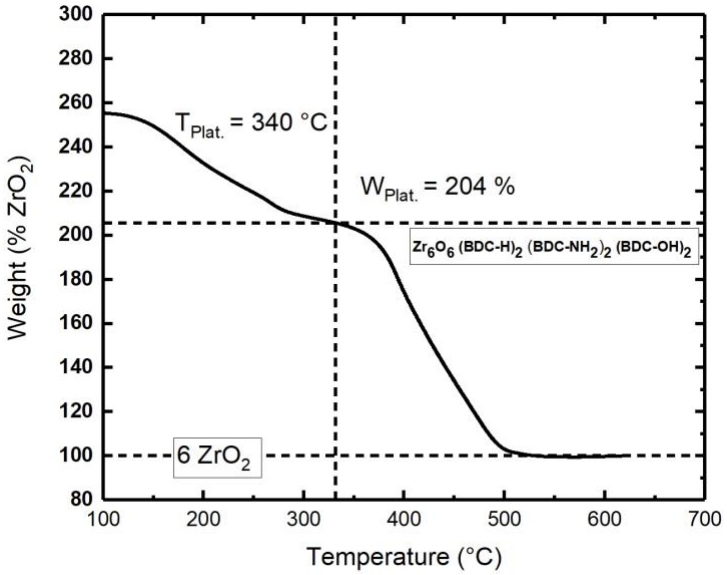

Figure 3S.46. TGA trace for MTV-UiO-66-ABC.

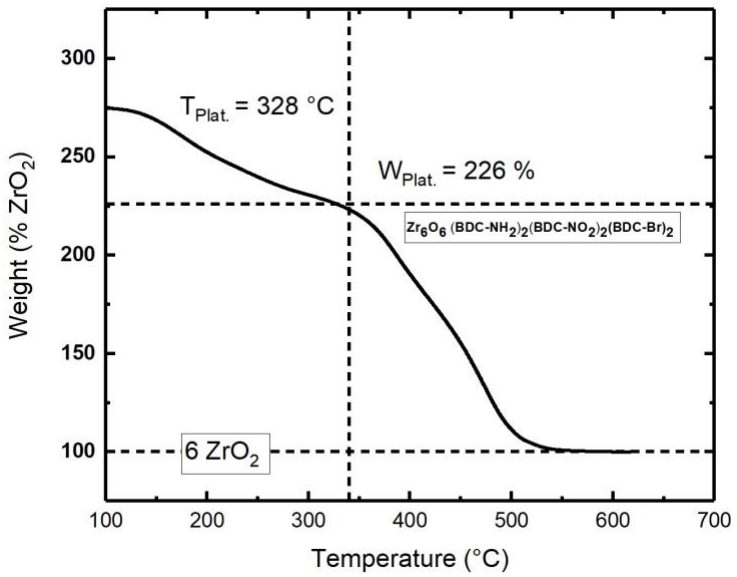

Figure 3S.47. TGA trace for MTV-UiO-66-BDE.

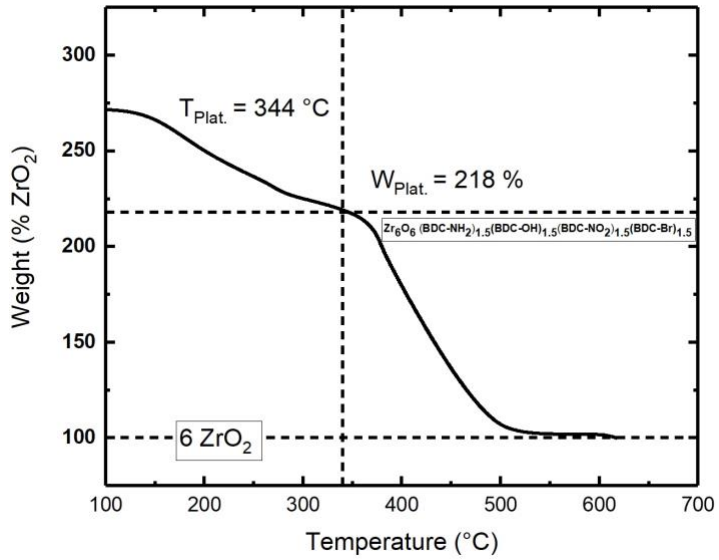

Figure 3S.48. TGA trace for MTV-UiO-66-BCDE.

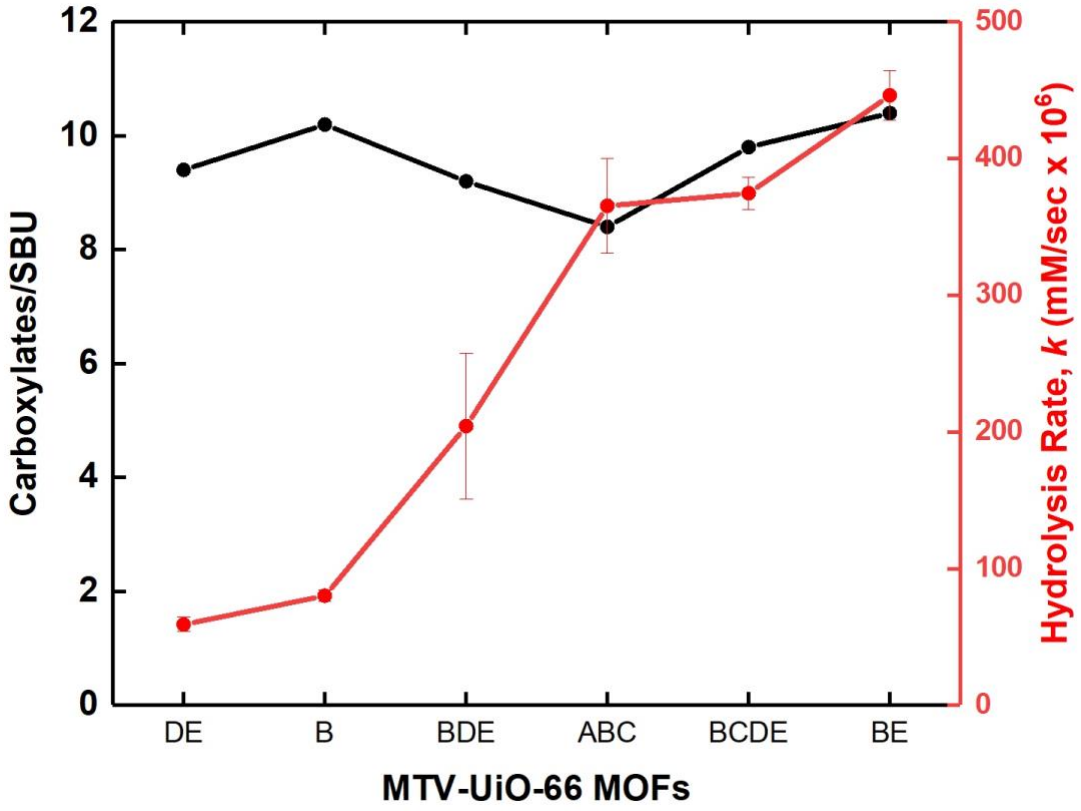

Figure 3S.49. Ratio of organic linkers per SBU of MTV-UiO-66 MOFs (black) vs. rate of DMNP degradation by MOFs (red).

Table 3S.2. Corrected hydrolysis calculation to account for increased mass of halogenated materials.

MOF	Molar Mass of MOF (*g/mol*)	Mole ratio to UiO-66 Standard	Expermental Hydrolysis Rate[a] (*k*, mM/sec)	Molar Mass Corrected Hydrolysis Rate (*k*, mM/sec)
NU-1000	1624	1.00	133	133
UiO-66	1628	1.00	161	161
UiO-66-F	1736	0.94	213	226
UiO-66-Cl	1835	0.89	172	194
UiO-66-Br	2101	0.77	134	173
UiO-66-$I_{50\%}$	2016	0.81	337	417
UiO-66-I	2383	0.68	413	605

[a] 6 mg of MOF used in each experiment.

Table 3S.3. Computed M06-L key bond distances of different DMNP bonded (transition states for water addition in parenthesis) UiO-66 MOFs as well as M062X(SMD) CM5 charges (see Figure 3S.9 for structures and atom labelling).

	***ortho*-UiO-66-I**	**alter-UiO-66-I**	***meta*-UiO-66-I**	**UiO-66-H**
I–O(Me)	3.405 (3.267)	3.398 (3.277)	5.829 (5.767)	-
I–O(P)	3.882 (3.651)	3.887 (3.713)	6.615 (6.702)	-
Q $_{Iodine}$	0.028 (0.013)	0.029 (0.025)	-0.004 (-0.004)	-
Q $_{O(Me)}$	-0.250 (-0.274)	-0.249 (-0.274)	-0.234 (-0.272)	-0.235 (-0.277)
Q $_{O(P)}$	-0.380 (-0.424)	-0.381 (-0.422)	-0.386 (-0.425)	-0.390 (-0.431)

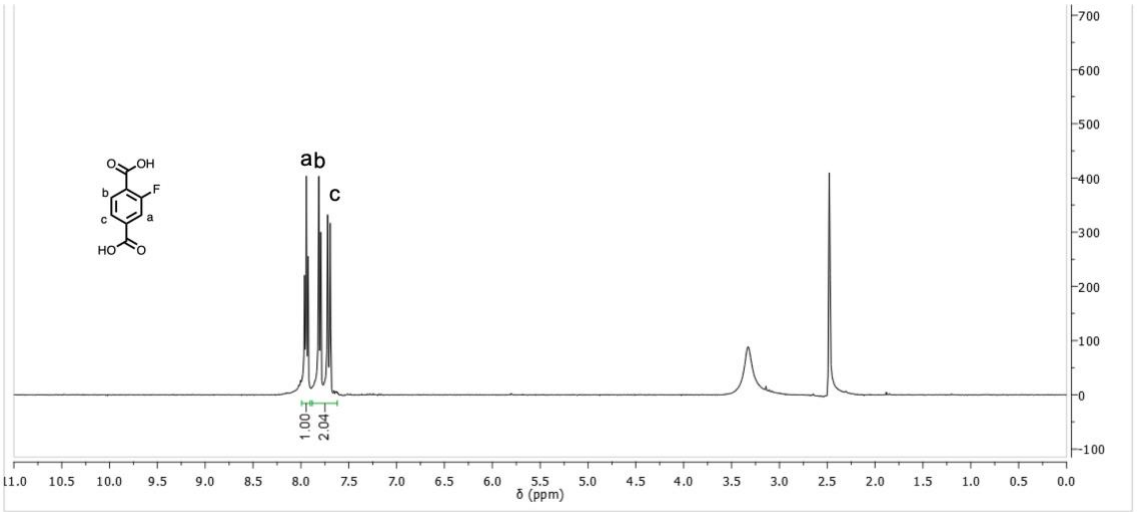

Figure 3S.50. ^{1}H NMR of 2-fluoroterephthalic acid.

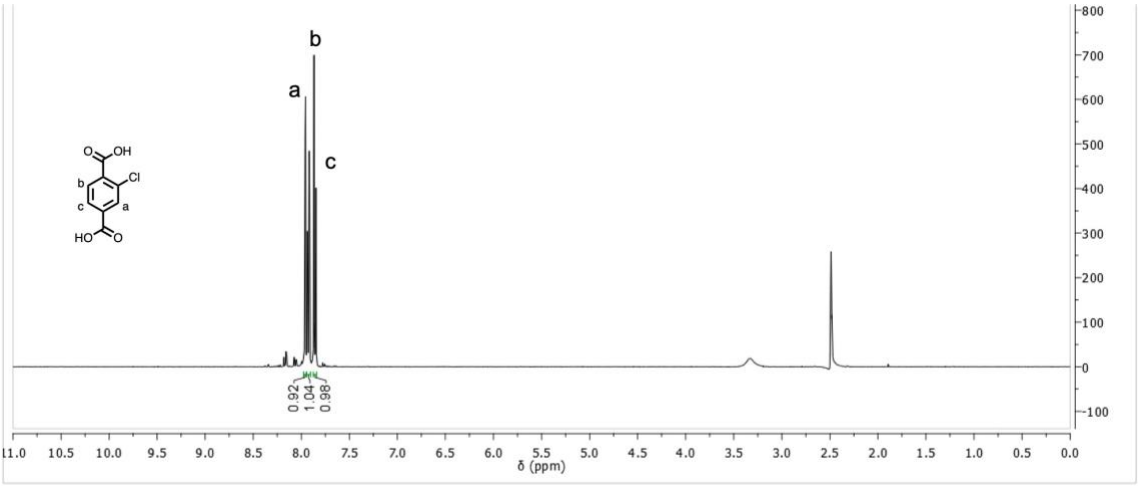

Figure 3S.51. ^{1}H NMR of 2-chloroterephthalic acid.

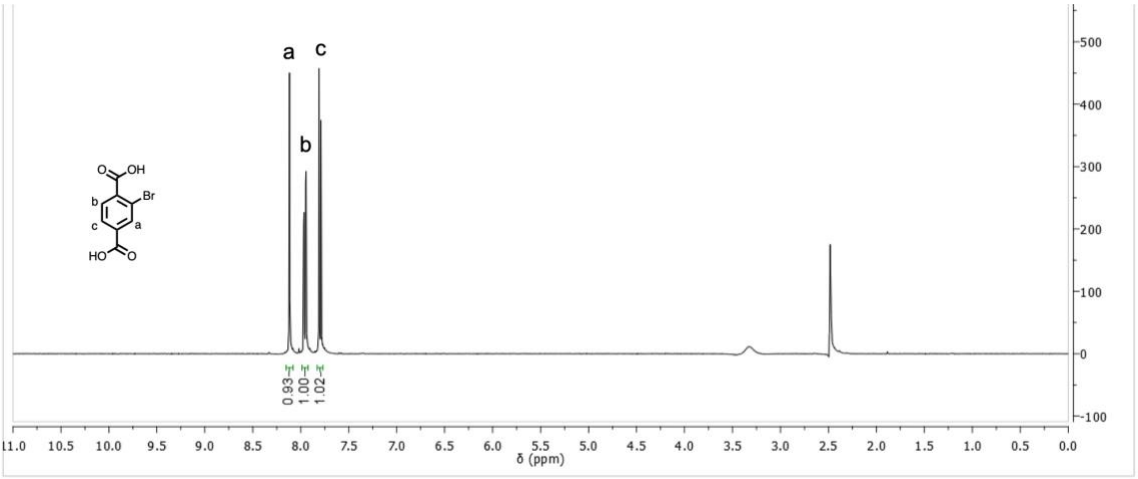

Figure 3S.52. ^{1}H NMR of 2-bromoterephthalic acid.

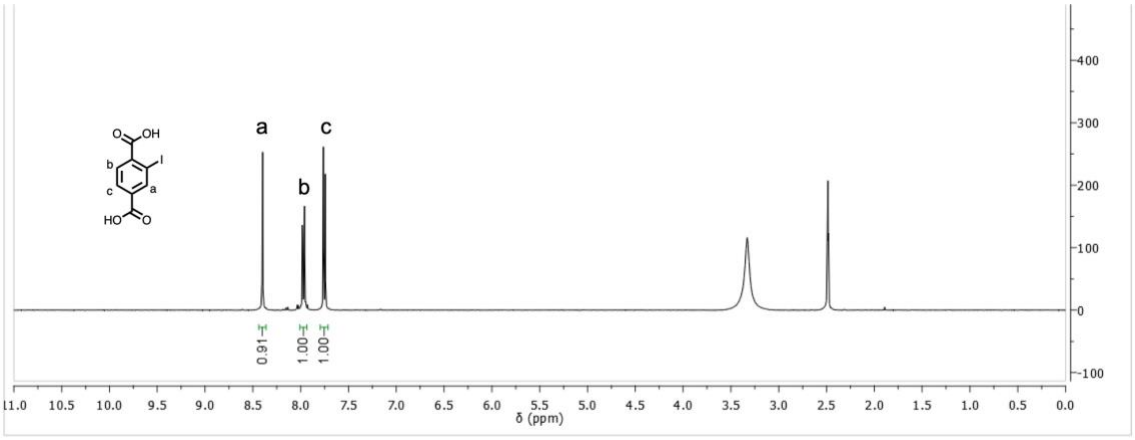

Figure 3S.53. ^{1}H NMR of 2-iodoterephthalic acid.

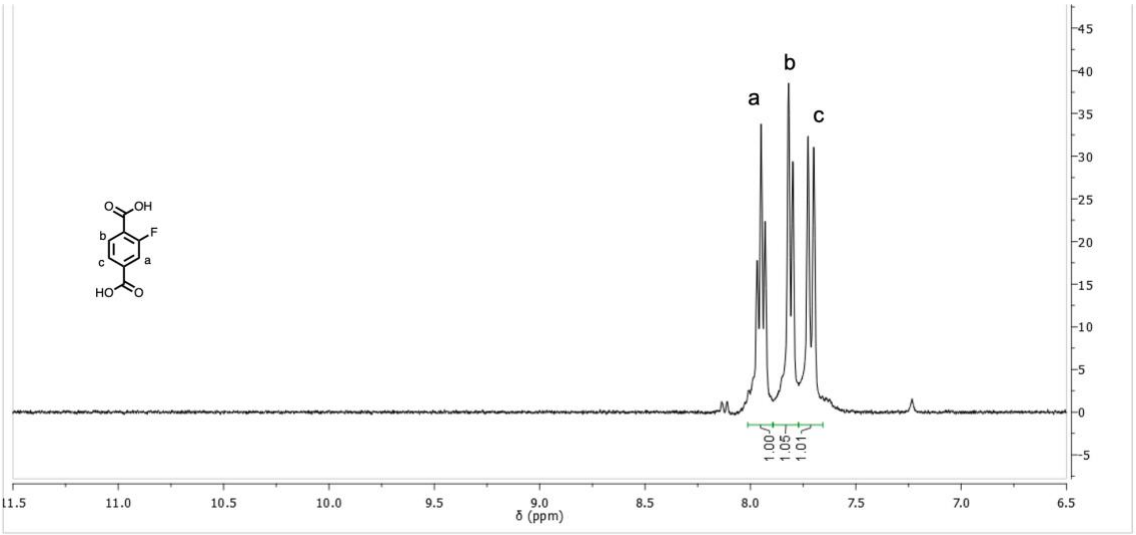

Figure 3S.54. ^{1}H NMR analysis of digested UiO-66-F.

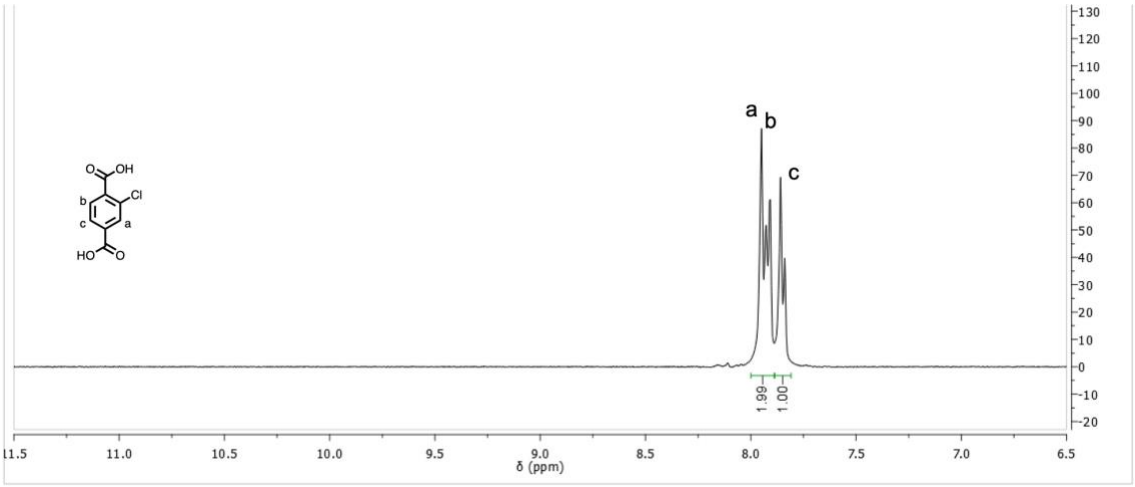

Figure 3S.55. ^{1}H NMR analysis of digested UiO-66-Cl.

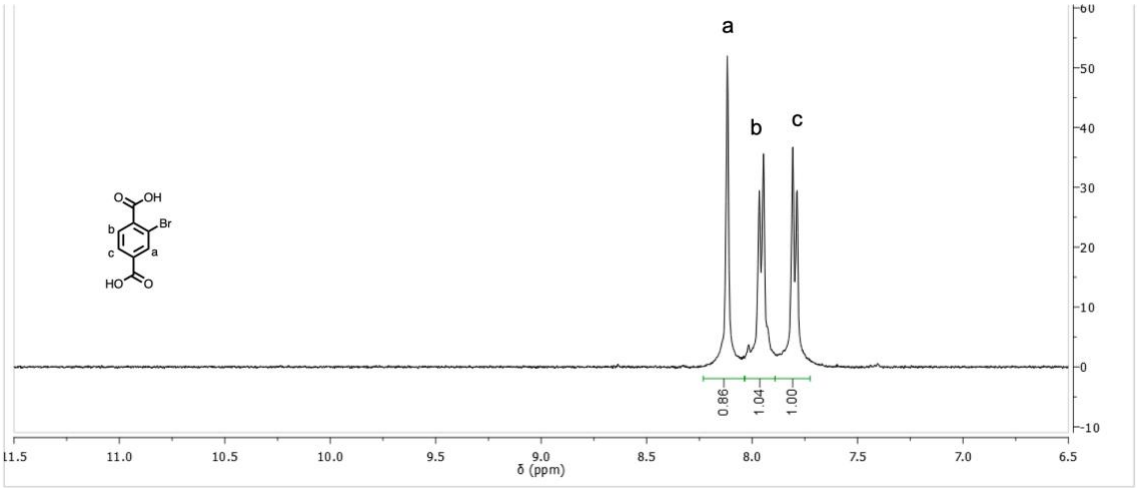

Figure 3S.56. ^{1}H NMR analysis of digested UiO-66-Br.

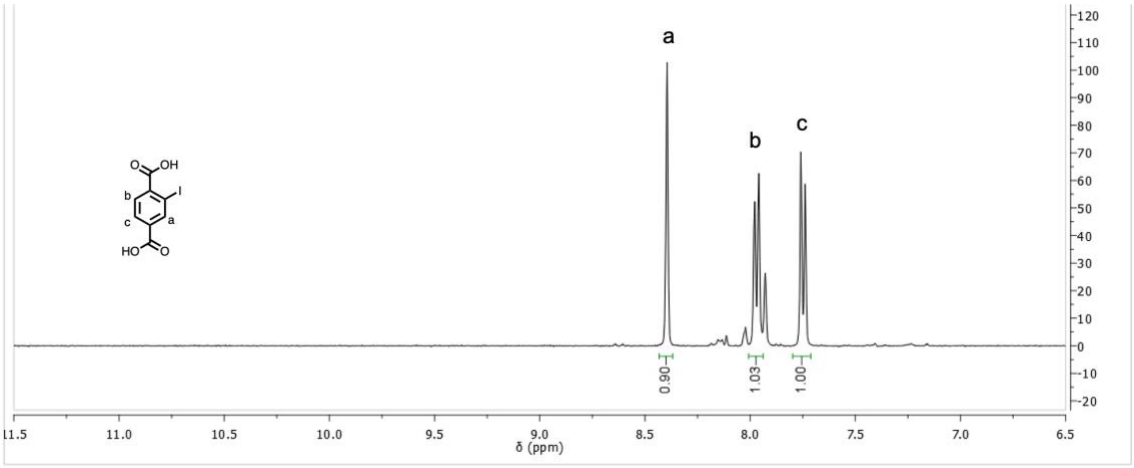

Figure 3S.57. ^{1}H NMR analysis of digested UiO-66-I.

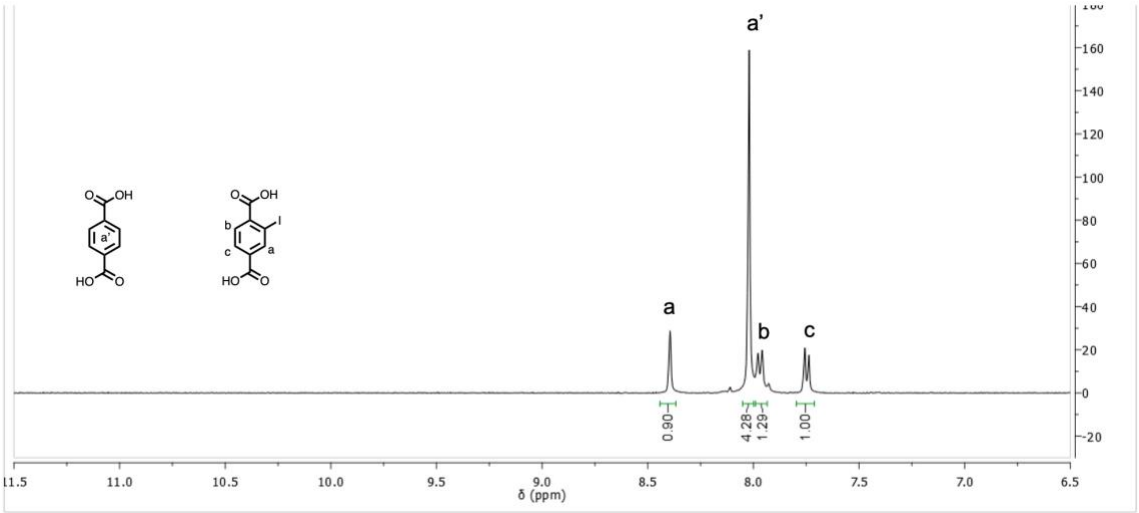

Figure 3S.58. ^{1}H NMR analysis of digested UiO-66-I$_{50\%}$.

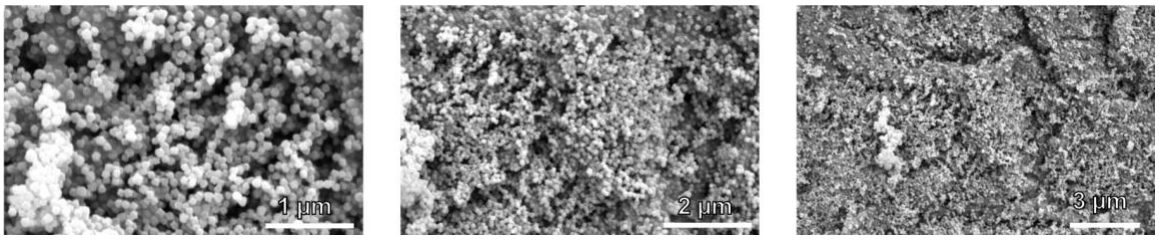

Figure 3S.59. SEM images of UiO-66.

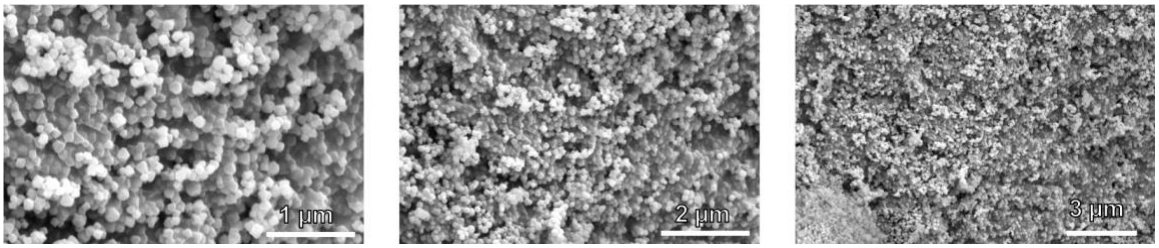

Figure 3S.60. SEM images of UiO-66-F.

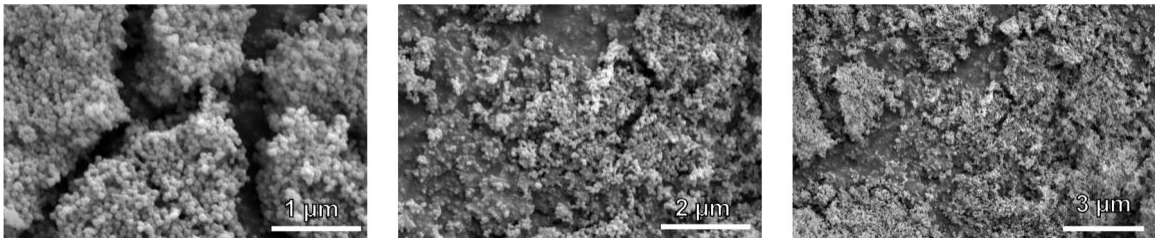

Figure 3S.61. SEM images of UiO-66-Cl.

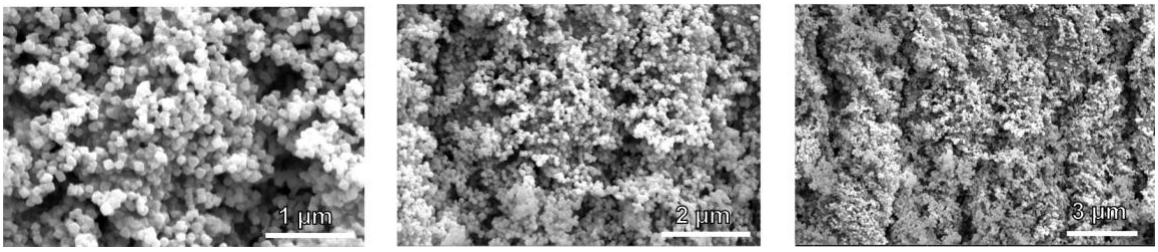

Figure 3S.62. SEM images of UiO-66-Br.

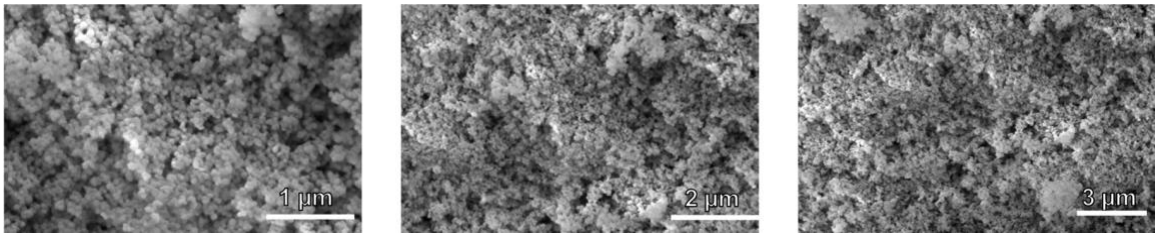

Figure 3S.63. SEM images of UiO-66-I.

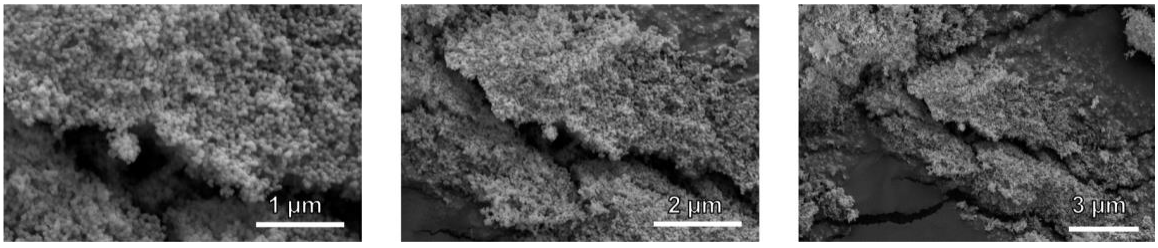

Figure 3S.64. SEM images of mixed ligand UiO-66-$I_{50\%}$.

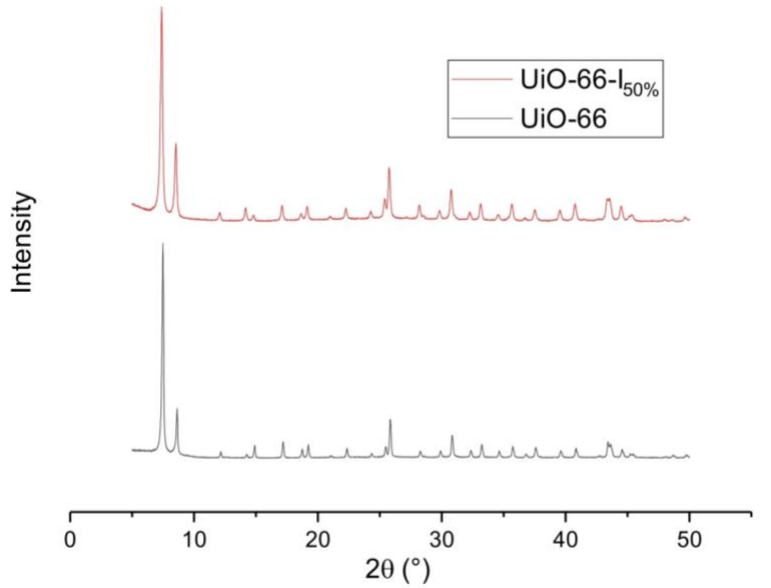

Figure 3S.65. PXRD of mixed ligand UiO-66-$I_{50\%}$.

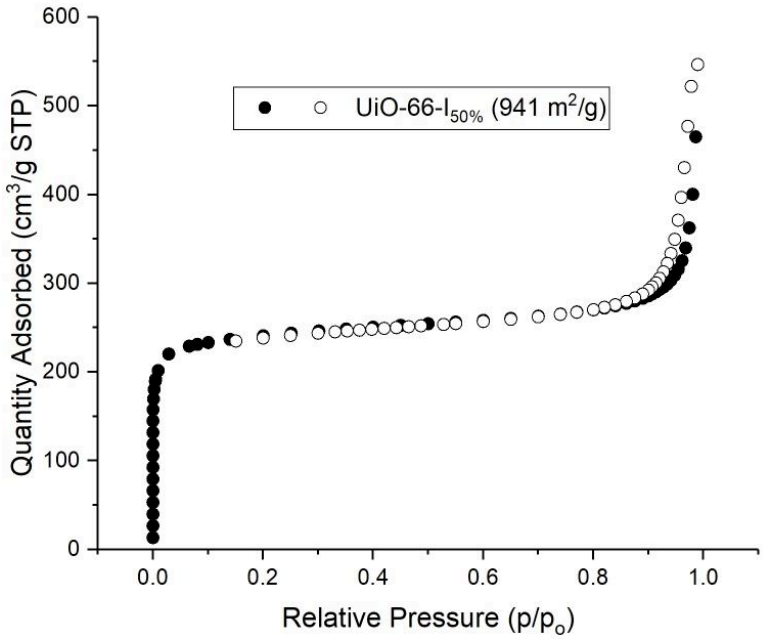

Figure 3S.66. N_2 sorption isotherm of mixed ligand UiO-66-$I_{50\%}$.

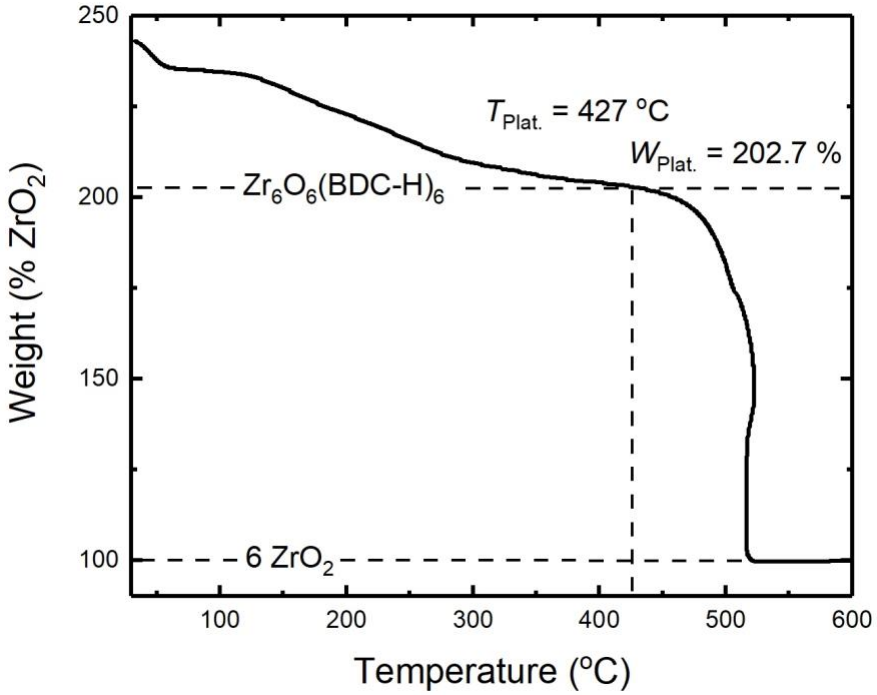

Figure 3S.67. TGA trace for UiO-66.

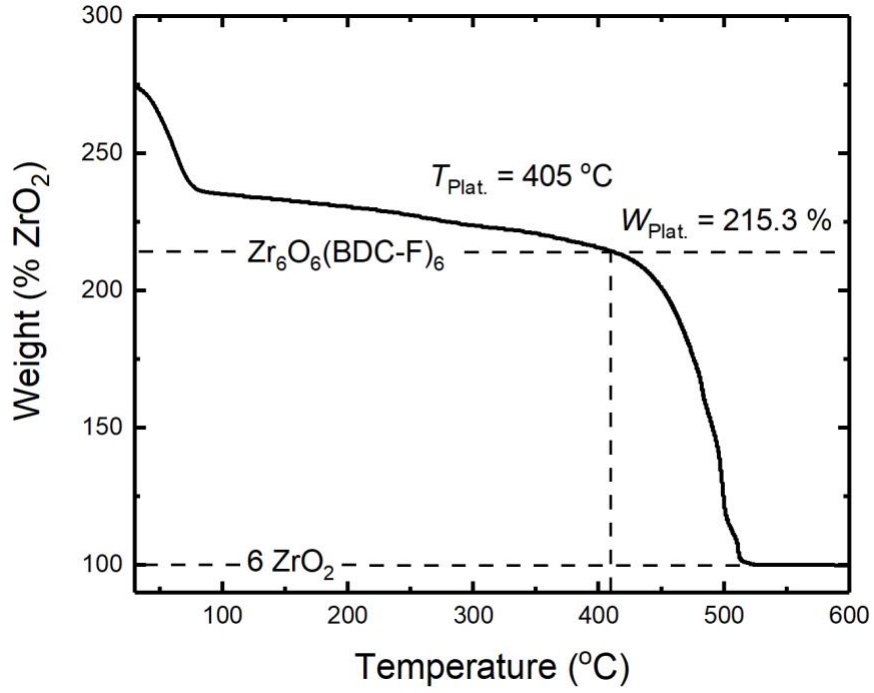

Figure 3S.68. TGA trace for UiO-66-F.

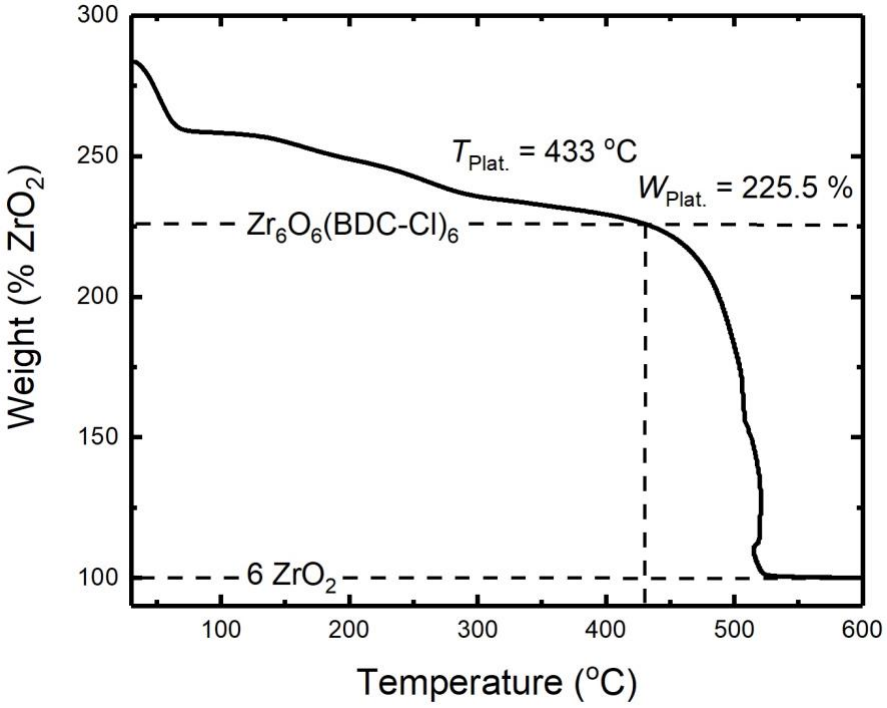

Figure 3S.69. TGA trace for UiO-66-Cl.

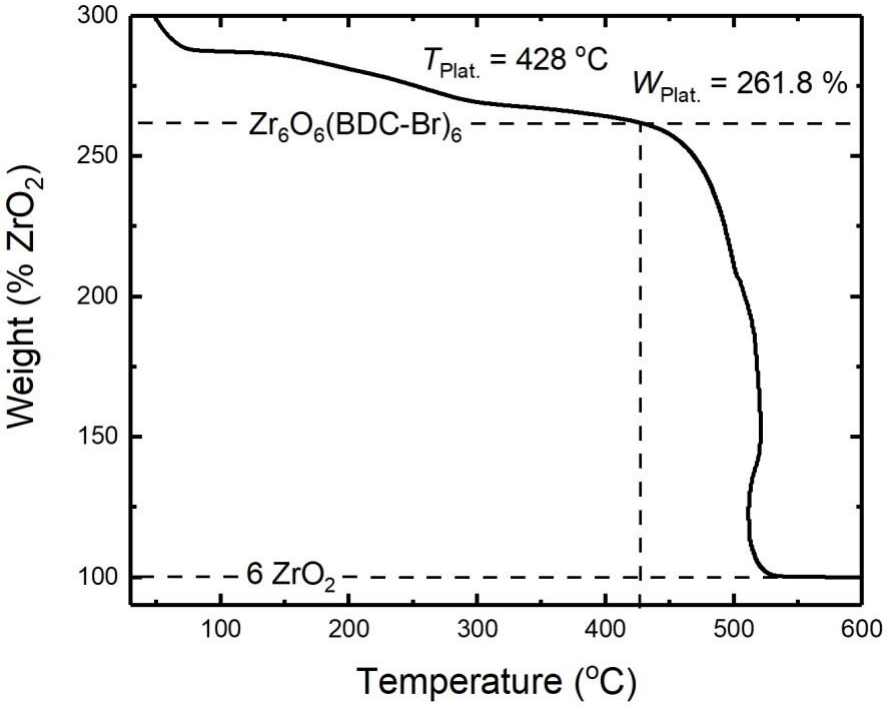

Figure 3S.70. TGA trace for UiO-66-Br.

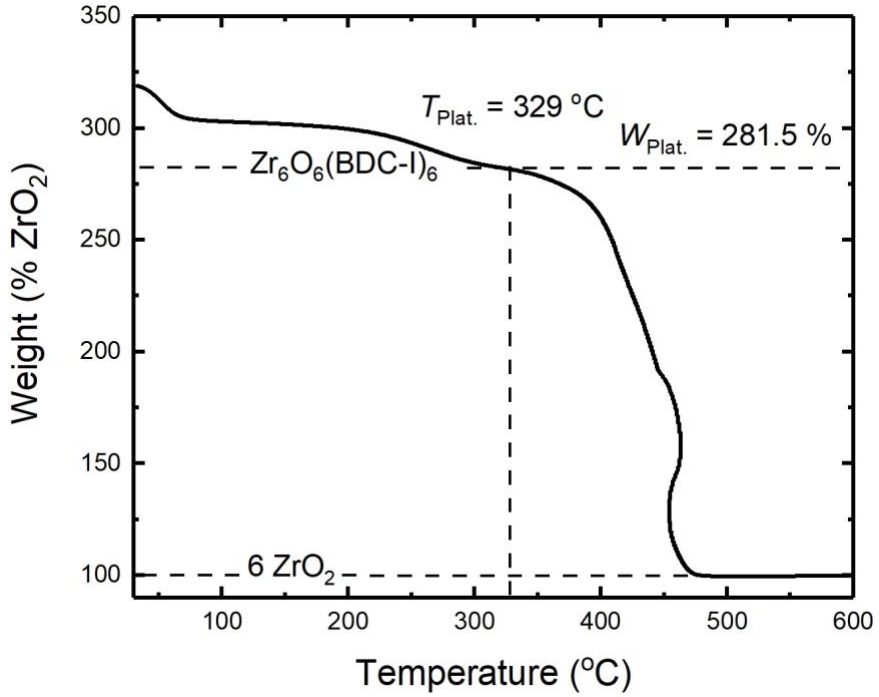

Figure 3S.71. TGA trace for UiO-66-I.

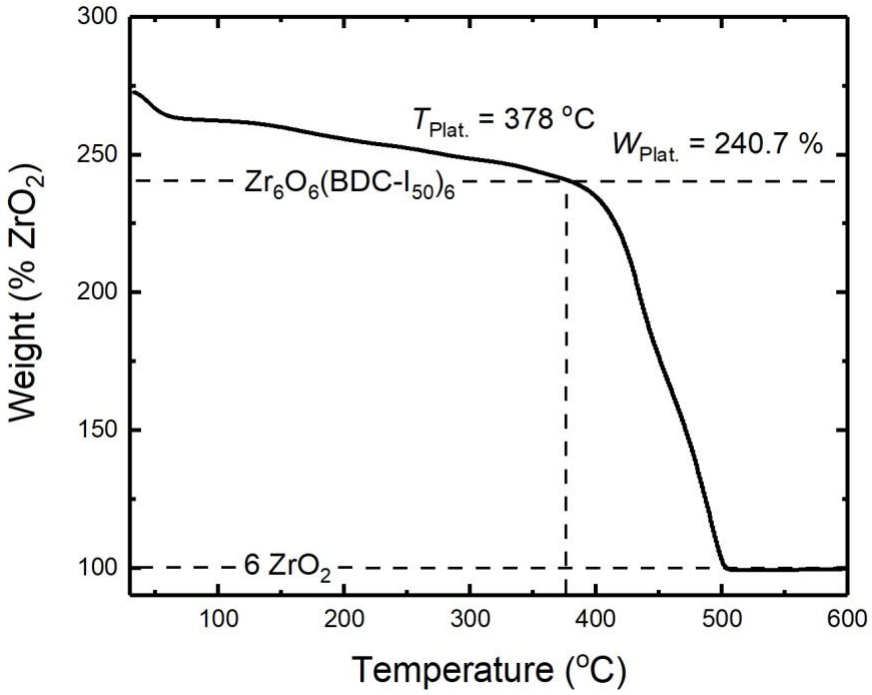

Figure 3S.72. TGA trace for UiO-66-$I_{50\%}$.

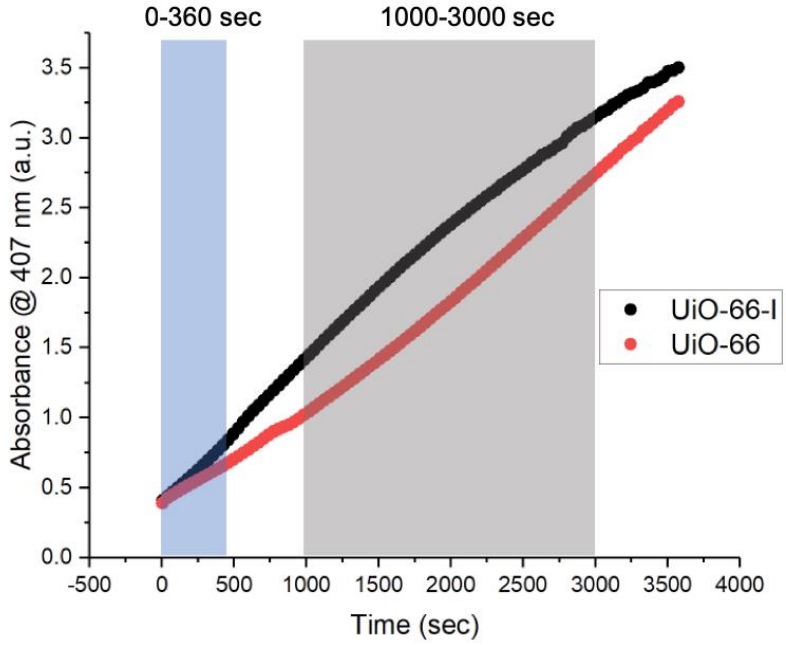

Figure 3S.73. Absorbance (407 nm) vs. time (sec) monitoring the conversion of DMNP to *p*-nitrophenol for UiO-66 and UiO-66-I. This chart highlights the change in slope in the rate of conversion after the 500 sec point for UiO-66-I.

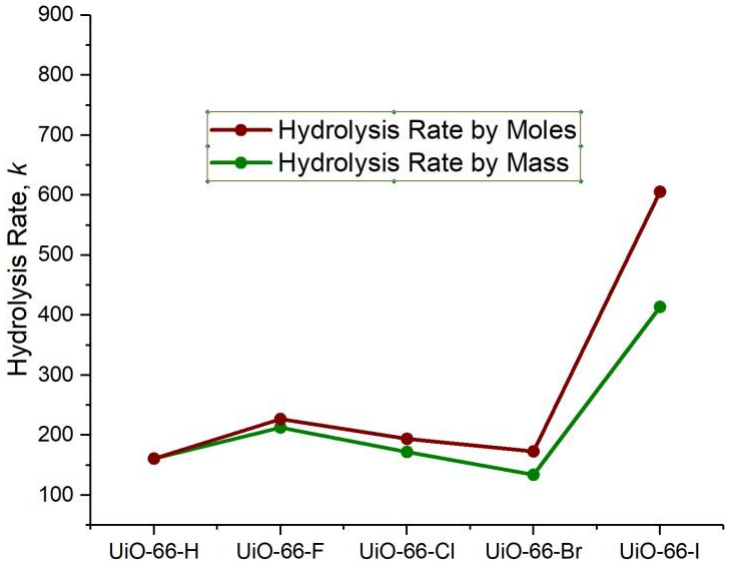

Figure 3S.74. DMNP hydrolysis rate of the MOFs in this study by mass vs. mole generated after applying the correction factor (vide infra).

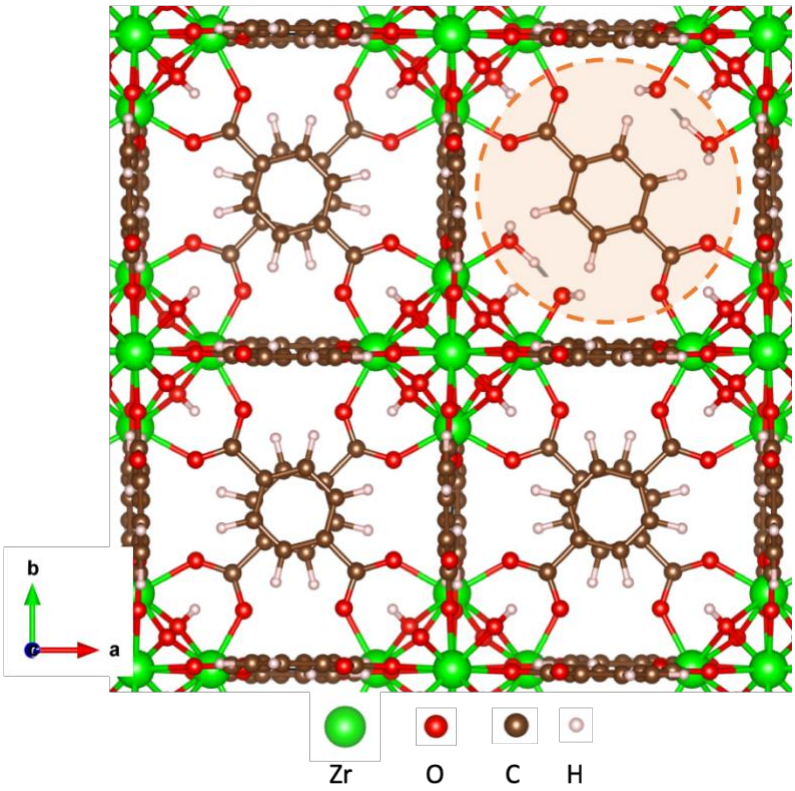

Figure 3S.75. PBE-D3/DZVP-MOLOPT optimized crystal structure of the mono-defective UiO-66 (i.e. with 11 bdc^{2-} linkers). Generated empty pore after the bdc^{2-} linker removal is highlighted.

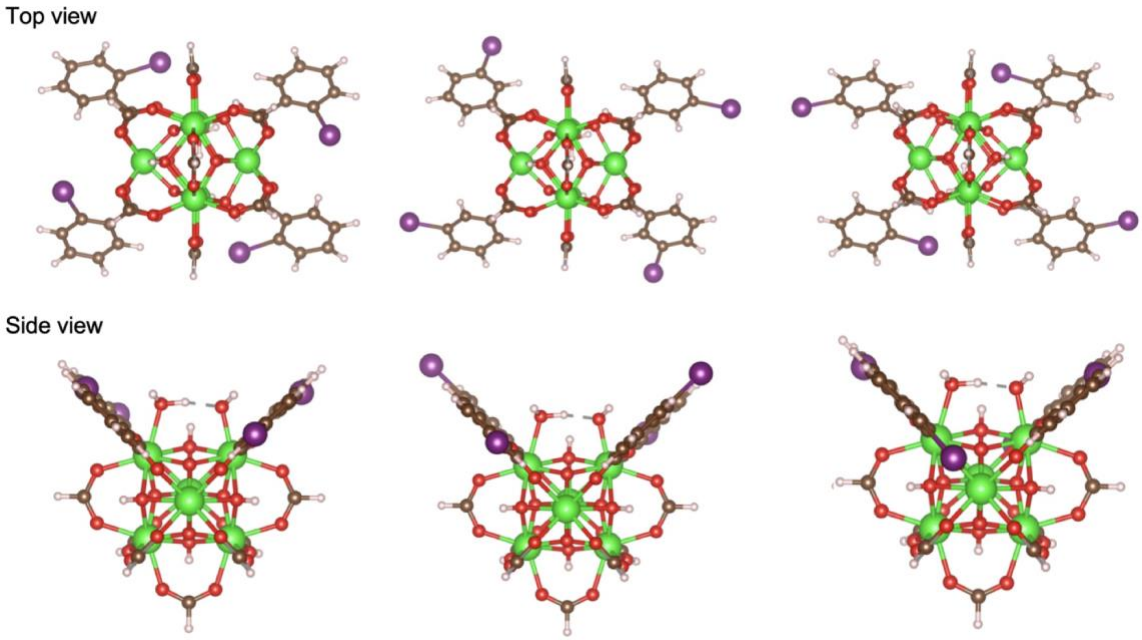

Figure 3S.76. Top view and side view of the M06-L(gas)/Def2-SVP|ECP28MDF optimized mono-defective *ortho* (left), *meta* (middle) and alternated *ortho* and *meta* (right) iodine functionalized UiO-66 MOFs.

3.6 Acknowledgements

Chapter 3, in part, is a reprint of the following materials: "Multiple Functional Groups in UiO-66 Improve Chemical Warfare Agent Simulant Degradation" *Chem. Commun.* **2019**, *55*; 5367-5370; "Halogen Bonding in UiO-66 Frameworks Promotes Superior Chemical Warfare Agent Simulant Degradation" *Chem. Commun.* **2019**, *55*, 3481-3484. The dissertation author was the primary author for both of these manuscripts and gratefully acknowledges the contributions of coauthors Mohammad R. Momeni, Kyle C. Bentz, Joseph M. Palomba, Kyle S. Barcus, Francesco Paesani, and Seth M. Cohen.

3.7 References

1. DeCoste, J. B.; Peterson, G. W., Metal–Organic Frameworks for Air Purification of Toxic Chemicals. *Chem. Rev.* **2014,** *114*, 5695-5727.

2. Islamoglu, T.; Chen, Z.; Wasson, M. C.; Buru, C. T.; Kirlikovali, K. O.; Afrin, U.; Mian, M. R.; Farha, O. K., Metal–Organic Frameworks against Toxic Chemicals. *Chem. Rev.* **2020**.

3. Kirlikovali, K. O.; Chen, Z.; Islamoglu, T.; Hupp, J. T.; Farha, O. K., Zirconium-Based Metal–Organic Frameworks for the Catalytic Hydrolysis of Organophosphorus Nerve Agents. *ACS Appl. Mater. Interfaces* **2020,** *12*, 14702-14720.

4. Islamoglu, T.; Ortuño, M. A.; Proussaloglou, E.; Howarth, A. J.; Vermeulen, N. A.; Atilgan, A.; Asiri, A. M.; Cramer, C. J.; Farha, O. K., Presence versus Proximity: The Role of Pendant Amines in the Catalytic Hydrolysis of a Nerve Agent Simulant. *Angew. Chem., Int. Ed.* **2018,** *57*, 1949-1953.

5. Katz, M. J.; Moon, S.-Y.; Mondloch, J. E.; Beyzavi, M. H.; Stephenson, C. J.; Hupp, J. T.; Farha, O. K., Exploiting Parameter Space in MOFs: A 20-fold Enhancement of Phosphate-Ester Hydrolysis with UiO-66-NH2. *Chem. Sci.* **2015,** *6*, 2286-2291.

6. Palomba, J. M.; Credille, C. V.; Kalaj, M.; DeCoste, J. B.; Peterson, G. W.; Tovar, T. M.; Cohen, S. M., High-Throughput Screening of Solid-State Catalysts for Nerve Agent Degradation. *Chem. Commun.* **2018,** *54*, 5768-5771.

7. Denny Jr, M. S.; Cohen, S. M., In Situ Modification of Metal–Organic Frameworks in Mixed-Matrix Membranes. *Angew. Chem., Int. Ed.* **2015,** *54*, 9029-9032.

8. Son, F. A.; Wasson, M. C.; Islamoglu, T.; Chen, Z.; Gong, X.; Hanna, S. L.; Lyu, J.; Wang, X.; Idrees, K. B.; Mahle, J. J., et al., Uncovering the Role of Metal–Organic Framework Topology on the Capture and Reactivity of Chemical Warfare Agents. *Chem. Mater.* **2020,** *32*, 4609-4617.

9. Peterson, G. W.; Destefano, M. R.; Garibay, S. J.; Ploskonka, A.; McEntee, M.; Hall, M.; Karwacki, C. J.; Hupp, J. T.; Farha, O. K., Optimizing Toxic Chemical Removal through Defect-Induced UiO-66-NH2 Metal–Organic Framework. *Chem. Eur. J.* **2017,** *23*, 15913-15916.

10. Shearer, G. C.; Chavan, S.; Ethiraj, J.; Vitillo, J. G.; Svelle, S.; Olsbye, U.; Lamberti, C.; Bordiga, S.; Lillerud, K. P., Tuned to Perfection: Ironing Out the Defects in Metal–Organic Framework UiO-66. *Chem. Mater.* **2014,** *26*, 4068-4071.

11. Gliese, J.-P.; Jungbauer, S. H.; Huber, S. M., A Halogen-Bonding-Catalyzed Michael Addition Reaction. *Chem. Commun.* **2017,** *53*, 12052-12055.

12. Jungbauer, S. H.; Huber, S. M., Cationic Multidentate Halogen-Bond Donors in Halide Abstraction Organocatalysis: Catalyst Optimization by Preorganization. *J. Am. Chem. Soc.* **2015,** *137*, 12110-12120.

13. Cinčić, D.; Friščić, T., Synthesis of an Extended Halogen-Bonded Metal–Organic Structure in a One-Pot Mechanochemical Reaction that Combines Covalent Bonding, Coordination Chemistry and Supramolecular Synthesis. *CrystEngComm* **2014,** *16*, 10169-10172.

14. Cavallo, G.; Metrangolo, P.; Milani, R.; Pilati, T.; Priimagi, A.; Resnati, G.; Terraneo, G., The Halogen Bond. *Chem. Rev.* **2016,** *116*, 2478-2601.

15. Politzer, P.; Murray, J. S.; Clark, T., Halogen Bonding and Other σ-hole Interactions: A Perspective. *Phys. Chem. Chem. Phys.* **2013,** *15*, 11178-11189.

16. Carter, K. P.; Kalaj, M.; Kerridge, A.; Cahill, C. L., Probing Hydrogen and Halogen-oxo Interactions in Uranyl Coordination Polymers: a Combined Crystallographic and Computational Study. *CrystEngComm* **2018,** *20*, 4916-4925.

17. Carter, K. P.; Kalaj, M.; Surbella Iii, R. G.; Ducati, L. C.; Autschbach, J.; Cahill, C. L., Engaging the Terminal: Promoting Halogen Bonding Interactions with Uranyl Oxo Atoms. *Chem. Eur. J.* **2017,** *23*, 15355-15369.

18. Carter, K. P.; Surbella Iii, R. G.; Kalaj, M.; Cahill, C. L., Restricted Speciation and Supramolecular Assembly in the 5f Block. *Chem. Eur. J.* **2018,** *24*, 12747-12756.

19. Kalaj, M.; Carter, K. P.; Cahill, C. L., Isolating Equatorial and Oxo Based Influences on Uranyl Vibrational Spectroscopy in a Family of Hybrid Materials Featuring Halogen Bonding Interactions with Uranyl Oxo Atoms. *Eur. J. Inorg. Chem.* **2017,** *2017*, 4702-4713.

20. Zhao, Y.; Truhlar, D. G., A New Local Density Functional for Main-Group Thermochemistry, Transition Metal Bonding, Thermochemical Kinetics, and Noncovalent Interactions. *J. Chem. Phys.* **2006,** *125*, 194101.

21. Troya, D., Reaction Mechanism of Nerve-Agent Decomposition with Zr-Based Metal Organic Frameworks. *J. Phys. Chem. C* **2016,** *120*, 29312-29323.

22. Perdew, J. P.; Burke, K.; Ernzerhof, M., D. of Physics and NOL 70118 J. Quantum theory group Tulane University. *Phys. Rev. Lett.* **1996,** *77*, 3865-3868.

23. Grimme, S., Semiempirical GGA-type Density Functional Constructed with a Long-Range Dispersion Correction. *J. Comput. Chem.* **2006,** *27*, 1787-1799.

24. Hutter, J.; Iannuzzi, M.; Schiffmann, F.; VandeVondele, J., cp2k: Atomistic Simulations of Condensed Matter Systems. *Wiley Interdisciplinary Rev. Comput. Mol. Sci.* **2014,** *4*, 15-25.

25. Planas, N.; Mondloch, J. E.; Tussupbayev, S.; Borycz, J.; Gagliardi, L.; Hupp, J. T.; Farha, O. K.; Cramer, C. J., Defining the Proton Topology of the Zr6-Based Metal–Organic Framework NU-1000. *J. Phys. Chem. Lett.* **2014,** *5*, 3716-3723.

26. Goedecker, S.; Teter, M.; Hutter, J., Separable Dual-Space Gaussian Pseudopotentials. *Phys. Rev. B* **1996,** *54*, 1703-1710.

27. Weigend, F., Accurate Coulomb-Fitting Basis Sets for H to Rn. *Phys. Chem. Chem. Phys.* **2006,** *8*, 1057-1065.

28. Peterson, K. A.; Shepler, B. C.; Figgen, D.; Stoll, H., On the Spectroscopic and Thermochemical Properties of ClO, BrO, IO, and Their Anions. *J. Phys. Chem. A* **2006,** *110*, 13877-13883.

29. Cramer, C. J., *Essentials of Computational Chemistry: Theories and Models*. John Wiley & Sons: 2013.

30. Zhao, Y.; Truhlar, D. G., The M06 Suite of Density Functionals for Main Group Thermochemistry, Thermochemical Kinetics, Noncovalent Interactions, Excited States, and Transition Elements: Two New Functionals and Systematic Testing of Four M06-Class Functionals and 12 Other Functionals. *Theor. Chem. Acc.* **2008,** *120*, 215-241.

31. Marenich, A. V.; Cramer, C. J.; Truhlar, D. G., Universal Solvation Model Based on Solute Electron Density and on a Continuum Model of the Solvent Defined by the Bulk Dielectric Constant and Atomic Surface Tensions. *J. Phys. Chem. B* **2009,** *113*, 6378-6396.

32. Marenich, A. V.; Jerome, S. V.; Cramer, C. J.; Truhlar, D. G., Charge Model 5: An Extension of Hirshfeld Population Analysis for the Accurate Description of Molecular Interactions in Gaseous and Condensed Phases. *J. Chem. Theory Comput.* **2012,** *8*, 527-541.

33. Frisch, M. J.; Trucks, G. W.; Schlegel, H. B.; Scuseria, G. E.; Robb, M. A.; Cheeseman, J. R.; Scalmani, G.; Barone, V.; Petersson, G. A.; Nakatsuji, H., et al. *Gaussian 16 Rev. C.01*, Wallingford, CT, 2016.

Chapter 4: Spray Coating of Catalytically Active MOF-Polythiourea through Postsynthetic Polymerization

4.1 Introduction

As outlined in Chapter 2, the synthesis of nylon-MOFs through PSP has proven to be an effective method for the synthesis of catalytically active MOF-polymer hybrid materials.[1] These materials displayed activity for the degradation of the CWA simulant DMNP; however, the MOF used in this synthesis (UiO-66-NH_2) was one of the weakest performing MOFs for DMNP degradation at pH = 8 compared to the library of MOFs analyzed in Chapter 3. In Chapter 3, after screening a larger library of MOFs the presence of highly polarizable halogen atoms (iodine) was determined to increase catalytic activity through a halogen bonding effect as determined by DFT calculations. As such, in this chapter, a MOF that contains a highly polarizable, negatively charged, polyatomic analogue of halogens, also known as pseudohalogens (cyanide, cyanate, thiocyanate, azide, etc), was explored. The incorporation of these molecules could potentially increase the activity of the MOF against CWAs due to the polarizability across several atoms. These polyatomic pseudohalogen groups could also potentially serve as reactive groups for PSP of the MOF particles into a functional composite material similar to that displayed in Chapter 2.

In Chapter 4, the synthesis of UiO-66-isothiocyanate (UiO-66-NCS) via PSM of UiO-66-NH_2 (Figure 4.1) is outlined.[3] The MOF was characterized and screened for the degradation of the CWA simulant DMNP, and was shown to display ~20-fold higher activity than UiO-66-NH_2 precursor at pH = 8, making UiO-66-NCS among the most active MOFs reported under these conditions. Additionally, the UiO-66-NCS MOF could be incorporated into a composite material via PSP through the formation of a thiourea bond (UiO-66-NCS-PTU, PTU = polythiourea).[4, 5] The MOF-polymer hybrid material could be spray coated onto Nyco (nylon and cotton blend) fibers. Control materials were synthesized by physically mixing the canonical UiO-66 and the PTU (UiO-66-PTU spray coating) polymer to determine the effects of the covalent linkages

between the MOF a polymer in terms of CWA degradation and robustness. Nyco fibers coated with the covalent UiO-66-NCS-PTU material display much better compatibility between the two materials whereas phase separation is evident in the physical UiO-66-PTU spray coating.

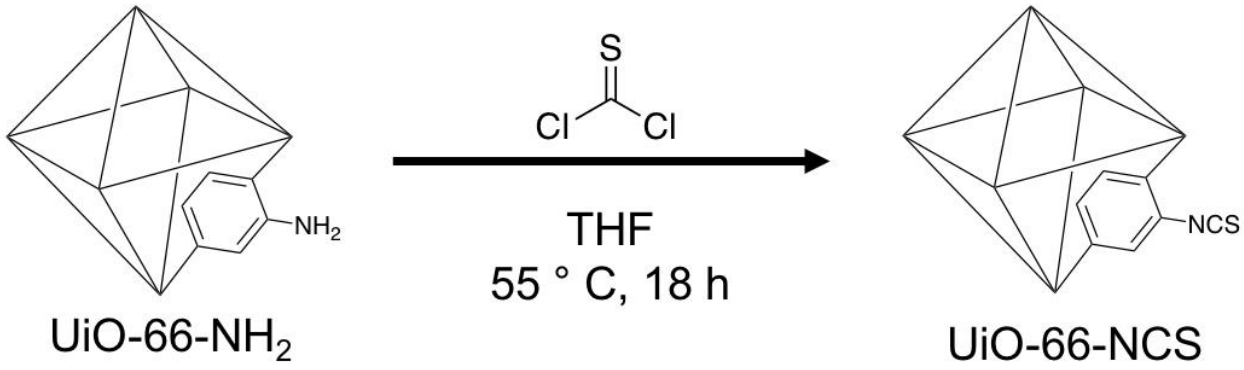

Figure 4.1. Synthetic scheme for the preparation of UiO-66-NCS via PSM.

4.2 Synthesis and Characterization of MOFs

UiO-66-NCS was synthesized using PSM, where UiO-66-NH_2 was treated with thiophosgene in tetrahydrofuran (THF) at 55 °C for 18 h (Figure 4.1, see appendix for complete procedure).[3] This procedure resulted in 100% conversion of -NH_2 functional groups to -NCS functional groups. Five other MOFs with varying -NH_2 to -NCS functional group content (25/75%, 50/50%, 75/25%, etc.) were synthesized to further probe the effects of the -NCS functional groups (see appendix for synthesis details). MOFs were characterized via PXRD to confirm retention of crystallinity (Figure 4S.1-4S.7). MOFs were digested in dilute acid and subsequently analyzed by ^{1}H NMR to confirm the presence of the -NCS functional group (Figure 4S.1-4S.7). ^{1}H NMR was then used to quantify the amount of -NH_2 functional groups compared to -NCS functional groups in the MOF linkers (Table 4S.1). Attenuated total reflectance Fourier transform infrared spectroscopy (ATR-FTIR) was also used to detect the formation of the UiO-

66-NCS MOF at the characteristic NCS vibrational frequency of ~2133 cm^{-1} (Figure 4.2).[3] The results showed an increase in the intensity of the stretch at ~2133 cm^{-1} as the amount of -NCS functional groups increased. Moreover, the materials via SEM were analyzed to determine if there are differences in the MOF particle size or if any chemical etching had occurred as a result of the PSM reaction conditions. As outlined in Chapter 3, MOF particle size can be a significant factor in governing the reactivity of MOFs toward the degradation of CWAs. The SEM images indicate nearly no difference in the MOF particle size as a result of the PSM and no etching was observed (Figure 4.3). The surface area of each of the MOFs was also analyzed using N_2 gas sorption measurements. As discussed in Chapter 3, literature evidence that surface area is another factor that can influence the catalytic activity of MOFs against CWAs. Gas sorption measurements showed that there was a decrease in the surface area as there is an increase in the content of -NCS functional groups compared to $-NH_2$. This loss in surface area has been attributed to the larger pore occupancy by the -NCS functional groups compared to $-NH_2$ (Table 4.1).

Table 4.1. BET Surface area of -NCS functionalized MOFs

MOF	BET Surface Area (m^2/g)
UiO-66-NH_2	1383
UiO-66-$NCS_{15\%}$	1232
UiO-66-$NCS_{25\%}$	1081
UiO-66-$NCS_{50\%}$	866
UiO-66-$NCS_{75\%}$	1001
UiO-66-$NCS_{85\%}$	1002
UiO-66-NCS	865

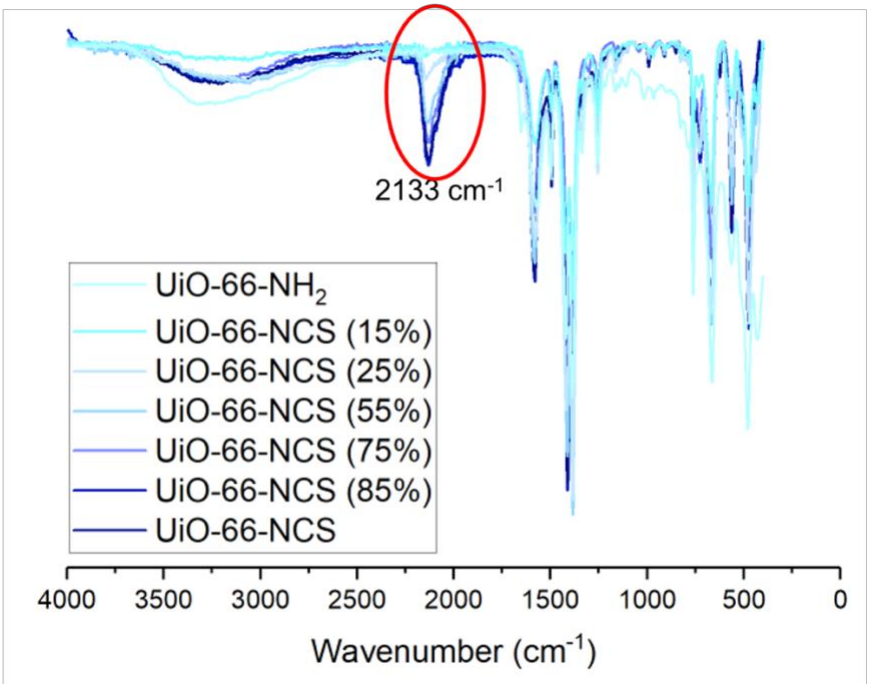

Figure 4.2. ATR-FTIR spectra of UiO-66-NCS MOFs highlighting the increasing intensity of the NCS stretch at ~2133 cm^{-1} with increasing PSM.

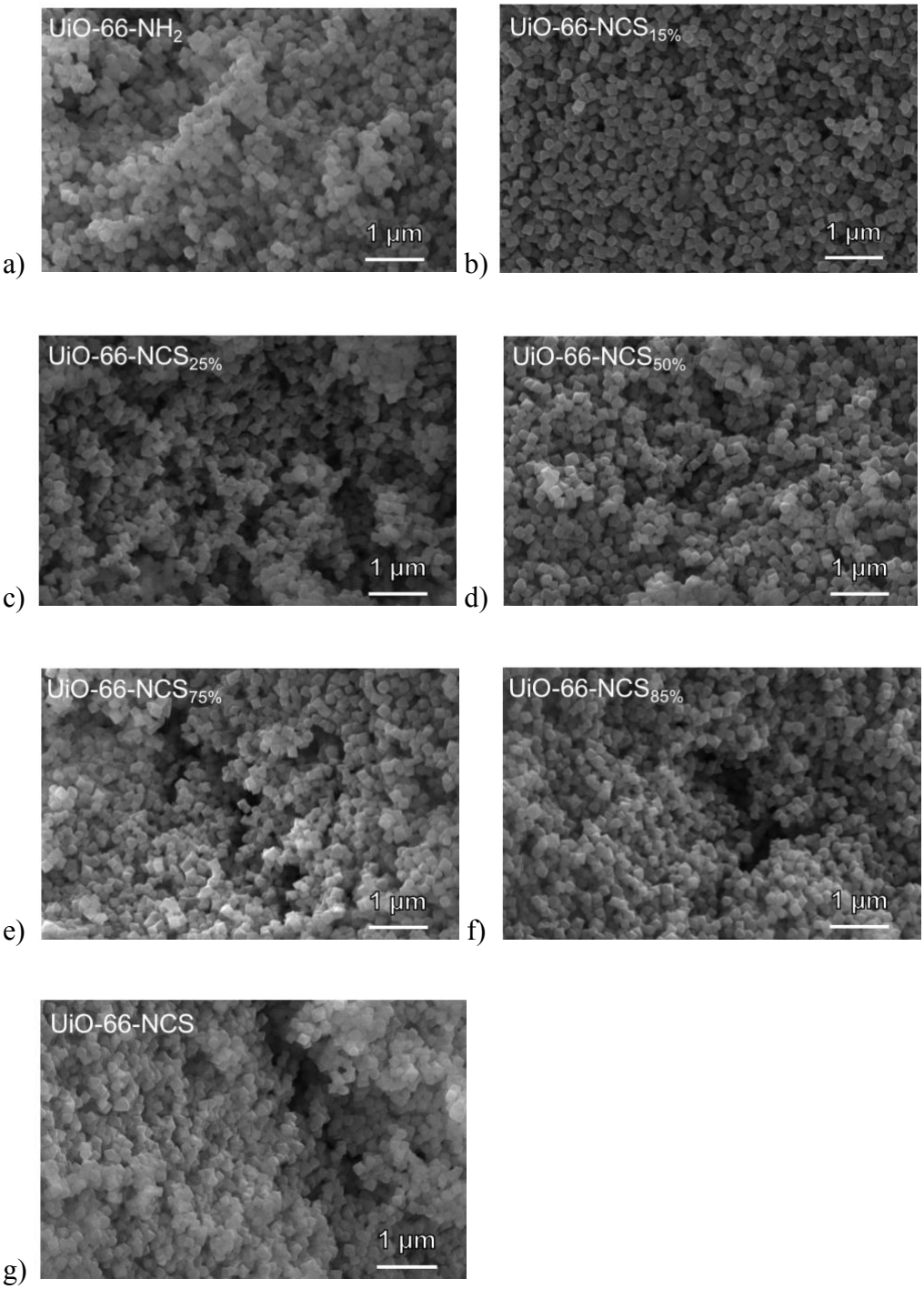

Figure 4.3. SEM images of UiO-66-NH_2 and all UiO-66-NCS MOFs.

DMNP Degradation. All MOFs were screened for the degradation of DMNP at pH = 8 using a previously validated HTS methodology outlined in Chapter 1.[6] It was found that 100% converted UiO-66-NCS degrades DMNP at a rate of ~20-fold faster than UiO-66-NH_2 (Figure 4.4). Other MOFs containing varying ratios of -NH_2 and -NCS functional groups (i.e., 15%, 25%, 50%, 75%, and 85% -NCS). The results show an increase in catalytic activity as a function of increasing -NCS present in the MOF with fully converted UiO-66-NCS (100% -NCS) being the best performing MOF (Figure 4.4). Of the >110 MOFs assayed by this HTS method in our laboratory, UiO-66-NCS displays the highest catalytic activity for DMNP hydrolysis.[1, 2, 6, 7] The origin of this increased effect may be the result of the proximity of the polarizable -NCS pseudohalogen moiety to the SBUs, which was previously shown in Chapter 3.[2] This hypothesis is consistent with an increase in the rate of hydrolysis as the number of polarizable -NCS functional groups in increased in the material (Figure 4.4). When UiO-66-NCS was combined with hexylamine to produce a MOF with a thiourea substituent (Figure 4.5). The hexylamine modified MOF (UiO-66-NCS-hexylamine) displays about 10-fold slower activity when compared to UiO-66-NCS.

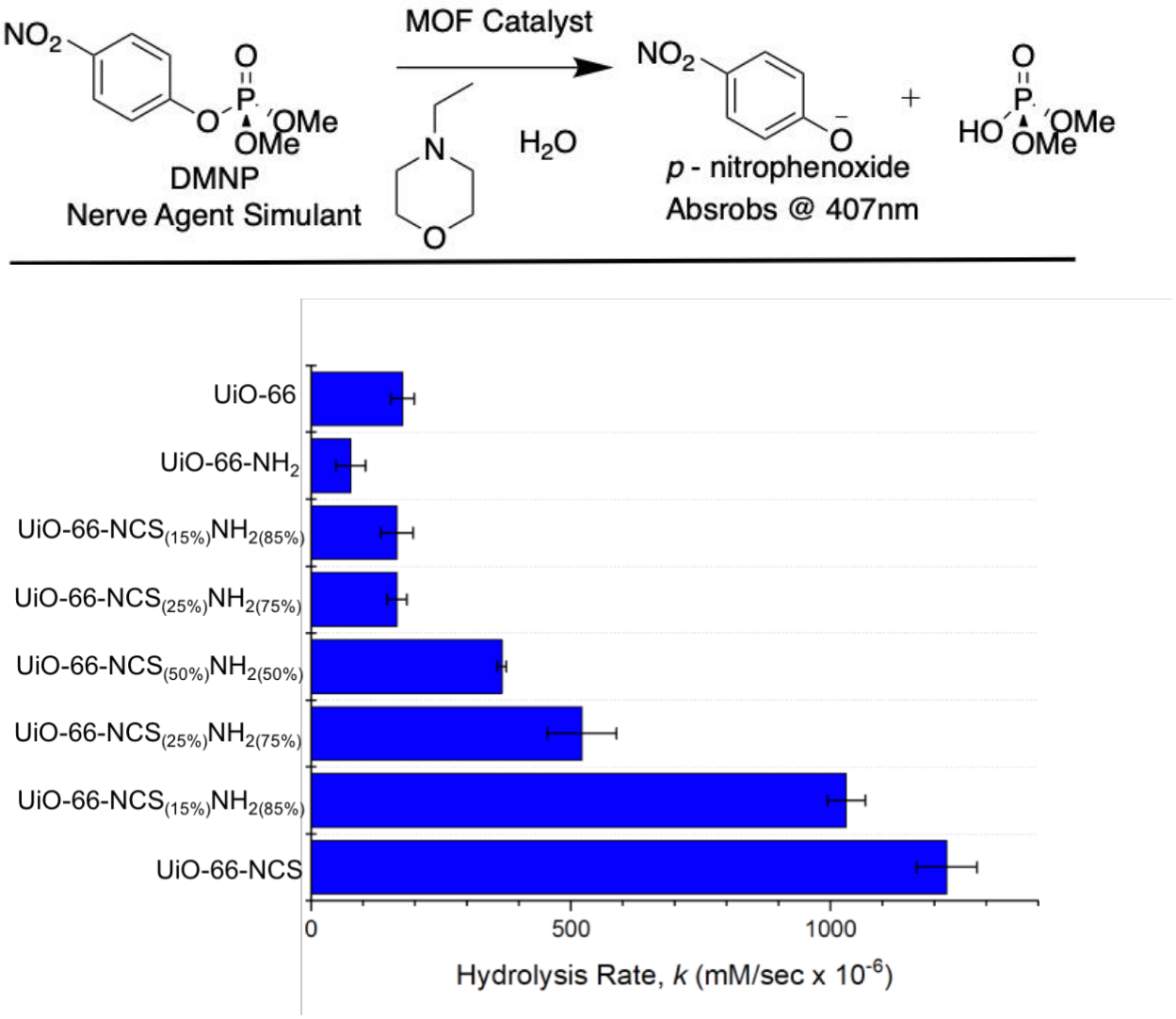

Figure 4.4. *Top:* DMNP degradation reaction. *Bottom:* Degradation of DMNP by UiO-66 MOFs with varying amounts of -NH_2 and -NCS functional groups as measured by UV-visible adsorption (407 nm) at pH = 8.

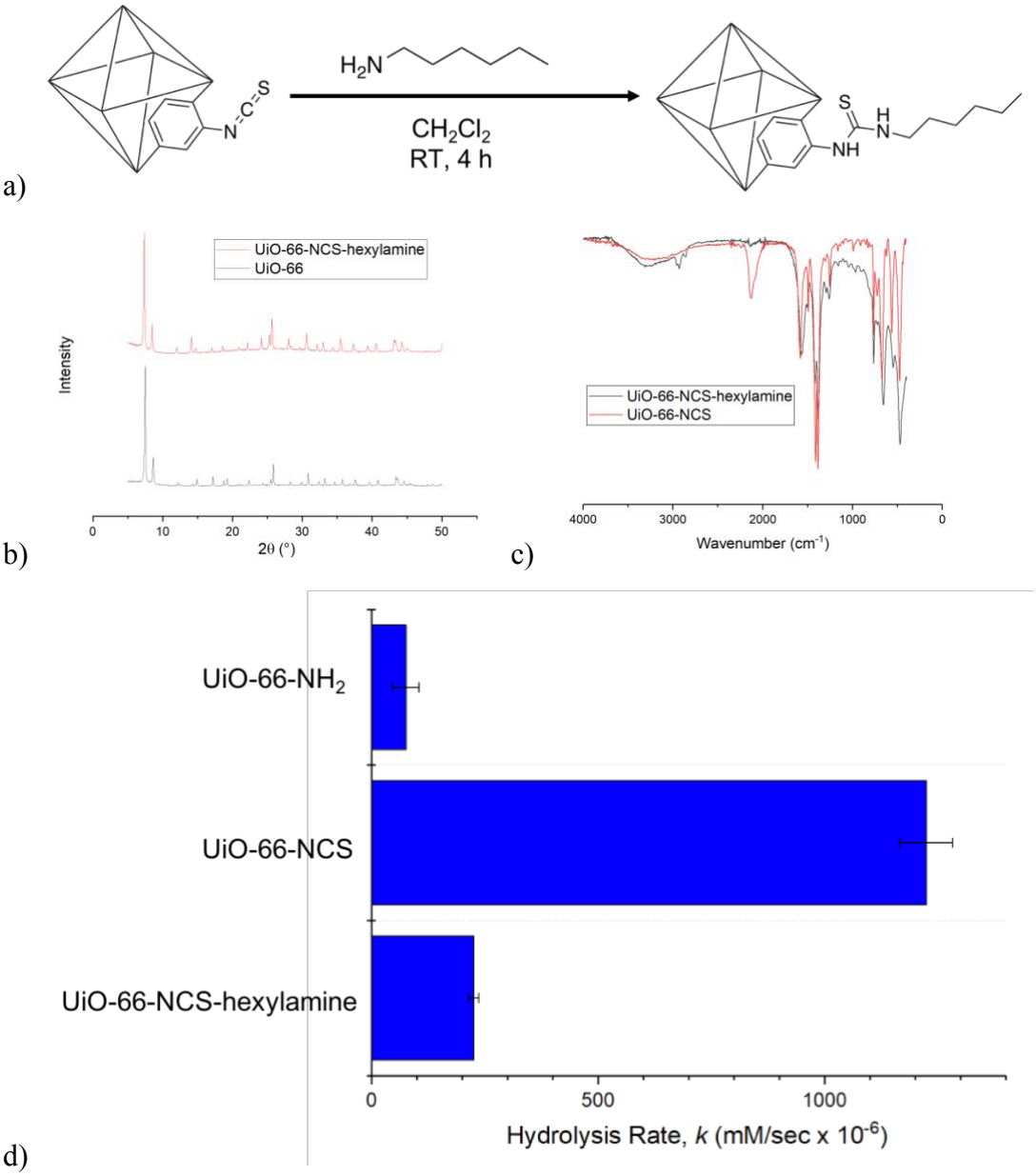

Figure 4.5. a) Scheme for the synthesis of UiO-66-NCS-hexylamine. b) PXRD and c) IR of UiO-66-NCS and UiO-66-NCS-hexylamine. d) Degradation of DMNP by UiO-66-NH_2, UiO-66-NCS, and UiO-66-NCS-hexylamine as measured by UV-visible adsorption (407nm) at pH = 8.

4.3 Synthesis and Characterization of MOF-PTU Composites

As described in the introduction of this chapter, the possibility of using the reactive pseudohalogen NCS handles as a point for PSP was explored. The NCS functional groups are known to readily react with amines to form thiourea linkages. As such, amine terminated polymers were used to synthesize MOF-polythiouea composites. To synthesize the composite, UiO-66-NCS was dispersed in CH_2Cl_2 and an excess of branched amine terminated polypropylene (Jeffamine T3000, Figure 4.6) was added to the mixture to promote formation of thiourea bonds. The reaction was allowed to proceed for ~10 minutes at RT. Subsequently, 1,4-phenylene diisothiocyanate was added to the mixture to form extended polymer chains from the MOF surface, resulting in linking of discrete MOF particles (Figure 4.6). The solution was then vortexed and cast out into a glass petri dish. The solvent was allowed to evaporate, and the resulting MOF-PTU composite was delaminated from the dish after swelling the polymer with ethanol (see appendix for details). The resulting composite polymer membrane film contains very well dispersed MOF particles and is flexible. MOF loading for the composites was varied with the highest achieved loading being about 13 wt% MOF as determined by TGA (Table 4S.2, Figure 4S.8-S.13).

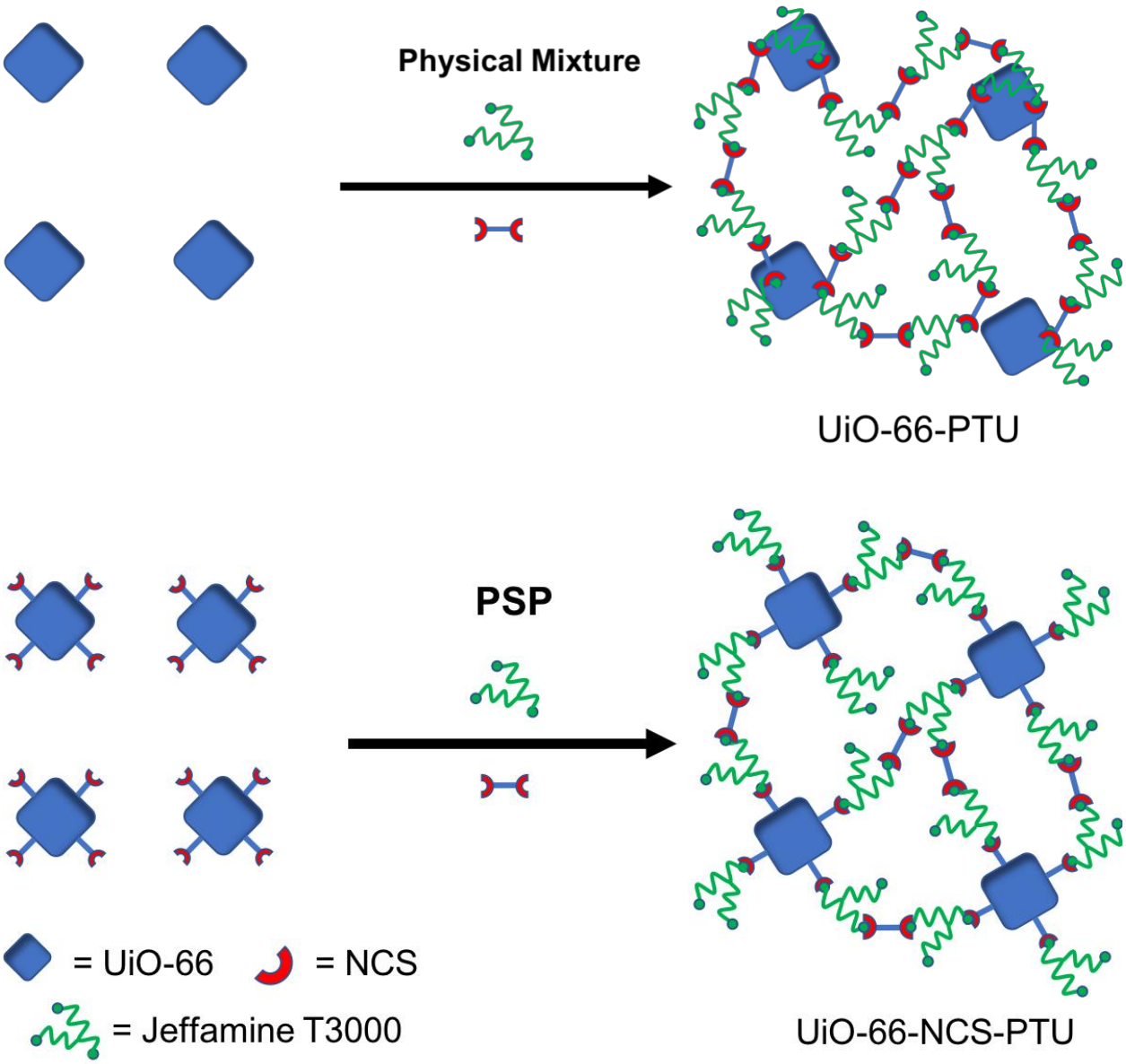

Figure 4.6. Scheme displaying the synthesis of MOF-PTU composite material. An amine terminated polypropylene polymer (Jeffamine T3000) is combined with UiO-66-NCS forming a thiourea linkage. Addition of 1,4-phenylene diisocyanate acts to further extended the thiourea polymers and crosslink MOF particles together resulting in a MOF-PTU membrane.

The same synthetic procedure was followed for the synthesis of PTU membranes using UiO-66 and UiO-66-NH_2. Using the exact procedure as outlined above, UiO-66-NH_2 MOF was suspended in CH_2Cl_2 and Jeffamine T3000 was subsequently added to the mixture. Upon addition

of 1,4-phenylene diisothiocyanate and evaporation of the solvent in a petri dish, the composite material failed to form resulting in a non-solid substance (Figure 4.7). This suggests the amine terminated polymer and UiO-66-NH_2 reacted with 1,4-phenylene diisothiocyanate molecule in a competitive fashion resulting in no composite material. The same procedure was followed with UiO-66, where a solid composite material was formed upon addition of the 1,4-phenylene diisothiocyante molecule (Figure 4.6). The UiO-66-PTU composite displays a distinct phase separation between the MOF and polymer components (Figure 4.7 and Figure 4.8). PXRD of the top and bottom side of the composite materials clearly indicate UiO-66 settles to the bottom of the petri dish (Figure 4S.14-4S.16). Furthermore, SEM and EDX images of the MOF-PTU composite cross sections clearly show phase separation of the MOF and polymer materials (Figure 4.8, Figure 4S.17). BET surface area measurements of the UiO-66-NCS-PTU and UiO-66-PTU composite materials display almost no porosity (data not shown). This suggests that the crosslinked polymer network is potentially blocking access to the MOF pores. By contrast, the UiO-66-NCS-PTU composite displays more uniform incorporation of MOF throughout as evidenced by PXRD, SEM, and EDX (Figure 4.7, Figure 4S.17-4S.21). This suggests the chemically reactive -NCS functional groups form covalent linkages with the polymer that are crucial for the formation of a uniform composite material. To further asses the applicability of these hybrid materials, a facile spray coating technique onto Nyco fibers was developed.

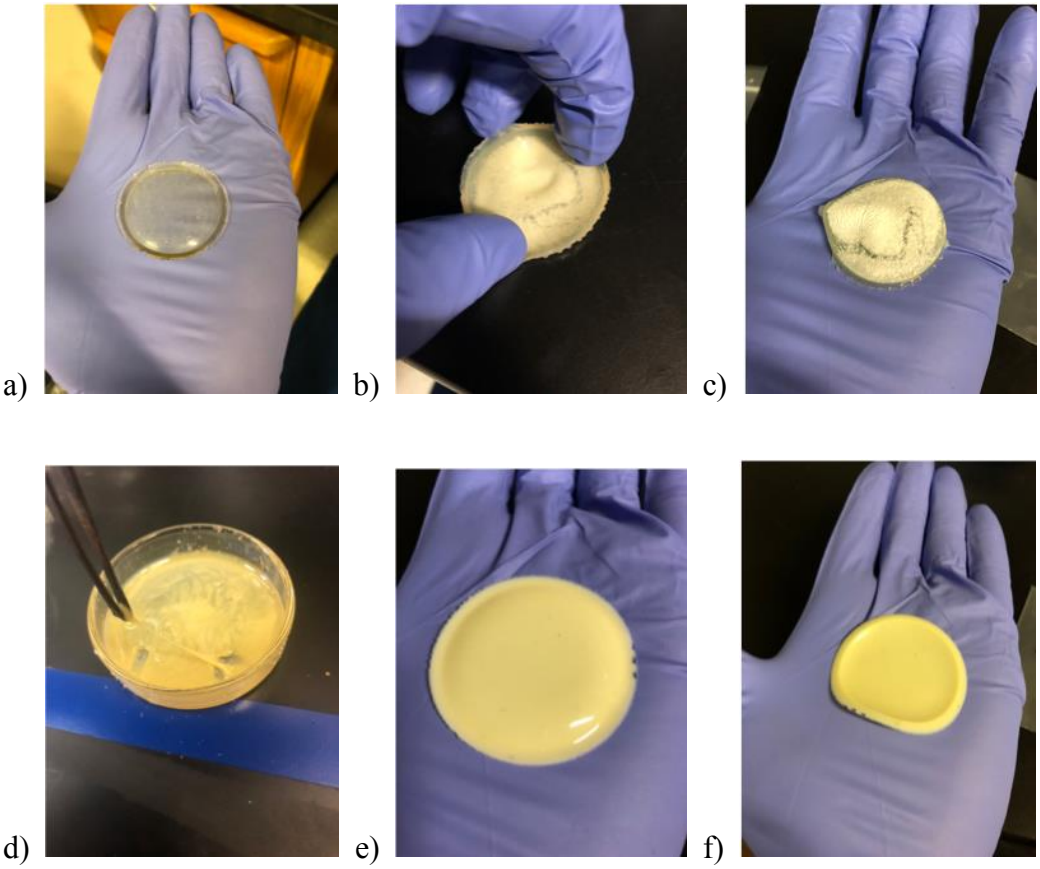

Figure 4.7. Photographic images of MOF-PTU composites. a) pure PTU composite b) top side of ~13% UiO-66-PTU composite c) bottom side of ~13% UiO-66-PTU composite d) UiO-66-NH_2-PTU attempted synthesis e) top side of ~13% UiO-66-NCS-PTU composite f) bottom side of ~13% UiO-66-NCS-PTU composite.

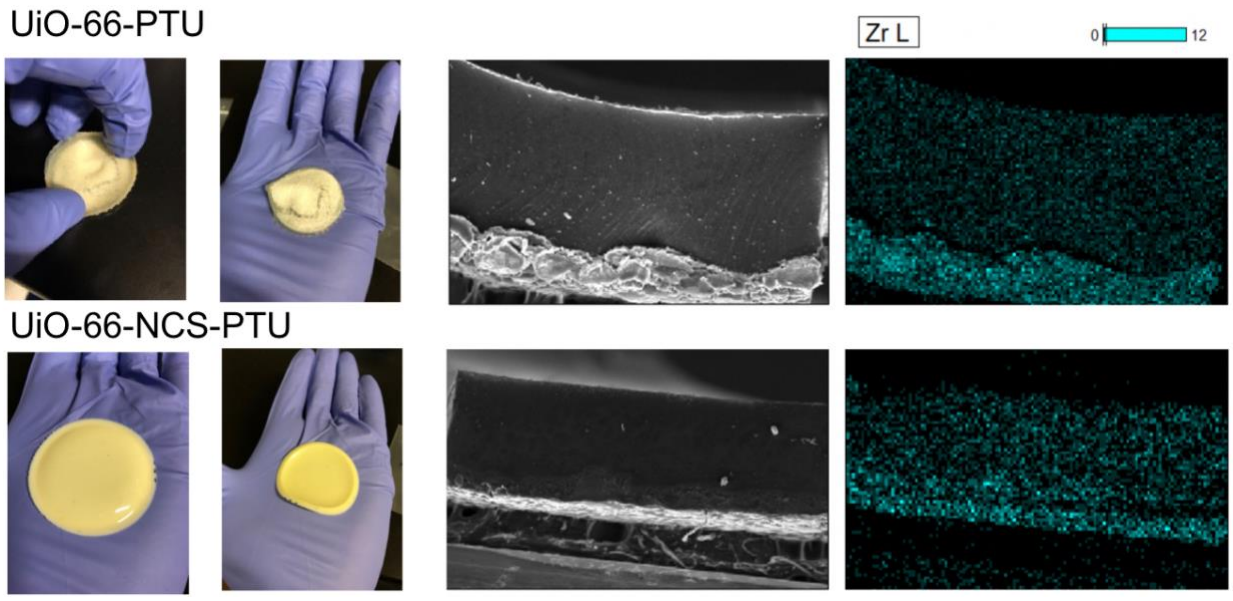

Figure 4.8. *Top:* Images of UiO-66-PTU membranes viewed from top (left) and bottom (right) faces. SEM and EDX images of the UiO-66-PTU cross section highlighting the phase separation of MOF and polymer components. *Bottom:* Images of UiO-66-NCS-PTU composite materials viewed from top and bottom, left and right, respectively. SEM and EDX images of the cross section highlighting well dispersed MOF as evidenced by the presence of Zr throughout the membrane.

While polyurea polymers are not commonly used textiles, they are utilized as commercial spray coating products. To test the spray coating ability of MOF-PTU materials, the composites were applied to common warfighter textiles known as Nyco (nylon and cotton blended fibers). Similar to the preparation of the MOF-PTU composite material, MOF was suspended in CH_2Cl_2 and Jeffamine T3000 was added to the solution, coupling the polymer to the MOF. Next, 1,4-phenylene diisothiocyanate was added to the mixture and the mixture was quickly loaded into a Preval Sprayer (see appendix for more details). The MOF-PTU solution was promptly sprayed onto a swatch of Nyco fibers which were subsequently dried under ambient conditions.

UiO-66-NCS-PTU spray coating onto Nyco fibers resulted in good adhesion to the fibers, with the Nyco material nearly indistinguishable from uncoated fibers (Figure 4.9). To determine

the mass loading of the composite, TGA analysis was performed on the spray coated Nyco fibers, which gave a MOF loading of 8.3±0.7 wt% (Table 4S.4). PXRD on the fibers display high intensity peaks indicating the presence of highly crystalline MOF (Figure 4S.22). To determine the extent of MOF adhesion to the Nyco fibers, a tape test was conducted (see appendix for details), where two-sided tape was used to examine if particles could be easily removed from the Nyco surface.[8] The tape test of UiO-66-NCS-PTU Nyco fibers indicated there was no MOF removed from the Nyco surface (Figure 4S.23). Coated Nyco fibers were also scratched with a laboratory spatula and no MOF was observed falling from the swatch. SEM images of the fibers after spray coating with UiO-66-NCS-PTU display a consistent layer of a MOF-polymer coating onto the fibers with little to no MOF aggregation (Figure 4S.24). The SEM images clearly indicate the presence of MOF embedded in polymer on the Nyco surface (Figure 4.8, Figure 4S.24).

Several control experiments were conducted to further analyze the significance of the MOF-polymer covalent linkage as well as the presence of polymer in the spray coating. First, pure PTU (a combination of phenyl diisothiocyanate and Jeffamine T3000) was spray coated on Nyco fibers and the SEM images and PXRD results indicate a cohesive polymer layer on the fibers (Figure 4S.25). Further, crystalline UiO-66-NCS suspending in CH_2Cl_2 was also sprayed on the fibers and the powdery material is shown to easily fall off the fibers after drying (Figure 4S.26). The tape test was conducted for pure MOF spray coated materials and the results clearly indicate abundant MOF removal from the Nyco surface (Figure 4S.27). Experiments were also performed with a physical mixture control consisting of the canonical UiO-66 and the PTU polymer sprayed onto Nyco fibers. PXRD indicates the presence of MOF on the surface of the fibers (Figure 4S.28). TGA analysis was performed on the Nyco fibers and the results indicate a MOF loading of 9.1±1.3 wt%, nearly identical to that of the UiO-66-NCS-PTU sprayed fibers (Table S4). Optical images

of the fibers after spray coating indicate a clear phase separation between the MOF, polymer and Nyco fibers (Figure 4.9). SEM images of the UiO-66-PTU Nyco coating display clear aggregation of the MOF particles and phase separation between the MOF particles and the polymer on the Nyco Fibers (Figure 4.9 and Figure 4S.29). Further, the tape test was performed on the UiO-66-PTU spray coated material the results indicate that MOF is removed from the Nyco surface as evidenced by optical images and PXRD (Figure 4S.30). Similar to the MOF-PTU composites, BET measurements of all the spray coated MOF-PTU on Nyco fibers show almost no porosity, which may result from partial pore blockage by the crosslinked polymer network.

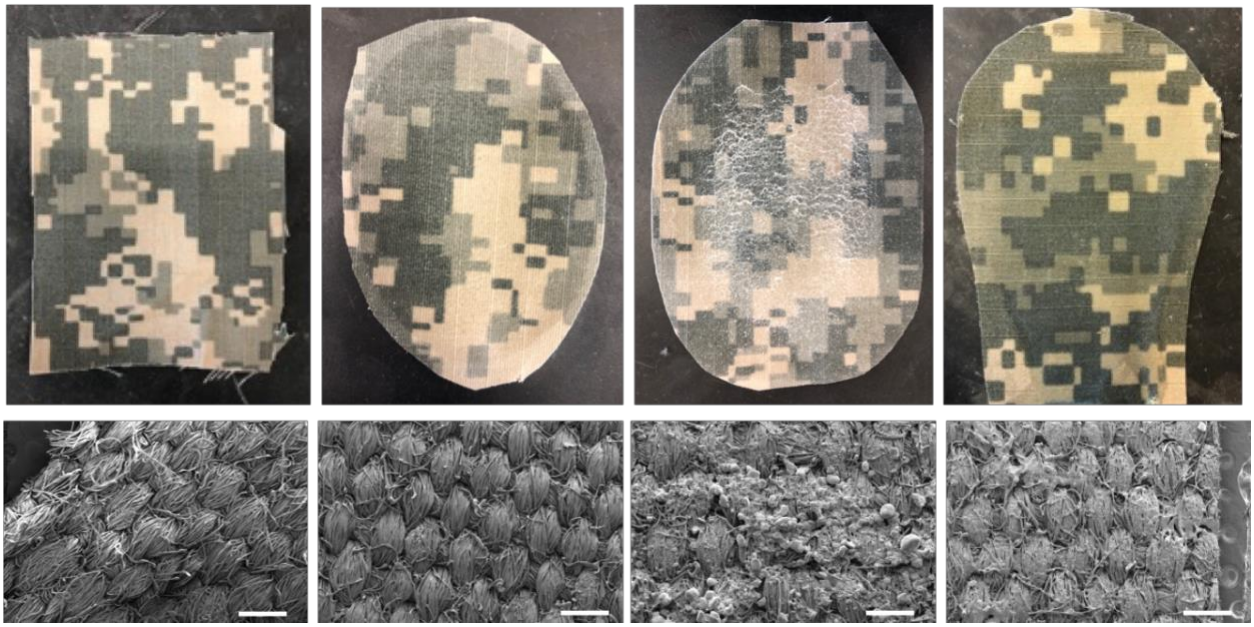

Figure 4.9. *Top:* Optical images of swatches of Nyco fibers (left to right): pure Nyco, PTU on Nyco, UiO-66-PTU on Nyco, and UiO-66-NCS-PTU on Nyco. *Bottom:* Corresponding SEM images of Nyco fibers. Scale bars are 500 μm.

Spray coated Nyco fibers and MOF-PTU composites were screened for the degradation of DMNP using a previously reported method (Figure 4.10 and Figure S31).[1] UiO-66-NCS-PTU fibers displayed similar activity to that of the UiO-66-PTU fibers (Figure 4.10). Pure Nyco and

PTU spray coated Nyco fibers displayed no catalytic activity. The catalytical activity of the as-synthesized MOF powders (Figure 4.4) displayed a 10-fold increase in activity for UiO-66-NCS compared to UiO-66. However, when coated on Nyco, the activity of UiO-66-NCS-PTU and UiO-66-PTU are approximately equal. The reduction in activity between the MOF-PTU hybrids when compared to the polycrystalline MOF may be the result of the crosslinked polymer limiting access to some of the active sites within the MOF pores. Further, the conversion of the -NCS functional group to a thiourea linkage as a function of the Jeffamine T3000 could also result in reduced CWA activity.

To test the durability of these fibers, Nyco UiO-66-NCS-PTU and UiO-66-PTU fibers were subjected to a wash test where Nyco swatches were stirred in a beaker containing water and soap for 3 h (see appendix for details). This test was performed as a proof-of -concept to mimic laundry conditions that these fibers would be exposed to if incorporated into fielded uniforms. PXRD of the UiO-66-NCS-PTU and UiO-66-PTU spray coated fibers show MOF is still present after the laundry test. SEM images of the UiO-66-NCS-PTU spray coated fibers display no difference in the fibers before and after the laundry test (Figure 4S.32). SEM images of the UiO-66-PTU spray coated fibers display a significant loss of large MOF aggregates on the surface of the Nyco fibers compared to the prewashed swatches; however, some MOF aggregates are still observed (Figure 4S.33). The fibers were then screened for their DMNP activity after the wash test. The Nyco UiO-66-PTU fibers displayed a substantial decrease in activity whereas the UiO-66-NCS-PTU fibers showed no decrease in catalytic activity. This result indicates that when these fibers are subjected to physical agitation the non-covalent composite materials are less durable when compared to the covalent UiO-66-NCS-PTU material.

While MOF powders have been extensively screened for the degradation of DMNP, significantly fewer reports have screened MOF-polymer hybrid materials. As outlined in Chapter 1, Existing reports are mainly from the work of Parsons and co-workers using MOF-polymer composites synthesized by ALD for the degradation of the DMNP simulant and CWAs.[9, 10] While these materials have shown promise in rapid degradation of both simulants and agents, the ALD methodology is time consuming and expensive. Moreover, the ALD materials lack covalent attachment to the polymer backbone making them potentially susceptible to physical agitation. Recently, Farha and coworkers also reported a method for coating textiles with Zr-based MOFs.[11] These materials displayed good activity for the degradation of nerve agents; however, tests for the physical durability, such as a laundry simulation test, of these MOF-textile composites were not described. The method described here is a facile route to synthesizing highly functional MOF-polymer textiles that can endure physical agitation and maintain catalytic activity.

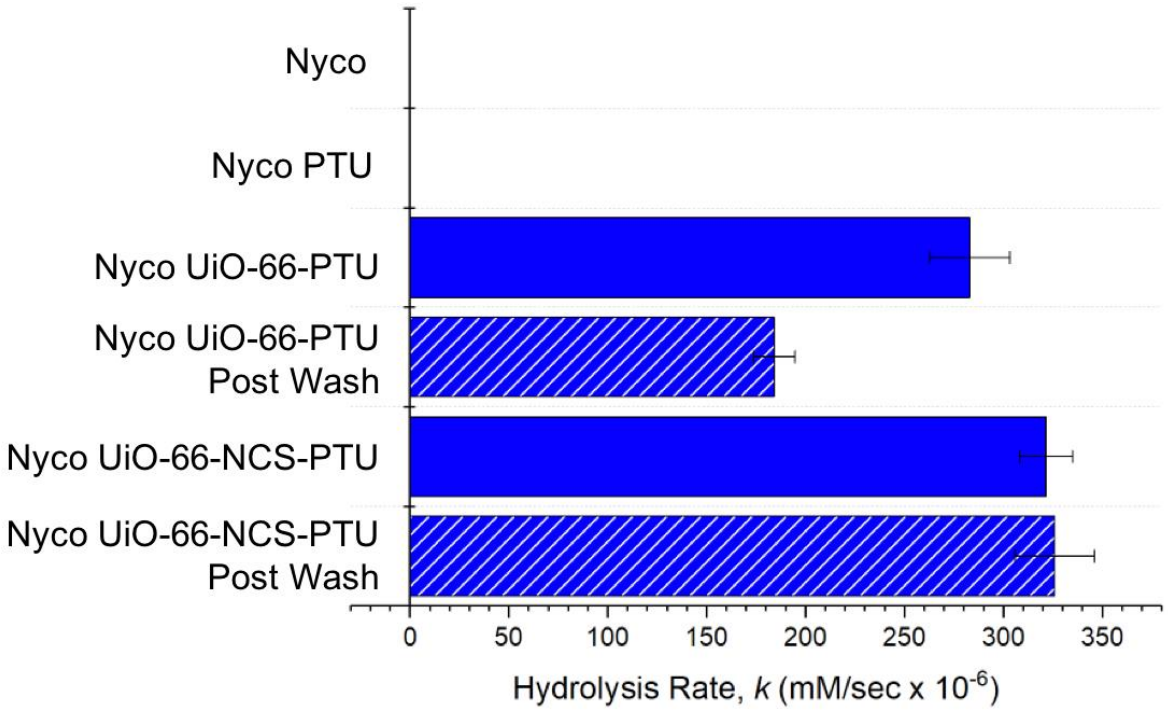

Figure 4.10. *Top:* DMNP hydrolysis rates by Nyco spray coated fibers before and after conducting the laundry wash simulation. Data shown is an average of three different swatches run in triplicate.

4.4 Conclusions

Herein, PSP has been shown to be an effective way of applying a catalytically active MOF-polymer spray coating onto textile fibers. UiO-66-NH_2 was first subjected to PSM yielding UiO-66-NCS. Using the HTS conditions reported above, this MOF displayed the highest catalytic activity to date (among 110 MOFs tested at pH = 8) for the degradation of the CWA simulant DMNP. The -NCS reactive handles on the MOF were further utilized to covalently connect the MOF to an amine terminated polymer. Through PSP a MOF-polymer hybrid material was synthesized under mild conditions. The MOF-polymer hybrid material was spray coated onto Nyco textile fibers and display good adhesion to the surface of the material compared to control experiments. More importantly, the MOF maintains catalytic activity against DMNP while coated on the Nyco fibers. Another notable feature of this material is the durability of the covalent MOF-polymer hybrid, which shows enhanced physical durability when compared with other formulations that do not result in PSP materials. This is a useful and facile way of synthesizing a catalytically active textile fiber for protection from CWAs. This method of PSP will open the door to tethering various amine terminated polymers to the surface of MOFs.

4.5 Appendix: Supporting Information

Materials

All solvents and starting materials were purchased from chemical suppliers and used without further purification (Sigma Aldrich, Alfa Aesar, EMD, and TCI).

MOF Synthesis

UiO-66. Zirconium(IV) chloride (61 mg, 0.26 mmol) and terephthalic acid (43 mg, 0.26 mmol) were dissolved in 15 mL DMF with 0.45 mL glacial acetic acid in a 20 mL vial with Teflon-lined cap. The vial was then placed in a 120 °C oven for 24 h. After cooling to ambient temperature, the particles were collected by centrifugation (fixed-angle rotor, 6000 rpm, 5 min), followed by washing with 3×10 mL DMF and 3×10 mL MeOH. The particles were then soaked in MeOH for 3 d with solvent changed daily, before being dried under vacuum at room temperature. The procedure was repeated in parallel 40 times and all products were combined. (2.76g)

UiO-66-NH_2. Zirconium(IV) chloride (61 mg, 0.26 mmol) and 2-aminoterephthalic acid (43 mg, 0.26 mmol) were dissolved in 15 mL DMF with 0.45 mL glacial acetic acid in a 20mL vial with Teflon-lined cap. The vial was then placed in a 120 °C oven for 24 h. After cooling to ambient temperature, the particles were collected by centrifugation (fixed-angle rotor, 6000 rpm, 5 min), followed by washing with 3×10 mL DMF and 3×10 mL MeOH. Using a modified procedure, the formyl groups were restored to free amine. 2 g of UiO-66-NH_2 was added to 100 mL MeOH:H_2O 1:1 mixture with 5 mL of conc. HCl and refluxed overnight. Solid was collected by filtration and washed with MeOH. The entire procedure was repeated in parallel 40 times and all products were combined. (3.23g)

UiO-66-NCS. UiO-66-NH_2 (0.37 mmol, 110 mg) was dispersed in tetrahydrofuran (10 mL) with ultrasonication for 10 min. Thiophosgene (varying amounts, see Table S1) was then added to this dispersion and heated to 55°C for 18 h. The particles were then washed 3x with 40 mL of CH_2Cl_2 and soaked in CH_2Cl_2 for 3 days with solvent changed daily before being dried under vacuum at room temperature (~110 mg).

UiO-66-NCS-hexylamine. UiO-66-NCS (0.30 mmol, 100 mg) was dispersed in CH_2Cl_2 (10 mL) with ultrasonication for 10 min. Hexylamine (0.8 mL, 10 mmol) was then added to this dispersion and stirred at RT for 4 h. The particles were then washed 3x with 40 mL of CH_2Cl_2 and soaked in CH_2Cl_2 for 3 days with solvent changed daily before being dried under vacuum at room temperature (~100 mg).

MOF-PTU Synthesis. Varying amounts of MOF (50 mg, 100 mg, and 200 mg) were added to a 6-Dram vial. Subsequently, 5 mL of CH_2Cl_2 was added and the MOF was dispersed in the solution by sonication for 15 min. Then, an excess of Jeffamine T3000 (1.0g, 0.33mmol) was added to the mixture and the solution is sonicated for exactly 10 min. In a separate 1-Dram vial, 1,4,-phenylene diisocyanate (100mg, 0.33mmol) is dissolved in 2mL of CH_2Cl_2 by sonication. The solutions are added together, the material is quickly vortexed and casted out on a glass petri dish. The solvent is allowed to evaporate, and the composite appears present after about 1 h. To delaminate the composite material from the petri dish, the edges of the composite and petri dish are slightly scratched. Subsequently, ethanol is added to the dish causing the composite to swell and rapidly delaminate from the dish.

Spray Coating of MOF-PTU on Nyco Fibers. In a 6-Dram vial, 100 mg of MOF are dispersed in 10 mL of CH_2Cl_2 for 20 min. To that MOF solution, 250mg (0.083 mmol) of Jeffamine T3000 are added and the mixture is then sonicated for exactly 10 min. In a separate 1-Dram vial, 25mg

(0.16 mmol) of 1,4-phenylene diisocyanate is dissolved in 2 mL of CH_2Cl_2 by sonication. The 1,4-phenylene diisothiocyanate solution is then added to the MOF solution and the mixture is rapidly stirred (~5 sec). The 6-Dram vial containing this mixture is then loaded into a Preval Sprayer and sprayed onto a swatch of precut Nyco fibers (4 inch by 4 inch) until the entire vial has been used. The fibers are then allowed to dry in ambient conditions for the next 24 h. Small pieces of these fibers (½ inch by ½ inch)

Are then used to perform characterization analysis of these materials unless indicated otherwise.

Table 4S.1. MOF synthesis conditions for varying amount of NCS ligand functionalization and amount functionalized by ^{1}H NMR digestion.

MOF	Thiophosgene	NCS groups by ^{1}H NMR Digestion
UiO-66-NCS$_{15\%}$	10 μL (0.125mmol)	16.4%
UiO-66-NCS$_{25\%}$	20 μL (0.250mmol)	29.8%
UiO-66-NCS$_{50\%}$	30 μL (0.375mmol)	56.2%
UiO-66-NCS$_{75\%}$	40 μL (0.500mmol)	77.6%
UiO-66-NCS$_{85\%}$	50 μL (0.625mmol)	85.5%
UiO-66-NCS	800 μL (10mmol)	100 %

Table 4S.2. MOF wt %in MOF-PTU hybrid materials as determined by TGA.

MOF	MOF loading	MOF wt % in composite as determined by TGA
UiO-66-NCS	50 mg	5.15 ± 1.07 %
UiO-66-NCS	100 mg	8.38 ± 0.71 %
UiO-66-NCS	200 mg	13.30 ± 0.75 %
UiO-66	50 mg	5.56 ± 0.74 %
UiO-66	100 mg	9.70 ± 1.20 %
UiO-66	200 mg	13.32 ± 1.52 %

Characterization Methods

Powder X-ray Diffraction (PXRD). PXRD data was collected at room temperature on a Bruker D8 Advance diffractometer running at 40 kV, 40 mA for Cu Kα (λ = 1.5418 Å), with a scan speed of 0.5 sec/step, a step size of 0.01° in 2θ, and a 2θ range of 3-50° at room temperature.

Scanning Electron Microscopy (SEM). MOF and MOF-polymer hybrids were placed on conductive carbon tape on an aluminum sample holder and coated using an iridium-sputter coating for 8 s. A FEI Quanta FEG 250 microscope was used for acquiring images using a 3-5 kV energy source with a spot size of 3 under high vacuum at a working distance of 10 mm.

Nuclear Magnetic Resonance. Proton nuclear magnetic resonance spectra (^{1}H NMR) were recorded on a JOEL ECA 500 MHz spectrometer. Chemical shifts are quoted in parts per million (ppm) referenced to the appropriate solvent peak or 0 ppm for TMS. MOFs were digested for NMR analysis by immersion of ~8-10 mg MOF in 580 μL DMSO-*d*$_6$ with 10 μL HF (48% in water). Samples were kept in this acidic solution at room temperature until the MOF was fully dissolved.

N_2 Gas Sorption Analysis: Samples for analysis were evacuated in a vacuum oven overnight at room temperature prior to analysis. ~50 mg of sample was then transferred to pre-weighed sample tubes and degassed at 105 °C on a Micromeritics ASAP 2020 Adsorption Analyzer for a minimum of 12 h or until the outgas rate was <5 mmHG. After degassing, the sample tubes were re-weighed to obtain a consistent mass for the samples. Sorption data and BET surface area (m^2/g)

measurements were collected at 77 K with N_2 on a Micromeritics ASAP 2020 Adsorption Analyzer using volumetric technique.

Thermogravimetric analysis (TGA). ~10 mg of sample were placed in a 100 μL aluminum crucible. Samples were analyzed on a Mettler Toledo Star TGA/DSC using a temperature range of 30-600 °C scanning at 10 °C/min under an N_2 atmosphere (75 cm^3/min N_2 flow rate) for sample degradation measurements. Samples were heated from room temperature to 300 °C then cooled back down to room temperature and subsequently heated to 600 °C.

Catalysis Experiments: In this study, DMNP hydrolysis was measured using a modified version of a previously reported procedure.[6] All catalytic monitoring was carried out using a BioTek Synergy H4 plate reader using single wavelength absorbance mode. 20 and 40 mM of *N*-ethylmorpholine buffer was prepared from deionized water adjusted to pH = 8.0. A plot of absorbance of *p*-nitrophenol at varying concentrations was measured yielding a calibration curve with a slope of 3.48 Abs/mM.[6]

MOF Powder Catalysis Experiments. All catalytic monitoring was carried out using a BioTek Synergy H4 plate reader using single wavelength absorbance mode. First a plot of absorbance of *p*-nitrophenol at varying concentrations was measured yielding a conversion factor of 3.48 Abs/mM.[6] MOF samples were prepared by weighing 6 mg of MOF powder and diluting this powder in 10 mL of deionized water. These solutions were rigorously sonicated and vortexed (>3× of each) and diluted in half with 40 mM buffer solution yielding 300 μg/mL MOF in 20 mM

buffer solution. Dimethyl *p*-nitrophenylphosphate (DMNP) hydrolysis assays with MOF powders were carried out in Olympus Plastics clear, flat-bottom 96-well plates. Each well was prepared with 100 μL total volume containing: 95 μL MOF suspension in buffer and 5 μL substrate (25 mM DMNP in MeOH; 1.25 mM total concentration; 0.125 μmol). Upon the addition of substrate using a multi-channel pipette, hydrolysis was monitored by the change in absorbance (λ_{max} = 407 nm) over 15 min at 24 °C with 3 sec shaking of the plate every 10 sec. Activity was measured as initial linear rates, assuming zero-order kinetics, using the change in absorbance from p-nitrophenoxide generated from the degradation of DMNP measured from 30 to 360 sec min using Excel software.[2] Reported activities for MOF samples are an average of seven replicates. Hydrolysis rates were adjusted to account for the increased mass of the various species such that a direct comparison could be made across all materials in this study as previously reported.[2]

MOF-polymer composite catalysis experiments. MOF-polymer composite and spray coated Nyco materials were screened using a previously reported method.[1] Fibers of each composite were cut into small segments (1 inch by ¼ inch, ~30mg) and placed into a well of a Genier Bio-one Cellstar 24well plate. Each well was prepared with 1.5 mL total volume containing: a single fiber, 1.5 mL of 20 mM buffer and 10 μL substrate (25mM DMNP in methanol). DMNP hydrolysis was monitored in the 60 to 600 sec time period. Reported activities for MOF-polymer composites are an average of three replicates.

Nyco MOF-PTU Tape Test. To test the adhesion of the MOF-PTU spray coating onto the Nyco fibers we conducted a tape test. A piece of double-sided tape (3 inches in length) was used. The

tape was pressed onto the spray coated Nyco fibers and removed from the surface in one quick swoop. To determine if MOF-PTU was removed from the surface the clean side of the tape was attached to a PXRD sample holder and the sample was analyzed (see Figure 4S.21, 4S.24 and 4S.27).

Nyco MOF-PTU Wash Test. To test the adhesion of the MOF-PTU spray coating onto the Nyco fibers we conducted a laundry simulation test. A MOF-PTU spray coated Nyco swatch was placed in a 500 mL beaker containing 300 mL of water and 50 mL of Alconox detergent (10g/L) liquid solution. The solution was stirred (500 rpm) at room temperature for 3 h. Subsequently, the swatch was taken out of the solution, rinsed thoroughly with H_2O and subsequently dried under vacuum overnight.

Table 4S.3. Corrected hydrolysis calculation to account for increased mass of halogenated materials.

MOF	Molar Mass of MOF (*g/mol*)	Mole ratio to UiO-66 Standard	Experimental Hydrolysis Rate[a] (*k*, mM/sec)	Molar Mass Corrected Hydrolysis Rate (*k*, mM/sec)
UiO-66-NH_2	1752	1.00	76	76
UiO-66-$NCS_{15\%}$	1789	0.98	162	165
UiO-66-$NCS_{25\%}$	1815	0.96	159	166
UiO-66-$NCS_{50\%}$	1878	0.93	338	363
UiO-66-$NCS_{75\%}$	1941	0.90	467	519
UiO-66-$NCS_{85\%}$	1966	0.89	911	1024
UiO-66-NCS	2004	0.87	1061	1220

[a] 6 mg of MOF used in each experiment.

MOF Characterization

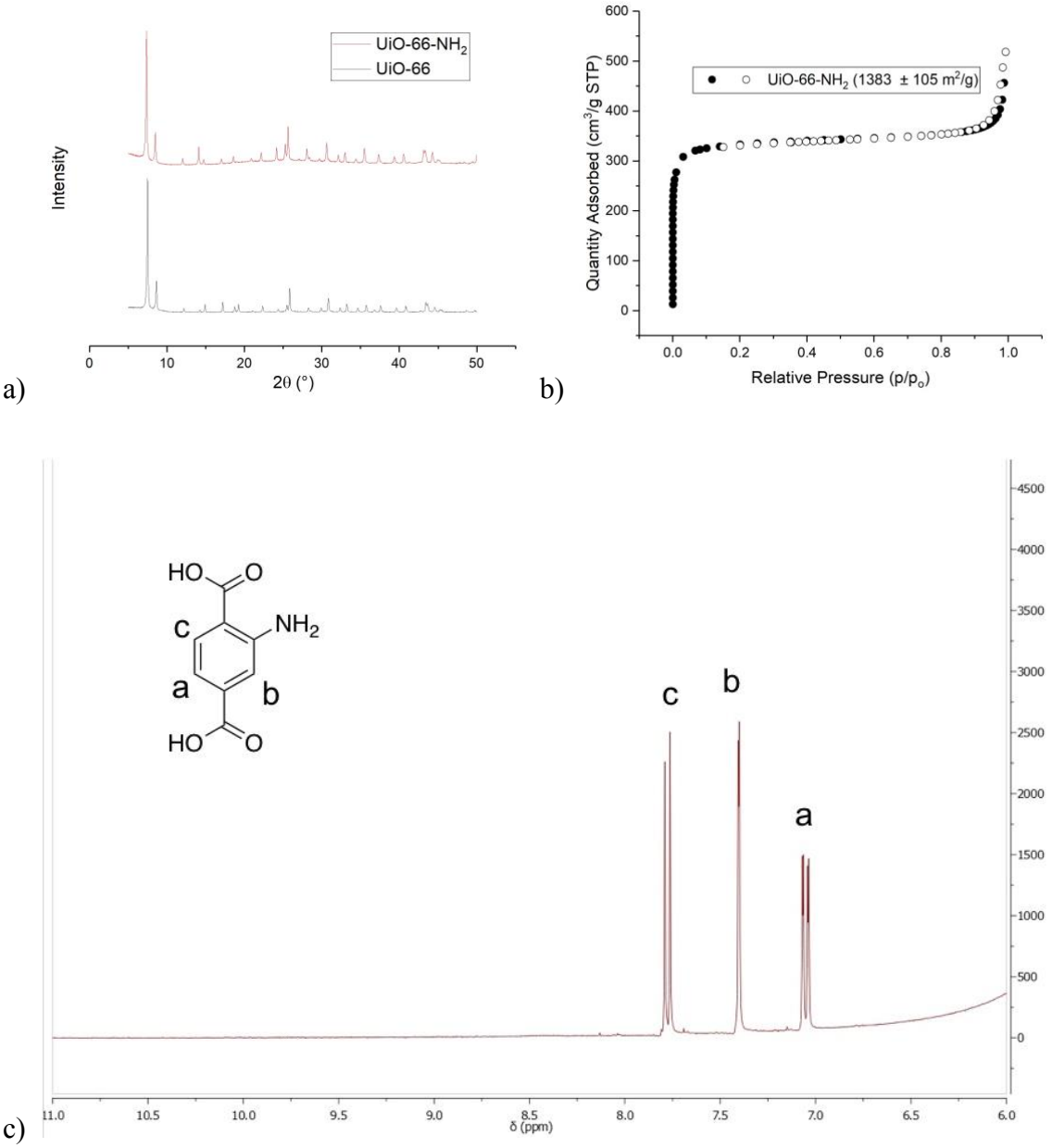

Figure 4S.1. Characterization of UiO-66-NH_2. a) PXRD, b) N_2 adsorption isotherm and c) ^1H NMR analysis of digested UiO-66-NH_2.

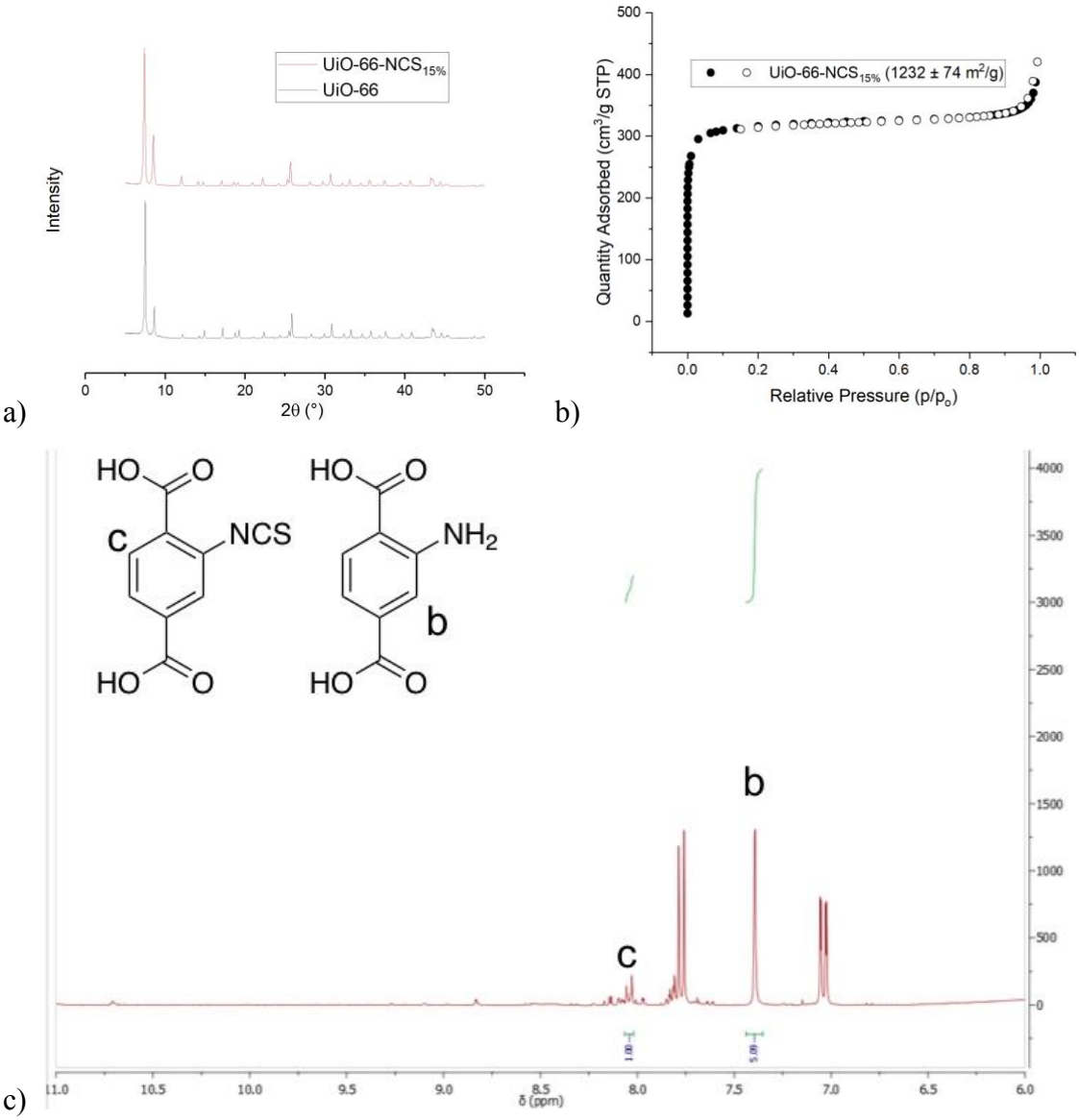

Figure 4S.2. Characterization of UiO-66-NCS$_{15\%}$. a) PXRD, b) N_2 adsorption isotherm and c) ^{1}H NMR analysis of digested UiO-66-NCS$_{15\%}$.

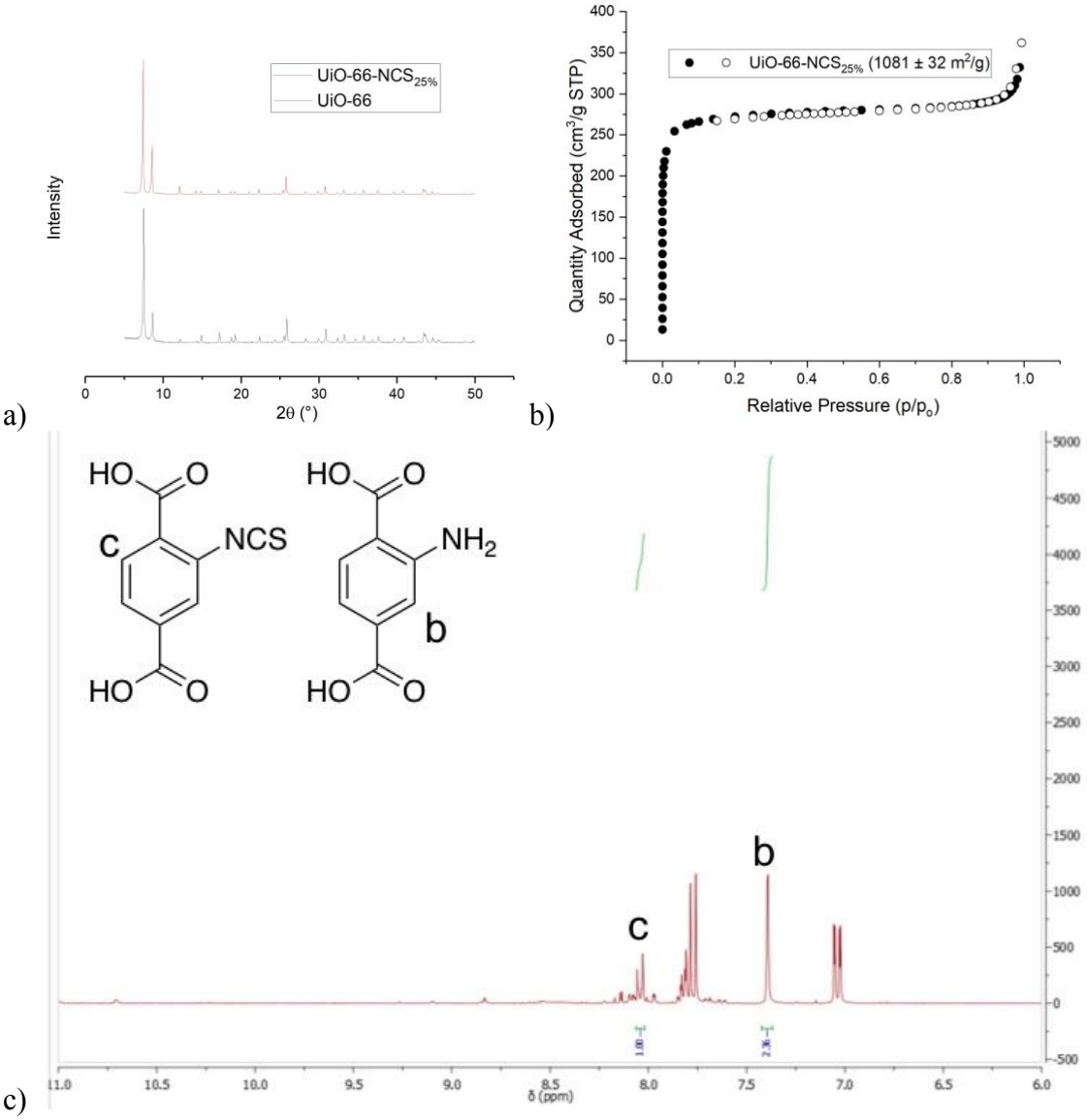

Figure 4S.3. Characterization of UiO-66-$NCS_{25\%}$. a) PXRD, b) N_2 adsorption isotherm and c) ^1H NMR analysis of digested UiO-66-$NCS_{25\%}$.

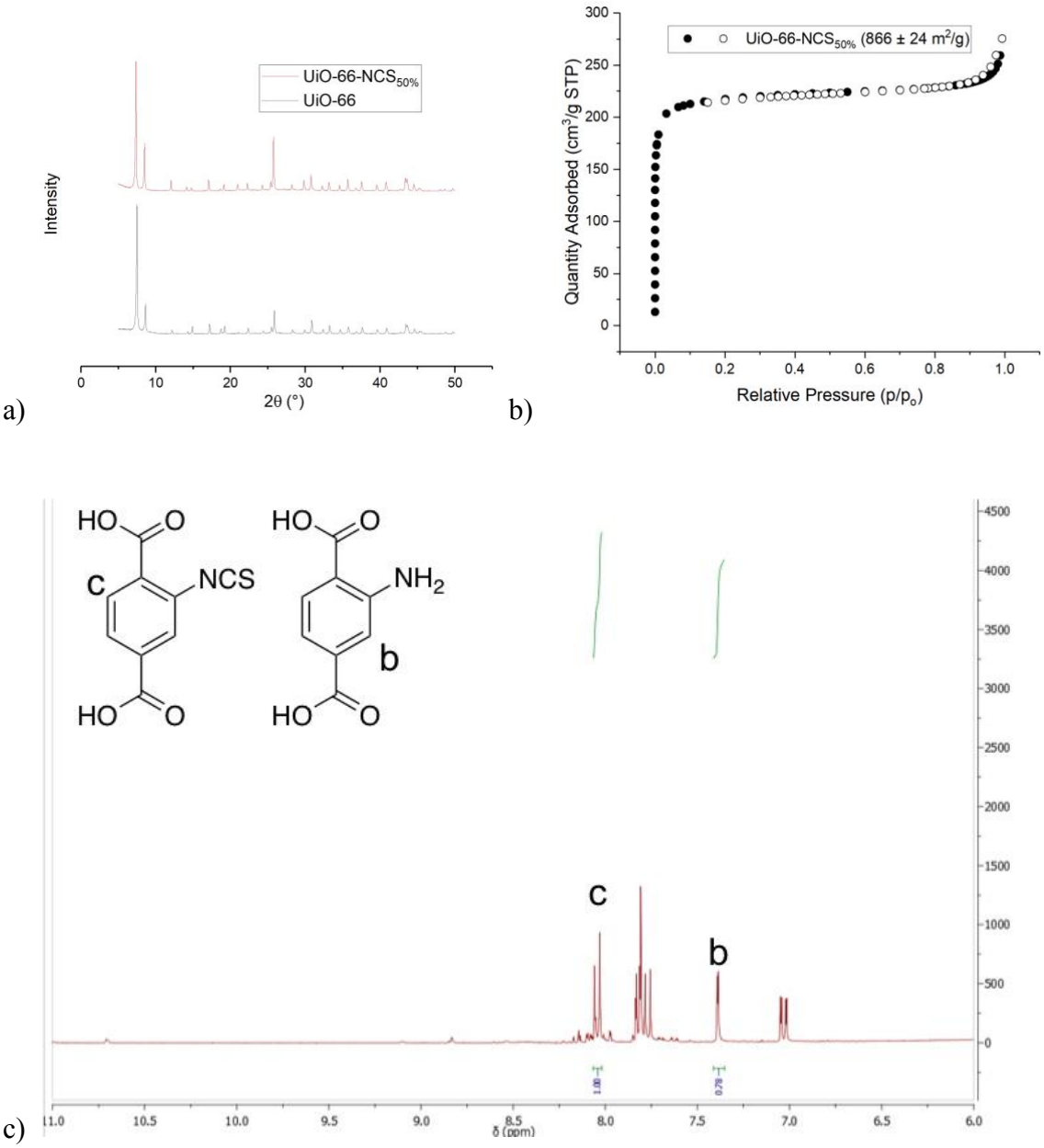

Figure 4S.4. Characterization of UiO-66-NCS$_{50\%}$. a) PXRD, b) N_2 adsorption isotherm and c) ^{1}H NMR analysis of digested UiO-66-NCS$_{50\%}$.

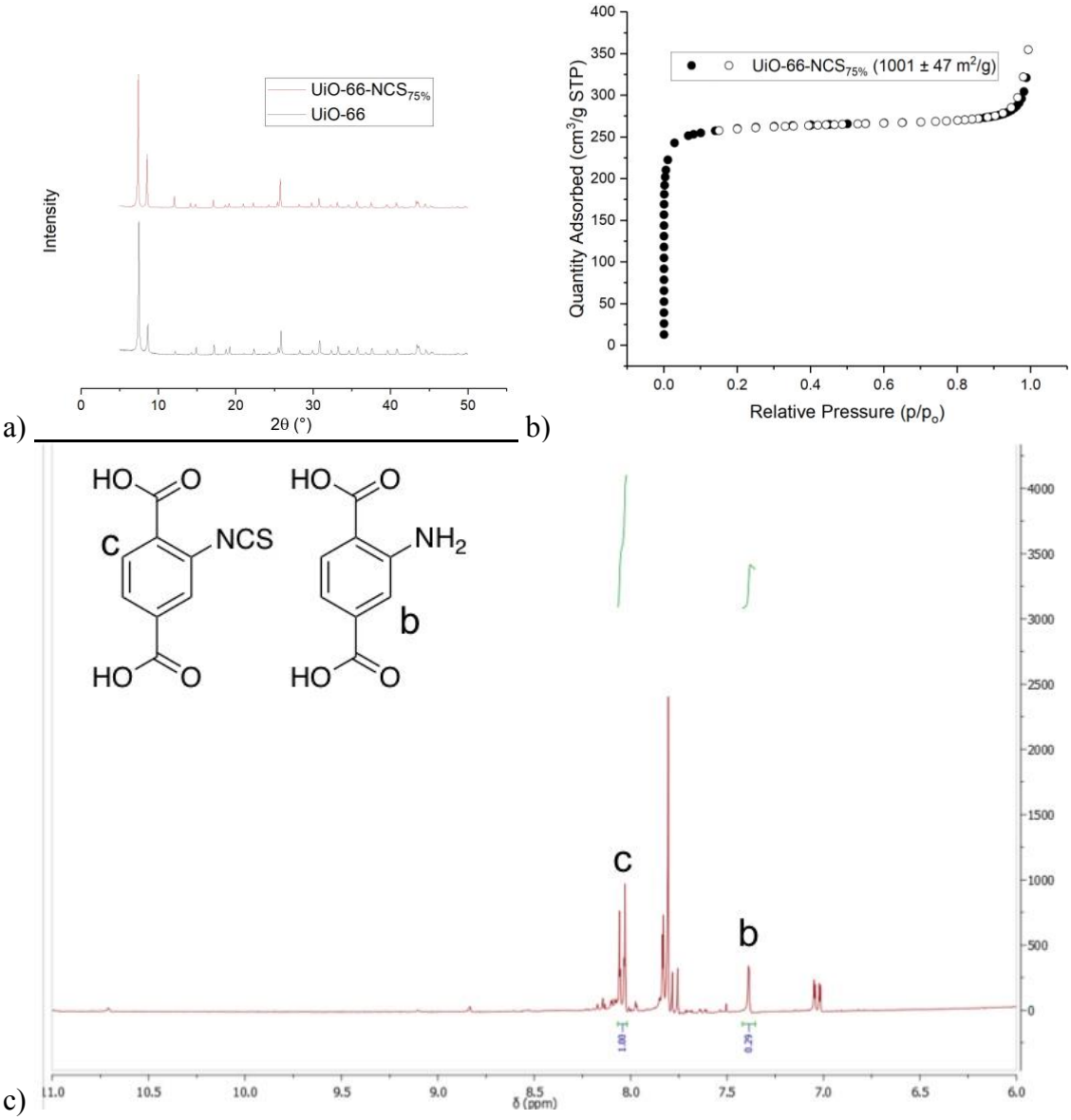

Figure 4S.5. Characterization of UiO-66-NCS$_{75\%}$. a) PXRD, b) N_2 adsorption isotherm and c) ^{1}H NMR analysis of digested UiO-66-NCS$_{75\%}$.

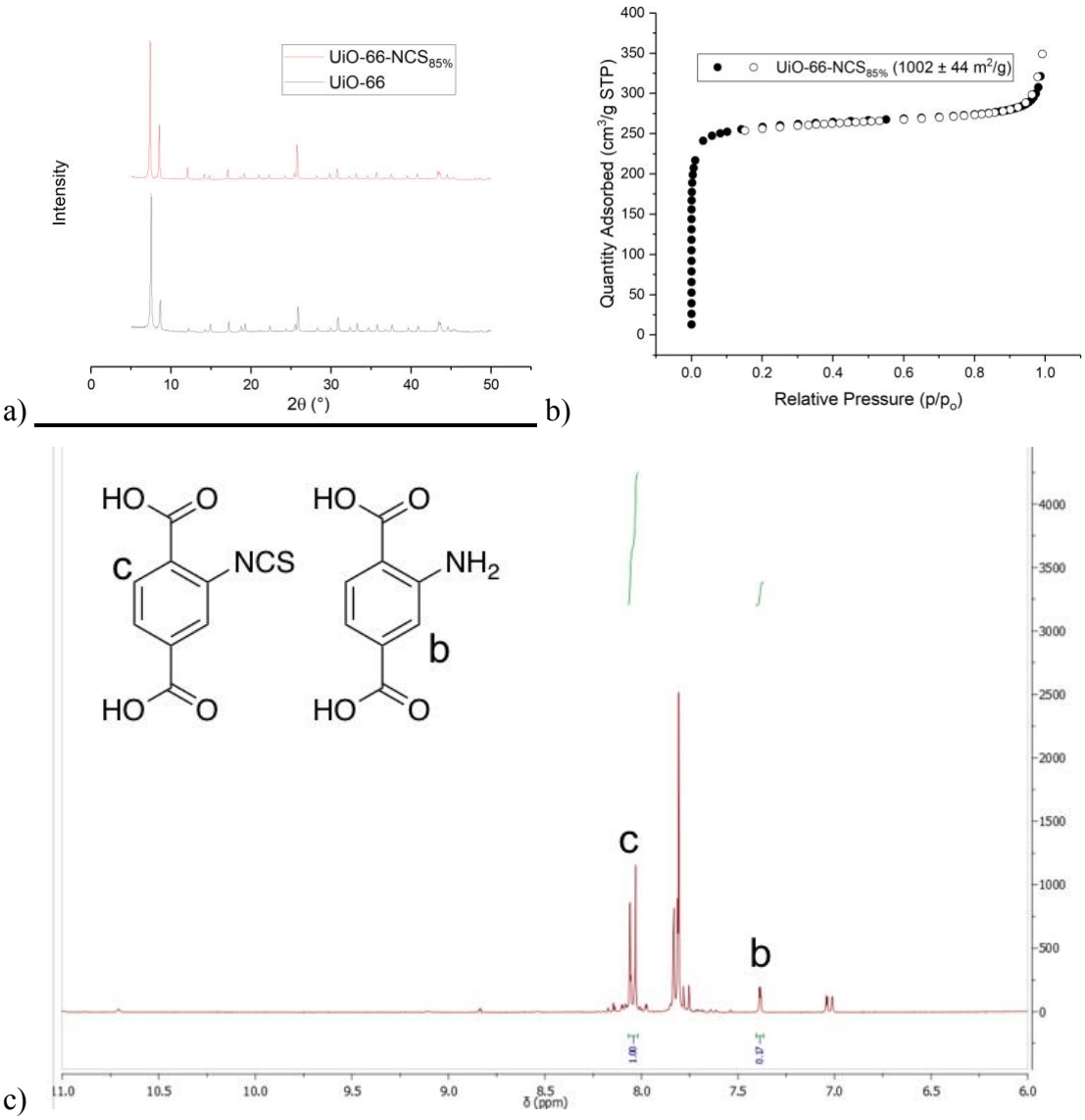

Figure 4S.6. Characterization of UiO-66-NCS$_{85\%}$. a) PXRD, b) N_2 adsorption isotherm and c) ^{1}H NMR analysis of digested UiO-66-NCS$_{85\%}$.

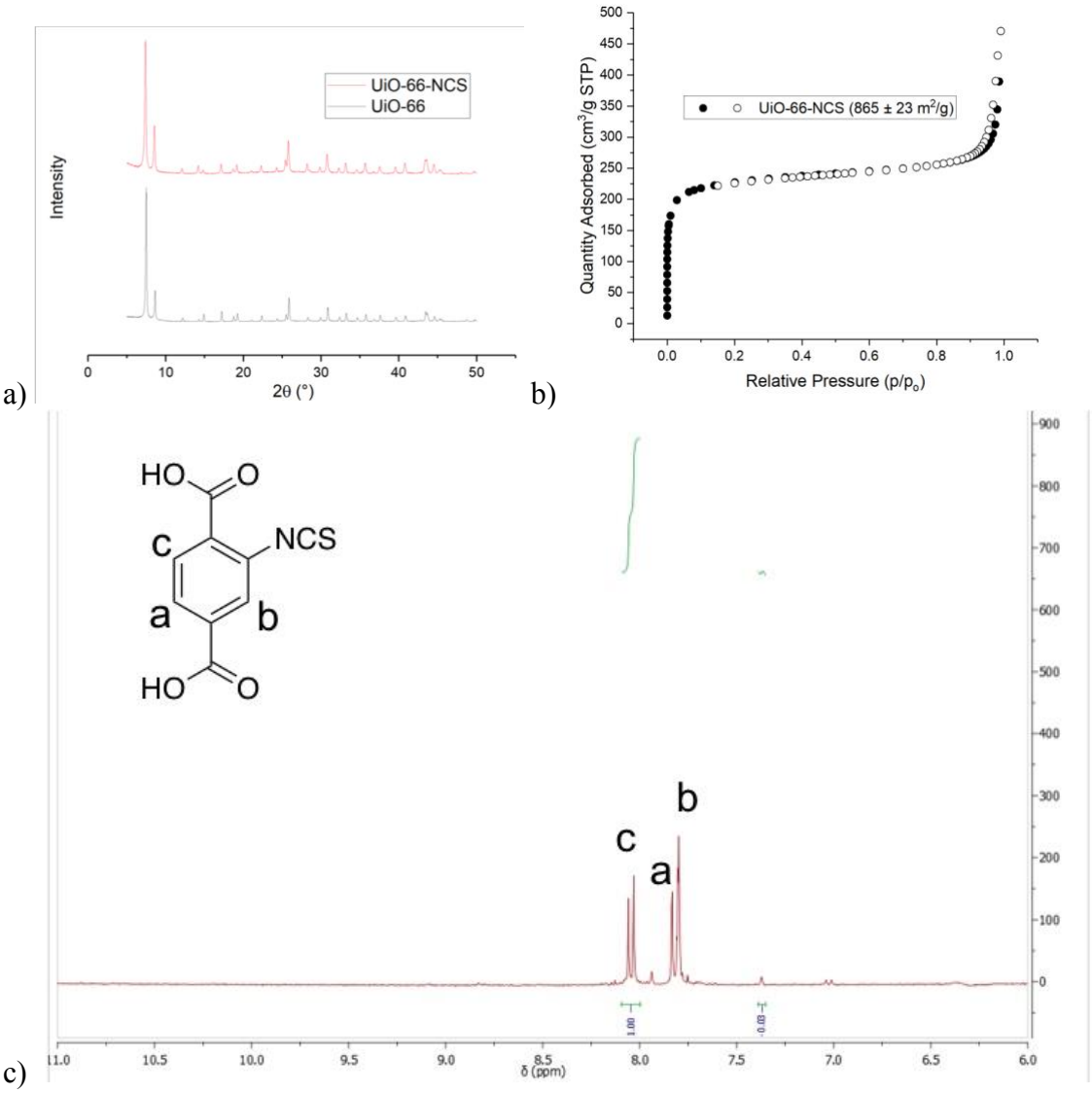

Figure 4S.7. Characterization of UiO-66-NCS. a) PXRD, b) N_2 adsorption isotherm and c) ^1H NMR analysis of digested UiO-66-NCS.

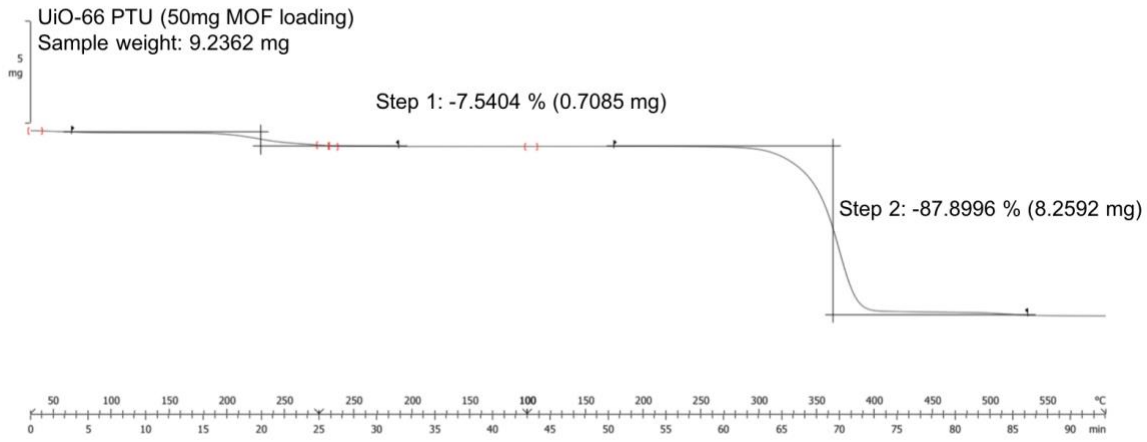

Figure 4S.8. TGA data of UiO-66-PTU with 50mg MOF loading.

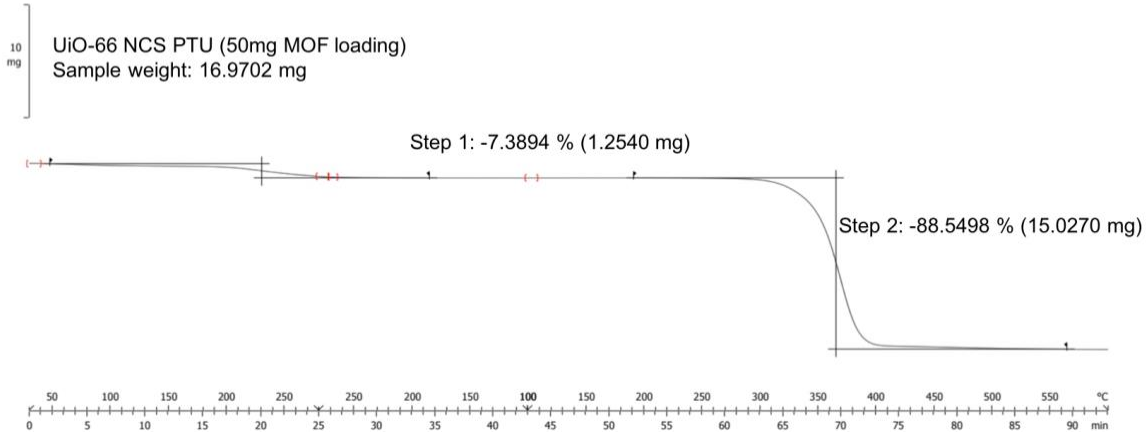

Figure 4S.9. TGA data of UiO-66-PTU with 100mg MOF loading.

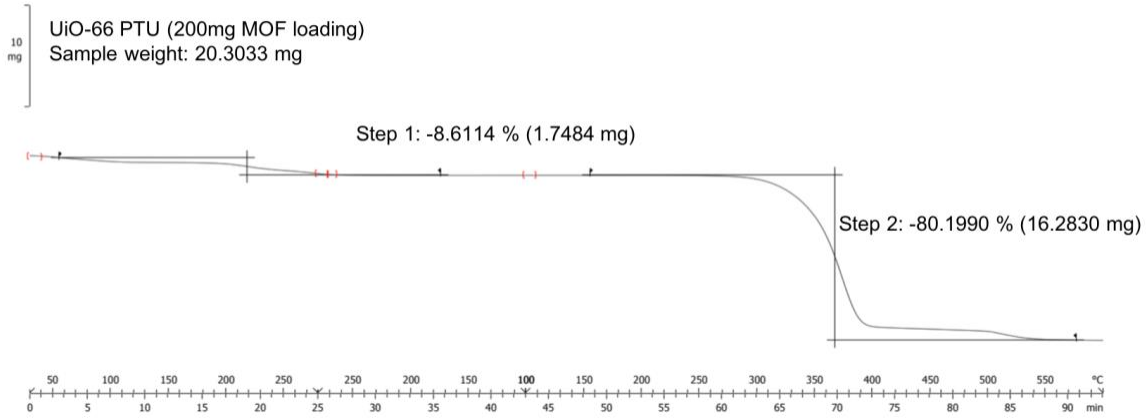

Figure 4S.10. TGA data of UiO-66-PTU with 200mg MOF loading.

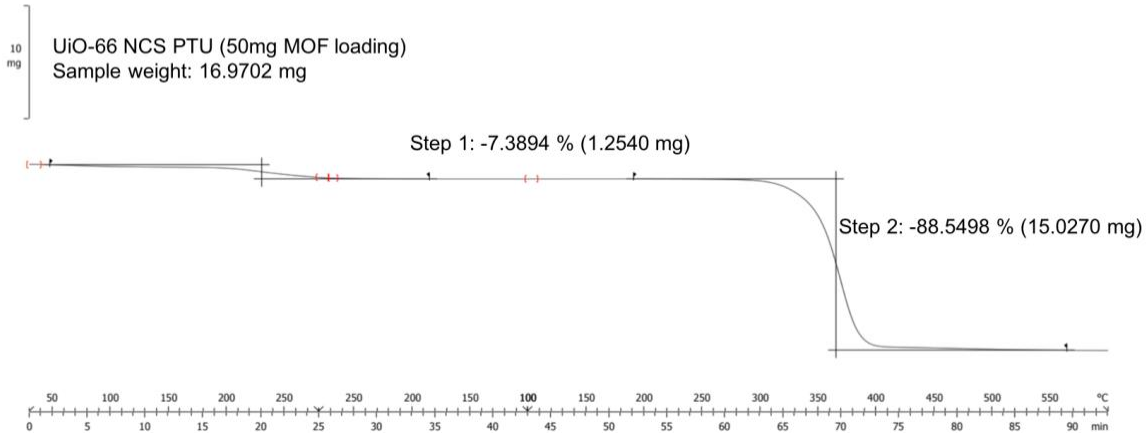

Figure 4S.11. TGA data of UiO-66-NCS-PTU with 50mg MOF loading.

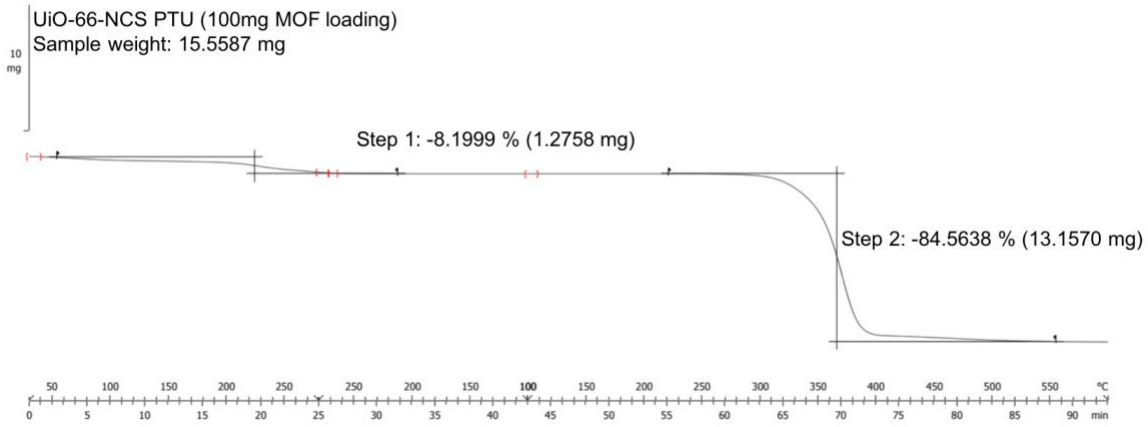

Figure 4S.12. TGA data of UiO-66-NCS-PTU with 100mg MOF loading.

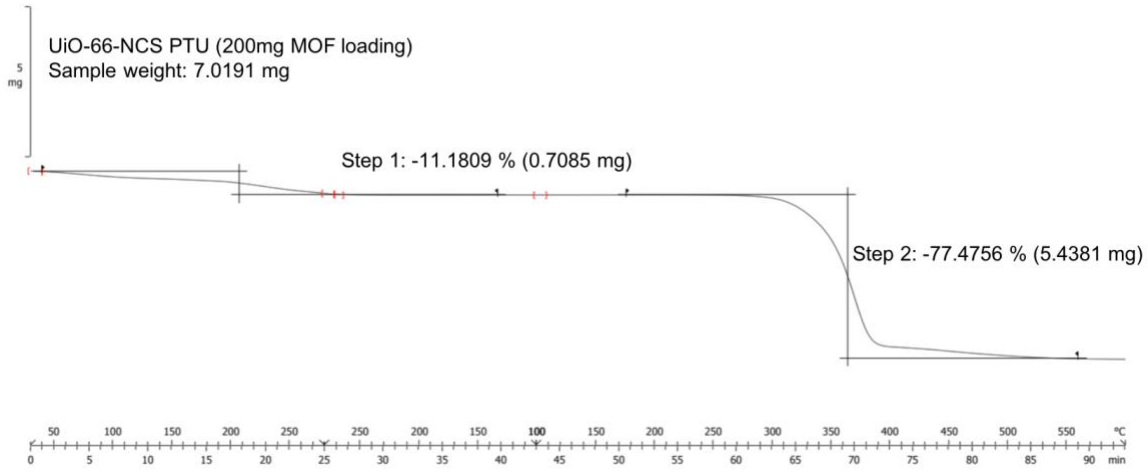

Figure 4S.13. TGA data of UiO-66-NCS-PTU with 200mg MOF loading.

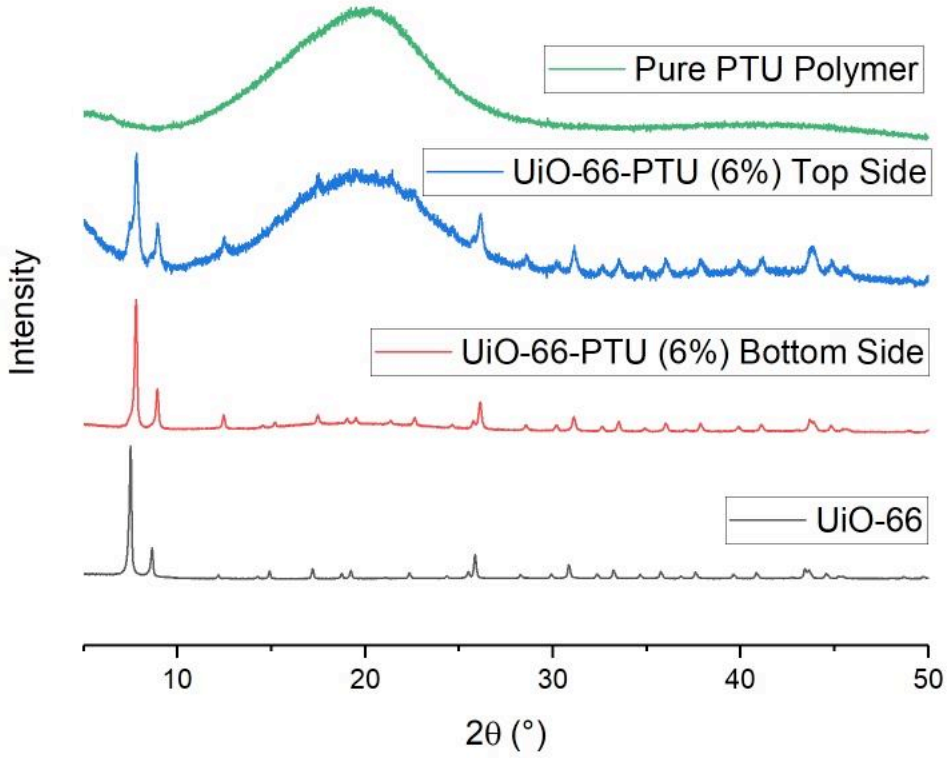

Figure 4S.14. PXRD spectra of pure PTU, top side of the UiO-66-PTU (6%) composite, bottom side of the UiO-66-PTU (6%) composite and a pure UiO-66 MOF.

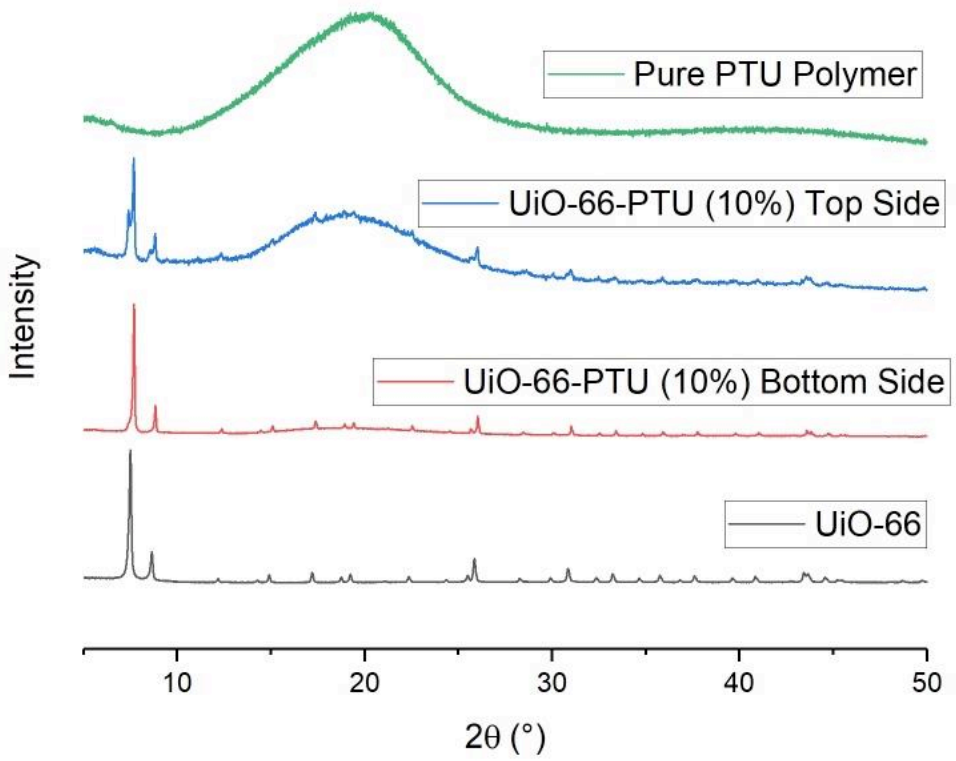

Figure 4S.15. PXRD spectra of pure PTU, top side of the UiO-66-PTU (10%) composite, bottom side of the UiO-66-PTU (10%) composite and a pure UiO-66 MOF.

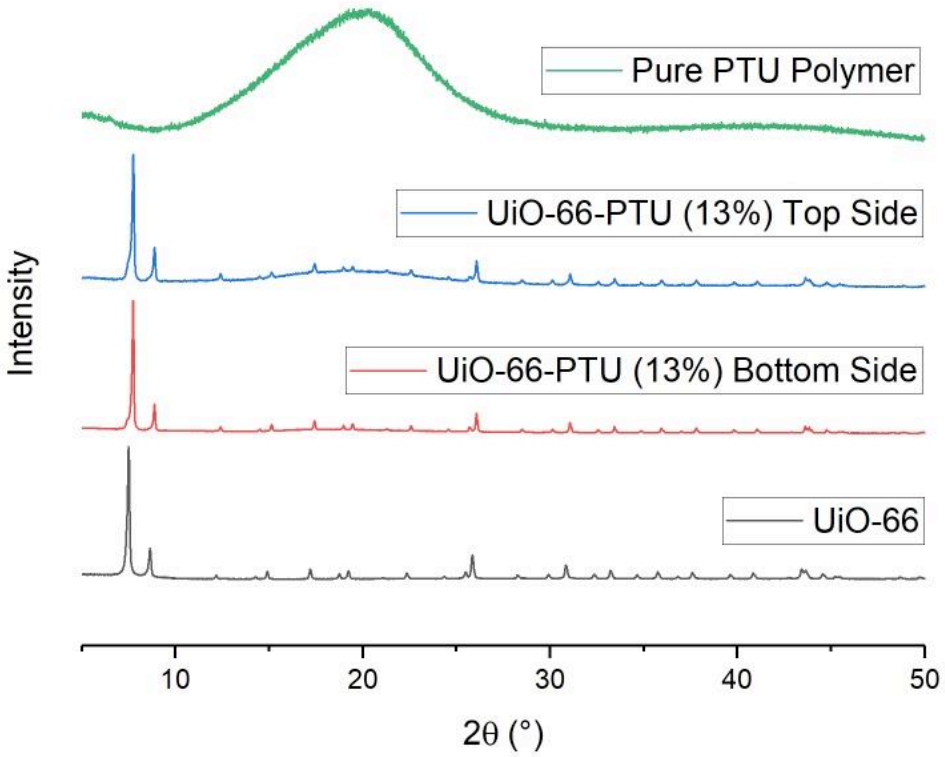

Figure 4S.16. PXRD spectra of pure PTU, top side of the UiO-66-PTU (13%) composite, bottom side of the UiO-66-PTU (13%) composite and a pure UiO-66 MOF.

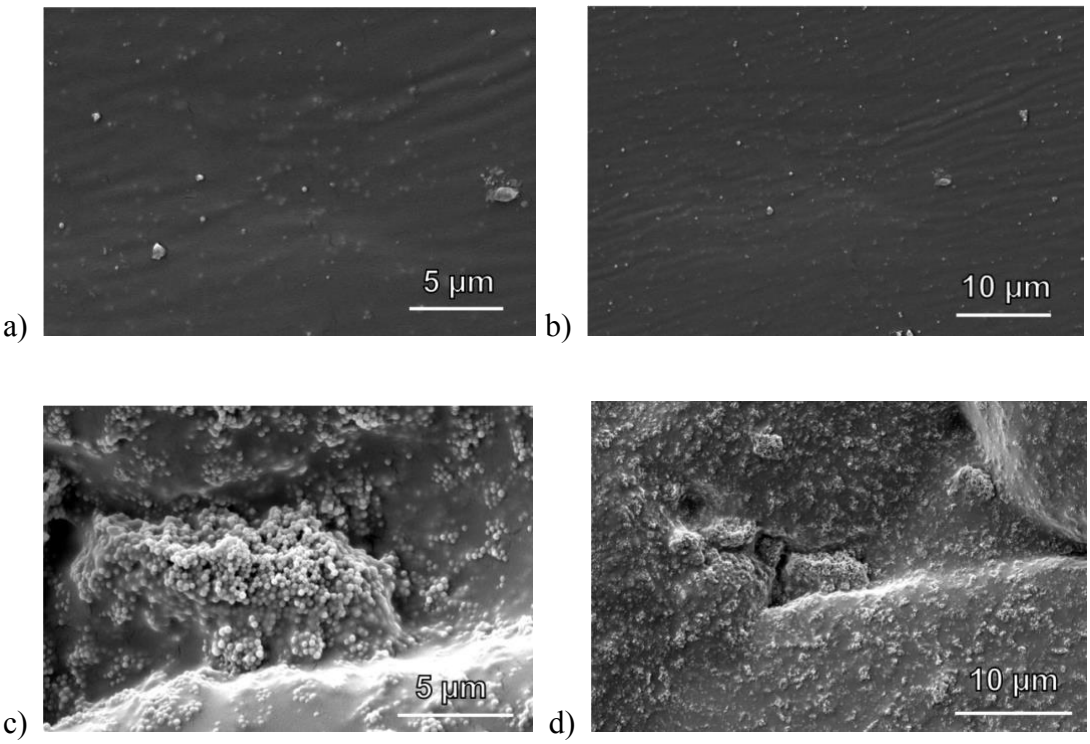

Figure 4S.17. SEM images of MOF-PTU composites. a) and b) top side of ~13% UiO-66-PTU composite c) and d) bottom side of ~13% UiO-66-PTU composite.

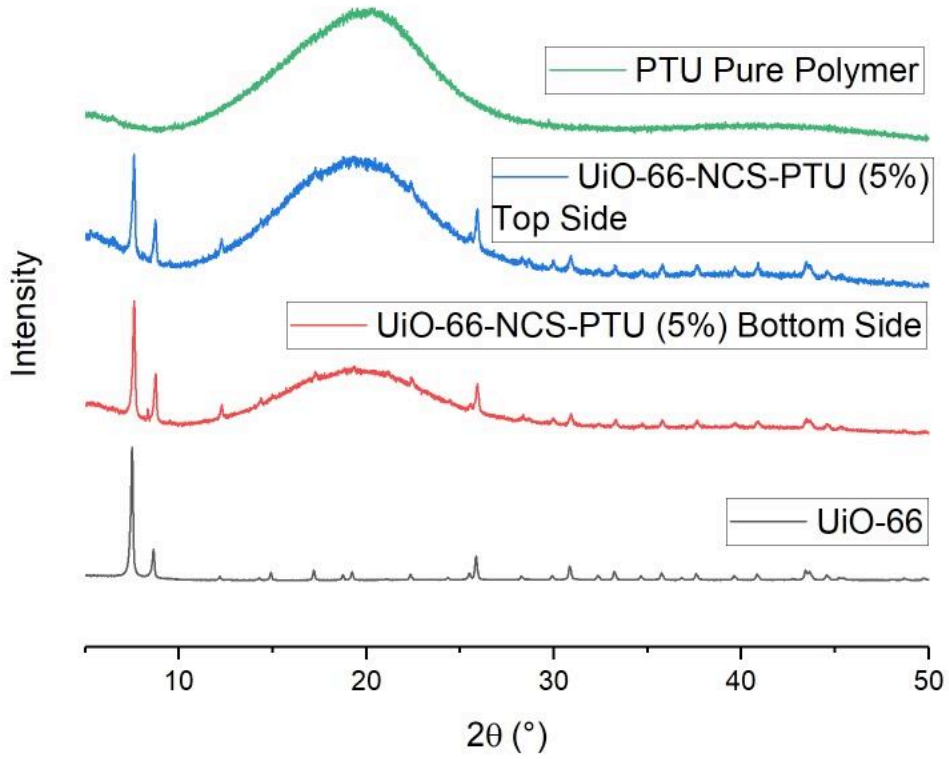

Figure 4S.18. PXRD spectra of pure PTU, top side of the UiO-66-NCS-PTU (5%) composite, bottom side of the UiO-66-NCS-PTU (5%) composite and a pure UiO-66 MOF.

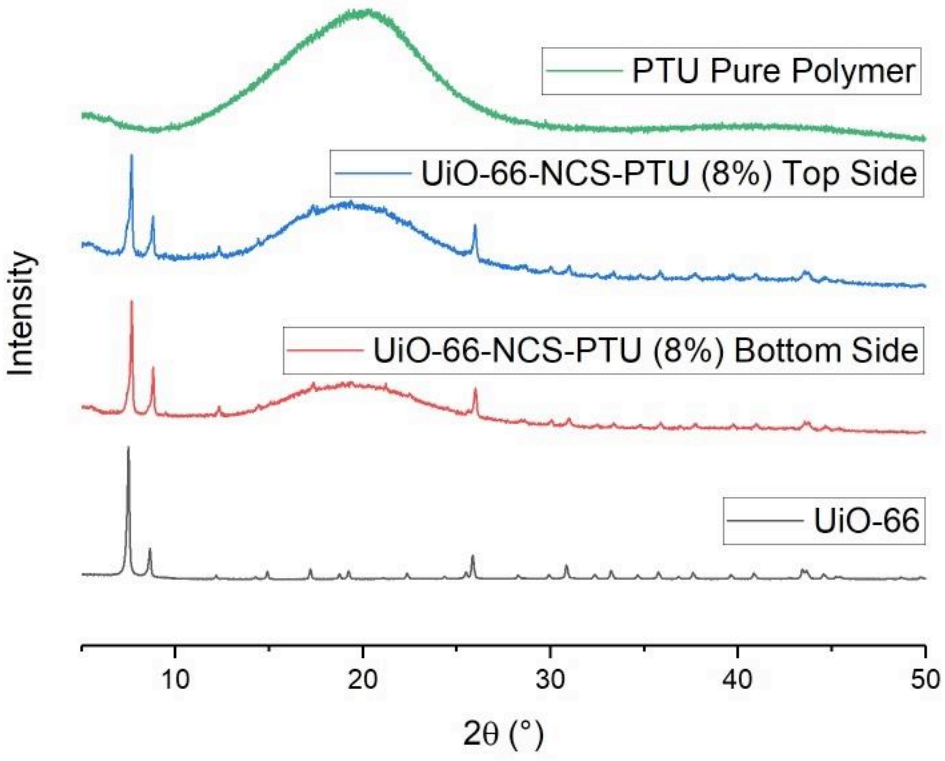

Figure 4S.19. PXRD spectra of pure PTU, top side of the UiO-66-NCS-PTU (8%) composite, bottom side of the UiO-66-NCS-PTU (8%) composite and a pure UiO-66 MOF.

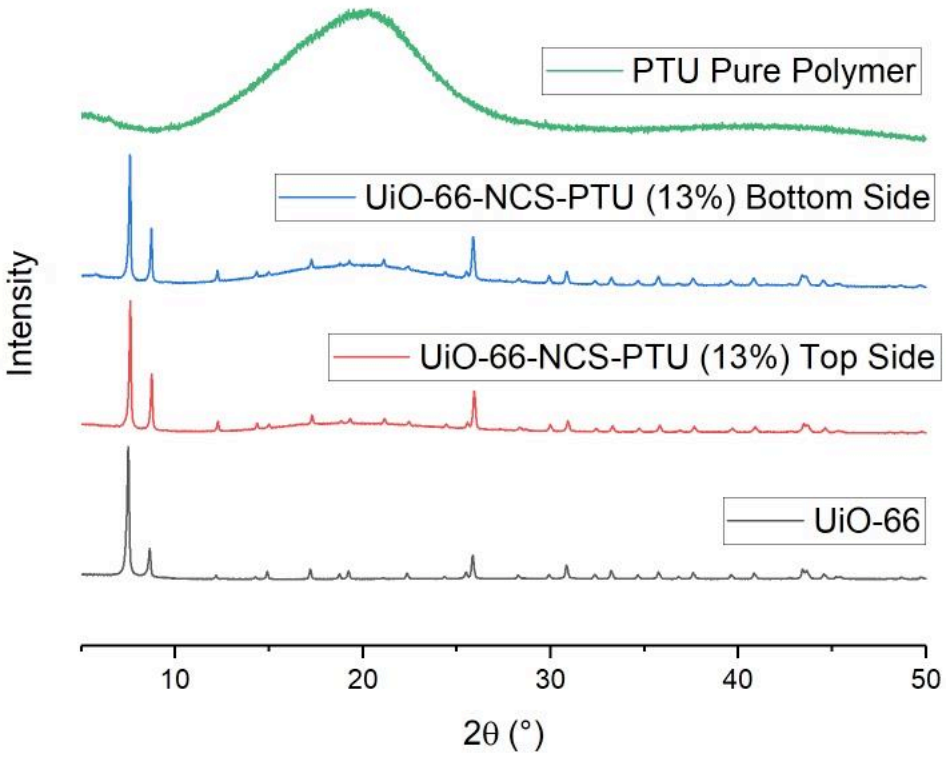

Figure 4S.20. PXRD spectra of pure PTU, top side of the UiO-66-NCS-PTU (13%) composite, bottom side of the UiO-66-NCS-PTU (13%) composite and a pure UiO-66 MOF.

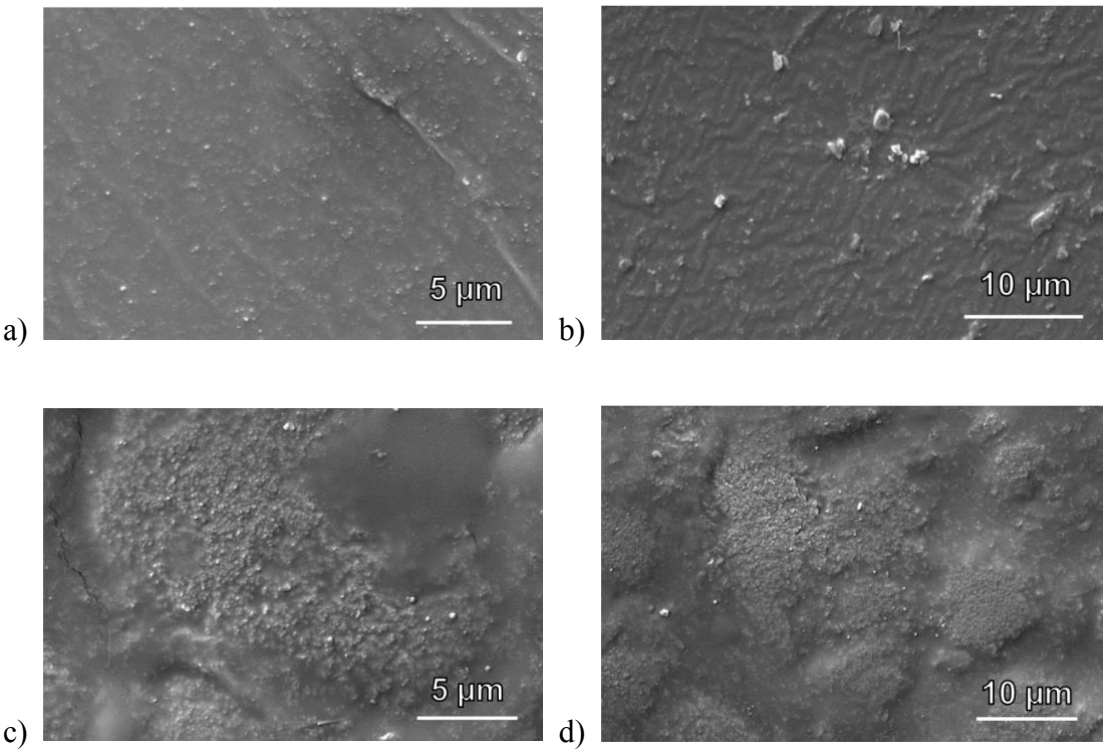

Figure 4S.21. SEM images of MOF-PTU composites. a) and b) top side of ~13% UiO-66-NCS-PTU composite c) and d) bottom side of ~13% UiO-66-NCS-PTU composite.

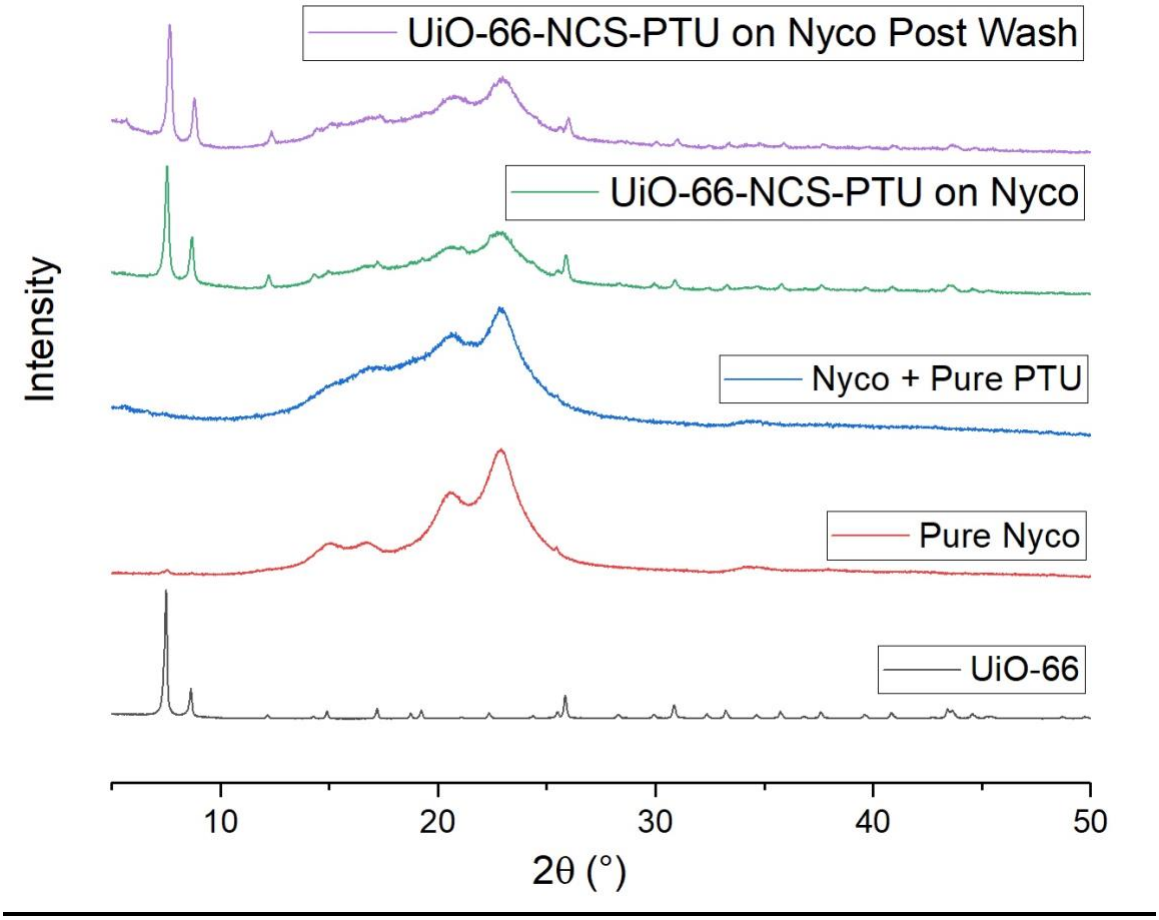

Figure 4S.22. PXRD spectra of pure Nyco, Nyco + pure PTU polymer, and UiO-66-NCS-PTU sprayed onto Nyco fibers and sprayed fibers after a laundry simulation.

a)  b) 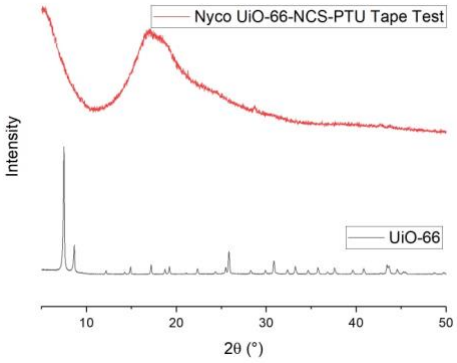

Figure 4S.23. Tape Test of UiO-66-NCS-PTU on Nyco Fibers. A) optical image of the tape and b) PXRD of the tape.

a) 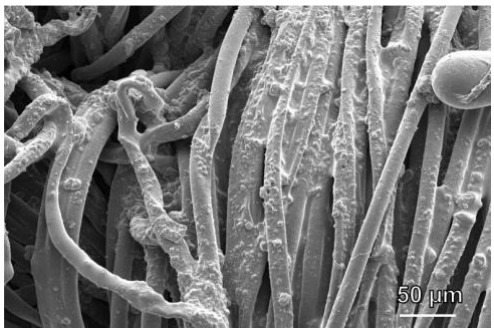

b) 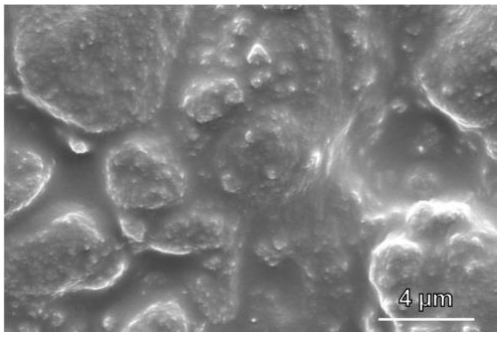

Figure 4S.24. SEM images of UiO-66-NCS-PTU spray coating on Nyco Fibers.

a) 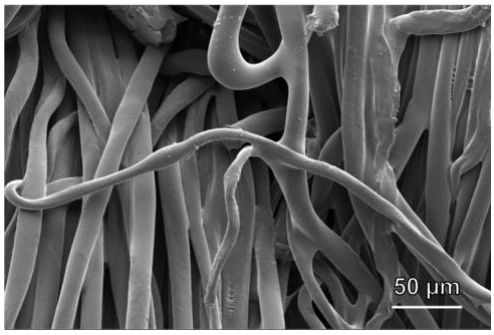

b) 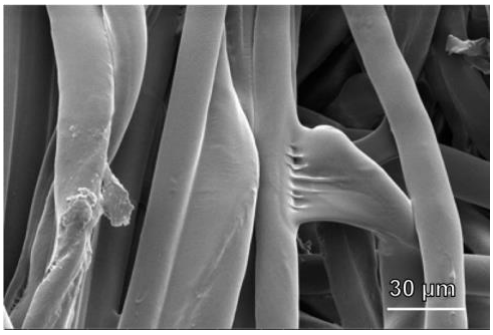

Figure 4S.25. SEM images of PTU spray coating on Nyco Fibers.

Figure 4S.26. Optical image of UiO-66-NCS spray coated on Nyco fibers.

a) 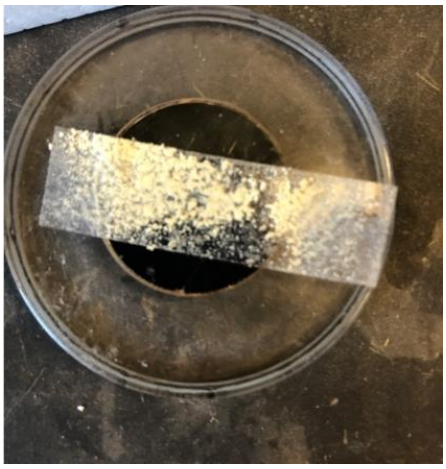

b) 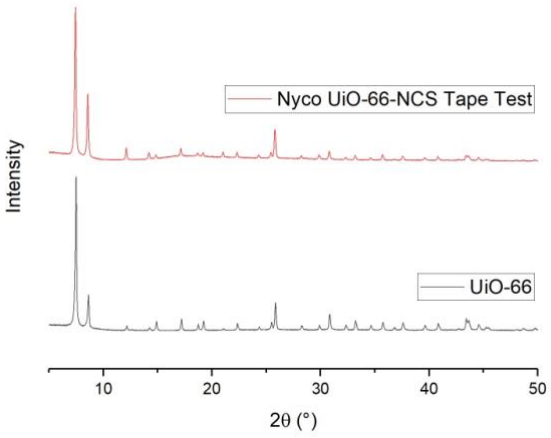

Figure 4S.27. Tape Test of UiO-66-NCS on Nyco Fibers. A) optical image of the tape and b) PXRD of the tape.

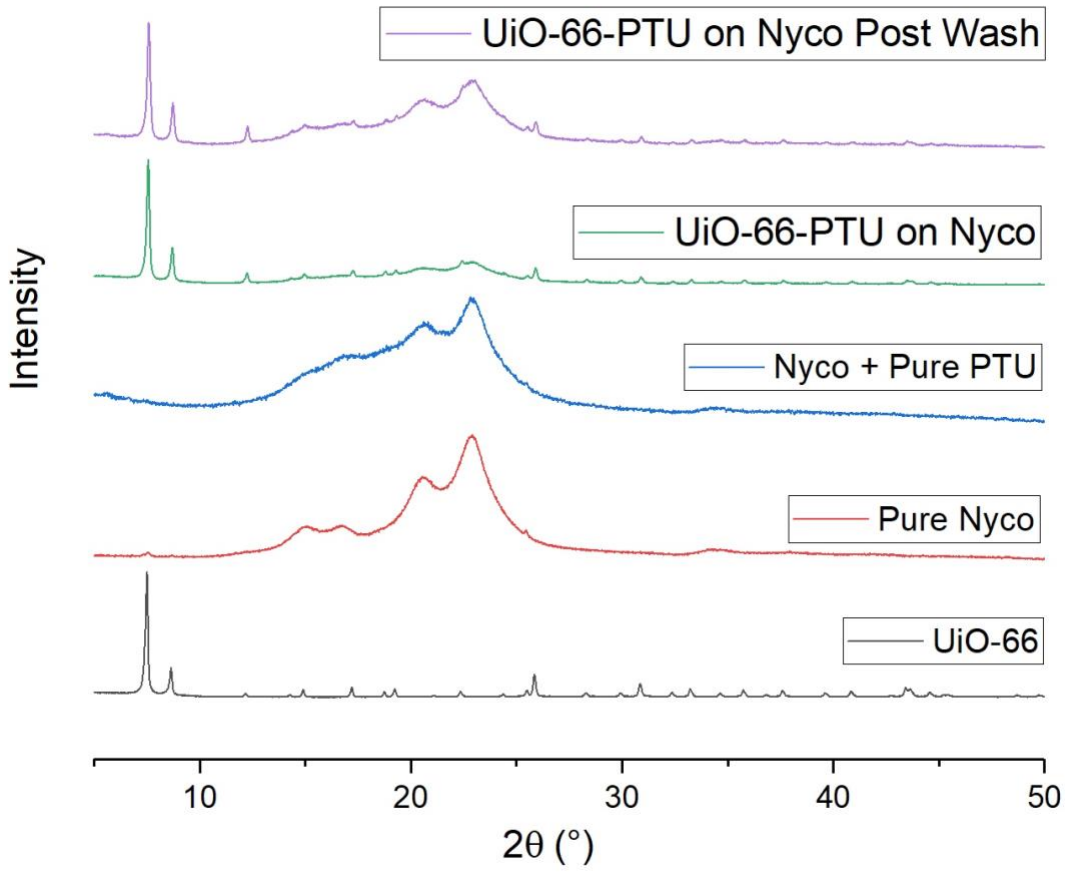

Figure 4S.28. PXRD spectra of pure Nyco, Nyco + pure PTU polymer, and UiO-66-PTU sprayed onto Nyco fibers and sprayed fibers after a laundry simulation.

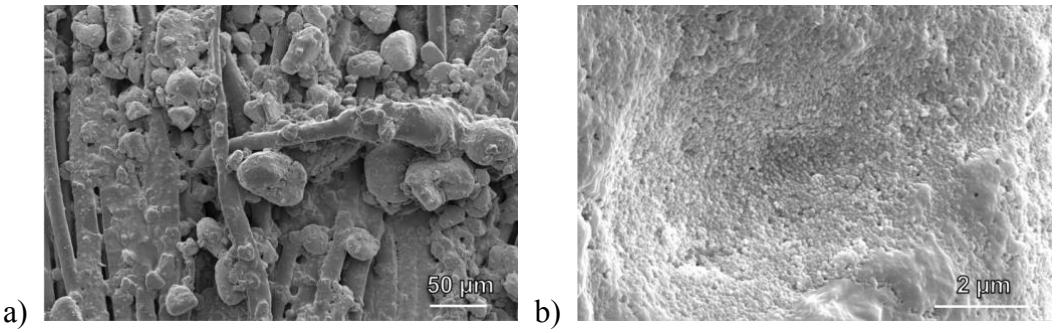

Figure 4S.29. SEM images of UiO-66-PTU spray coating on Nyco Fibers.

a)  b) 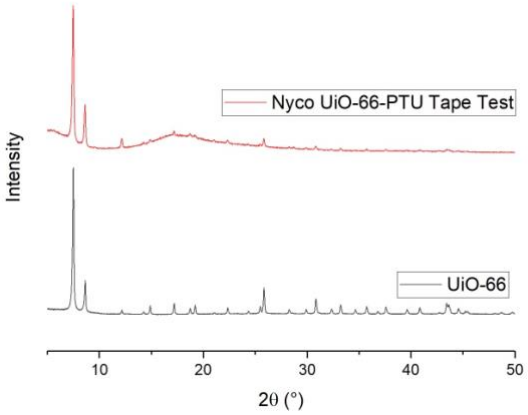

Figure 4S.30. Tape Test of UiO-66-PTU on Nyco Fibers. A) optical image of the tape and b) PXRD of the tape.

Table 4S.4. MOF wt % of MOF-PTU spray coating on Nyco fibers as determined by TGA.

Material	MOF wt % in composite as determined by TGA
Nyco Fibers	0 %
PTU on Nyco	0 %
UiO-66-NCS-PTU on Nyco	8.3 ± 0.7 %
UiO-66-PTU on Nyco	9.1 ± 1.3 %

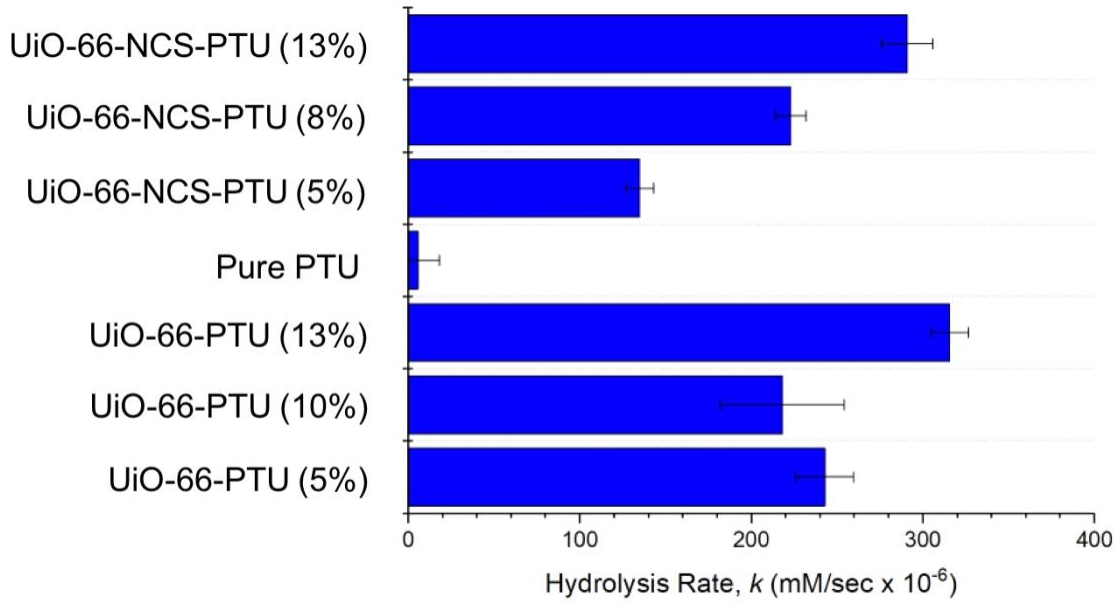

Figure 4S.31. DMNP hydrolysis rates by MOF-PTU composites. Data shown is an average of three different swatches run in triplicate.

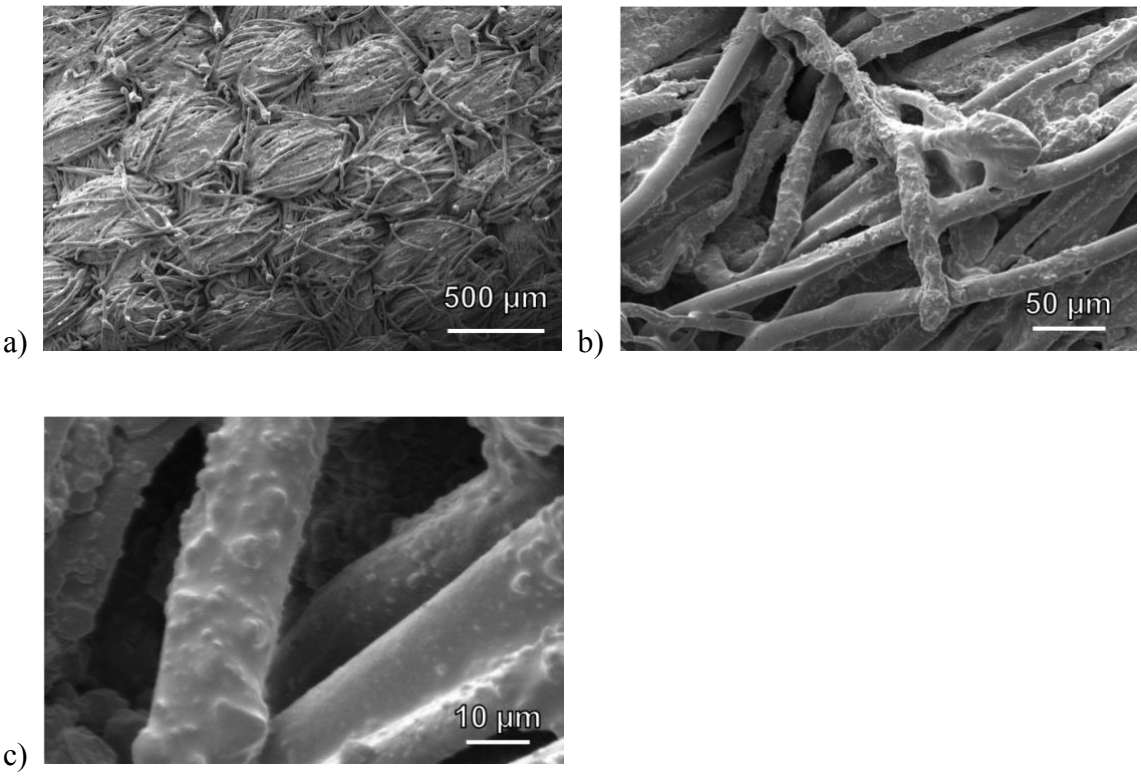

Figure 4S.32. SEM images of UiO-66-NCS PTU spray coating on Nyco Fibers after laundry simulation test.

a) 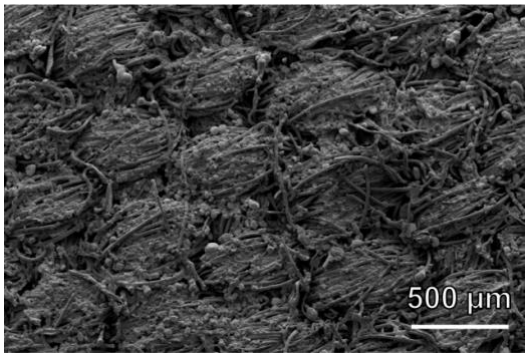

b) 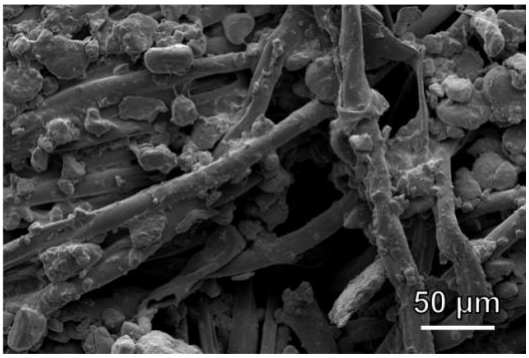

c) 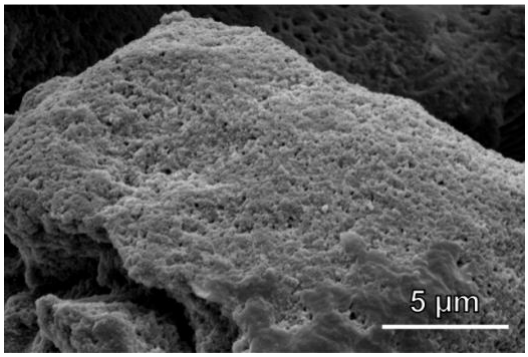

Figure 4S.33. SEM images of UiO-66-NCS PTU spray coating on Nyco Fibers after laundry simulation test.

4.6 Acknowledgements

Chapter 4, in part, is a reprint of the material, "Spray Coating of Catalytically Active MOF-Polythiourea through Postsynthetic Polymerization" *Angew. Chem. Int. Ed.* **2020**, *59*, 13984-13989. The dissertation author was the primary author of this manuscript and gratefully acknowledges the contributions of coauthor Seth M. Cohen.

4.7 References

1. Kalaj, M.; Denny Jr, M. S.; Bentz, K. C.; Palomba, J. M.; Cohen, S. M., Nylon–MOF Composites through Postsynthetic Polymerization. *Angew. Chem., Int. Ed.* **2019,** *58*, 2336-2340.

2. Kalaj, M.; Momeni, M. R.; Bentz, K. C.; Barcus, K. S.; Palomba, J. M.; Paesani, F.; Cohen, S. M., Halogen bonding in UiO-66 frameworks promotes superior chemical warfare agent simulant degradation. *Chem. Commun.* **2019,** *55*, 3481-3484.

3. Volkringer, C.; Cohen, S. M., Generating Reactive MILs: Isocyanate- and Isothiocyanate-Bearing MILs through Postsynthetic Modification. *Angew. Chem., Int. Ed.* **2010,** *49*, 4644-4648.

4. Nam, D.; Huh, J.; Lee, J.; Kwak, J. H.; Jeong, H. Y.; Choi, K.; Choe, W., Cross-linking Zr-based metal–organic polyhedra via postsynthetic polymerization. *Chem. Sci.* **2017,** *8*, 7765-7771.

5. Zhang, Y.; Feng, X.; Li, H.; Chen, Y.; Zhao, J.; Wang, S.; Wang, L.; Wang, B., Photoinduced Postsynthetic Polymerization of a Metal-Organic Framework toward a Flexible Stand-Alone Membrane. *Angew. Chem., Int. Ed.* **2015,** *54*, 4259-4263.

6. Palomba, J. M.; Credille, C. V.; Kalaj, M.; DeCoste, J. B.; Peterson, G. W.; Tovar, T. M.; Cohen, S. M., High-throughput screening of solid-state catalysts for nerve agent degradation. *Chem. Commun.* **2018,** *54*, 5768-5771.

7. Kalaj, M.; Palomba, J. M.; Bentz, K. C.; Cohen, S. M., Multiple functional groups in UiO-66 improve chemical warfare agent simulant degradation. *Chem. Commun.* **2019,** *55*, 5367-5370.

8. Zhang, C.; Li, Y.; Wang, H.; He, S.; Xu, Y.; Zhong, C.; Li, T., Adhesive bacterial amyloid nanofiber-mediated growth of metal–organic frameworks on diverse polymeric substrates. *Chem. Sci.* **2018,** *9*, 5672-5678.

9. Lee, D. T.; Zhao, J.; Oldham, C. J.; Peterson, G. W.; Parsons, G. N., UiO-66-NH2 Metal–Organic Framework (MOF) Nucleation on TiO2, ZnO, and Al2O3 Atomic Layer Deposition-Treated Polymer Fibers: Role of Metal Oxide on MOF Growth and Catalytic Hydrolysis of Chemical Warfare Agent Simulants. *ACS Appl. Mater. Interfaces* **2017,** *9*, 44847-44855.

10. Lee, D. T.; Zhao, J.; Peterson, G. W.; Parsons, G. N., Catalytic "MOF-Cloth" Formed via Directed Supramolecular Assembly of UiO-66-NH2 Crystals on Atomic Layer Deposition-Coated Textiles for Rapid Degradation of Chemical Warfare Agent Simulants. *Chem. Mater.* **2017,** *29*, 4894-4903.

11. Ma, K.; Islamoglu, T.; Chen, Z.; Li, P.; Wasson, M. C.; Chen, Y.; Wang, Y.; Peterson, G. W.; Xin, J. H.; Farha, O. K., Scalable and Template-Free Aqueous Synthesis of Zirconium-Based Metal–Organic Framework Coating on Textile Fiber. *J. Am. Chem. Soc.* **2019,** *141*, 15626-15633.

Chapter 5: Room Temperature Aqueous Synthesis of UiO-66 Derivatives via Postsynthetic Exchange

5.1 Introduction

As outlined in Chapter 1 and described throughout this thesis, the synthesis of Zr-based MOFs generally requires high temperatures (80-150 °C) and environmentally unfriendly solvents such as DMF or DEF.[1, 2] Several groups have developed elegant methods to synthesize UiO-66 under more mild conditions (e.g aqueous or RT). Some attempts to achieve mild conditions for the synthesis of UiO-66 and its derivative have focused on breaking up the synthesis into initial cluster (i.e., SBU) formation followed by subsequent MOF synthesis.[3-5] For example, Farha, Hupp, and co-workers initially synthesized the Zr(IV)-cluster at elevated temperatures and the clusters were linked together at room temperature by bdc^{2-} and bdc^{2-} derivatives to form UiO-66 and functionalized derivatives in DMF.[4] In another approach, Szilágyi and coworkers reported the synthesis of UiO-66-NH_2 by first forming the Zr(IV) cluster in water at 50 °C and subsequently synthesizing the MOF with the disodium salt version of the amine ligands (Na_2NH_2-bdc^{2-}) in water at room temperature.[5] In both of these cases, elevated temperatures were required for the synthesis of the Zr(IV) cluster.[4, 5] Subsequent MOF formation then occurs readily upon the introduction of a dicarboxylic acid linker.[4, 5]

Other groups have focused on synthesizing MOFs through either entirely aqueous or solvent free conditions through direct one pot synthesis. Some aqueous one pot syntheses of UiO-66 have been reported successfully; however, these syntheses typically require high temperatures to either form the MOF or metal cluster.[6-8] By using acetylacetonate (acac) metal salts as the metal source, Maspoch and coworkers were able to successfully eliminate the use of heat in synthesizing UiO-66 based MOFs.[9] They reported the one pot, room temperature, aqueous synthesis of two UiO-66 derivatives (UiO-66-NH_2 and UiO-66-$(OH)_2$) using $Zr(acac)_4$. The crystallinity of these frameworks was relatively poor compared to that of solvothermal synthesized UiO-66; however,

the surface area of the MOFs was not compromised. In a unique approach, Friscic and coworkers demonstrated a one pot synthesis of UiO-66 through mechanochemical routes using a zirconium propoxide solution (70 wt% in *n*-PrOH) with the addition of MeOH grinding to achieve a crystalline UiO-66 MOF.[10] Finally, in a report of importance to our findings here, UiO-66-$(COOH)_2$ and UiO-66-F_4 could be prepared at room temperature synthesis under aqueous conditions; however, the canonical UiO-66 or UiO-66-NH_2 were not accessible via this method.[11]

In Chapter 5, a room temperature, aqueous, green synthesis of UiO-66 and several derivatives (UiO-66-NH_2, UiO-66-Br, UiO-66-I, and UiO-66-Napthalene) is described through postsynthetic exchange (PSE) from UiO-66-F_4, a UiO-66 derivative prepared from a tetrafluorinated bdc^{2-} (F_4-bdc^{2-}) ligand. UiO-66-F_4 was prepared in aqueous media using the aforementioned method (Figure 5.1).[11] The presence of four electron withdrawing fluorine atoms on the organic linker results in a weaker bond between the carboxylate linkers and Zr(IV) metal centers. This enables the use of PSE to replace the F_4-bdc^{2-} linker with bdc^{2-}, NH_2-bdc^{2-}, Br-bdc^{2-}, I-bdc^{2-}, and napth-bdc^{2-} (1,4-napthalenedicarboxylic acid). Nearly complete exchange of the F_4-bdc^{2-} linkers is achieved at room temperature, in water within the span of 4 h at a 1:1 linker ratio. The resulting MOFs were fully characterized for porosity and crystallinity.

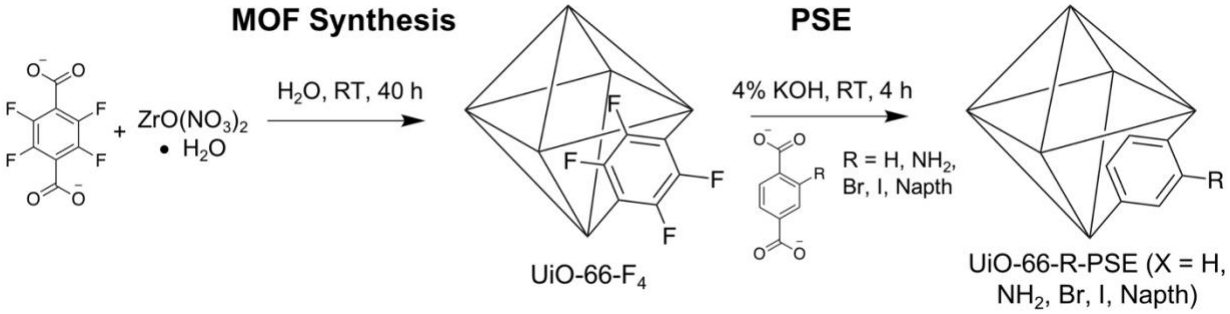

Figure 5.1. Synthetic scheme for UiO-66 and a range of derivatives at room temperature in aqueous solution via PSE from UiO-66-F_4.

5.2 Synthesis and Characterization of MOFs under Mild Conditions

Typically, when synthesizing UiO-66 and its derivatives (-NH_2, -Br, -I, etc.), the ligand and metal salts are dissolved in DMF and subsequently heated >100 °C for 24+ h. Circumventing these harsh conditions (i.e., high temperature in nonaqueous solvent), a range of UiO-66 derivatives were synthesized in aqueous solutions at room temperature using PSE from UiO-66-F_4. UiO-66-F_4 was selected for PSE as the F_4-bdc^{2-} linker is labile and coordinates weakly to the Zr(IV) metal nodes as a consequence of the four electron withdrawing atoms on the benzene ring. UiO-66-F_4 was synthesized using an acetic acid modulated, aqueous synthesis (see appendix for details) previously reported by Farha and co-workers.[11]

PSE experiments were conducted by dissolving a R-bdc linker in a 4% KOH solution as previously reported.[12, 13] The ligand solution was then neutralized to pH = 7 via the slow addition of 1M HCl (see appendix for details). A 1:1 ratio of UiO-66-F_4 was mixed with the ligand solution, and the mixture was then sonicated for 10 min and then left to stand at room temperature for 4 h. After incubation, the MOF was collected via centrifugation and thoroughly washed over the course of three days to ensure any excess ligand was removed. The product MOFs were then digested in dilute acid and characterized using ^{1}H and ^{19}F NMR. A coaxial tube with 40 μmol trifluorotoluene (CF_3-toluene, Figure 5.2) in DMSO-d_6 was used to quantify the amount of F_4-bdc^{2-} and the exchanged R-bdc^{2-} in each sample by NMR. The CF_3-toluene was used as an internal standard as it contains both F and H atoms with appropriate chemical shifts (Figure 5S.1-5S.5). After the UiO-66-PSE MOF was digested, the coaxial tube of CF_3-toluene was inserted into the sample and both ^{1}H and ^{19}F NMR were used to analyze the sample. The amount of each linker in the MOF was quantified by comparing the PSE introduced R-bdc^{2-} (~7.0 - 8.0 ppm) linker to the CF_3-toluene peaks (7.3 – 7.7 ppm) in the ^{1}H NMR and also comparing the amount of F_4-bdc^{2-} remaining (-61.2

ppm) to the CF_3-toluene (-140.0 ppm) via the ^{19}F NMR (Figure 5.2a and 5.2b). This analysis allowed for the total quantity of ligand in the MOF to be determined, from which the fraction of F_4-bdc^{2-} and R-bdc^{2-} was calculated.

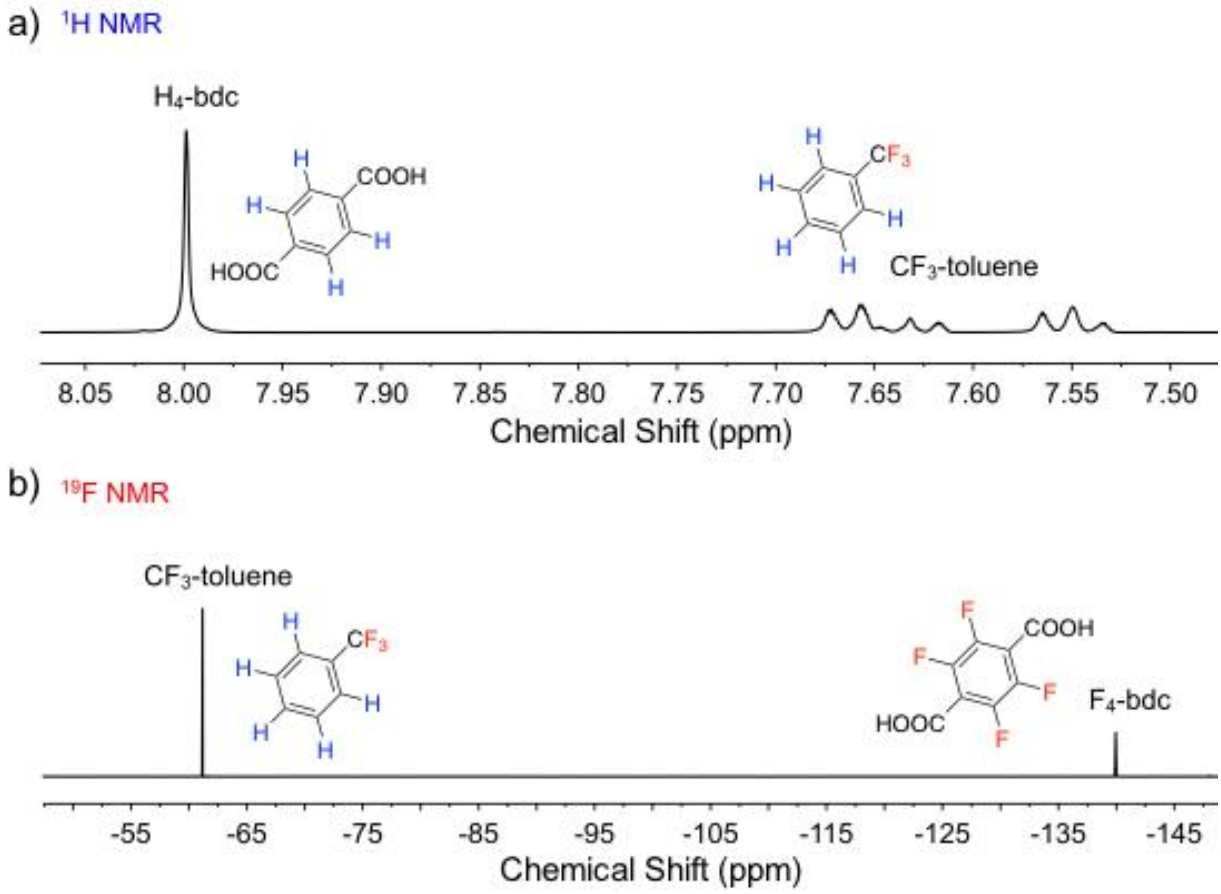

Figure 5.2. a)^1H and ^{19}F NMR analysis of the PSE experiments performed with UiO-66-F_4. a) Representative ^1H and b) ^{19}F NMR spectra of digested UiO-66-PSE.

NMR data for the digested samples shows that when exchanging the F_4-bdc^{2-} linker out for the canonical bdc^{2-} linker, 93±2% ligand exchange is obtained in the MOF in ~4 h (Figure 5.2). PSE of the UiO-66-F_4 with NH_2-bdc^{2-} gave 95±3% ligand exchange (Figure 5S.3. PSE on UiO-66-F_4 with Br-bdc^{2-} and I-bdc^{2-}gave 89±3% and 80±2% PSE, respectively (Figure 5S.3-4). The

lower PSE conversion with Br-bdc^{2-} and I-bdc^{2-} is attributed to the electron withdrawing groups on these halogenated bdc^{2-} derivatives, making them bulkier, as well as weaker donors. PSE on UiO-66-F_4 using a sterically bulkier napth-bdc^{2-} linker gave a 77±3% ligand incorporation (Figure 5S.5); the slightly less efficient PSE is attributed to the steric bulk of the napth-bdc^{2-} linker. Residual F_4-bdc^{2-} linkers in the PSE MOFs indicate that these materials are by definition multivariate (MTV) MOFs. MTV-MOFs have shown some interesting synergistic properties in making MOFs better sorbents or catalysts.[14, 15] In this case, residual F_4-bdc^{2-} linkers could potentially be used for labeling purposes as a function of the F atoms characteristically unique spectroscopic properties.

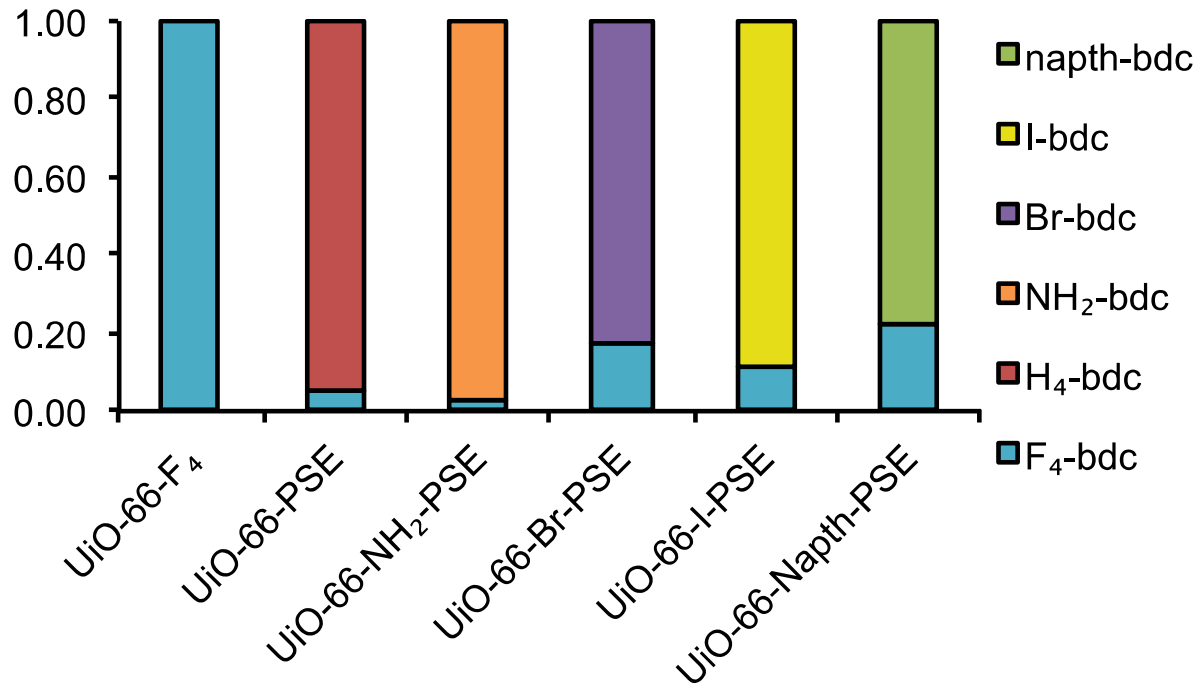

Figure 5.3. Relative amounts of the starting F_4-bdc^{2-} and the PSE R-bdc^{2-} derivatives in each of the PSE experiments performed.

The All MOFs were characterized via PXRD to confirm the crystallinity of the UiO-66 framework after PSE. All of the MOFs synthesized via PSE display the characteristic UiO-66 reflections (Figure 5.4). The MOFs were also analyzed by SEM to evaluate the particle size before and after PSE and to make sure that no etching occurred due to the PSE conditions. As-synthesized UiO-66-F_4 particles were small (~100 nm) and polydisperse in size.[11] Following PSE, SEM images verify that the crystallites are approximately the same size and dispersity as the parent UiO-66-F_4 and no etching is observed (Figure 5.5 and Figures 5S.6-5S.9).

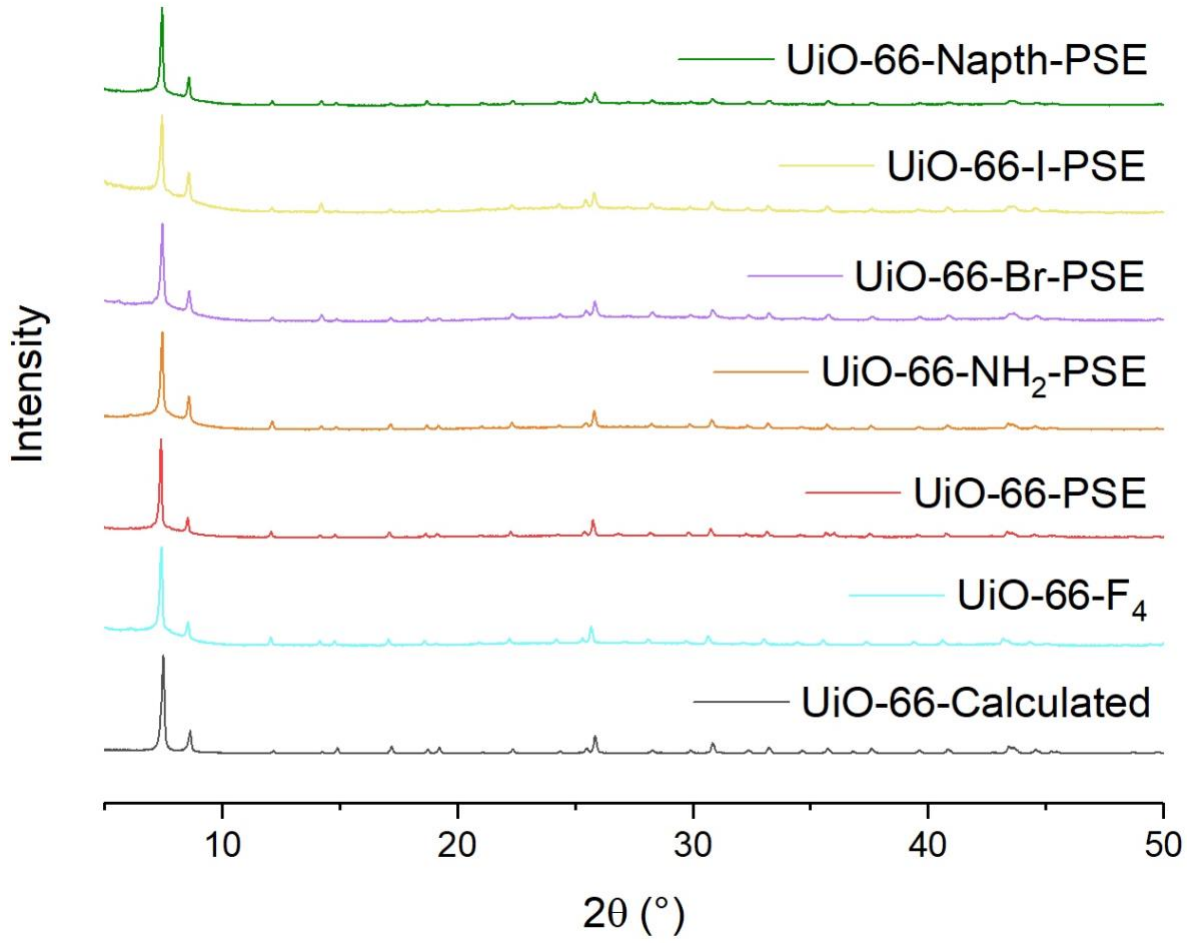

Figure 5.4. PXRD of the MOFs prepared in this study. The calculated UiO-66 pattern (black) is shown at the bottom; all other PXRD patterns are experimental results: UiO-66-F_4 (cyan), UiO-66-PSE (red), UiO-66-NH_2-PSE (orange), UiO-66-Br-PSE (purple), UiO-66-I-PSE (yellow), and UiO-66-Napth-PSE (green).

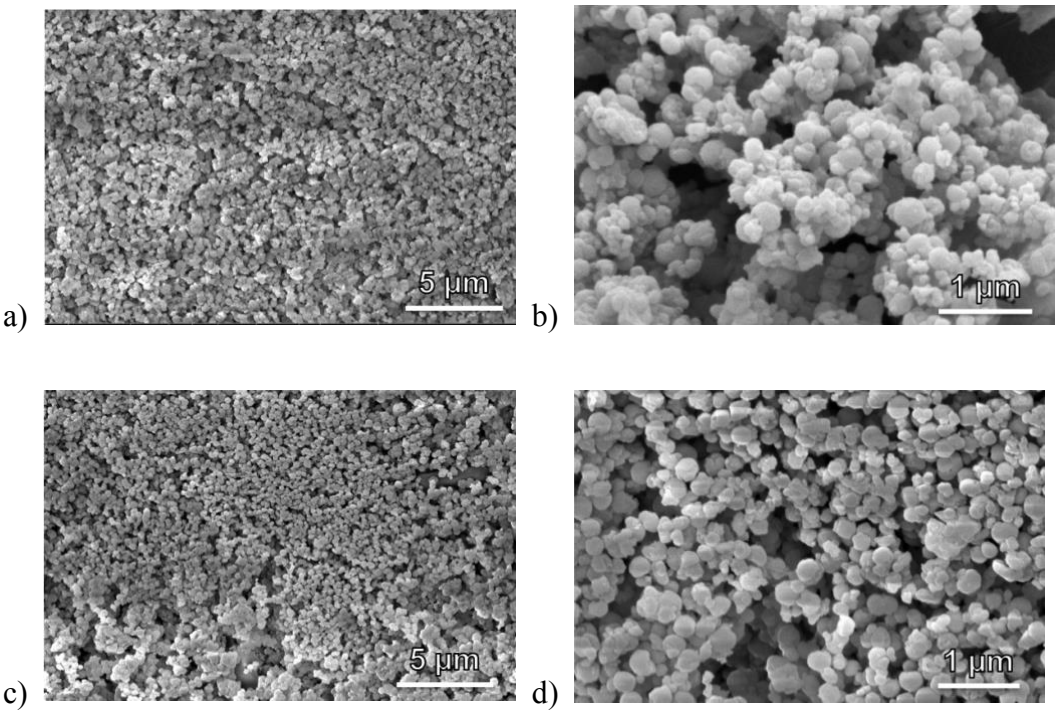

Figure 5.5. SEM images of UiO-66-F_4 (a and b) and UiO-66-PSE (c and d).

All MOFs were analyzed to determine the BET surface area of the materials using N_2 adsorption isotherms. The parent UiO-66-F_4 MOF displays a BET surface area of 628±8 m^2/g, which is consistent with literature reports (Figure 5.6).[11] Upon PSE of the MOF with other linkers a general decrease in the BET surface area was observed. Surface areas for other PSE MOFs were: 463±46 m^2/g for UiO-66-PSE, 407±6 m^2/g for UiO-66-NH_2-PSE, 378±22 m^2/g for UiO-66-Br-PSE, 472±21 m^2/g for UiO-66-I-PSE, and 467±42 m^2/g for UiO-66-Napth-PSE. All of these UiO-66 derivatives, when synthesized by the typical hydrothermal method, display surface areas of >1000 m^2/g.[2, 16] The lower surface area of the PSE prepared materials is attributed to the poorer porosity of the UiO-66-F_4 template. Nevertheless, the lower surface area of these materials does

not detract from the value of these materials for many potential applications, especially if a greener synthetic route is desired.

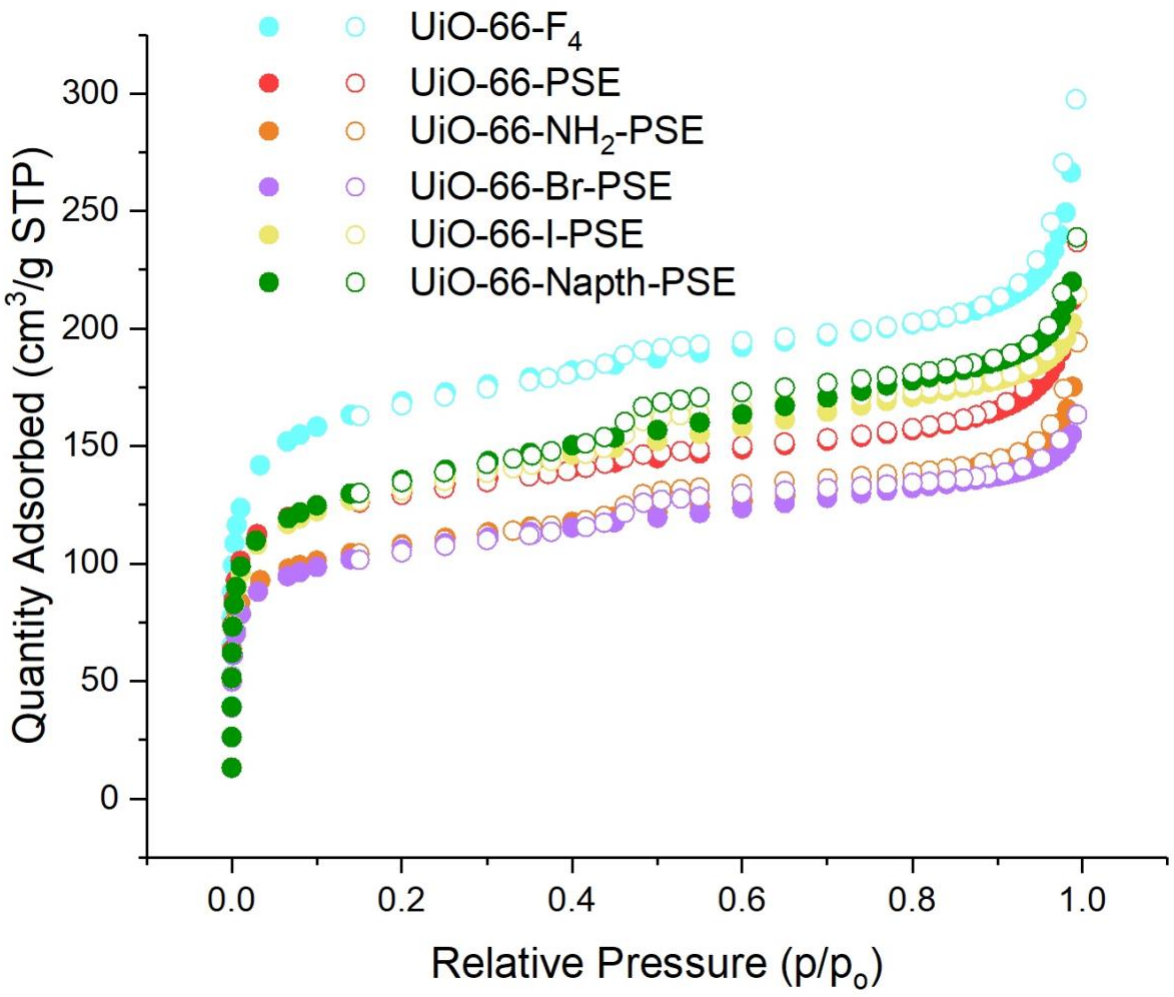

Figure 5.6. N_2 adsorption isotherms of UiO-66-F_4 and UiO-66-PSE MOFs: UiO-66-F_4 (cyan), UiO-66-PSE (red), UiO-66-NH_2-PSE (orange), UiO-66-Br-PSE (purple), UiO-66-I-PSE (yellow), and UiO-66-Napth-PSE (green).

Zr(IV)-based MOFs have been shown to be useful for the catalytic degradation of CWAs and their simulants.[15, 17] Several factors have been suggested to affect activity toward CWAs such as particle size, defect sites, and ligand effects.[15, 17-20] To determine the catalytic activity of these

'green' MOFs, UiO-66-F_4, UiO-66-PSE, and UiO-66-NH_2-PSE were screened for the degradation of the CWA simulant DMNP using the method previously described in Chapter 2 a previously reported method.[20] The results of these assays indicate an increase in activity for both UiO-66-PSE and UiO-66-NH_2-PSE when compared to the as-synthesized UiO-66-F_4 MOF. The UiO-66-PSE and UiO-66-NH_2-PSE displayed >2-times the activity of the UiO-66-F_4 (Figure 5.7). It is important to note that the PSE MOFs (UiO-66-PSE and UiO-66-NH_2-PSE) displayed about half of the catalytic activity than their hydrothermally synthesized UiO-66 and UiO-66-NH_2 counterparts.[18] Overall, this result shows that PSE can be used to prepare materials under more mild, green conditions that display the expected MOF properties.

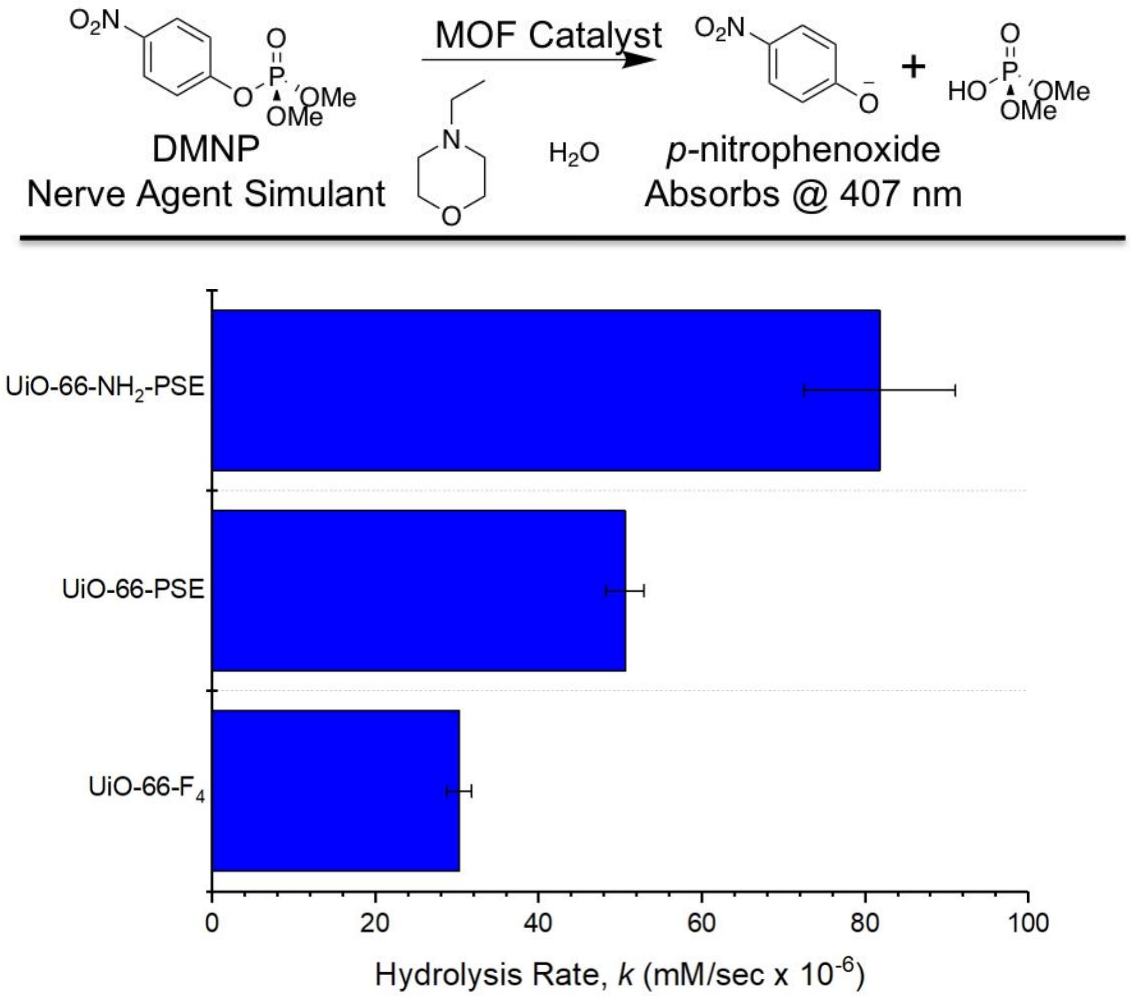

Figure 5.7. *Top:* DMNP degradation reaction. *Bottom:* Rate of catalytic degradation of DMNP by MOFs measured by UV-visible adsorption (407 nm) at pH = 8 (corrected for differences in the molar mass of each MOF).

5.3 Conclusions

In conclusion, UiO-66 and a series of UiO-66 derivatives have been synthesized through a green aqueous and room temperature PSE route that uses UiO-66-F_4 as a template. These results highlight the power of postsynthetic chemistry to enhance not only the functionality, but synthetic accessibility of valuable MOF materials.

5.4 Appendix: Supporting Information

Materials

All solvents and starting materials were purchased from chemical suppliers and used without further purification (Sigma Aldrich, Alfa Aesar, EMD, and TCI).

MOF Synthesis

UiO-66-F_4. This MOF was synthesized using a previously reported method (CrystEngComm, **2019**, *21*, 2409-2415). In a 100 mL Erlenmeyer flask, zirconium (IV) oxynitrate hydrate ($ZrO(NO_3)_2 \bullet xH_2O$) (1.62 g, 7.02 mmol) was dissolved in 36 mL of DI H_2O via sonication. In a separate 100 mL Erlenmeyer flask, tetrafluoroterephthalic acid (1.08 g, 4.54 mmol) was dissolved in 36 mL of DI H_2O via sonication. The two solutions were mixed together and stirred for 40 h at room temperature. The crystalline powder was collected by centrifugation (8500 rpm for 10 min). The crystalline powder was washed 3´40 mL of DI H_2O and subsequently with 2´40 mL of ethanol and immersed in acetone for 2 d. Fresh acetone was exchanged every 24 h. The powder was isolated and dried in a vacuum oven at room temperature overnight.

UiO-66 PSE Synthesis. Terephthalic acid (1.65 g, 9.93 mmol) was dissolved in 50 mL of 4% KOH solution (0.2 mM). The solution was then neutralized to pH = 7 using 1M HCl. 4 mL (0.8 mmol) of terephthalic acid solution was added to 256 mg (0.8 mmol ligand) of UiO-66-F_4. The mixture was sonicated for 5 min and allowed to sit at room temperature for 2 h. The crystalline powder was collected by centrifugation (8000 rpm for 10 min). The solids were then washed 3´20 mL of H_2O and 3´20 mL of methanol. After washing the solids were immersed in methanol for 3 d, with fresh methanol being exchanged every 24 h.

UiO-66-NH_2 PSE Synthesis. 2-Aminoterephthalic acid (1.80 g, 9.93 mmol) was dissolved in 50 mL of 4% KOH solution (0.2 mM). The solution was then neutralized to pH = 7 using 1M HCl. 4 mL (0.8 mmol) of 2-aminoterephthalic acid solution was added to 256 mg (0.8 mmol ligand) of UiO-66-F_4. The mixture was sonicated for 5 min and allowed to sit at room temperature for 2 h. The crystalline powder was collected by centrifugation (8000 rpm for 10 min). The solids were then washed 3´20 mL of H_2O and 3´20 mL of methanol. After washing the solids were immersed in methanol for 3 d, with fresh methanol being exchanged every 24 h.

UiO-66-Br PSE Synthesis. 2-Bromoerephthalic acid (2.43 g, 9.93 mmol) was dissolved in 50mL of 4% KOH solution (0.2 mmol). The solution was then neutralized to pH = 7 using 1M HCl. 4 mL (0.8 mmol) of 2-bromoterephthalic acid solution was added to 256 mg (0.8 mmol ligand) of UiO-66-F_4. The mixture was sonicated for 5 min and allowed to sit at room temperature for 2 h. The crystalline powder was collected by centrifugation (8000 rpm for 10 min). The solids were then washed 3´20 mL of H_2O and 3´20 mL of methanol. After washing the solids were immersed in methanol for 3 d, with fresh methanol being exchanged every 24 h.

UiO-66-I PSE Synthesis. 2-Iodoterephthalic acid (2.90 g, 9.93 mmol) was dissolved in 50mL of 4% KOH solution (0.2 mM). The solution was then neutralized to pH = 7 using 1M HCl. 4 mL (0.8 mmol) of 2-iodoterephthalic acid solution was added to 256 mg (0.8 mmol ligand) of UiO-66-F_4. The mixture was sonicated for 5 min and allowed to sit at room temperature for 2 h. The crystalline powder was collected by centrifugation (8000 rpm for 10 min). The solids were then washed 3´20 mL of H_2O and 3´20 mL of methanol. After washing the solids were immersed in methanol for 3 d, with fresh methanol being exchanged every 24 h.

UiO-66-Napth PSE Synthesis. Naphthalene terephthalic acid (2.15 g, 9.93 mmol) was dissolved in 50mL of 4% KOH solution (0.2 mM). The solution was then neutralized to pH = 7 using 1M

HCl. 4 mL (0.8 mmol) of naphthalene terephthalic acid solution was added to 256 mg (0.8 mmol ligand) of UiO-66-F_4. The mixture was sonicated for 5 min and allowed to sit at room temperature for 2 h. The crystalline powder was collected by centrifugation (8000 rpm for 10 min). The solids were then washed 3´20 mL of H_2O and 3´20 mL of methanol. After washing the solids were immersed in methanol for 3 d, with fresh methanol being exchanged every 24 h.

Table 5S.1. Ligand percentages of MOFs synthesized through postsynthetic exchange (PSE) of UiO-66-F_4.

MOF	% bdc-F_4 linker after PSE	% bdc-R linker after PSE
UiO-66-F_4	100%	0%
UiO-66-PSE	7 ± 2%	93 ± 2%
UiO-66-NH_2-PSE	4 ± 2%	96 ± 2%
UiO-66-Br-PSE	10 ± 2%	90 ± 2%
UiO-66-I-PSE	19 ± 2%	81 ± 2%
UiO-66-Napth-PSE	24 ± 2%	76 ± 2%

Characterization Methods

Nuclear Magnetic Resonance.

NMR experiments were carried out on a JOEL ECA 500 MHz spectrometer equipped with a Jeol 2 channel inverse-detect $^1H/^{19}F$ probe. MOFs were digested for NMR analysis by immersion of ~5-10 mg MOF in 500 µL DMSO-d_6 with 5 µL HF (48% in water). Samples were kept in this acidic solution at room temperature until the MOF was fully dissolved. In each NMR experiment was included a coaxial tube containing a reference sample of 40 µmol of trifluorotoluene in 100 µL deuterated DMSO. The parameters used for each NMR nuclei are included in Table S2.

Table 5S.2. NMR parameters used to analyze digested MOF samples.

Parameter	^{1}H experiment	^{19}F experiment
Gain	36	50
Sweep Center	5 ppm	-100 ppm
Sweep Width	15 ppm	150 ppm
X-pts	32768	262144
Scan Number	128	128
Acquisition time	4.367 s	3.713 s
Acquisition delay	5 s	5 s

Catalysis Experiments. In this study, DMNP hydrolysis was measured using a modified version of a previously reported procedure.[20] All catalytic monitoring was carried out using a BioTek Synergy H4 plate reader using single wavelength absorbance mode. 20 and 40 mM of *N*-ethylmorpholine buffer was prepared from deionized water adjusted to pH = 8.0. A plot of absorbance of *p*-nitrophenol at varying concentrations was measured yielding a calibration curve with a slope of 3.48 Abs/mM.[20] MOF samples were prepared by weighing 6 mg of MOF powder and diluting this powder in 10 mL of deionized water. These solutions were rigorously sonicated and vortexed (>3× of each) and diluted in half with 40 mM buffer solution yielding 300 μg/mL MOF in 20 mM buffer solution. Dimethyl *p*-nitrophenylphosphate (DMNP) hydrolysis assays with MOF powders were carried out in Olympus Plastics clear, flat-bottom 96-well plates. Each well was prepared with 100 μL total volume containing: 95 μL MOF suspension in buffer and 5 μL substrate (25 mM DMNP in MeOH; 1.25 mM total concentration; 0.125 μmol). Upon the addition of substrate using a multi-channel pipette, hydrolysis was monitored by the change in absorbance (λ_{max} = 407 nm) over 15 min at 24 °C with 3 sec shaking of the plate every 10 sec. The

absorbance was monitored from the 30 to 360 sec time period, as previously reported in.[17]

Table 5S.3. Corrected hydrolysis calculation to account for increased mass of MOFs used in this study MOF materials.

MOF	**Molar Mass of MOF (*g/mol*)**	**Mole ratio to UiO-66 Standard**	**Experimental Hydrolysis Rate[a] (*k*, mM/sec)**	**Molar Mass Corrected Hydrolysis Rate (*k*, mM/sec)**
UiO-66-F_4	2070	0.80	24.2	30.3
UiO-66-PSE	1662	1.00	50.6	50.6
UiO-66-NH_2-PSE	1752	0.94	76.9	81.8

[a] 6 mg of MOF used in each experiment.

NMR Spectroscopy

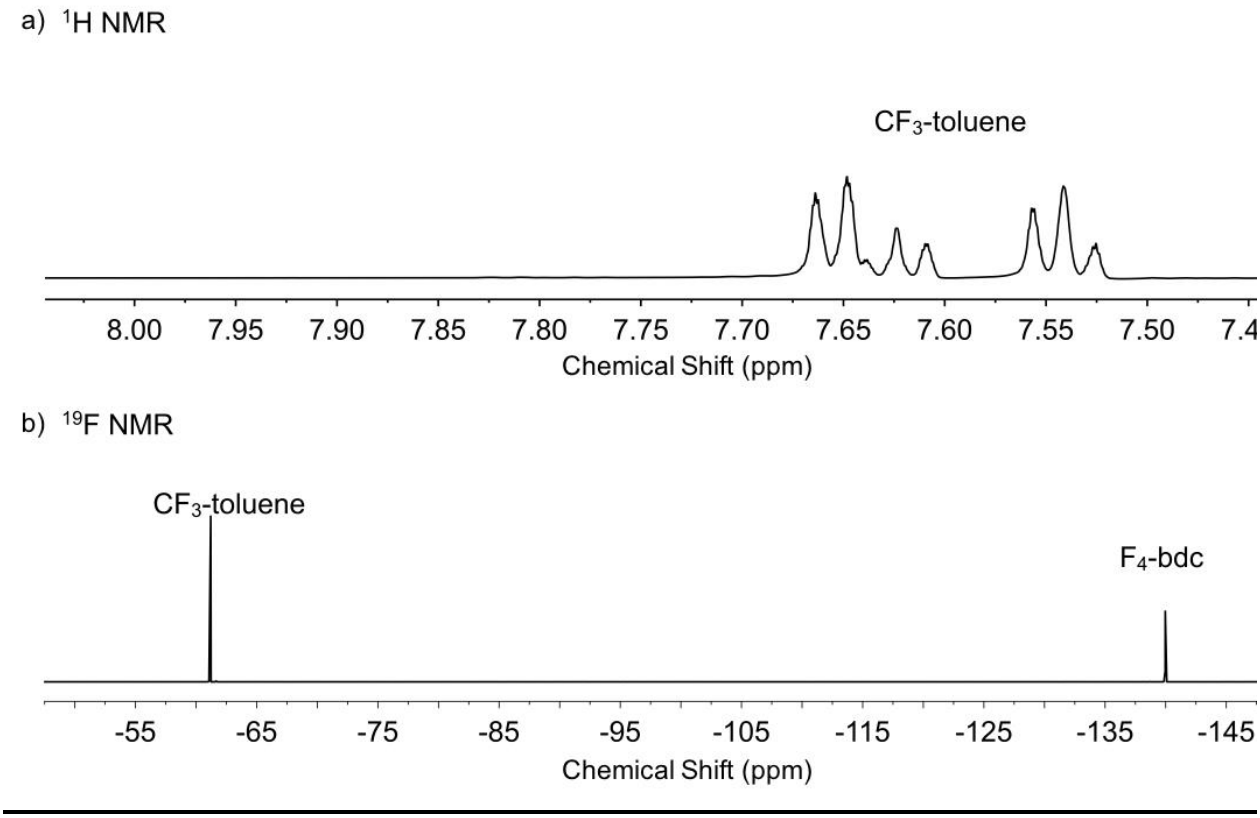

Figure 5S.1. a) ^{1}H NMR spectra of digested UiO-66-F_4. b) ^{19}F NMR spectra of digested UiO-66-F_4.

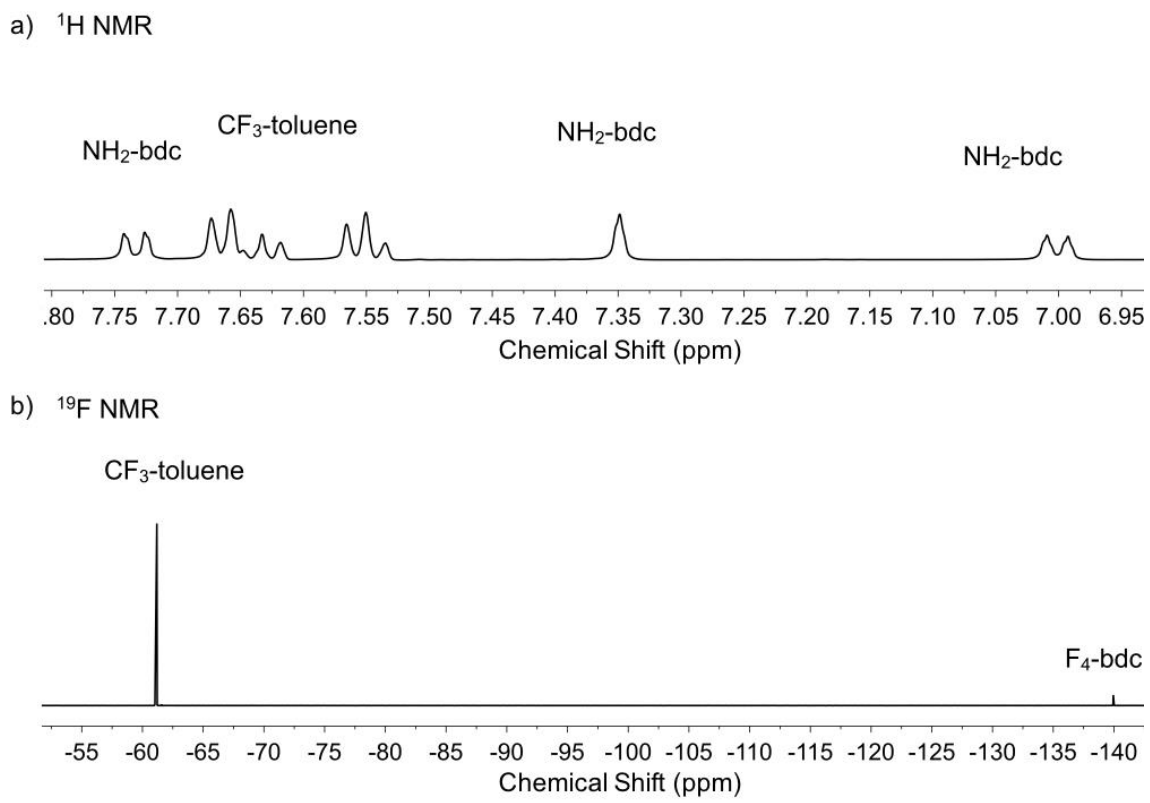

Figure 5S.2. a) ^{1}H NMR spectra of digested UiO-66-NH_2-PSE. b) ^{19}F NMR spectra of digested UiO-66-NH_2-PSE.

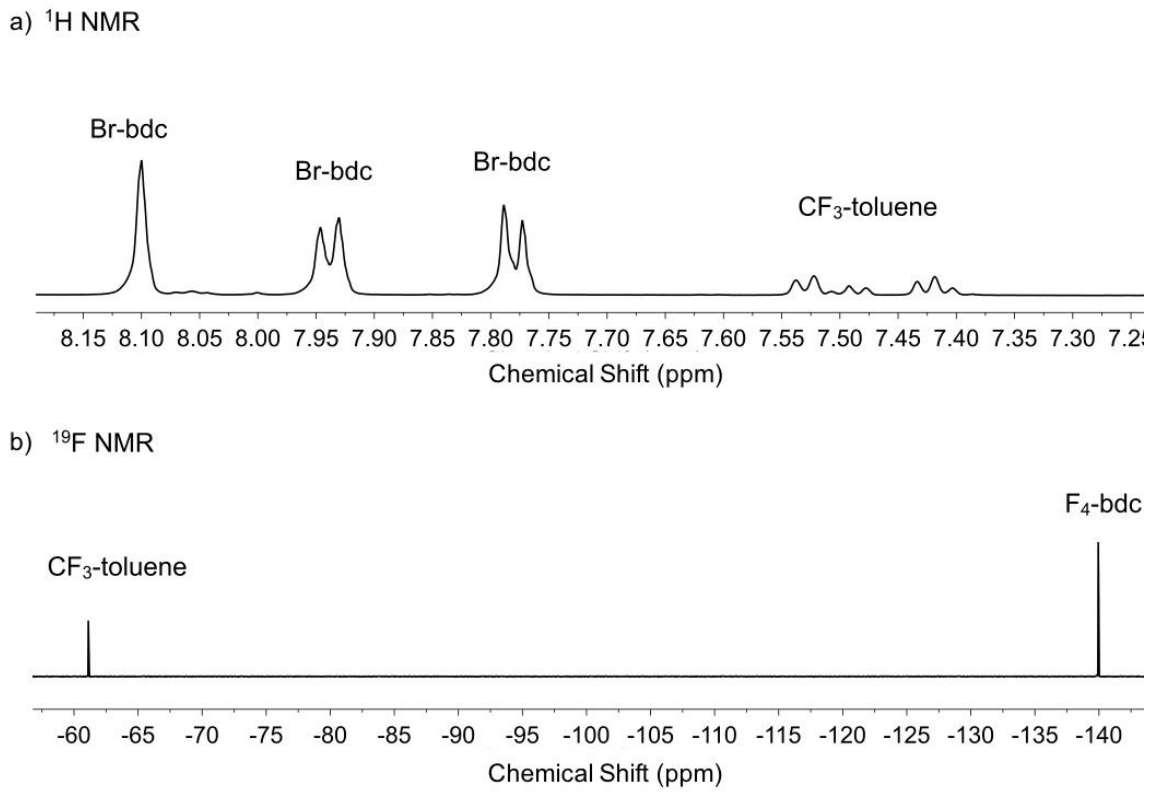

Figure 5S.3. a) ^{1}H NMR spectra of digested UiO-66-Br-PSE. b) ^{19}F NMR spectra of digested UiO-66-Br-PSE.

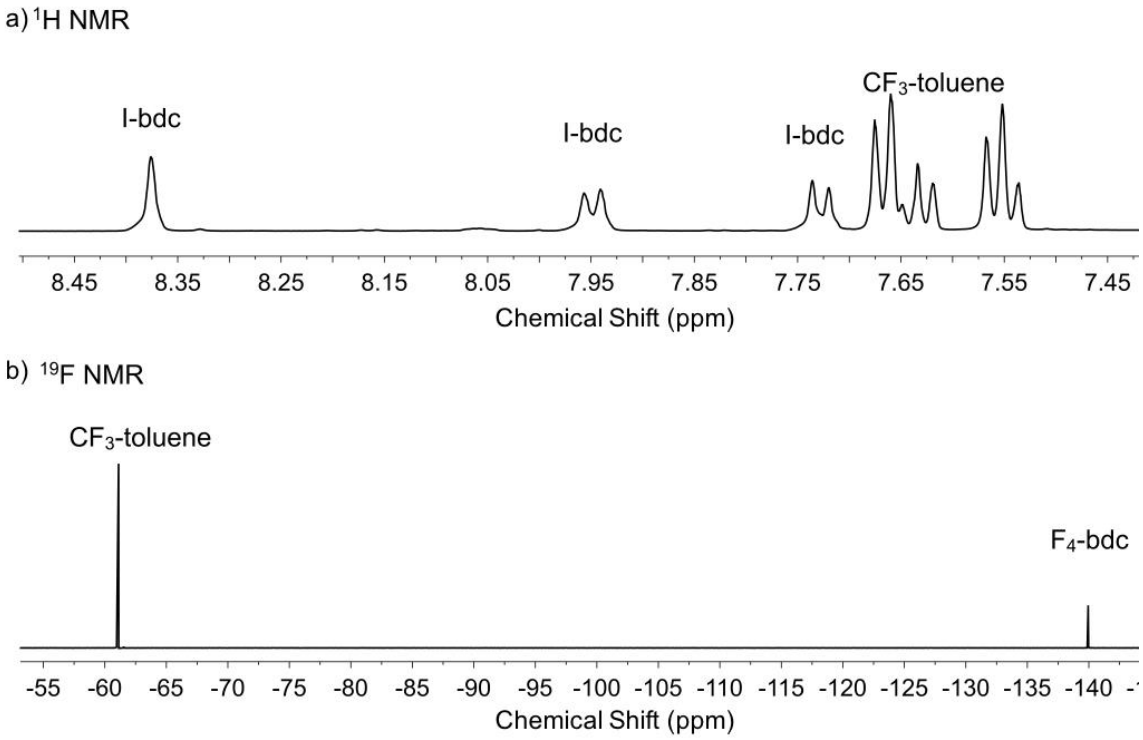

Figure 5S.4. a) ^{1}H NMR spectra of digested UiO-66-I-PSE. b) ^{19}F NMR spectra of digested UiO-66-I-PSE.

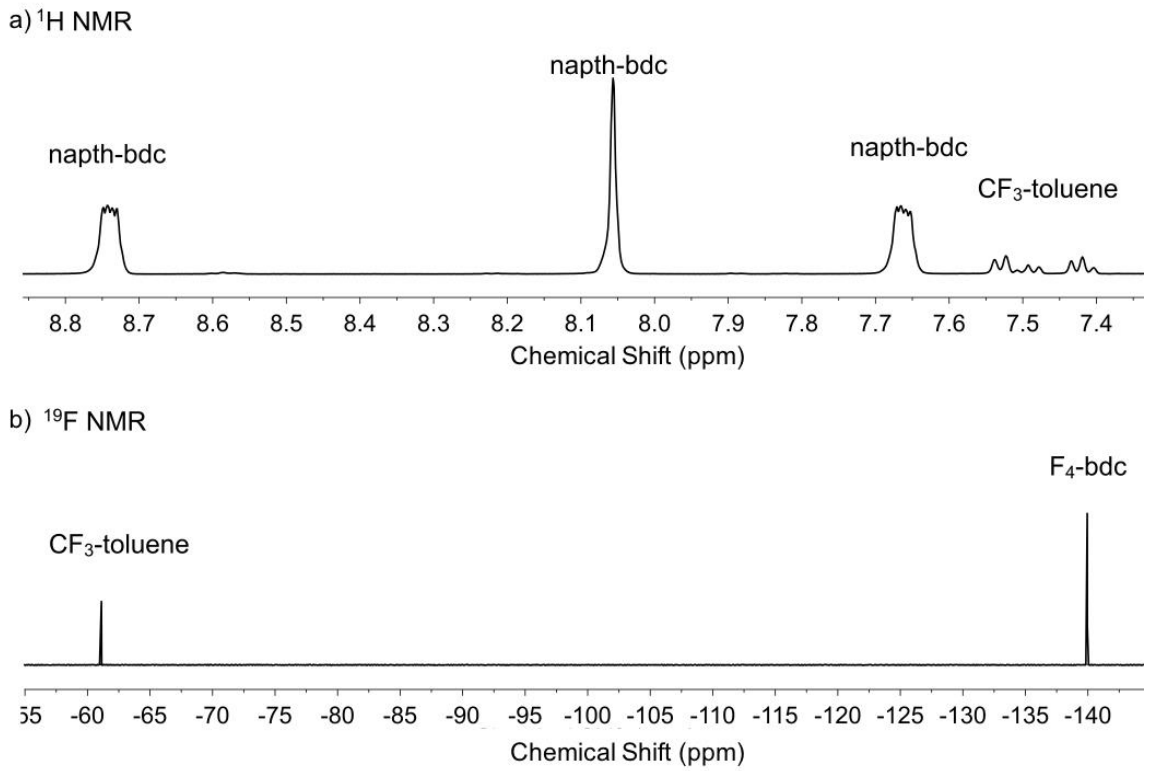

Figure 5S.5. a) ^{1}H NMR spectra of digested UiO-66-Napth-PSE. b) ^{19}F NMR spectra of digested UiO-66-Napth-PSE.

Scanning Electron Microscopy (SEM)

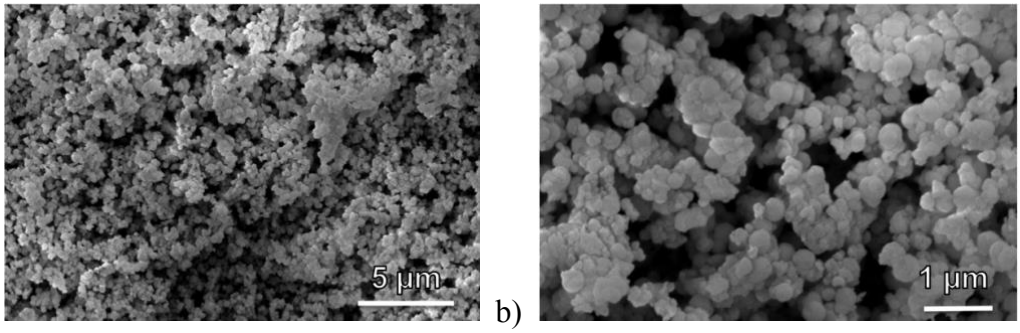

Figure 5S.6. SEM images of UiO-66-NH_2.

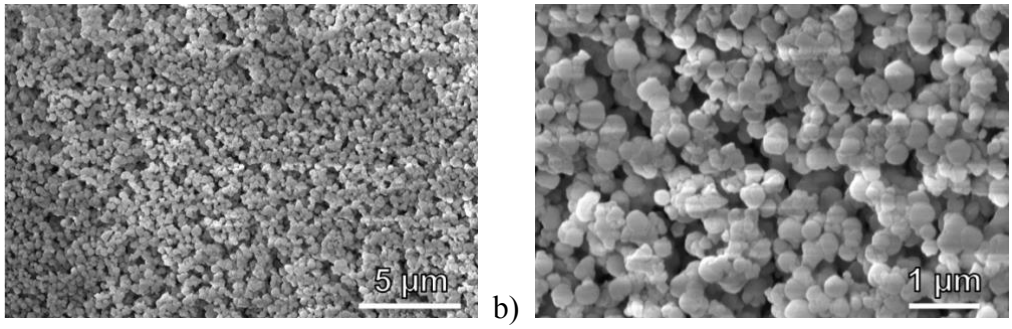

Figure 5S.7. SEM images of UiO-66-Br-PSE.

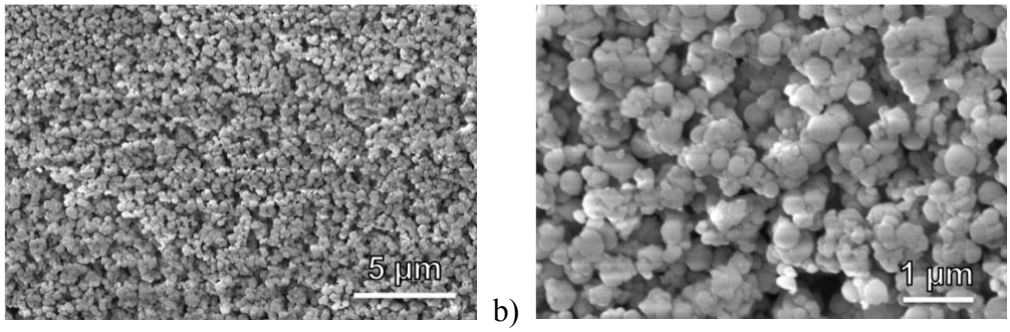

Figure 5S.8. SEM images of UiO-66-I-PSE.

a) 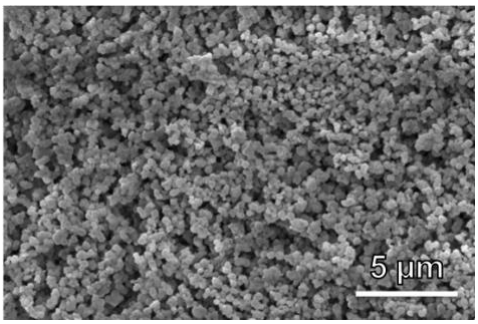

b) 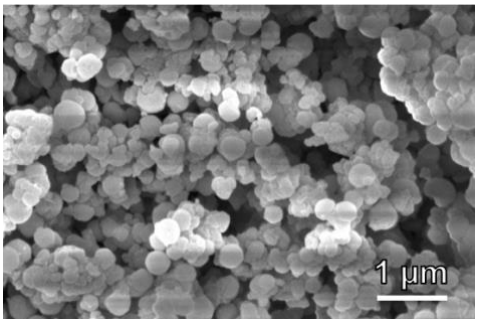

Figure 5S.9. SEM images of UiO-66-Napth-PSE.

5.5 Acknowledgements

Chapter 5, in part, is a reprint of the material, “Room Temperature Aqueous Synthesis of UiO-66 Derivatives via Postsynthetic Exchange” *Dalton Trans.* **2020**, *49*, 8841-8845. The dissertation author was the primary author of this manuscript and gratefully acknowledges the contributions of coauthors Kathleen E. Prosser and Seth M. Cohen.

5.6 References

1. Mondloch, J. E.; Bury, W.; Fairen-Jimenez, D.; Kwon, S.; DeMarco, E. J.; Weston, M. H.; Sarjeant, A. A.; Nguyen, S. T.; Stair, P. C.; Snurr, R. Q.; Farha, O. K.; Hupp, J. T., Vapor-Phase Metalation by Atomic Layer Deposition in a Metal–Organic Framework. *J. Am. Chem. Soc.* **2013,** *135*, 10294-10297.

2. Cavka, J. H.; Jakobsen, S.; Olsbye, U.; Guillou, N.; Lamberti, C.; Bordiga, S.; Lillerud, K. P., A New Zirconium Inorganic Building Brick Forming Metal Organic Frameworks with Exceptional Stability. *J. Am. Chem. Soc.* **2008,** *130*, 13850-13851.

3. Guillerm, V.; Gross, S.; Serre, C.; Devic, T.; Bauer, M.; Férey, G., A zirconium methacrylate oxocluster as precursor for the low-temperature synthesis of porous zirconium(iv) dicarboxylates. *Chem. Commun.* **2010,** *46*, 767-769.

4. DeStefano, M. R.; Islamoglu, T.; Garibay, S. J.; Hupp, J. T.; Farha, O. K., Room-Temperature Synthesis of UiO-66 and Thermal Modulation of Densities of Defect Sites. *Chem. Mater.* **2017,** *29*, 1357-1361.

5. Pakamorė, I.; Rousseau, J.; Rousseau, C.; Monflier, E.; Szilágyi, P. Á., An Ambient-Temperature Aqueous Synthesis of Zirconium-Based Metal–Organic Frameworks. *Green Chem.* **2018,** *20*, 5292-5298.

6. Hu, Z.; Peng, Y.; Kang, Z.; Qian, Y.; Zhao, D., A Modulated Hydrothermal (MHT) Approach for the Facile Synthesis of UiO-66-Type MOFs. *Inorg. Chem.* **2015,** *54*, 4862-4868.

7. Reinsch, H.; Bueken, B.; Vermoortele, F.; Stassen, I.; Lieb, A.; Lillerud, K.-P.; De Vos, D., Green synthesis of zirconium-MOFs. *CrystEngComm* **2015,** *17*, 4070-4074.

8. Yang, Q.; Vaesen, S.; Ragon, F.; Wiersum, A. D.; Wu, D.; Lago, A.; Devic, T.; Martineau, C.; Taulelle, F.; Llewellyn, P. L.; Jobic, H.; Zhong, C.; Serre, C.; De Weireld, G.; Maurin, G., A Water Stable Metal–Organic Framework with Optimal Features for CO2 Capture. *Angew. Chem., Int. Ed.* **2013,** *52*, 10316-10320.

9. Avci-Camur, C.; Perez-Carvajal, J.; Imaz, I.; Maspoch, D., Metal Acetylacetonates as a Source of Metals for Aqueous Synthesis of Metal–Organic Frameworks. *ACS Sustainable Chem. Eng.* **2018,** *6*, 14554-14560.

10. Užarević, K.; Wang, T. C.; Moon, S.-Y.; Fidelli, A. M.; Hupp, J. T.; Farha, O. K.; Friščić, T., Mechanochemical and solvent-free assembly of zirconium-based metal–organic frameworks. *Chem. Commun.* **2016,** *52*, 2133-2136.

11. Chen, Z.; Wang, X.; Noh, H.; Ayoub, G.; Peterson, G. W.; Buru, C. T.; Islamoglu, T.; Farha, O. K., Scalable, room temperature, and water-based synthesis of functionalized zirconium-based metal–organic frameworks for toxic chemical removal. *CrystEngComm* **2019,** *21*, 2409-2415.

12. Kim, M.; Cahill, J. F.; Fei, H.; Prather, K. A.; Cohen, S. M., Postsynthetic Ligand and Cation Exchange in Robust Metal-Organic Frameworks. *J. Am. Chem. Soc.* **2012,** *134*, 18082-18088.

13. Kim, M.; Cahill, J. F.; Su, Y.; Prather, K. A.; Cohen, S. M., Postsynthetic ligand exchange as a route to functionalization of metal-organic frameworks. *Chem. Sci.* **2012,** *3*, 126-130.

14. Deng, H.; Doonan, C. J.; Furukawa, H.; Ferreira, R. B.; Towne, J.; Knobler, C. B.; Wang, B.; Yaghi, O. M., Multiple Functional Groups of Varying Ratios in Metal-Organic Frameworks. *Science* **2010,** *327*, 846-850.

15. Kalaj, M.; Palomba, J. M.; Bentz, K. C.; Cohen, S. M., Multiple functional groups in UiO-66 improve chemical warfare agent simulant degradation. *Chem. Commun.* **2019,** *55*, 5367-5370.

16. Kandiah, M.; Nilsen, M. H.; Usseglio, S.; Jakobsen, S.; Olsbye, U.; Tilset, M.; Larabi, C.; Quadrelli, E. A.; Bonino, F.; Lillerud, K. P., Synthesis and Stability of Tagged UiO-66 Zr-MOFs. *Chem. Mater.* **2010,** *22*, 6632-6640.

17. Kalaj, M.; Momeni, M. R.; Bentz, K. C.; Barcus, K. S.; Palomba, J. M.; Paesani, F.; Cohen, S. M., Halogen bonding in UiO-66 frameworks promotes superior chemical warfare agent simulant degradation. *Chem. Commun.* **2019,** *55*, 3481-3484.

18. Kalaj, M.; Denny Jr, M. S.; Bentz, K. C.; Palomba, J. M.; Cohen, S. M., Nylon–MOF Composites through Postsynthetic Polymerization. *Angew. Chem., Int. Ed.* **2019,** *58*, 2336-2340.

19. Mondloch, J. E.; Katz, M. J.; Isley Iii, W. C.; Ghosh, P.; Liao, P.; Bury, W.; Wagner, G. W.; Hall, M. G.; DeCoste, J. B.; Peterson, G. W.; Snurr, R. Q.; Cramer, C. J.; Hupp, J. T.; Farha, O. K., Destruction of chemical warfare agents using metal–organic frameworks. *Nat. Mater.* **2015,** *14*, 512-516.

20. Palomba, J. M.; Credille, C. V.; Kalaj, M.; DeCoste, J. B.; Peterson, G. W.; Tovar, T. M.; Cohen, S. M., High-throughput screening of solid-state catalysts for nerve agent degradation. *Chem. Commun.* **2018,** *54*, 5768-5771.